Springer ThesesRecognizing Outstanding Ph.D. Research

Santiago Erroz-Ferrer

Morphology,
Kinematics and Star
Formation Across the
Hubble Sequence
of Galaxies



Springer Theses

Recognizing Outstanding Ph.D. Research

Aims and Scope

The series "Springer Theses" brings together a selection of the very best Ph.D. theses from around the world and across the physical sciences. Nominated and endorsed by two recognized specialists, each published volume has been selected for its scientific excellence and the high impact of its contents for the pertinent field of research. For greater accessibility to non-specialists, the published versions include an extended introduction, as well as a foreword by the student's supervisor explaining the special relevance of the work for the field. As a whole, the series will provide a valuable resource both for newcomers to the research fields described, and for other scientists seeking detailed background information on special questions. Finally, it provides an accredited documentation of the valuable contributions made by today's younger generation of scientists.

Theses are accepted into the series by invited nomination only and must fulfill all of the following criteria

- They must be written in good English.
- The topic should fall within the confines of Chemistry, Physics, Earth Sciences, Engineering and related interdisciplinary fields such as Materials, Nanoscience, Chemical Engineering, Complex Systems and Biophysics.
- The work reported in the thesis must represent a significant scientific advance.
- If the thesis includes previously published material, permission to reproduce this must be gained from the respective copyright holder.
- They must have been examined and passed during the 12 months prior to nomination.
- Each thesis should include a foreword by the supervisor outlining the significance of its content.
- The theses should have a clearly defined structure including an introduction accessible to scientists not expert in that particular field.

More information about this series at http://www.springer.com/series/8790

Santiago Erroz-Ferrer

Morphology, Kinematics and Star Formation Across the Hubble Sequence of Galaxies

Doctoral Thesis accepted by the University of La Laguna, Spain



Author
Dr. Santiago Erroz-Ferrer
Instituto de Astrofísica de Canarias
University of La Laguna
San Cristóbal de La Laguna
Spain

Supervisor
Prof. Johan Knapen
Instituto de Astrofísica de Canarias
University of La Laguna
San Cristóbal de La Laguna
Spain

and

Case Western Reserve University Cleveland, OH USA

ISSN 2190-5053 ISSN 2190-5061 (electronic) Springer Theses ISBN 978-3-319-26397-7 ISBN 978-3-319-26398-4 (eBook) DOI 10.1007/978-3-319-26398-4

Library of Congress Control Number: 2015954963

Springer Cham Heidelberg New York Dordrecht London © Springer International Publishing Switzerland 2016

This work is subject to copyright. All rights are reserved by the Publisher, whether the whole or part of the material is concerned, specifically the rights of translation, reprinting, reuse of illustrations, recitation, broadcasting, reproduction on microfilms or in any other physical way, and transmission or information storage and retrieval, electronic adaptation, computer software, or by similar or dissimilar methodology now known or hereafter developed.

The use of general descriptive names, registered names, trademarks, service marks, etc. in this publication does not imply, even in the absence of a specific statement, that such names are exempt from the relevant protective laws and regulations and therefore free for general use.

The publisher, the authors and the editors are safe to assume that the advice and information in this book are believed to be true and accurate at the date of publication. Neither the publisher nor the authors or the editors give a warranty, express or implied, with respect to the material contained herein or for any errors or omissions that may have been made.

Printed on acid-free paper

Springer International Publishing AG Switzerland is part of Springer Science+Business Media (www.springer.com)

Supervisor's Foreword

Galaxies are the building blocks of the Universe, and the study of their formation and evolution is key to the understanding of how the Universe has acquired its present shape. Of particular interest is the detailed study of the internal, or secular, evolution of galaxies. This describes the evolution induced by internal processes such as the actions of spiral arms, bars, ovals, galactic winds, black holes, and dark matter haloes. Secular evolution plays an important role in the evolution of spiral galaxies, and one key advantage is that one can study the relevant physics in great detail through observations of the nearest galaxies.

This thesis describes a study of the morphology, kinematics, and star formation properties of carefully selected samples of nearby galaxies. The work is closely related to the *Spitzer* Survey of Stellar Structure of Galaxies (S^4G), a mid-infrared imaging study of some 3000 nearby galaxies. This Survey has provided accurate measurements of many basic parameters of the sample galaxies, such as morphological type, stellar mass, and the presence of structural components such as bars, lenses, or rings. In the context of this thesis, a subsample of 29 galaxies was selected from the overall sample for follow-up study, and observed with two different instruments on the 4.2 m William Herschel Telescope in La Palma: ACAM and $GH\alpha FAS$. With those, imaging in the $H\alpha$ line and Fabry-Perot spectroscopy was obtained, to derive star formation rates and gas kinematics, respectively.

Among the main results of the thesis is the study of correlations of kinematic parameters of the sample galaxies, such as the central slope of the rotation curve, with the overall parameters of the galaxies and their spiral arms and bars. A fundamental advance here is that a sample of 29 galaxies was used, spanning a wide range in morphological type, stellar mass, and bar and spiral properties, and that kinematic data at high spatial and spectral resolution were obtained for all of them. In combination with the accurate parameters yielded by the S⁴G survey, important results are obtained on streaming and other non-circular motions in galaxies, on the distribution and rates of star formation, and on how correlations of these parameters and of the rotation curve shape with basic galaxy parameters yield clues on the evolutionary processes taking place in disk galaxies. The data

obtained for this project have all been made public, and form part of the lasting legacy of this work.

This thesis work, carried out between September 2010 and October 2014 at the University of La Laguna and the Instituto de Astrofísica de Canarias, has led to a number of publications in refereed journals and presentations at international conferences. The thesis was defensed at the Aula Magna of the Physics Faculty of the University of La Laguna (Tenerife, Spain), and was honoured Summa Cum Laude.

San Cristóbal de La Laguna July 2015 Prof. Johan Knapen

Preface

The topic of this thesis is the study of the morphology, kinematics, and star formation of nearby galaxies, aiming to clarify a number of long-standing open questions about their formation, evolution, and physical properties.

First, I have addressed the star formation and its distribution across the Hubble sequence of galaxies. In particular, I have studied massive star formation in elliptical, lenticular, and early-type galaxies. Although these galaxies have generally low gas content and low levels of star formation, there is a significant subset that shows evidence of ongoing star formation in the form of extended UV emission. I have obtained H α imaging of ten such galaxies, finding that in most cases, their star formation rates are comparable to those found in disk galaxies. This is probably because the sample selection is biased toward star-forming galaxies. I confirm that massive star formation causes the extended UV emission in our sample, in the form of outer spiral arms and/or outer (pseudo) rings.

This thesis has been developed in the context of the *Spitzer* Survey of Stellar Structure in Galaxies (S^4G), which has obtained mid-IR images of more than 2350 galaxies in the local Universe. These images and the studies within the S^4G collaboration have been complemented with the ancillary kinematic data obtained within the framework of this thesis. I present a kinematical study of 29 spiral galaxies included in the S^4G sample, using H α Fabry-Perot (FP) data obtained with the Galaxy H α Fabry-Perot System instrument at the William Herschel Telescope in La Palma, complemented with images in the *R* band and in H α . The primary goal is to study the evolution and properties of the main structural components of galaxies through the kinematical analysis of the FP data, complemented with studies of morphology, star formation, and mass distribution. In this thesis, I describe how these data have been obtained, processed, and analyzed. This program of 3D kinematics enables the study of the motions of the ionized gas within the galaxies, including in-depth investigations of the rotation curves, velocity moment maps, velocity residual maps, and position–velocity diagrams.

Galaxy disks are supported by rotation to minimize the total energy when conserving the angular momentum. However, through the evolution of a galaxy,

viii Preface

several processes interfere on the kinematics of the galaxy and provoke deviations from the pure rotation, what we call non-circular motions. In particular, non-axisymmetric structures such as bars are understood to create potentials that influence the way material move toward the center of the galaxy. As a first step to understand the non-circular motions, I present detailed results on the barred galaxy NGC 864 from the kinematical program. I find asymmetries in the velocity field in the bar zone, caused by non-circular motions, probably in response to the potential of the bar.

The study regarding the non-circular motions is expanded to the whole sample of galaxies. In particular, those motions found along the bars and spiral arms. The data indicate that the amplitude of the non-circular motions created by the bar in the $H\alpha$ gas does not correlate with the strength of the bar. The amplitude of those non-circular motions related to the spiral arms does not correlate with either arm class or star formation rate along the spiral arms. This implies that the presence and magnitude of streaming motions in the arms seem to be a local phenomenon. I also study here the global SFRs of the galaxies of the sample, and in particular the star formation within the bar and its relationship with its kinematics.

The dynamics in the central parts of galaxies are influenced by both baryonic matter (gas and stars) and DM. This thesis will try to find out which contribution is more important regarding the dynamics of the central parts of the galaxy. Taking advantage of the high angular and spectral resolution of the kinematic data, I perform a detailed study of the shape of the innermost part of the rotation curve of the sample galaxies. In particular, I quantify the steepness of the rotation curve by measuring its slope. As previously noted in the literature and, in fact, physically intuitive, I find that the compactness of the mass in the central parts of a galaxy (more concretely, the presence of the bulge) is translated into steeper slopes. Otherwise, I find no influence of the degree of secular evolution of a galaxy on the value of the slope, as the presence of the bar and the star formation rate does not correlate with the slope. I find that although the luminous matter dominates the gravitational potential in the central parts of the galaxies, dark matter is also present.

Acknowledgments

I would like to thank Johan Knapen, Ryan Leaman, Mauricio Cisternas, and Barry Madore for his comments and suggestions during the preparation of this thesis. I would like to thank Inma Martínez Valpuesta for her suggestions as the referee of the thesis. I would like to thank Joan Font and José Ramón Sánchez-Gallego for their assistance with the reduction and calibration of the FP and $H\alpha$ data. I would like to thank the Carnegie Observatories for hospitality and facility support.

The thesis is based on observations made with the NOT and WHT operated on the island of La Palma, in the Spanish Observatorio del Roque de Los Muchachos of the Instituto de Astrofísica de Canarias. The data presented here were obtained in part with ALFOSC, which is provided by the Instituto de Astrofísica de Andalucia under a joint agreement with the University of Copenhagen and NOTSA.

Some of the data presented in this paper were obtained from the Mikulski Archive for Space Telescopes (MAST). STScI is operated by the Association of Universities for Research in Astronomy, Inc., under NASA contract NAS5-26555. Support for MAST for non-*HST* data is provided by the NASA Office of Space Science via grant NNX09AF08G and by other grants and contracts. I thank the entire S⁴G team for their efforts in this project. This research has made use of the HyperLeda database (http://leda.univ-lyon1.fr) and the NASA/IPAC Extragalactic Database (NED), which is operated by JPL, Caltech, under contract with NASA.

Contents

1	Intr	oductio	n	1
	1.1	Secula	r Evolution	1
	1.2	Morph	ology and the Hubble Sequence of Galaxies	3
		1.2.1	Classical Galaxy Classification	3
		1.2.2	The Kinematics-Based Classification of Galaxies	
			by ATLAS ^{3D}	4
		1.2.3	The Comprehensive de Vaucouleurs Revised	
			Hubble-Sandage System	5
	1.3	Kinem	atics of Nearby Galaxies	7
	1.4	Massiv	ve Star Formation	10
		1.4.1	Historical Introduction and Generalities	10
		1.4.2	Star Formation Tracers	12
	1.5	The S	G Survey	15
	1.6	Thesis	Outline	16
	Refe	erences .		16
2	Mas	sive Sta	ar Formation in Galaxies with Excess UV Emission	23
	0.1	Introdu	action	23
	2.1	muoat	action	20
	2.1		Selection	25
		Target		
	2.2	Target	Selection	25
	2.2	Target Observ	Selection	25 26
	2.2	Target Observ 2.3.1 2.3.2	Selection	25 26 26
	2.2 2.3	Target Observ 2.3.1 2.3.2	Selection	25 26 26 28
	2.2 2.3	Observe 2.3.1 2.3.2 Results	Selection	25 26 26 28 28
	2.2 2.3	Target Observ 2.3.1 2.3.2 Results 2.4.1	Selection	25 26 26 28 28 28
	2.2 2.3	Target Observ 2.3.1 2.3.2 Results 2.4.1 2.4.2 2.4.3	Selection. vations and Data Reduction ALFOSC R-Band and Hα. GALEX UV. S. Morphology: General. Morphology: Individual Galaxies.	25 26 26 28 28 28 29
	2.2 2.3 2.4	Target Observ 2.3.1 2.3.2 Results 2.4.1 2.4.2 2.4.3	Selection. Vations and Data Reduction ALFOSC R-Band and Hα. GALEX UV. S. Morphology: General. Morphology: Individual Galaxies. Star Formation Rates.	25 26 28 28 28 29 33
	2.2 2.3 2.4	Target Observed 2.3.1 2.3.2 Results 2.4.1 2.4.2 2.4.3 Discussion	Selection. Vations and Data Reduction ALFOSC R-Band and Hα. GALEX UV. S. Morphology: General. Morphology: Individual Galaxies. Star Formation Rates	25 26 28 28 28 29 33 36
	2.2 2.3 2.4	Target Observ 2.3.1 2.3.2 Result 2.4.1 2.4.2 2.4.3 Discus 2.5.1	Selection. vations and Data Reduction ALFOSC R-Band and Hα. GALEX UV. S. Morphology: General. Morphology: Individual Galaxies. Star Formation Rates ssion Morphology.	25 26 26 28 28 28 29 33 36 36

xii Contents

3	Ηα	Kinematics of S ⁴ G Spiral Galaxies: The Data 43	3
	3.1	Introduction	3
	3.2	Target Selection	4
	3.3	Observations	6
	3.4	Data Reduction	8
		3.4.1 Fabry-Perot: $GH\alpha FaS$	8
		3.4.2 Hα Imaging: ACAM	1
	3.5	Rotation Curves	2
	3.6	Non-circular Motion Maps	5
	3.7	Data Release	5
	3.8	Discussion: Data Quality	6
		3.8.1 Effects from the Nature of the H α Data	6
		3.8.2 Kinematical Parameters Versus Photometric	
		Parameters	6
		3.8.3 Comparison with Literature Data 58	8
	Refe	ences	3
4	CAmo	ming Motions in the Spiral Galaxy NGC 864 65	_
4	Stre 4.1	· · · · · · · · · · · · · · · · · · ·	
	4.1		
	4.2	ϵ	
	4.3		
		4.3.1 ACAM	
		4.3.2 GH α FaS	_
		4.3.3 SAURON	
	4.4	4.3.4 S ⁴ G image	
	4.4	Results	
		4.4.1 Morphology	
		4.4.2 Kinematics	
		4.4.3 Star Formation Rate	
	4.5	Discussion: Influence of the Bar on the Kinematics	
	Refe	ences	2
5	Non	circular Motions and Star Formation in S ⁴ G Galaxies 83	5
	5.1	Introduction	5
	5.2	Methodology 86	6
		5.2.1 Non-circular Motions 86	6
		5.2.2 Structural Parameters	8
		5.2.3 Star Formation Rates	0
	5.3	Results	1
		5.3.1 Bar-Induced Non-circular Motions	1
		5.3.2 Spiral-Induced Non-circular Motions	4
		5.3.3 Special Case: NGC 5678	5
	Dofe	ences 09	Q

Contents xiii

6	Inne	er Rota	tion Curves	101	
	6.1	Introd	uction	101	
	6.2	The D	Oata	104	
		6.2.1	Sample, Observations and Data Reduction	104	
		6.2.2	$H\alpha$ Luminosities and Star Formation Rates	104	
		6.2.3	Rotation Curves Derived from the Stellar Mass Maps	106	
		6.2.4	Asymmetric Drift Correction	107	
		6.2.5	Determination of the Rotation Curve Slopes	109	
	6.3	Result	is	110	
		6.3.1	Rotation Curve Slopes and Physical Properties		
			of Galaxies	112	
	6.4	Discus	ssion: Cosmological Versus Secular	120	
		6.4.1	Secular Evolution	121	
		6.4.2	Cosmological Parameters	125	
		6.4.3	Implications on Dark Matter Distribution	126	
	Refe	erences		126	
7	Con	clusion	s and Future Work	131	
	7.1	Concl	usions	131	
	7.2 Future Work				
	Refe	erences		136	
Αŗ	pend	lix A: F	Figures: Individual Maps	137	
Αŗ	pend	lix B: F	Rotation Curves	153	
Αŗ	pend	lix C: I	Position-Velocity Diagrams	159	
Αŗ	pend	lix D: F	Rotation Curve Fits	169	
Αŗ	pend	lix E: (Other Relevant Studies	175	
In	dex .			201	

Chapter 1 Introduction

A galaxy can be defined as a massive, gravitationally bound system consisting of stars, stellar remnants, an interstellar medium of gas and dust, and finally dark matter, an important but poorly understood component. Galaxies are understood to be the basic building blocks of the Universe as they are the substructures that constitute it. Galaxies are part of the hierarchical distribution of matter within the Universe. It has been nearly a century since the term galaxy was first introduced (de Sitter 1917; Crommelin 1918; Shapley 1919) to define systems that were external to our Milky Way and expanding away from it (Slipher 1917; Friedmann 1922; Hubble 1926; Lemaître 1927). In this thesis, I will study the characteristics of these structures, in particular, their morphology, kinematics and star formation across the Hubble Sequence of galaxies.

1.1 Secular Evolution

From the moment that a galaxy is formed, it undergoes through certain processes which vary its characteristics. Depending on the nature of these processes, they can be grouped into internally or externally driven. Also, it is possible to divide those processes regarding the timescales in which they operate, leaving two groups: fast and slow processes. I will refer to the slow processes as *secular* processes. Figure 1.1 represents the scheme of processes based on Fig. 1 of Kormendy and Kennicutt (2004) that shows this twofold organization. One should note that all processes belong to one group or another in both time/nature classifications. For instance, the process of galaxy merging belongs to the fast processes, and to the externally driven ones. On the other side, from the point of view of Kormendy, the formation of a disc-like bulge is a slow and internal process.

1

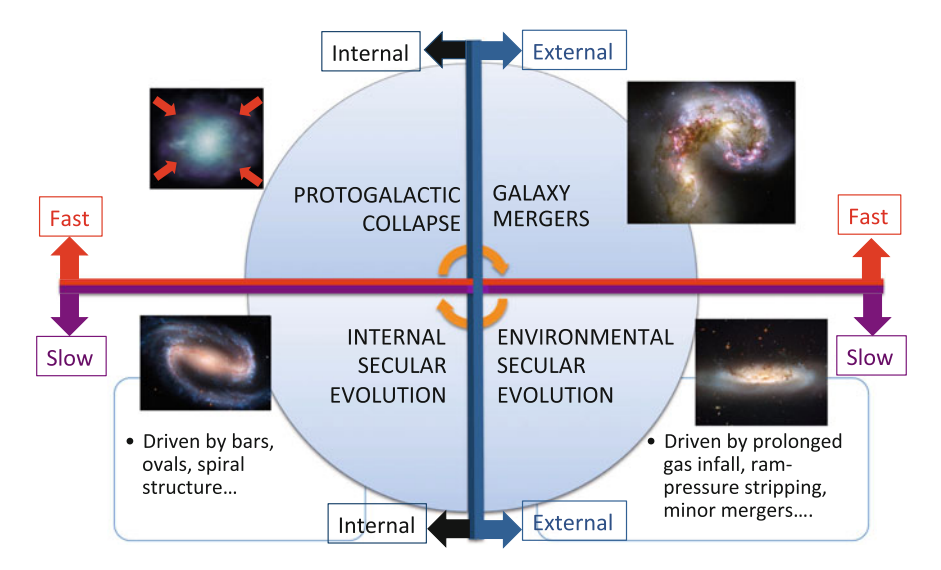


Fig. 1.1 Scheme of the processes that occur throughout the evolution of a galaxy, updated from Fig. 1 of Kormendy and Kennicutt (2004). Here, the double division between fast/slow processes and internal and externally driven processes is shown

In this thesis, I will in particular study the secular processes, giving more importance to those driven by internal processes. When I say secular/slow processes, I mean the gradual processes of a galaxy over timescales much longer than the crossing time or collapse time. The topic of secular evolution in galaxies have been widely studied in the literature. In the past years, excellent reviews have been written by Kormendy and Kennicutt (2004) and Kormendy and Bender (2012) from an observational point of view; and by Sellwood (2014) from a more theoretical perspective.

Also, this topic was addressed in the XXIII Canary Islands Winter School of Astrophysics, with lectures from nine renowned experts (see the proceedings in Secular Evolution of Galaxies, XXIII Canary Islands Winter School of Astrophysics, Falcón-Barroso and Knapen 2013).

The reviews and lectures cited above explain the picture of internally-driven processes that gradually rearrange the structure of galaxies. These processes involve redistribution of material (gas, stars) and angular momentum transfer between the different galaxy components (bars, spiral arms, stellar haloes, ovals, rings or black holes). Some of these processes are: disc growth through slow accretion of gas, the formation and evolution of bars, recurring spiral instabilities, the response of the stellar system to the radial rearrangement of matter, etc.

The footprints of secular evolution can be found by analysing the galaxy shape (commonly called galaxy morphology), the way the material inside the galaxy moves (galaxy kinematics), and the formation of stars (star formation). By studying all these, we can have an idea of the formation and evolution of the galaxies. Concretely, nearby galaxies are the vivid result of the evolution of the Universe. They contain the

1.1 Secular Evolution 3

footprints of the evolution processes that have led to the present status of the galaxies, which I will study here. The key of this thesis is the comprehensive study of the three topics cited above (morphology, kinematics and star formation), implicitly referencing to the secular evolution that is intimately connected to the studied processes. This thorough study will address a number of points that are not completely understood (see the reviews cited above), such as the influence of the bar on the kinematics in barred galaxies, the relationship between the presence of a bulge (possible merging formation) and the distribution of mass within galaxies, and the relationship between star formation and the evolution of the structural components of a galaxy.

1.2 Morphology and the Hubble Sequence of Galaxies

1.2.1 Classical Galaxy Classification

The discovery that some of the observed *nebulae* are external objects to our galactic system led to several studies regarding their characterisation. In the first half of the XXth century, several studies regarding the morphology of these *nebulae* began. Thorough studies of the morphology of galaxies are an important clue to understand the formation and evolution of these objects. As noted by Peng (2002): "clues to galaxy formation and evolution are hidden in the fine details of galaxy structure".

The development of visual classification of galaxies gained importance with the development of telescopes. One of the first descriptive classifications of nebulae was carried out by William Herschel and his son John, with 47-cm reflectors. They used a simple classification based on brightness, size, shape and central concentration, compiled in Herschel (1864). The observations carried out by William Parsons with the 1.8 m Leviathan of Parsonstown telescope had much more detail than those of the Herschels, and could show detailed structures of these *nebulae*, such as spiral arms, rings, bars or dust lanes. Wolf (1908), Knox-Shaw (1915), Curtis (1918) and Reynolds (1920) started the division between spiral and elliptical galaxy types. Hubble (1926) published a possible sequence of galaxies that consisted of a transition from elliptical-shaped objects to well-developed spirals, in which spirals were divided into barred and non-barred. This sequence constitutes the so-called Hubble Sequence of Galaxies. Inspired by Hubble's work, Jeans (1928) presented this sequence through a tuning fork diagram, and finally this diagram gained popularity with the illustration presented in Hubble's book *The Realm of the Nebulae*, published in Hubble (1936b).

Despite Hubble's will to revise this classification, he died before finishing it. Allan Sandage took Hubble's notes and prepared the *Hubble atlas of galaxies* (Sandage 1961), which solidified Hubble's classification scheme and improved it by adding S0 galaxies as well as a division into ringed and non-ringed varieties. This work done by Allan Sandage is known as the Revised Hubble-Sandage (RHS) system, further

developed in Sandage et al. (1975) and revised in the *Carnegie Atlas of Galaxies* (Sandage and Bedke 1994).

During the second half of the XXth century, many studies regarding galaxy morphology have been carried out to improve Hubble's sequence of galaxies. One of the most important advances was developed by Gerard de Vaucouleurs, named *de Vaucouleurs Revised Hubble Classification System* (VRHS). Through his *Classification volume*, also known as *Three-pronged swirling two-handed tuning fork* (de Vaucouleurs 1959), he expanded the idea of the Hubble sequence of galaxies through a three-dimensional continuous scheme: continuous sequence of classes (E, S0, Sam, Im) horizontally, families (SA, SAB, SB) vertically and varieties [(r), (rs), (s)] perpendicular to the page. The VHRS introduced several developments with respect to the original Hubble scheme, such as the addition of the extreme late-type spirals and the division or "stages" within ellipticals (E and E⁺) and lenticulars (S0⁻, S0^o and S0⁺).

The VRHS system has had several revisions and additions. Morgan (1958, 1959) developed a classification system based largely on the importance of the bulge and the stellar populations. Van den Bergh (1960a, b, 1966) presented the relationship between the total luminosity of the galaxy and the galaxy morphology. He introduced the term *luminosity classes* I–V, based on the idea that the more luminous the galaxy, the better-structured. Motivated by Spitzer and Baade (1951), Baade and Gaposchkin (1963) and van den Bergh (1976a) proposed that S0s formed a parallel sequence to spiral galaxies (known as the *parallel sequence classification*. Inner and outer lenses were added to the VRHS by Buta (1995), using the notation suggested by Kormendy (1979). The flattening index *n* written after E for elliptical galaxies has no physical meaning, and Kormendy and Bender (1996) tried to solve this by distinguishing between *boxy* and *disky* Es.

One of the revisions of the VRHS system (that is still under debate nowadays) arises from the inclusion of dwarf galaxy types by Binggeli et al. (1985): dE-dwarf ellipticals; cE-compact ellipticals; dE,N-nucleated compact dwarf ellipticals; dS0s-dwarf lenticulars; dS0,N-nucleated dwarf S0; BCD-blue compact dwarf and large dE. The controversy of the origin of dwarf ellipticals has been thoroughly studied by, e.g., Kormendy (1985), Kormendy et al. (2009) and Kormendy and Bender (2012), reclassifying dE and dS0 as spheroidal galaxies, and defining them as the descendants of late spirals and not the low-luminosity versions of ellipticals.

1.2.2 The Kinematics-Based Classification of Galaxies by ATLAS^{3D}

Although not used in this thesis, it is important to mention the work done by the ATLAS^{3D} team who created a galaxy classification based on the kinematics rather than on visual morphology. Cappellari et al. (2011b) suggest to order early-type galaxies (ETGs) kinematically instead of morphologically. They propose a "comb"

diagram as an alternative to Hubble's tuning fork diagram to classify galaxies. ETGs arranged on the handle, are classified according to their net rotation into slow and fast rotators. The spirals are placed along three teeth. The fast-rotators at the junction of the teeth and comb likely evolved from that family of spirals. This classification of galaxies supports the *parallel sequence classification* by van den Bergh (1976b).

1.2.3 The Comprehensive de Vaucouleurs Revised Hubble-Sandage System

The latest large development in galaxy morphology classification has been carried out by Ronald Buta in the last 20 years (e.g., Buta et al. 1994, 2007, 2010b; Buta 2013a,b), including his last paper regarding *The Comprehensive de Vaucouleurs revised Hubble-Sandage System* (CVRHS, Buta et al. 2015, explained below).

Buta has improved galaxy classification by making use of the developments in the understanding of galaxy features. In the first place, he has carried out a thorough study of galactic rings and their relationship with resonances (e.g., Buta 1986, 1995; Buta and Combes 1996; Buta et al. 1998; Buta 1999). Secondly, he has studied the morphology of bars and bar strengths in galaxies (Buta 1996; Buta et al. 2005, 2010a), as well as spiral strengths (Buta et al. 2005) and the relationship between bars and spiral density waves (Buta et al. 2009).

The most recent review of galaxy morphology is the CVRHS. In this paper, Buta et al. (2015) use the notation of the classical galaxy classification (VRHS) and expand it by including new features to the classification of galaxies: inner, outer, and nuclear lenses; nuclear rings, bars, and discs; spheroidal galaxies; X patterns and box/peanut structures; OLR subclass outer rings and pseudorings; bar ansae and barlenses; parallel sequence late-types; thick discs and embedded discs in 3D early-type systems. With respect to galaxy types, the CVRHS is based on the VRHS system, and includes new galaxy types such as the disky/boxy E types (Kormendy and Bender 1996), the Sph types (Kormendy and Bender 2012), dE and dS0 of (Binggeli et al. 1985) and the S0 parallel sequence subtypes of van den Bergh (1976b). The CVRHS classification also provides with T-types introduced by The Third Reference Catalogue of Bright Galaxies (RC3; de Vaucouleurs et al. 1991). Table 3A of Buta et al. (2015) shows the correspondence between numerical T-types and stages of galaxies. For example, cE galaxies have T = -6, E⁺ has T = -5, S0/a has T = 0, Sc galaxies have T = 5, Im galaxies have T = 10 and dSph have T = 11.

As in Buta et al. (2010b), the CVRHS has been applied to the $3.6\,\mu m$ images from the *Spitzer* Survey of Stellar Structure in Galaxies survey (S⁴G, Sheth et al. 2010), as this wavelength traces the stellar mass within galaxies (although it is not perfect, see the corrections to hot dust and polycyclic aromatic hydrocarbons (PAHs) contaminants in Meidt et al. (2012, 2014), resulting in the mass maps presented in Querejeta et al. 2015). The mid-IR classification has some advantages (bars and bulges appear more prominent due to their content of old stars,

less dust extinction) and disadvantages (the contrast of the spiral structure is low compared to the background disc light) with respect to the classical VRHS system based on blue light (historically *B*-band). However, the same essential morphological features are seen in both bands. Table 2.1 of Sect. 1.2 shows examples of different classifications for the same list of galaxies using *B*-band and mid-IR. These differences can be significant, as for NGC 7371, that was classified in the RC3 as an unbarred ringed S0/a galaxy, and as an SAB grand-design multi-armed Sab spiral in Buta et al. (2010b).

Throughout this thesis, I have adopted the mid-IR classification in the CVRHS for the galaxies in our studies. The morphological classifications by Buta et al. (2010b) and the CVRHS give detailed information about the structure of a galaxy, which is crucial to understand the physical processes that *mold* the shapes of galaxies. These classifications offer a great level of detail. For example the CVRHS classification for NGC 4151 is $SAB_a(l,nl)0/a$, which means that it is a spiral galaxy (S) with a bar of intermediate apparent bar strength (AB), with brightness enhancements (*ansae*, Sandage 1961; Danby 1965) at its ends ($_a$), with an inner and a nuclear lense (l,nl), and finally the galaxy type, which is a transition between S0 and Sa (S0/a). However, in some cases, the level of detail is greater than I need (e.g., the subtle difference between Sab or Sab). In Table 1 of Buta et al. (2015), there is a detailed explanation of the CVRHS symbols such as those explained before for the classification of NGC 4151.

Finally, the CVRHS includes information about the morphology of spiral arms for nearly half of the S⁴G sample. Arm classifications are based on the symmetry, continuity, length and number of spiral arms, and may be related to the spiral density wave. A numerical value for the arm class (AC) was determined for the first time in Elmegreen and Elmegreen (1982): AC 1-4 correspond to flocculent galaxies (those with spiral structure composed of small pieces and with a lack of bimodal structure), whereas AC 5-12 correspond to grand design galaxies (two symmetric and continuous arms). In Elmegreen and Elmegreen (1987), a detailed AC classification was performed for 762 galaxies using B-band images. Elmegreen et al. (2011) have studied arm classes using S⁴G 3.6 µm images, showing that arm classes do not change substantially when using 3.6 \(\mu\) m images. They classified the spiral arms of 46 galaxies into three categories: flocculent (F), multi-armed (M) and grand design (G). This classification (F, M, G) has been expanded to the whole S⁴G sample, including arm classification for 1114 spiral galaxies that are not too inclined to make the arm class indistinguishable, and can be found in Table 8 of Buta et al. (2015). This detailed classification will be used in Chap. 5 to study the strength of the spiral arms.

This thesis will benefit from the detailed morphological classifications cited above, in particular those from the CVRHS. The visual description of the structural components is an important step, needed to understand a galaxy's formation and evolution. Concretely, the spiral AC in conjunction with the morphological classification of a galaxy describe the actual status of a galaxy, and hints at the evolutionary processes that a galaxy has undergone. However, this study is not complete, as the visual classification of a galaxy does not give the full information of the processes that the galaxy is going through. We need dynamical and kinematical information of the

structures of the galaxy to constrain these processes and better understand the actual "appearance" of a galaxy. For example, the degree of openness of the arms is a visual characteristic resulting from physical processes that cannot be understood without dynamical studies. Also, the dynamical effects of a bar can be hinted from the density of the gas in a certain region, but kinematic data will characterise the movement of the material inside the galaxy.

1.3 Kinematics of Nearby Galaxies

In order to better understand the evolutionary history of the Universe, it is necessary to study the structure and dynamics of current galaxies. By studying the kinematics of galaxies, it is possible to trace the motions of both their baryonic (gas and stars) and dark matter.

The rotation of galaxies (spiral *nebulae* as they were known at that time) was discovered during the second decade of the XXth century, when Slipher detected inclined absorption lines in the nuclear spectra of the Sombrero Galaxy (Slipher 1914a) and M31 (Slipher 1914b), and (Wolf 1914) detected inclined lines in the spectrum of M81. This discovery led to the measurement of radial velocities along the minor and major axes of the galaxies, yielding the first plots representing the radial velocities as a function of radius: the first rotation curves. These were first derived with low-resolution absorption line data (e.g., Pease 1916, 1918 for M104 and M31; Babcock 1939 in M31). These observations had long exposure times (about 80 h per absorption spectrum for Pease and 236 h for Babcock), and they demonstrated that the radial velocities increased linearly with radius. Later, emission line regions were used to derive the rotation curves of galaxies, e.g., by Mayall and Aller (1942) in M33 and in the extensive programme carried out by the Burbidges in the late '50s and early '60s using the H α and NII emission lines (e.g., Burbidge and Burbidge 1959 in NGC 5128; Burbidge et al. 1959 in NGC 2146; Burbidge et al. 1960 in NGC 7479).

Traditionally, radial velocity measurements were performed using the radio observations of the 21-cm HI line. This line traces the atomic gas content of the galaxy, which usually extends out to three or four times the optical disc. HI observations started in the fifties with studies of our Galaxy (Kwee et al. 1954) and M31 (van de Hulst et al. 1957), and were continued by Roberts at the National Radio Astronomy Observatory (NRAO) with single dish telescopes (e.g., Roberts 1966 for M31). The first radial velocity field for a galaxy was presented by Argyle (1965) for M31. Later, Westerbork Synthesis Radio Telescope (WSRT) data became available (see A. Bosma's thesis, Bosma 1978). Rots (1975), van der Hulst (1979), Bosma (1981) and Gottesman (1982) and others demonstrated the power of rotation curves in deriving the total mass distribution of disc galaxies. The drawback with these HI radio observations was the poor angular resolution and the lack of HI gas in the central regions of some intermediate-type galaxies such as M31 or M81.

CO radio observations have traditionally been used to trace the molecular gas. They were initially carried out at low angular resolution (e.g., Young and Scoville

1982), improved later on with sensitive single dish observations, for example those performed at the Institut de Radioastronomie Millimétrique (IRAM) with resolutions of 22" (CO 1–0 line) and 11" (CO 2–1 line) (see Table 1 in Young and Scoville 1991 for a list of CO observations of individual galaxies, telescopes, spatial resolutions and references therein). Nowadays, CO observations provide us with high spatial resolution (comparable to optical), and also high spectral resolution (from one to several km s⁻¹), but across small fields. The Plateau de Bure Interferometer Arcsecond Whirlpool Survey (PAWS; Schinnerer et al. 2013) is the first survey that targets molecular gas data combining high spatial resolution (~ 1 ") with enough field of view (FOV) (270" $\times 170$ " in the inner disc of M51).

To improve the spatial resolution inherent in traditional radio observations, optical (H α , NII) observations yield high (arcsecond) angular resolution two-dimensional kinematic maps, enabling the study of the small-scale structures within galaxies. H α is often the brightest emission line in the visible wavelength range due to the cosmic abundance of this element. In spiral galaxies, this line traces primarily the ionised gas in HII regions around young massive stars. In the 20th century, most of the optical observations were based on long-slit spectroscopy. Long-slit observations have traditionally been used to deduce the rotation curves of galaxies (e.g., Rubin et al. 1980, 1982, 1985; Mathewson et al. 1992; Persic and Salucci 1995; Mathewson and Ford 1996; Courteau 1997; Dale et al. 1997, 1998, 1999).

However, 3D spectroscopy [integral field unit (IFU), Fabry-Perot (FP), multi long-slit spectroscopy] of galaxies is one of the best methods nowadays to obtain information about the kinematics of galaxies, as it is possible to obtain kinematic information across a galaxy. Moreover, with 2D velocity maps derived using 3D spectroscopy, one can explore the kinematics of a whole galaxy, whereas using slit spectra along a single line, the velocity field of the galaxy is not completely reproduced. H α observations using FP instruments have been used for some 40 years now (Tully 1974; Deharveng and Pellet 1975; Dubout et al. 1976; de Vaucouleurs and Pence 1980; Atherton et al. 1982 or Boulesteix et al. 1984), and have been employed to create high signal-to-noise ratio (S/N) rotation curves for many spiral galaxies (e.g., Marcelin et al. 1985; Bonnarel et al. 1988; Pence et al. 1990; Corradi and Capaccioli 1991; Amram et al. 1992; Cecil et al. 1992; Amram et al. 1994; Sicotte et al. 1996; Ryder et al. 1998; Jiménez-Vicente et al. 1999; Knapen et al. 2000 and many more).

Taking everything into account, the development of new instrumentation has enabled kinematical studies with better and better angular and spectral resolution in the last century, also diminishing the observing time. Depending on the scientific goal, one instrument would be preferred over another. For example, HI data is needed to study the outermost parts of the galaxy disc, H α FP instrumentations provide very high angular and spectral resolution data, and IFU instrumentation is required to obtain information about stellar and gas kinematics as well as stellar populations. New state-of-the-art instrumentation and surveys such as CALIFA (Sánchez et al. 2012), MaNGA (Bundy et al. in preparation), MUSE (Bacon et al. 2010), WEAVE (Dalton et al. 2012), KMOS (Sharples et al. 2004) or SAMI (Croom et al. 2012) will bring brand new kinematic data to the scientific community. These surveys will

provide data of galaxy samples one to two orders of magnitude larger than previous kinematic surveys such as GHASP (Epinat et al. 2008), THINGS (Walter et al. 2008), ATLAS^{3D} (Cappellari et al. 2011a), or ours (Chap. 3).

Kinematics and secular evolution

Galactic discs are understood to be self-gravitating systems that are supported by rotation (Lynden-Bell and Kalnajs 1972; Lynden-Bell and Pringle 1974; Tremaine 1989; see e.g., Binney and Tremaine 2008 and Kormendy 2008 and references therein). They evolve by spreading in two dimensions, achieving a lower state of energy which conserves the angular momentum. On the contrary, massive ellipticals are not supported by rotation but by random motions. During this spreading, the structures within the galaxy exchange angular momentum and there is a redistribution of material (as explained in Sect. 1.1).

Bars and ovals are the best *engines* of these evolution processes. Due to the influence of these substructures when redistributing the material, the kinematics of the galactic components change. There are, consequently, deviations from the rotation arising from the influence of the potential of these substructures that drive these evolutionary processes on the galactic components (gas and/or stars). These deviations from the rotation are commonly called non-circular motions. In this thesis, I will try to understand where do these non-circular motions take place and what components cause them.

This thesis is based on kinematic observations of a sample of galaxies spanning a wide range of basic properties, so we can make statistical inferences. Concretely, this thesis will use one of the newest FP instruments observing the H α line. As I will explain in Sect. 1.4, this line traces the hot gas ionized by massive young stars. Therefore, H α FP data correspond to kinematic data of the ionized gas. Hereafter in the thesis, the kinematical studies will refer to those of the ionized gas if not specified, except for the cases where I use other data and mention which component of the galaxy those data trace.

The galaxy structures (disc, bulge, halo) and sub-structures (bar, spiral arms) may have had different formation scenarios and experienced different evolution processes (secular or dynamical, fast or slow, internal or externally driven). Thus, the kinematics of these structures could be altered by any of the interaction between stars or gas and the substructures (bars, spiral arms or haloes). As discs are supported by rotation, studies of the shape of the rotation curve can also bring information of the interactions among components. Several studies of the relationships between the shape of the rotation curve and the properties of individual galaxies have been carried out in the literature. On the one hand, some studies suggest that the total luminosity of a galaxy determines the rotation curve, as the idea of a universal rotation curve presented by Persic and Salucci (1991) and Persic et al. (1996). On the other hand, other studies suggest that the total luminosity of the galaxy is not the only parameter that influences the shape of the rotation curve (see Chap. 6 for a full list of references). Again, the conjunction between morphological classifications (such as those of bars and arms) and detailed studies of the rotation curves result in a comprehensive study of the secular evolution processes which occur inside galaxies.

1.4 Massive Star Formation

One of the most important clues to understand the formation and evolution of galaxies is the formation of stars. This process comprises the transformation of gas into stars and planetary systems. Star formation (SF) encompasses a series of physical processes that occur at different physical scales: from the contraction of cores to form stars (\sim 0.1 pc), to the formation of molecular clouds (\sim 10–100 pc) to the large scale accretion of gas onto discs from satellite objects and the intergalactic medium (\sim Mpc). Throughout this thesis, I will focus on the *global* formation of massive stars of the whole galaxy and structures such as bars or spiral arms, not on the *local* formation of stars (regions within galaxies, sub-galactic/sub-kpc scale).

In this context, I am interested in measuring the quantity of stars that are being formed via the star formation rate (SFR) parameter, measured as the stellar mass formed within a certain period of time (usually expressed in units of M_{\odot} year⁻¹). The global SFR measures unresolved populations where individual stars cannot be counted. In this sense, the global SFRs are computed via the total luminosity (L) of a galaxy with an expression SFR $\propto L$. As a consequence, the SFRs are averaged measurements through the star formation history. Also, I assume that the stellar initial mass function (IMF) is constant across all environments. The underlying stellar IMF is expressed generally as a power-law relation (Salpeter 1955), double power law (Kroupa 2001) or log-normal distribution (Chabrier 2003).

To quantify the rate at which stars are being formed, one has to measure the emission that probes recently formed stars (young stars), avoiding the contribution from evolved stellar populations. Therefore, I study newly formed stars, in other words, I will refer to timescales $\approx 10-100\,\mathrm{Myr}$ when considering whole galaxies.

1.4.1 Historical Introduction and Generalities

The study of the formation of stars in galaxies is a very wide topic. The first measurements of the young stellar content in galaxies were performed through studies of resolved stellar populations carried out by Hubble and Baade (e.g., Hubble 1936a or Baade and Minkowski 1937). Roberts (1963) established a continuous sequence in present-day SFRs and past SFRs across the Hubble sequence of galaxies. However, the first quantitative measurements of SFRs arose from evolutionary synthesis models of galaxy colours (Tinsley 1968, 1972; Searle et al. 1973), confirming Roberts' picture. Later models of blue galaxies (Bagnuolo 1976; Huchra 1977; or Larson and Tinsley 1978) started to reveal the importance of star formation bursts in the evolution of galaxies.

The development of telescopes and instrumentation opened windows to explore different wavelength ranges and new diagnostics on SFRs: integrated optical emission-line fluxes (Cohen 1976; Kennicutt 1983b), infrared (IR) continuum fluxes (Harper and Low 1973; Rieke and Lebofsky 1978; Telesco and Harper 1980),

near-ultraviolet (NUV) continuum fluxes (Donas and Deharveng 1984), far-IR luminosities (e.g., Kennicutt et al. 1987), radio luminosities (e.g., Condon 1992; Cram et al. 1998) or direct UV emission (e.g., Bell and Kennicutt 2001).

The launch of the *Infrared Astronomical Satellite (IRAS*; Neugebauer et al. 1984) permitted the discovery of a population of ultraluminous IR starburst galaxies at higher redshifts (Steidel et al. 1996; Ellis 1997), expanding the studies of SFRs to distant galaxies and, as a consequence, to a cosmological lookback time. Later, substantial advances were made in the understanding of high-redshift star formation (e.g., Madau et al. 1996, 1998; Steidel et al. 1999; Hopkins et al. 2000; Lanzetta et al. 2002).

 $H\alpha$ emission line has traditionally been used for studies of recent SF. This line traces the light from massive young stars (massive SF), and is usually the brightest line observed in a galaxy's optical spectrum (see Sect. 1.4.2 for a detailed description of this SF tracer). Global SFRs in normal galaxies have been widely studied in several $H\alpha$ surveys (e.g., Cohen 1976; Kennicutt and Kent 1983; Gallagher et al. 1984; Romanishin 1990; Gavazzi et al. 1991; Ryder and Dopita 1994; Gallego et al. 1995, 1996; Young et al. 1996; Koopmann et al. 2001; Charlot et al. 2002). Also, interacting galaxies (Kennicutt et al. 1987) and bright spiral and irregular galaxies (Kennicutt 1994) have been observed in $H\alpha$.

One of the most important $H\alpha$ surveys to study the star formation activity in the local Universe is the $H\alpha$ Galaxy Survey (HAGS; James et al. 2004). These authors quantify SFRs across the full range of galaxies, from S0/a to the faintest dwarf irregular galaxies. They find that there is a strong correlation between SFR and the morphological Hubble type, with the peak near isolated Sbc-Sc types.

The formation of stars has not only been studied to understand the distribution of SFR across the Hubble sequence of galaxies. Studies about SF and SFRs have been developed to tackle many scientific topics, summarised as follows:

- Scaling-laws such as the relationship between SFR surface densities and the mean gas surface densities (the so-called Kennicutt-Schmidt law, Kennicutt 1989, 1998), or the non-linear dependence between total SFR and total molecular gas mass (e.g., Solomon and Sage 1988; Gao and Solomon 2004).
- 2. The properties of galaxies that can affect the global SFR of a galaxy: the galaxy mass and its luminosity (e.g., Gavazzi and Scodeggio 1996; Gavazzi et al. 1996; Kauffmann et al. 2003, 2004; Zheng et al. 2007; Bell et al. 2007, 2012; Santini et al. 2009; Conroy and Wechsler 2009; Karim et al. 2011; Gunawardhana et al. 2013; Sobral et al. 2014), the presence of a bar (see Kennicutt 1994; Phillips 1996; James et al. 2004; Fisher 2006), spiral arm structure (Elmegreen and Elmegreen 1986; McCall and Schmidt 1986; Cepa and Beckman 1990; Knapen et al. 1992; Seigar and James 2002; Dobbs and Pringle 2009; Foyle et al. 2010; Elmegreen 2011; Eden et al. 2013; Dobbs 2014), interactions of galaxies (e.g., Knapen and James 2009 and Knapen et al. 2014 and references therein), or cluster environment (e.g., Kennicutt 1983a; Kennicutt et al. 1984; Gavazzi et al. 1991; Moss and Whittle 1993; Balogh et al. 1998; Lewis et al. 2002; Bretherton et al. 2013; Crossett et al. 2014).

3. During the past decade, large galaxy surveys have been designed to study the radial distribution of star formation and gas: *Spitzer* Infrared Nearby Galaxies Survey (SINGS, Kennicutt et al. 2003), the *Galaxy Evolution Explorer* (*GALEX*; Martin et al. 2005) Nearby Galaxy Survey (NGS; Gil de Paz et al. 2007), the *Spitzer/GALEX* Local Volume Legacy Survey (Dale et al. 2009; Lee et al. 2011), and the *Herschel* KINGFISH Project (Kennicutt et al. 2011). All these surveys exploit the improvements in angular resolution of the up-to-date instrumentation, allowing detailed analysis of resolved and dust-corrected SFRs.

1.4.2 Star Formation Tracers

About half of the luminous energy in the universe, integrated over all redshifts, emerge as direct stellar light, meaning that a similar amount of energy is emitted through dust-reprocessed light (e.g., Dole et al. 2006). Thus, to compute the overall SFR of a galaxy, dust effects and extinction must be taken into account. Here I will give a brief summary of the SFR tracers, firstly those based on direct stellar light and secondly, those based on dust-reprocessed light. Finally, a combination of direct and dust-processed tracers will be presented as a more complete technique reducing the uncertainties when computing the total SFR of a galaxy. A detailed description of these SFR calibrators can be found in the recent review by Kennicutt and Evans (2012) and in the XXIII Canary Islands Winter School of Astrophysics section about Star formation rate indicators, by Daniela Calzetti (Calzetti 2013).

Calibrators based on direct stellar light

The best way to measure directly the formation of stars in galaxies is by studying the emission from massive, young stars (O, B). This emission is found in the electromagnetic spectrum from the UV and optical to the near-IR range ($\sim 0.1-5 \,\mu m$).

(a) Stellar continuum Ultraviolet

Continuum (non-ionising) UV traces the photospheric emission from the youngest stellar populations (10–200 Myr). The launch of *GALEX* (Martin et al. 2005) has had a great impact on the study of the SFR(UV), imaging approximately two-thirds of the sky in two bands: far-UV (FUV) and NUV, giving SFR estimates of hundreds of thousands of external galaxies. Nevertheless, dust attenuation is present and corrections need to be applied (e.g., Wang and Heckman 1996; Calzetti 2001; Hopkins et al. 2001; Sullivan et al. 2001; Calzetti et al. 2007). The FUV-NUV colour or the UV spectral slope (denoted by β) have been proposed to give estimations of the dust attenuation (e.g., Calzetti et al. 1994; Kong et al. 2004; Seibert et al. 2005; Johnson et al. 2007; Salim et al. 2007; Treyer et al. 2007; Hao et al. 2011); although the large scatter in these estimations leads to a preference to use multi-wavelength calibrations when possible (see below). The resulting SFR calibrations for UV, and specifically for the *GALEX* bands FUV and NUV can be found in Table 1.1.

Luminosity	C	Age range (Myr)	References
L(UV)	$3.0 \times 10^{-47} \lambda$	0-10-100 ⁽¹⁾	H11 and M11
L(FUV)	4.6×10^{-44}	0-10-100	H11 and M11
L(NUV)	6.8×10^{-44}	0-10-200	H11 and M11
L(TIR)	2.8×10^{-44}	0-5-100 ⁽²⁾	H11 and M11
L(H\alpha)	5.5×10^{-42}	0-3-10 ⁽³⁾	K09
L(24 µm)	2.04×10^{-43}	0-3-10 ⁽²⁾	R09
L(70 µm)	5.9×10^{-44}	0-3-10 ⁽²⁾	C10

Table 1.1 Model-based luminosity-to-SFR calibrations

Column I Luminosities from the different wavelength range, in erg/s. Stellar and dust continuum luminosities are given as vL_v . Total-IR (TIR) is assumed to be equal to the bolometric luminosity. SFR is in units of M_{\odot} year⁻¹. Column II Calibration constant C, expressed so that SFR(λ) = $CL(\lambda)$. For the UV, the numerical value is multiplied by the wavelength λ in Å. Column III Age range based on the assumed IMF. In this case, I adopt a Kroupa (2001) stellar IMF with a mass range of 0.1– $100\,M_{\odot}$. The second number gives the mean age of the stellar population contributing to the emission, whereas the third number gives the age below 90% of the emission is contributed. Column IV References: K09 (Kennicutt et al. 2009); R09 (Rieke et al. 2009); C10 (Calzetti et al. 2010); H11 (Hao et al. 2011) and M11 (Murphy et al. 2011). Notes (1) Dependent on the wavelength range. The number shown corresponds to an effective wavelength of 1516 Å. (2) Numbers sensitive to the SF history (SFH). Those shown here assume a constant SF over 0–100 Myr. (3) $T_{\rm e}$ = 10^4 K, $n_{\rm e}$ = $100\,{\rm cm}^{-3}$ are adopted for the hydrogen calibrator

(b) Ionised gas emission

The gas surrounding massive young stars is ionised by this young population. As a consequence, emission lines are produced when recombination cascades take place (e.g., Balmer H α and H β , Paschen P α or Brackett B α and B γ). These lines are usually the strongest lines found in a galaxy's spectrum. Specifically, the H α (λ =6563 Å) and H β (λ =4861 Å) lines have traditionally been used as SFR indicators for being strong and located in the optical wavelength range (see the review by Kennicutt 1998 and references therein). The great advantages of these recombination lines are that they trace very recent SF (timescales \sim 6–8 Myr), and that they have lower sensitivity to dust attenuation than UV (although not negligible, Cardelli et al. 1989). Forbidden lines such as the metal lines OII (λ =3627 Å), NII (λ =122 μ m) or CII (λ =158 μ m) suffer from the same limitations as the hydrogen recombination lines, and also depend on the metal content and ionization conditions of a galaxy region. In Table 1.1, the updated calibration for SFR(H α) is presented.

Indicators based on dust-reprocessed light

Stellar light re-processed by dust is emitted in the mid/far-IR wavelength range (\sim 5–1000 μ m). Early studies of dust emission as a SFR tracer used the integrated total IR emission (TIR), as it represents the bolometric luminosity of a completely dust-covered stellar population (see Kennicutt 1998 and references therein). However, this wavelength coverage is not always accessible and monochromatic IR bands have become more important thanks to the *Spitzer Space Telescope* (Werner et al. 2004)

and the Herschel Space Observatory (Pilbratt et al. 2010). Dust models are needed to set up the relevant SFR calibrations, and different dust components need to be taken account. The emission at wavelengths $\sim 5-20\,\mu m$ is dominated by molecular bands arising from PAHs. Thermal continuum emission from the main dust grains dominate the emission at wavelengths over $20\,\mu m$. Emission from small grains stochastically heated by intense radiation fields is important up to $60\,\mu m$, and larger grains dominate the emission at longer wavelengths. The different response from distinct dust morphologies and components is translated into different spectral energy distributions (SEDs) within galaxies (e.g., Dale and Helou 2002; Dale et al. 2005; Smith et al. 2007). Consequently, the conversion from IR luminosities into SFRs should be different depending on the wavelength (see Calzetti et al. 2010 for a complete list of SFR calibrators from the IR). In Table 1.1, the calibrations for TIR and the monochromatic bands 24 and $70\,\mu m$ are presented.

Some drawbacks are found when using IR as a SFR tracer. In the first place, not all the stellar emission in a galaxy is absorbed by dust. Secondly, IR emission may come from not only young but also old population stars (e.g., Gordon et al. 2000; Kong et al. 2004; Buat et al. 2005), and therefore the IR can be problematic as a SFR tracer in systems with low specific SFR (sSFR).

Composite multiwavelength tracers

As mentioned before, half of the starlight in the Universe is processed and re-emitted by dust. To overcome this complication and reduce the uncertainties when measuring the total SF of a galaxy, mixed SFR indicators using dust-obscured and dust-unobscured light have been empirically calibrated (e.g., Calzetti et al. 2005, 2007; Kennicutt et al. 2007; Zhu et al. 2008; Kennicutt et al. 2009; Treyer et al. 2010; Liu et al. 2011; Hao et al. 2011). The mixed indicators are usually expressed as:

$$SFR(\lambda_1, \lambda_2) = C(\lambda_1)[L(\lambda_1)_{obs} + a_{\lambda_2}L(\lambda_2)_{obs}]$$
 (1.1)

where SFR(λ_1, λ_2) is in M_{\odot} year⁻¹, λ_1 refers to a direct light calibrator (e.g., H α), and λ_2 corresponds to a dust-processed tracer (e.g., TIR). The luminosities $L(\lambda_1)_{\rm obs}$ and $L(\lambda_2)_{\rm obs}$ correspond to the observed luminosities (i.e., not corrected for dust attenuation) and their units are erg s⁻¹. It is also possible to define a dust-corrected luminosity for the direct light calibrator:

$$L(\lambda_1)_{\text{corr}} = L(\lambda_1)_{\text{obs}} + a_{\lambda_2} L(\lambda_2)_{\text{obs}}, \tag{1.2}$$

and therefore use the calibration factors C listed in Table 1.1, as Eq. 1.1 can be written now as

$$SFR(\lambda_1) = CL(\lambda_1)_{corr}.$$
 (1.3)

Kennicutt and Evans (2012) present a complete set of multiwavelength relationships. Here, I list some of them:

$$L(FUV)_{corr} = L(FUV)_{obs} + 0.46L(TIR)$$

$$L(FUV)_{corr} = L(FUV)_{obs} + 3.89L(25 \,\mu\text{m})$$

$$L(NUV)_{corr} = L(NUV)_{obs} + 0.27L(TIR)$$

$$L(NUV)_{corr} = L(NUV)_{obs} + 2.26L(25 \,\mu\text{m})$$

$$L(H\alpha)_{corr} = L(H\alpha)_{obs} + 0.0024L(TIR)$$

$$L(H\alpha)_{corr} = L(H\alpha)_{obs} + 0.02L(25 \,\mu\text{m})$$
(1.4)

1.5 The S⁴G Survey

The S⁴G survey has obtained 3.6 and 4.5 μ m images of 2352 nearby galaxies using the Infrared Array Camera (IRAC; Fazio et al. 2004). The sample is composed by galaxies that fulfil these requirements: d < 40 Mpc, $m_b < 15.5$, $D_{25} > 1$ arcmin, and includes galaxies selected using values from HyperLeda (Paturel et al. 2003), with a radial velocity $v_{\rm radio} < 3000\,{\rm km~s^{-1}}$ and galactic latitude $|b| > 30^{\circ}$. The cornerstone of the S⁴G survey is the quantitative analysis of photometric parameters, enabling a variety of studies on secular evolution, outer disc and halo formation, galaxy morphology, etc.

The data have been made public (http://irsa.ipac.caltech.edu/data/SPITZER/S4G/). I refer to Sheth et al. (2010) for a complete description of the survey goals and S⁴G sample selection. All the images have been processed using the S⁴G pipeline, consisting of the following steps: transformation of the raw data into science-ready FITS images, mask design, ellipse fitting, photometric structural decompositions and finally, mass maps creation.

Since the *Spitzer* observations were carried out and the first data were available for their study, several papers using these data have been published in the literature: thick discs seen in edge-on galaxies (Comerón et al. 2011a, b, c), disc truncation (Comerón et al. 2012), breaks and disc truncations (Martín-Navarro et al. 2012), mid-IR flocculent and grand design spiral structure and star-forming regions embedded in spiral arms (Elmegreen et al. 2011, 2014), faint outskirts of galaxies and of tidal debris (Kim et al. 2012; Laine et al. 2014), relationship between bar strength and nuclear activity (Cisternas et al. 2013), mid-IR asymmetries and the mid-IR Tully-Fisher relation (Zaritsky et al. 2013, 2014), atlas of galactic rings (Comerón et al. 2014), mid-IR morphological classification (Buta et al. 2010b; CVRHS), quantitative morphology using cosmologically relevant parameters (Holwerda et al. 2014) and conversion of 3.6 and 4.5 µm light into stellar mass maps (Meidt et al. 2012, 2014; Querejeta et al. 2015).

The S^4G mid-IR imaging is complemented by significant amounts of archival and new ancillary data, of which the present thesis forms a part (H α FP data, Chap. 3; H α narrow-band imaging, Chap. 3 and broad-band optical images, Sect. E.2). I will concentrate on those areas where S^4G data are bound to bring significant progress: stellar mass distribution, the shape of the potential, and the detailed structure within and outside the optical discs, all at very high accuracy.

1.6 Thesis Outline

The combination of the S⁴G mid-IR images with complementary kinematic FP data at high resolution will allow us to tackle the scientific goals of this thesis, summarised as follows:

- 1. Study the distribution of the SF across the Hubble sequence of galaxies, in particular in ETGs, to study the evolutionary sequence of galaxies and constrain the physical processes that have occurred.
- 2. Perform a detailed study of the kinematical interplay between the interstellar medium and regions of star formation, dust absorption, or other activity.
- 3. Use the kinematics as a probe of the secular evolution, as manifested in the deviations from pure circular rotation caused by the different structural components (such as bars, spiral arms, rings, lenses, etc.).
- 4. Exploit the high spatial resolution of the kinematic data to study the inner parts of the rotation curves, and relate the galaxy kinematics to the mass distribution and specific observed properties, as well as probing the coupling between the stellar density and the gravitational potential in the inner parts of the galaxies.

Some of the results of this thesis have been published in: Erroz-Ferrer et al. (2012, 2013, 2015) and Erroz-Ferrer et al. (in preparation).

References

P. Amram, E. Le Coarer, M. Marcelin et al., A&AS 94, 175 (1992)

P. Amram, M. Marcelin, C. Balkowski et al., A&AS 103, 5 (1994)

E. Argyle, ApJ 141, 750 (1965)

P.D. Atherton, K. Taylor, C.D. Pike et al., MNRAS 201, 661 (1982)

W. Baade, C.H.P. Gaposchkin, Evolution of stars and galaxies (1963)

W. Baade, R. Minkowski, ApJ 86, 123 (1937)

H.W. Babcock, Lick Obs. Bull. 19, 41 (1939)

R. Bacon, M. Accardo, L. Adjali et al, in *Society of Photo-Optical Instrumentation Engineers* (SPIE) Conference Series, vol. 7735, Society of Photo-Optical Instrumentation Engineers (SPIE) Conference Series (2010)

W.G. Bagnuolo Jr, PhD thesis, California Institute of Technology, Pasadena (1976)

M.L. Balogh, D. Schade, S.L. Morris et al., ApJ **504**, L75 (1998)

E.F. Bell, R.C. Kennicutt Jr, ApJ **548**, 681 (2001)

E.F. Bell, A. van der Wel, C. Papovich et al., ApJ 753, 167 (2012)

E.F. Bell, X.Z. Zheng, C. Papovich et al., ApJ **663**, 834 (2007)

B. Binggeli, A. Sandage, G.A. Tammann, AJ 90, 1681 (1985)

J. Binney, S. Tremaine, Galactic Dynamics, 2nd edn. (Princeton University Press, Princeton, 2008)

F. Bonnarel, J. Boulesteix, Y.P. Georgelin et al., A&A 189, 59 (1988)

A. Bosma, PhD Thesis, Groningen University (1978)

A. Bosma, AJ 86, 1791 (1981)

J. Boulesteix, Y. Georgelin, M. Marcelin, G. Monnet, in *Society of Photo-Optical Instrumentation Engineers (SPIE) Conference Series*, ed. by A. Boksenberg, D.L. Crawford, vol. 445, Instrumentation in astronomy V, pp. 37–41 (1984)

References 17

- C.F. Bretherton, C. Moss, P.A. James, A&A 553, A67 (2013)
- V. Buat, J. Iglesias-Páramo, M. Seibert et al., ApJ 619, L51 (2005)
- E.M. Burbidge, G.R. Burbidge, ApJ **129**, 271 (1959)
- E.M. Burbidge, G.R. Burbidge, K.H. Prendergast, ApJ, 130, 739 (1959)
- E.M. Burbidge, G.R. Burbidge, K.H. Prendergast, AJ, 65, 342 (1960)
- R. Buta, ApJS 61, 609 (1986)
- R. Buta, ApJS 96, 39 (1995)
- R. Buta, in *Astronomical Society of the Pacific Conference Series*, ed. by R. Buta, D.A. Crocker, B.G. Elmegreen, vol. 91, IAU Colloq. 157: Barred Galaxies 11 (1996)
- R. Buta, Ap&SS 269, 79 (1999)
- R. Buta, A.J. Alpert, M.L. Cobb, D.A. Crocker, G.B. Purcell, AJ 116, 1142 (1998)
- R. Buta, F. Combes, Fund. Cosmic Phys. 17, 95 (1996)
- R. Buta, E. Laurikainen, H. Salo, J.H. Knapen, ApJ 721, 259 (2010a)
- R. Buta, S. Mitra, G. de Vaucouleurs, H.G. Corwin Jr, AJ 107, 118 (1994)
- R. Buta, S. Vasylyev, H. Salo, E. Laurikainen, AJ 130, 506 (2005)
- R.J. Buta, Galaxy Morphology, ed. by T.D. Oswalt, W.C. Keel 1 (2013a)
- R.J. Buta, Galaxy Morphology, ed. by J. Falcón-Barroso, J.H. Knapen 155 (2013b)
- R.J. Buta, H.G. Corwin, S.C. Odewahn, The de Vaucouleurs Altlas of Galaxies, ed. by R.J. Buta, H.G. Corwin, S.C. Odewahn (Cambridge University Press, Cambridge, 2007)
- R.J. Buta, J.H. Knapen, B.G. Elmegreen et al., AJ 137, 4487 (2009)
- R.J. Buta, K. Sheth, E. Athanassoula, et al., ApJS 217, 32 (2015)
- R.J. Buta, K. Sheth, M. Regan et al., ApJS 190, 147 (2010b)
- D. Calzetti, PASP 113, 1449 (2001)
- D. Calzetti, Star Formation Rate Indicators, ed. by J. Falcón-Barroso, J.H. Knapen, 419 (2013)
- D. Calzetti, R.C. Kennicutt, C.W. Engelbracht et al., ApJ 666, 870 (2007)
- D. Calzetti, R.C. Kennicutt Jr, L. Bianchi et al., ApJ 633, 871 (2005)
- D. Calzetti, A.L. Kinney, T. Storchi-Bergmann, ApJ 429, 582 (1994)
- D. Calzetti, S.-Y. Wu, S. Hong et al., ApJ **714**, 1256 (2010)
- M. Cappellari, E. Emsellem, D. Krajnović et al., MNRAS 413, 813 (2011a)
- M. Cappellari, E. Emsellem, D. Krajnović et al., MNRAS 416, 1680 (2011b)
- J.A. Cardelli, G.C. Clayton, J.S. Mathis, ApJ **345**, 245 (1989)
- G. Cecil, A.S. Wilson, R.B. Tully, ApJ **390**, 365 (1992)
- J. Cepa, J.E. Beckman, ApJ **349**, 497 (1990)
- G. Chabrier, PASP **115**, 763 (2003)
- S. Charlot, G. Kauffmann, M. Longhetti et al., MNRAS 330, 876 (2002)
- M. Cisternas, D.A. Gadotti, J.H. Knapen et al., ApJ 776, 50 (2013)
- J.G. Cohen, ApJ 203, 587 (1976)
- S. Comerón, B.G. Elmegreen, J.H. Knapen et al., ApJ 741, 28 (2011a)
- S. Comerón, B.G. Elmegreen, J.H. Knapen et al., ApJ 738, L17 (2011b)
- S. Comerón, B.G. Elmegreen, H. Salo et al., ApJ 759, 98 (2012)
- S. Comerón, J.H. Knapen, K. Sheth et al., ApJ 729, 18 (2011c)
- S. Comerón, H. Salo, E. Laurikainen et al., A&A 562, A121 (2014)
- J.J. Condon, ARA&A 30, 575 (1992)
- C. Conroy, R.H. Wechsler, ApJ 696, 620 (2009)
- R.L.M. Corradi, M. Capaccioli, A&AS 90, 121 (1991)
- S. Courteau, AJ **114**, 2402 (1997)
- L. Cram, A. Hopkins, B. Mobasher, M. Rowan-Robinson, ApJ 507, 155 (1998)
- A.C.D. Crommelin, JRASC 12, 33 (1918)
- S.M. Croom, J.S. Lawrence, J. Bland-Hawthorn et al., MNRAS 421, 872 (2012)
- J.P. Crossett, K.A. Pimbblet, J.P. Stott, D.H. Jones, MNRAS 437, 2521 (2014)
- H.D. Curtis, Publ. Lick Obs. 13, 9 (1918)
- D.A. Dale, G.J. Bendo, C.W. Engelbracht et al., ApJ 633, 857 (2005)
- D.A. Dale, S.A. Cohen, L.C. Johnson et al., ApJ 703, 517 (2009)

- D.A. Dale, R. Giovanelli, M.P. Haynes, E. Hardy, L.E. Campusano, AJ 118, 1468 (1999)
- D.A. Dale, R. Giovanelli, M.P. Haynes et al., AJ 114, 455 (1997)
- D.A. Dale, R. Giovanelli, M.P. Haynes et al., AJ 115, 418 (1998)
- D.A. Dale, G. Helou, ApJ 576, 159 (2002)
- G. Dalton, S.C. Trager, D.C. Abrams et al. in Society of Photo-Optical Instrumentation Engineers (SPIE) Conference Series, vol. 8446, Society of Photo-Optical Instrumentation Engineers (SPIE) Conference Series (2012)
- J.M.A. Danby, AJ 70, 501 (1965)
- W. de Sitter, MNRAS 78, 3 (1917)
- G. de Vaucouleurs, Handbuch der Physik **53**, 275 (1959)
- G. de Vaucouleurs, A. de Vaucouleurs, H.G. Corwin Jr et al. in *Third Reference Catalogue of Bright Galaxies*, ed. by G. de Vaucouleurs, A. de Vaucouleurs, H.G. Corwin Jr, R.J. Buta, G. Paturel, P. Fouque (1991)
- G. de Vaucouleurs, W.D. Pence, ApJ **242**, 18 (1980)
- J.M. Deharveng, A. Pellet, A&A 38, 15 (1975)
- C.L. Dobbs, in *IAU Symposium*, , ed. by S. Feltzing, G. Zhao, N.A. Walton, P. Whitelock, vol. 298, IAU Symposium, pp. 221–227 (2014)
- C.L. Dobbs, J.E. Pringle, MNRAS 396, 1579 (2009)
- H. Dole, G. Lagache, J.-L. Puget et al., A&A 451, 417 (2006)
- J. Donas, J.M. Deharveng, A&A 140, 325 (1984)
- R. Dubout, A. Laval, A. Maucherat et al., Astrophys. Lett. 17, 141 (1976)
- D.J. Eden, T.J.T. Moore, L.K. Morgan, M.A. Thompson, J.S. Urquhart, MNRAS 431, 1587 (2013)
- R.S. Ellis, ARA&A 35, 389 (1997)
- B.G. Elmegreen, in EAS Publications Series, ed. by C. Charbonnel, T. Montmerle, vol. 51, EAS Publications Series, pp. 19–30 (2011)
- B.G. Elmegreen, D.M. Elmegreen, ApJ 311, 554 (1986)
- D.M. Elmegreen, B.G. Elmegreen, MNRAS 201, 1021 (1982)
- D.M. Elmegreen, B.G. Elmegreen, ApJ **314**, 3 (1987)
- D.M. Elmegreen, B.G. Elmegreen, S. Erroz-Ferrer et al., ApJ 780, 32 (2014)
- D.M. Elmegreen, B.G. Elmegreen, A. Yau et al., ApJ 737, 32 (2011)
- B. Epinat, P. Amram, M. Marcelin, MNRAS 390, 466 (2008)
- S. Erroz-Ferrer, J.H. Knapen, J. Font et al., MNRAS 427, 2938 (2012)
- S. Erroz-Ferrer, J.H. Knapen, R. Leaman et al., MNRAS 451, 1004 (2015)
- S. Erroz-Ferrer, J.H. Knapen, E.A.N. Mohd Noh Velastín, J.E. Ryon, L.M.Z. Hagen, MNRAS, 436, 3135 (2013)
- G.G. Fazio, J.L. Hora, L.E. Allen et al., ApJS 154, 10 (2004)
- D.B. Fisher, ApJ 642, L17 (2006)
- J. Falcón-Barroso, J.H. Knapen, Secular Evolution of Galaxies (2013)
- K. Foyle, H.-W. Rix, F. Walter, A.K. Leroy, ApJ 725, 534 (2010)
- A. Friedmann, Zeitschrift für Physik 10, 377 (1922)
- J.S.I.I.I. Gallagher, D.A. Hunter, A.V. Tutukov, ApJ, 284, 544 (1984)
- J. Gallego, J. Zamorano, A. Aragon-Salamanca, M. Rego, ApJ 455, L1 (1995)
- J. Gallego, J. Zamorano, M. Rego, O. Alonso, A.G. Vitores, A&AS 120, 323 (1996)
- Y. Gao, P.M. Solomon, ApJ 606, 271 (2004)
- G. Gavazzi, A. Boselli, R. Kennicutt, AJ 101, 1207 (1991)
- G. Gavazzi, D. Pierini, A. Boselli, A&A **312**, 397 (1996)
- G. Gavazzi, M. Scodeggio, A&A 312, L29 (1996)
- A. Gil de Paz, S. Boissier, B.F. Madore et al., ApJS 173, 185 (2007)
- K.D. Gordon, G.C. Clayton, A.N. Witt, K.A. Misselt, ApJ 533, 236 (2000)
- S.T. Gottesman, AJ **87**, 751 (1982)
- M.L.P. Gunawardhana, A.M. Hopkins, J. Bland-Hawthorn et al., MNRAS 433, 2764 (2013)
- C.-N. Hao, R.C. Kennicutt, B.D. Johnson et al., ApJ 741, 124 (2011)
- D.A. Harper Jr, F.J. Low, ApJ 182, L89 (1973)

References 19

- J.F.W. Herschel, Philosophical Transactions of the Royal Society of London Series I 154, 1 (1864)
- B.W. Holwerda, J.-C. Muñoz-Mateos, S. Comerón et al., ApJ 781, 12 (2014)
- A.M. Hopkins, A.J. Connolly, D.B. Haarsma, L.E. Cram, AJ 122, 288 (2001)
- A.M. Hopkins, A.J. Connolly, A.S. Szalay, AJ 120, 2843 (2000)
- E. Hubble, ApJ **84**, 158 (1936a)
- E.P. Hubble, ApJ 64, 321 (1926)
- E.P. Hubble, Realm of the Nebulae (1936b)
- J.P. Huchra, ApJ 217, 928 (1977)
- P.A. James, N.S. Shane, J.E. Beckman et al., A&A 414, 23 (2004)
- J.H. Jeans, Astronomy and Cosmogony (1928)
- J. Jiménez-Vicente, E. Battaner, M. Rozas, H. Castañeda, C. Porcel, A&A 342, 417 (1999)
- B.D. Johnson, D. Schiminovich, M. Seibert et al., ApJS 173, 392 (2007)
- A. Karim, E. Schinnerer, A. Martínez-Sansigre et al., ApJ 730, 61 (2011)
- G. Kauffmann, T.M. Heckman, S.D.M. White et al., MNRAS 341, 54 (2003)
- G. Kauffmann, S.D.M. White, T.M. Heckman et al., MNRAS 353, 713 (2004)
- R.C. Kennicutt, D. Calzetti, G. Aniano et al., PASP 123, 1347 (2011)
- R.C. Kennicutt, N.J. Evans, ARA&A **50**, 531 (2012)
- R.C. Kennicutt Jr, AJ 88, 483 (1983a)
- R.C. Kennicutt Jr, ApJ **272**, 54 (1983b)
- R.C. Kennicutt Jr, ApJ 344, 685 (1989)
- R.C. Kennicutt Jr, in Mass-Transfer Induced Activity in Galaxies, ed. by I. Shlosman, 131 (1994)
- R.C. Kennicutt Jr, ARA&A 36, 189 (1998a)
- R.C. Kennicutt Jr, ApJ 498, 541 (1998b)
- R.C. Kennicutt Jr, L. Armus, G. Bendo et al., PASP 115, 928 (2003)
- R.C. Kennicutt Jr, G.D. Bothun, R.A. Schommer, AJ 89, 1279 (1984)
- R.C. Kennicutt Jr, D. Calzetti, F. Walter et al., ApJ 671, 333 (2007)
- R.C. Kennicutt Jr, C.-N. Hao, D. Calzetti et al., ApJ 703, 1672 (2009)
- R.C. Kennicutt Jr, S.M. Kent, AJ 88, 1094 (1983)
- R.C. Kennicutt Jr, K.A. Roettiger, W.C. Keel, J.M. van der Hulst, E. Hummel, AJ 93, 1011 (1987)
- T. Kim, K. Sheth, J.L. Hinz et al., ApJ 753, 43 (2012)
- J.H. Knapen, J.E. Beckman, J. Cepa, T. van der Hulst, R.J. Rand, ApJ 385, L37 (1992)
- J.H. Knapen, P.A. James, ApJ 698, 1437 (2009)
- J.H. Knapen, I. Shlosman, C.H. Heller et al., ApJ 528, 219 (2000)
- H. Knox-Shaw, Helwan Inst. Astron. Geophys. Bull. 15, 129 (1915)
- X. Kong, S. Charlot, J. Brinchmann, S.M. Fall, MNRAS 349, 769 (2004)
- R.A. Koopmann, J.D.P. Kenney, J. Young, ApJS 135, 125 (2001)
- J. Kormendy, ApJ 227, 714 (1979)
- J. Kormendy, ApJ **295**, 73 (1985)
- J. Kormendy, in IAU Symposium, ed. by M. Bureau, E. Athanassoula, B. Barbuy, vol. 245, IAU Symposium, pp. 107–112 (2008)
- J. Kormendy, R. Bender, ApJ 464, L119 (1996)
- J. Kormendy, R. Bender, ApJS 198, 2 (2012)
- J. Kormendy, D.B. Fisher, M.E. Cornell, R. Bender, ApJS 182, 216 (2009)
- J. Kormendy, R.C. Kennicutt Jr, ARA&A 42, 603 (2004)
- P. Kroupa, MNRAS **322**, 231 (2001)
- K.K. Kwee, C.A. Muller, G. Westerhout, Bull. Astron. Inst. Netherlands 12, 211 (1954)
- J. Laine, E. Laurikainen, H. Salo et al., MNRAS 441, 1992 (2014)
- K.M. Lanzetta, N. Yahata, S. Pascarelle, H.-W. Chen, A. Fernández-Soto, ApJ 570, 492 (2002)
- R.B. Larson, B.M. Tinsley, ApJ 219, 46 (1978)
- J.C. Lee, A. Gil de Paz, R.C. Kennicutt Jr et al., ApJS 192, 6 (2011)
- G. Lemaître, Annales de la Societe Scietifique de Bruxelles 47, 49 (1927)
- I. Lewis, M. Balogh, R. De Propris et al., MNRAS **334**, 673 (2002)
- G. Liu, J. Koda, D. Calzetti, M. Fukuhara, R. Momose, ApJ 735, 63 (2011)

- D. Lynden-Bell, A.J. Kalnajs, MNRAS 157, 1 (1972)
- D. Lynden-Bell, J.E. Pringle, MNRAS 168, 603 (1974)
- P. Madau, H.C. Ferguson, M.E. Dickinson et al., MNRAS 283, 1388 (1996)
- P. Madau, L. Pozzetti, M. Dickinson, ApJ 498, 106 (1998)
- M. Marcelin, J. Boulesteix, Y.P. Georgelin, A&A 151, 144 (1985)
- D.C. Martin, J. Fanson, D. Schiminovich et al., ApJ 619, L1 (2005)
- I. Martín-Navarro, J. Bakos, I. Trujillo et al., MNRAS 427, 1102 (2012)
- D.S. Mathewson, V.L. Ford, ApJS **107**, 97 (1996)
- D.S. Mathewson, V.L. Ford, M. Buchhorn, ApJS **81**, 413 (1992)
- N.U. Mayall, L.H. Aller, ApJ 95, 5 (1942)
- M.L. McCall, F.H. Schmidt, ApJ 311, 548 (1986)
- S.E. Meidt, E. Schinnerer, J.H. Knapen et al., ApJ 744, 17 (2012)
- S.E. Meidt, E. Schinnerer, G. van de Ven et al., ApJ 788, 144 (2014)
- W.W. Morgan, PASP 70, 364 (1958)
- W.W. Morgan, PASP 71, 394 (1959)
- C. Moss, M. Whittle, ApJ 407, L17 (1993)
- E.J. Murphy, R.-R. Chary, M. Dickinson et al., ApJ 732, 126 (2011)
- G. Neugebauer, H.J. Habing, R. van Duinen et al., ApJ 278, L1 (1984)
- G. Paturel, C. Petit, P. Prugniel et al., A&A 412, 45 (2003)
- F.G. Pease, Proc. Natl. Acad. Sci. 2, 517 (1916)
- F.G. Pease, Proc. Natl. Acad. Sci. 4, 21 (1918)
- W.D. Pence, K. Taylor, P. Atherton, ApJ 357, 415 (1990)
- C.Y. Peng, AJ 124, 294 (2002)
- M. Persic, P. Salucci, ApJ 368, 60 (1991)
- M. Persic, P. Salucci, ApJS 99, 501 (1995)
- M. Persic, P. Salucci, F. Stel, MNRAS 281, 27 (1996)
- A.C. Phillips, in Astronomical Society of the Pacific Conference Series, ed. by R. Buta, D.A. Crocker,
 - B.G. Elmegreen, vol. 91, IAU Collog. 157: Barred Galaxies, 44 (1996)
- G.L. Pilbratt, J.R. Riedinger, T. Passvogel et al., A&A 518, L1 (2010)
- M. Querejeta, S.E. Meidt, E. Schinnerer et al., ApJS 219, 5 (2015)
- J.H. Reynolds, MNRAS 81, 129 (1920)
- G.H. Rieke, A. Alonso-Herrero, B.J. Weiner et al., ApJ **692**, 556 (2009)
- G.H. Rieke, M.J. Lebofsky, ApJ 220, L37 (1978)
- M.S. Roberts, ARA&A 1, 149 (1963)
- M.S. Roberts, ApJ 144, 639 (1966)
- W. Romanishin, AJ **100**, 373 (1990)
- A.H. Rots, A&A **45**, 43 (1975)
- V.C. Rubin, D. Burstein, W.K. Ford Jr, N. Thonnard, ApJ 289, 81 (1985)
- V.C. Rubin, W.K. Ford Jr, N. Thonnard, D. Burstein, ApJ 261, 439 (1982)
- V.C. Rubin, W.K.J. Ford, N. Thonnard, ApJ, 238, 471 (1980)
- S.D. Ryder, M.A. Dopita, ApJ 430, 142 (1994)
- S.D. Ryder, A.V. Zasov, O.K. Sil'chenko, V.J. McIntyre, W. Walsh, MNRAS 293, 411 (1998)
- S. Salim, R.M. Rich, S. Charlot et al., ApJS 173, 267 (2007)
- E.E. Salpeter, ApJ 121, 161 (1955)
- S.F. Sánchez, R.C. Kennicutt, A. Gil de Paz et al., A&A **538**, A8 (2012)
- A. Sandage, The Hubble atlas of galaxies (1961)
- A. Sandage, J. Bedke, The Carnegie Atlas of Galaxies, vol. I, II (1994)
- A. Sandage, M. Sandage, J. Kristian, Galaxies and the Universe (1975)
- P. Santini, A. Fontana, A. Grazian et al., A&A **504**, 751 (2009)
- E. Schinnerer, S.E. Meidt, J. Pety et al., ApJ **779**, 42 (2013)
- L. Searle, W.L.W. Sargent, W.G. Bagnuolo, ApJ 179, 427 (1973)
- M. Seibert, D.C. Martin, T.M. Heckman et al., ApJ **619**, L55 (2005)
- M.S. Seigar, P.A. James, MNRAS 337, 1113 (2002)

References 21

- J.A. Sellwood, Rev. Modern Phys. **86**, 1 (2014)
- H. Shapley, PASP 31, 261 (1919)
- R.M. Sharples, R. Bender, M.D. Lehnert et al., in *Society of Photo-Optical Instrumentation Engineers (SPIE) Conference Series*, ed. by A.F.M. Moorwood, M. Iye, vol. 5492, Ground-based Instrumentation for Astronomy, pp. 1179–1186 (2004)
- K. Sheth, M. Regan, J.L. Hinz et al., PASP 122, 1397 (2010)
- V. Sicotte, C. Carignan, D. Durand, AJ 112, 1423 (1996)
- V.M. Slipher, Lowell Observ. Bull. 2, 66 (1914a)
- V.M. Slipher, Popular Astron. 22, 19 (1914b)
- V.M. Slipher, Proc. Am. Philos. Soc. 56, 403 (1917)
- J.D.T. Smith, B.T. Draine, D.A. Dale et al., ApJ 656, 770 (2007)
- D. Sobral, P.N. Best, I. Smail et al., MNRAS 437, 3516 (2014)
- P.M. Solomon, L.J. Sage, ApJ 334, 613 (1988)
- L. Spitzer Jr, W. Baade, ApJ 113, 413 (1951)
- C.C. Steidel, K.L. Adelberger, M. Giavalisco, M. Dickinson, M. Pettini, ApJ 519, 1 (1999)
- C.C. Steidel, M. Giavalisco, M. Pettini, M. Dickinson, K.L. Adelberger, ApJ 462, L17 (1996)
- M. Sullivan, B. Mobasher, B. Chan et al., ApJ 558, 72 (2001)
- C.M. Telesco, D.A. Harper, ApJ 235, 392 (1980)
- B.M. Tinsley, ApJ 151, 547 (1968)
- B.M. Tinsley, A&A 20, 383 (1972)
- S. Tremaine, in *Dynamics of Astrophysical Discs*, ed. by J.A. Sellwood, pp. 231–238 (1989)
- M. Treyer, D. Schiminovich, B. Johnson et al., ApJS 173, 256 (2007)
- M. Treyer, D. Schiminovich, B.D. Johnson et al., ApJ 719, 1191 (2010)
- R.B. Tully, ApJS 27, 415 (1974)
- H.C. van de Hulst, E. Raimond, H. van Woerden, Bull. Astron. Inst. Netherlands 14, 1 (1957)
- S. Van den Bergh, ApJ 131, 558 (1960a)
- S. Van den Bergh, ApJ 131, 215 (1960b)
- S. Van den Bergh, AJ **71**, 922 (1966)
- S. van den Bergh, ApJ **206**, 883 (1976a)
- S. van den Bergh, AJ 81, 797 (1976b)
- J.M. van der Hulst, A&A **75**, 97 (1979)
- F. Walter, E. Brinks, W.J.G. de Blok et al., AJ 136, 2563 (2008)
- B. Wang, T.M. Heckman, ApJ 457, 645 (1996)
- M.W. Werner, T.L. Roellig, F.J. Low et al., ApJS **154**, 1 (2004)
- M. Wolf, Publikationen des Astrophysikalischen Instituts Koenigstuhl-Heidelberg 3, 109 (1908)
- M. Wolf, Vierteljahresschr. Astron. Ges. 49, 162 (1914)
- J.S. Young, L. Allen, J.D.P. Kenney, A. Lesser, B. Rownd, AJ 112, 1903 (1996)
- J.S. Young, N. Scoville, ApJ 258, 467 (1982)
- J.S. Young, N.Z. Scoville, ARA&A 29, 581 (1991)
- D. Zaritsky, H. Courtois, J.-C. Muñoz-Mateos et al., AJ 147, 134 (2014)
- D. Zaritsky, H. Salo, E. Laurikainen et al., ApJ **772**, 135 (2013)
- X.Z. Zheng, E.F. Bell, C. Papovich et al., ApJ **661**, L41 (2007)
- Y.-N. Zhu, H. Wu, C. Cao, H.-N. Li, ApJ 686, 155 (2008)

Chapter 2 Massive Star Formation in Galaxies with Excess UV Emission

2.1 Introduction

Early type galaxies and early-type spirals (ETSs) are frequent in the Universe. These are classified with morphologies from E to Sab. They are regarded as evolved galaxies which have undergone a series of merging processes of less or more gas-rich galaxies occurring on cosmological timescales (essentially the ellipticals; see e.g., Toomre and Toomre 1972; Schweizer and Seitzer 1992; Kormendy et al. 2009), or experienced a continued process of secular evolution which gradually converted later into earlier-type galaxies (essentially lenticular galaxies, e.g., Laurikainen et al. 2010).

In the mid-1970s, the first studies of SFRs in early-type galaxies were performed, when van den Bergh (1976) and Kormendy (1977) reported detecting no H α in the knots seen in two early-type galaxies, NGC 4594 (the Sombrero Galaxy) and NGC 2841. The impression that ETSs are associated with low levels of SF comes from the H α equivalent width measurements presented in Kennicutt and Kent (1983). They found that the H α equivalent widths systematically decrease from later to earlier-type spirals, indicating that ETSs have less massive young star formation than late-type spiral galaxies. Several studies confirm that galaxies with morphological types between E and Sab are generally characterised by low SFRs, with values $<0.6M_{\odot}$ yr⁻¹ (e.g., Kennicutt and Kent 1983; Trinchieri and di Serego Alighieri 1991; Caldwell et al. 1991, 1994; Pogge and Eskridge 1999; James et al. 2004) and low content of gas (e.g., Roberts 1969 or Roberts and Haynes 1994).

More recent observations have suggested that some ellipticals, S0s and ETSs are not as relaxed and inactive as considered before, finding a very wide range of SFRs, from near-zero to several M_{\odot} yr⁻¹. Young et al. (1996) and Usui et al. (1998) found several ETSs with SFRs comparable to those of late-type galaxies. Hameed and Devereux (2005) found that the majority of Sa-Sab galaxies in their sample are forming stars at a modest rate, but a significant fraction (around 29 %) exhibit

the Hubble Sequence of Galaxies, Springer Theses,

S. Erroz-Ferrer, Morphology, Kinematics and Star Formation Across

SFRs greater than 1 M_{\odot} yr⁻¹. Later on, emission lines from the central regions in the majority of E and S0 galaxies were found by the SAURON survey (Sarzi et al. 2006), although the emission in around 50 % of the cases arises from young massive stars (Sarzi et al. 2010).

As explained in Sect. 1.4, there are many SFR tracers. Most of the studies cited before come from $H\alpha$ observations. Additionally, the emission from young and massive stars in the ultraviolet (UV) traces the current SFR (e.g. Donas et al. 1987; Kennicutt 1998). The launch of the *Galaxy Evolution Explorer* (*GALEX*; Martin et al. 2005) has opened a new window by bringing the possibility of obtaining deep UV images of tens of thousand galaxies.

This project is based on the first analysis of over 5000 *GALEX* UV images of galaxies classified between E and Sab. A significant subset of these galaxies shows unusual UV emission for their type. This emission is not located in the central parts, and is mostly concentrated in complete or incomplete rings, spiral arms or fragments of those, or in other structures. With the goal to understand the nature of the UV emission in these early-type galaxies and ETSs, we have obtained H α images of a small subsample of these galaxies. If H α emission is found, we would be able to discriminate between the possible origin scenarios of the UV emission. If H α emission is not found, it is possible that the initial mass function is populated enough to produce UV emission but not populated enough to produce H α emission (see Lee et al. 2011).

Another possible phenomenon that can explain the UV emission in early-type galaxies is the UV-upturn phenomenon, where old stars (most likely extreme horizontal branch stars) emit in the UV (Code and Welch 1979; Burstein et al. 1988; see the reviews by O'Connell 1999 and Yi 2008). Old stars can produce UV emission (Greggio and Renzini 1990; Horch et al. 1992; Bressan et al. 1994; Dorman et al. 1995; Brown et al. 2000; Buzzoni 2007), and many ellipticals show residual levels of SF (Yi et al. 2005). The UV-upturn phenomenon occurs in ellipticals and bulges in spiral galaxies (O'Connell 1999), but unlikely explains the UV emission originated in the outer regions of the galaxies. GALEX observations have demonstrated that less than 10 % of the ellipticals show UV spectral shapes that are consistent with the general definition of the UV-upturn. Furthermore, the fraction of ellipticals showing UV-upturn decreases dramatically with mass, being found almost exclusively in giant ellipticals (Yi et al. 2005; Kaviraj et al. 2007; Schawinski et al. 2007). If $H\alpha$ counterparts are found in our images, the UV-upturn would not be the origin of the UV emission. It is important to mention the work done by Salim et al. (2012), who analysed UV images of some ellipticals, S0s, and ETSs, finding low-level SFRs of $\sim 0.5 M_{\odot} \text{ yr}^{-1}$ in the form of rings and other structures. They considered these results to be inconsistent with the UV-upturn.

This chapter is organized as follows: the sample galaxies is explained in Sect. 2.2. Section 2.3 describes the observations and data reduction. Section 2.4 presents the results, which are discussed in Sect. 2.5.

2.2 Target Selection

The starting point are 4822 images of galaxies classified between E and Sab present in the *GALEX* Large Galaxy Atlas (GLGA; Seibert 2007) with diameters over 0.8 arcmin. From those, 80 galaxies had no UV emission. Additionally, we chose a limit of 27 mag arcsec⁻² at a signal-to-noise ratio of 5. These restrictions let to a final sample of 1899 galaxies. For each of these galaxies, we performed a visual comparison between *GALEX* images and optical data in order to identify the UV in morphological structures such as spiral arms, rings, clumpy material or even streams of material. We identify UV emission in the outer parts of 531 of the 1899 galaxies, which corresponds to 28 %. UV emission in morphological structures were found in 18 % of E galaxies, increasing to 28 % for S0 and 45 % for S0/a-ab. Regarding UV emission not present in an specific morphological feature, the numbers are: 1 % in E, 3 % in S0 and 7 % in S0/a-Sab.

Ten galaxies were selected to be observed in $H\alpha$ from the sample of 531 galaxies with UV emission. The selection was randomly performed, not according to specific features or properties, but on the altitude on the sky at the time of the observations. We made certain, however, that at least two ellipticals were observed. The observed sample is: NGC 160, NGC 262, NGC 4698, NGC 5173, NGC 5389, NGC 5982, NGC 6962, NGC 7371, NGC 7787 and PGC 065981. Table 2.1 presents the general properties of the observed galaxies.

C-1	T (DC2) (1)	II. 1.4. 1 T	D (M) (2)	D (:-) (4)
Galaxy name	Type (RC3) (1)	Updated Type	$D (\mathrm{Mpc}) (3)$	D_{25} (arcmin) (4)
		(Buta) (2)		
NGC 160	(R)SA0^+pec		70.5 ± 14.1	2.95
NGC 262	SA0/a?(s)		60.7 ± 12.1	1.07
NGC 4698	SA(s)ab	(R)SA(rr)0/a/E2	13.7 ± 2.7	3.98
NGC 5173	E0:	E∧+1	40.6 ± 8.1	1.78
NGC 5389	SAB0/a?(r)		32.2 ± 6.4	3.47
NGC 5982	E3	E2	47.9 ± 9.6	2.57
NGC 6962	SAB(r)ab		61.1 ± 12.2	2.88
NGC 7371	(R)SA0/a?(r)	SAB(s)ab	37.9 ± 7.6	2.04
NGC 7787	(R')SB0/a?(rs)		89.8 ± 18.0	1.78
PGC 065981	SAB(s)ab?		122.5 ± 14.5	1.55

 Table 2.1 General properties of the sample galaxies

Notes (1) Morphological classifications from the third reference catalogue of bright galaxies (RC3; de Vaucouleurs et al. 1991). (2) Updated morphological classifications from Buta et al. (2010) and Buta et al. (2015). (3) Distance values, calculated with the Virgo, GA and shapley corrections, using H_0 = 73 \pm 5 km s⁻¹ Mpc⁻¹, from the NASA/IPAC extragalactic database (NED). These distances have been measured using the Tully-Fisher relationship, and we estimate an uncertainty of 20 % in the distance values. (4) Apparent major isophotal diameter, D_{25} , measured at or reduced to the surface brightness level B = 25.0 mag arcsec⁻², as explained in Sect. 3.4.a, page 21, of Volume I of the printed RC3

2.3 Observations and Data Reduction

2.3.1 ALFOSC R-Band and Ha

The H α narrow-band images were obtained in conjunction with *R*-band images with the Andalucia Faint Object Spectrograph and Camera (ALFOSC) at the 2.5 m Nordic Optical Telescope (NOT), in Roque de los Muchachos Observatory, in La Palma, during the nights of July 24–25th 2011, and June 2nd 2013. ALFOSC field of view (FOV) is 6.4 arcmin², and delivers 0.19 arcsec/pixel images. A Bessel filter of 6500/1300 (central wavelength/FHWM, in Å) was used to perform the *R*-band observations. Depending on the galaxy distance, several H α filters were used: 6655/55: NGC 160, NGC 262 and NGC 6962; 6615/50: NGC 5173, NGC 5389, NGC 5982 and NGC 7371; 6584/36: NGC 4698; 6704/45: NGC 7787; 6745/50: PGC 065981. The galaxies were observed 5 × 900 s in H α and 5 × 120 s in the *R*-band. The seeing varied from 0.6" to 1.6", with a typical value of 1".

The images have been reduced using IRAF packages, following these steps: bias and flat corrections, sky subtraction, image combination and photometric calibration. After that, surface photometry was performed using the ELLIPSE task in IRAF. The resulting fluxes were corrected for Galactic absorption, A(R), taken from NED, from the Schlafly and Finkbeiner (2011) recalibration of the Schlegel et al. (1998) IR-based dust map. We computed the instrumental magnitude of each galaxy, and derived the m_R magnitudes and the corresponding absolute R magnitudes (M_R) using the distances in Table 2.1. The results are presented in Table 2.2. Note that the errors on M_R are dominated by the uncertainties in the distances (assumed 20 %).

The continuum subtraction of the $H\alpha$ images was performed with the methods from Knapen et al. (2004), Bradley et al. (2006) and Sánchez-Gallego et al. (2012). We used spectrophotometric standard stars to calibrate the continuum-subtracted $H\alpha$ images. The observed fluxes and corresponding luminosities for the whole galaxies were calculated as

$$L(H\alpha)[erg/s] = 4\pi D^2 (3.086 \times 10^{24})^2 F_{H\alpha}^*,$$
 (2.1)

with D the distance to the galaxy in Mpc (Table 2.1) and $F_{\rm H\alpha}^*$ the flux corrected for Galactic absorption. We isolated the regions of interest (i.e., outer features such as external rings or spiral arms) and measured the fluxes and luminosities there. These fluxes were also corrected for Galactic absorption (see Sect. 2.4.2).

 Table 2.2 Results from the surface photometry

Ianic 2.2 Nos	saits moin aic s	lable 2.2 Results If the surface protonieus	cuy					
Galaxy name $A(R)$ (mag)	A(R) (mag)	A(B) (mag)	A(V) (mag)	$A(B)$ (mag) $A(V)$ (mag) $E(B-V)$ (mag) M_R (mag)	M _R (mag)	FUV (mag)	NUV (mag)	FUV—NUV (mag)
NGC 160	0.071	0.119	0.090	0.029	-21.77 ± 1.00	17.31 ± 0.03	16.81 ± 0.03	0.50 ± 0.05
NGC 262	0.145	0.242	0.183	0.059	-20.27 ± 1.00	16.19 ± 0.04	15.90 ± 0.04	0.29 ± 0.06
NGC 4698	0.056	0.094	0.071	0.023	-20.28 ± 1.00	16.38 ± 0.03	15.36 ± 0.03	1.01 ± 0.05
NGC 5173	0.059	0.063	0.048	0.015	-20.61 ± 1.00	17.10 ± 0.03	16.59 ± 0.03	0.52 ± 0.04
NGC 5389	0.043	0.073	0.055	0.018	-20.93 ± 1.00	17.60 ± 0.03	16.96 ± 0.03	0.64 ± 0.04
NGC 5982	0.038	0.171	0.129	0.042	-22.65 ± 1.00	17.92 ± 0.03	16.46 ± 0.04	1.47 ± 0.05
NGC 6962	0.212	0.355	0.269	0.086	-22.48 ± 1.00	15.74 ± 0.05	15.30 ± 0.05	0.44 ± 0.07
NGC 7371	0.128	0.213	0.161	0.052	-21.00 ± 1.00	15.42 ± 0.04	14.92 ± 0.04	0.50 ± 0.06
NGC 7787	0.082	0.137	0.104	0.033	-20.90 ± 1.00	18.28 ± 0.03	17.62 ± 0.04	0.66 ± 0.05
PGC 065981	0.102	0.171	0.129	0.042	-22.27 ± 1.00	16.70 ± 0.04	16.33 ± 0.04	0.37 ± 0.05

Column I Galaxy name. Columns II, III and IV Galactic absorption A(R), A(B) and A(V) from the Schlafty and Finkbeiner (2011) recalibration of the Schlegel et al. (1998) dust map. Column V Colour excess E(B - V). Column VI Absolute R magnitude. Columns VII and VIII FUV and NUV asymptotic magnitudes. R and UV magnitudes have been corrected for Galactic absorption. Column IX (FUV-NUV) colour

2.3.2 *GALEX UV*

GALEX images were obtained through The Barbara A. Mikulski Archive for Space Telescopes (MAST¹) from the All-sky Imaging Survey (AIS), Medium Imaging Survey (MIS), Guest Investigator Program (GIP) and NGS. We refer the reader to Martin et al. (2005) and Morrissey et al. (2005) for information about the scientific objectives and characteristics of the telescope and the observing surveys mentioned before. The GALEX FOV is circular with a diameter of 1.2°. The two channels (FUV and NUV) have effective wavelengths of 1516 and 2267 Å, and image resolutions (FWHM) of 4.3″ and 5.3″, respectively.

After subtracting the sky background in both the FUV and NUV images, we measured the fluxes of the same regions previously defined in the $H\alpha$ images (i.e. whole galaxy and outer regions). To convert intensities into magnitudes, the *GALEX* zero point magnitudes presented in Morrissey et al. (2007) were used. The FUV and NUV flux densities were corrected for Galactic absorption using the Schlafly and Finkbeiner (2011) recalibration of the Schlegel et al. (1998) infrared-based dust map and the Galactic Extinction curve derived by Cardelli et al. (1989) for a total-to-selective extinction of $R_V=3.1$. In this case, $A(\text{FUV})_{\text{MW}}=7.9\ E(B-V)$ and $A(\text{NUV})_{\text{MW}}=8.0\ E(B-V)$. The resulting magnitudes are presented in Table 2.2.

2.4 Results

2.4.1 Morphology: General

The morphological comparison between the galaxies from the GALEX UV and H α narrow band images reveals several similarities, as shown in Figs. 2.1, 2.2 and 2.3. The selected galaxies (ten out of 531) in our sample present extra UV emission in the form of rings or spiral arms, confirmed in both the UV and H α images. The rings are perfectly identified in the UV images, and also outlined in the H α images. Nonetheless, these features are not traced that well in the R-band images. In our sample galaxies, three of those present uncertain morphological classification in the RC3 and have not been studied by Buta et al. (2010). Our analysis confirm that the uncertainties in the morphological classification can be removed in those cases (i.e., NGC 262: SA(s)0/a, NGC 5389: SAB(r)0/a and PGC 065981: SAB(s)ab).

Additionally, the different angular resolution of the *GALEX* images (4.3" and 5.3" for the NUV and FUV images, respectively) compared to that of the $H\alpha$ images (seeing limited, with values from 0.7" to 1.6") can be translated into extended features in the UV than in $H\alpha$. Moreover, the UV emission is expected to be more extended as it tracer older stellar populations than $H\alpha$.

¹http://archive.stsci.edu/.

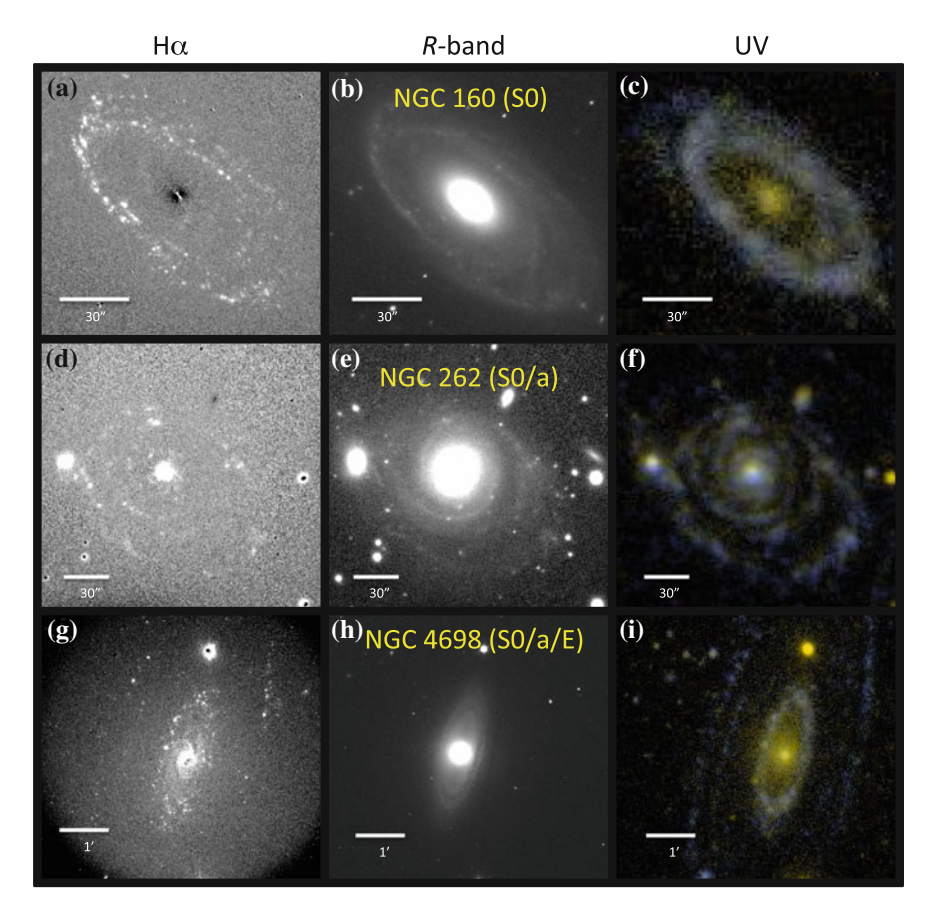


Fig. 2.1 Left H α continuum-subtracted images. Middle R-band images. Right False-colour GALEX maps. These false-colour RGB images are 'asinh' scaling versions (Lupton et al. 2004) of the 2-pixel-smoothed FUV image (blue), the original NUV image (red), and a linear combination of the two (green). **a**, **b** and **c** NGC 160. **d**, **e** and **f** NGC 262. **g**, **h** and **i** NGC 4698. In the images, North is up and East to the left

2.4.2 Morphology: Individual Galaxies

NGC 160

The morphological classification of NGC 160 in the RC3 is (R)SA0 $^+$ +pec. This case shows great correlation between the UV and H α emissions, as the outer ring can be easily recognized in both the H α and UV images (panels a and c of Fig. 2.1). The patchiness typical of the H α emission is seen in this ring. In the central parts, although there is UV emission, there are no H α counterparts. There are, however,

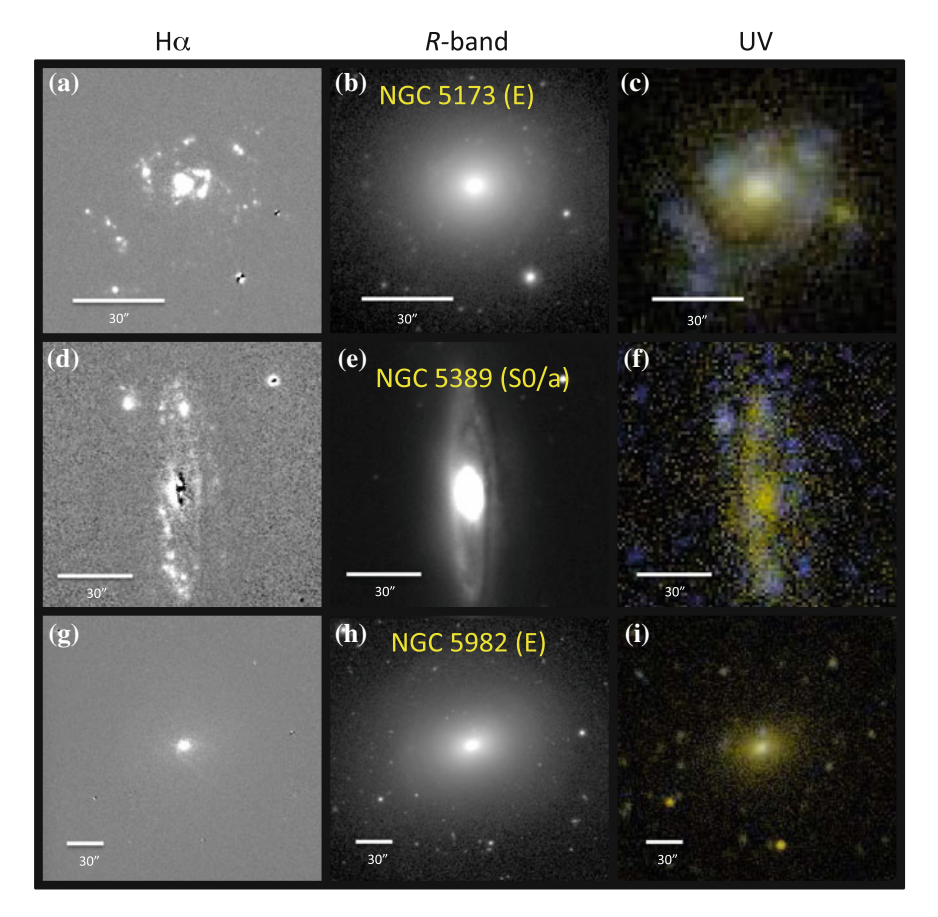


Fig. 2.2 As Fig. 2.1 but now: **a**, **b** and **c** NGC 5173. **d**, **e** and **f** NGC 5389. **g**, **h** and **i** NGC 5982. In the images, North is up and East to the left

residuals in the H α image due to the continuum-subtraction, arising from the large R-band emission there, normally found in S0s.

NGC 262

NGC 262 has been classified as SA0/a?(s) in the RC3. According to nuclear activity, the galaxy was classified as a Seyfert 2 galaxy in the Second Reference Catalogue of Bright Galaxies (RC2; de Vaucouleurs et al. 1976). As a matter of fact, the nuclear emission dominates the flux of the galaxy. However, in both the H α (panel d in Fig. 2.1) and UV (panel f in Fig. 2.1) images, the spiral arms are perfectly traced.

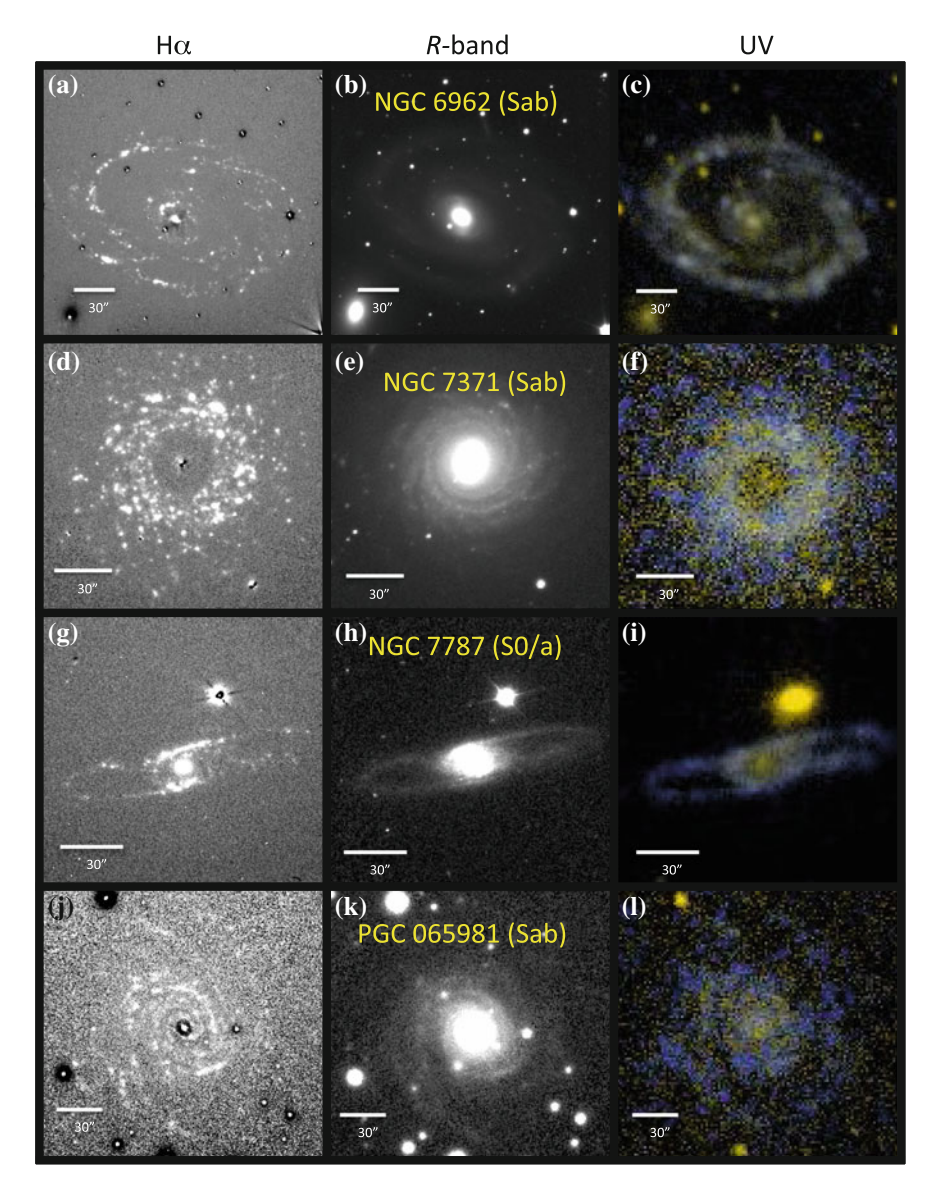


Fig. 2.3 As Fig. 2.1 but now: **a**, **b** and **c** NGC 6962. **d**, **e** and **f** NGC 7371. **g**, **h** and **i** NGC 7787. **j**, **k** and **l** PGC 065981. In the images, North is up and East to the left

NGC 4698

Morphologically, NGC 4698 was classified as SA(s)ab in the RC3. Buta et al. (2015) reclassify it as (R)SA(rr)0/a/E2, a double-stage spiral where inner and outer spiral pattern are different (described by Vorontsov-Vel'Yaminov 1987). Here, there is an E-like bulge at the start of the spiral arms. This galaxy was classified in The Carnegie

Atlas of Galaxies (Sandage and Bedke 1994) in the earliest 30 % of the Sa group due to the smooth inner disc, to the large bulge without recent SF defined by the dust lanes and to the tightly wound spiral arms. Two outer rings can be seen in both the UV and H α images. A third ring in between the other two can hardly be recognised in H α (panel g in Fig. 2.1) but which can be easily seen in the UV image (panel i in Fig. 2.1). In this case, as in NGC 160, the H α emission is patchier than the ultraviolet one. The galaxy is a low-luminosity Seyfert 2 galaxy (Ho et al. 1995) with a strong nuclear emission.

NGC 5173

The morphological classification of NGC 5173 is E0, which is consistent with the elliptical shape from the *R*-band image. Yet, some features not belonging to an spherical component can be distinguished in both the $H\alpha$ and UV images. This clumpy material (likely to be incomplete spiral arms) seen in $H\alpha$ and UV correspond to recently born stars, in other words, star formation. In the central parts, the UV emission may not be caused by star formation but to the UV-upturn phenomenon. Therefore, the derived SFRs for the centre and whole galaxy (Sect. 2.4.3) may be overestimated.

NGC 5389

The morphological classification in the RC3 of NGC 5389 is SAB0/a?(r). Both H α and UV images (panels d and e of Fig. 2.2) show the outer ring. The left part (West) of the ring is brighter than the right (East) one, likely because of the inclination, causing the right part to be more obscured by dust than the left part.

NGC 5982

NGC 5982 has been classified as an elliptical galaxy, clearly seen in the R-band image. The central emission is present in both H α an UV images. This central emission may not be due to star formation and overestimates the SFRs, especially since this galaxy has been classified as a LINER (Ho et al. 1997). In this case, the UV-upturn phenomenon may contribute to the central UV emission. Contrary to what is found for the other elliptical NGC 5173, NGC 5982 does not seem to present clear UV emission in the outer parts, just some faint blue blobs.

NGC 6962

The morphological classification of NGC 6962 is a SAB(r)ab in the RC3. Two main, faint outer arms can be easily recognised in both H α and UV images (panels a and c of Fig. 2.3). Here, we also see that the H α emission is patchier than the UV emission.

NGC 7371

This galaxy is classified as (R)SA0/a?(r) in the RC3, and reclassified as SAB(s)ab in Buta et al. (2010). In this galaxy, there is not recent star formation in the central parts. Although the poor *GALEX* spatial resolution leads to the false perception that there is a ring (see panel f in Fig. 2.3), the H α (panel d in Fig. 2.3) and the *R*-band (panel e in Fig. 2.3) images allows us to distinguish the spiral arms.

2.4 Results 33

NGC 7787

In the RC3, NGC 7787 has been clasified as (R')SB0/a?(rs). An outer (pseudo-)ring can be distinguished in both the H α and UV images (panels g and i of Fig. 2.3).

PGC 065981

This galaxy is classified as SAB(s)ab?. The spiral arms can be easily identified in both the UV and H α and UV images (panels i and j of Fig. 2.3). Due to the different angular resolutions of the images or due to the different stellar populations, the spiral arms are better traced in the H α image than in the UV image (see Sect. 2.4.1). Moreover, the inter-arm region cannot be easily identified in the UV image.

2.4.3 Star Formation Rates

Global measurements

In Sect. 1.4.2, I presented some of the star formation calibrators (radio, IR, optical, UV or X-ray), as well as combination of some of those to take into account dust absorption (e.g., UV + IR). Mixed calibrators reduce the uncertainties regarding dust attenuation, although uncertainties related to the IMF remain. Here, we have adopted a double-power-law Kroupa IMF Kroupa (2001), where the range in stellar mass is 0.1– $100~M_{\odot}$, and the timescales are $t(H\alpha) \geq 6$ Myr and $t(UV) \geq 100$ Myr. To take into account the dust attenuation, we have used mixed calibrators using UV and $H\alpha$ with IR. UV data from GALEX traces directly recent star formation, but with the drawback of the sensitivity to dust obscuration/attenuation. To correct for this attenuation, we compute the TIR using data from the 25, 60 and 100 μ m bands of the *Infrared Astronomical Satellite* (*IRAS*) for 9 of the 10 galaxies in our sample and following the expression in Dale and Helou (2002):

$$L(TIR) = 2.403\nu L_{\nu}(25 \,\mu\text{m}) - 0.2454\nu L_{\nu}(60 \,\mu\text{m}) + 1.6381\nu L_{\nu}(100 \,\mu\text{m}).$$
 (2.2)

For the PGC 065981, which did not have *IRAS* data, we estimated L(TIR) from the FUV-NUV colour (Cortese et al. 2006):

$$\log \left[\frac{L(\text{TIR})}{L(\text{FUV})} \right] = 0.7[2.201(FUV - NUV) - 1.804] + 1.3.$$
 (2.3)

All these *IRAS* values are collected in Table 2.3.

The next step is to compute the dust-corrected luminosities using the empirical calibration factors from Kennicutt et al. (2009) and Hao et al. (2011):

$$L(FUV)_{corr} = L(FUV)_{obs} + 0.46 L(TIR), \tag{2.4}$$

$$L(\text{NUV})_{\text{corr}} = L(\text{NUV})_{\text{obs}} + 0.27 L(\text{TIR}) \text{ and}$$
 (2.5)

$$L(H\alpha)_{corr} = L(H\alpha)_{obs} + 0.0024 L(TIR). \tag{2.6}$$

Galaxy name	$f_{\nu}(25) (\mathrm{Jy})$	$f_{\nu}(60) (\mathrm{Jy})$	$f_{\nu}(100) (\mathrm{Jy})$	Refs.	$L(TIR) (erg s^{-1})$
NGC 160	0.034 ± 0.034	0.140 ± 0.048	0.650 ± 0.082	(1)	$(2.38 \pm 1.15) \times 10^{43}$
NGC 262	0.835 ± 0.025	1.290 ± 0.116	1.549 ± 0.201	(2)	$(1.33 \pm 0.54) \times 10^{44}$
NGC 4698	0.154 ± 0.154	0.258 ± 0.062	1.864 ± 0.168	(2)	$(2.99 \pm 1.58) \times 10^{42}$
NGC 5173	0.031 ± 0.031	0.350 ± 0.042	0.530 ± 0.159	(1)	$(6.05 \pm 3.40) \times 10^{42}$
NGC 5389	0.014 ± 0.014	0.410 ± 0.018	1.960 ± 0.072	(1)	$(1.18 \pm 0.49) \times 10^{43}$
NGC 5982	0.022 ± 0.022	0.033 ± 0.033	0.370 ± 0.035	(1)	$(6.62 \pm 3.24) \times 10^{42}$
NGC 6962	0.144 ± 0.144	0.338 ± 0.047	2.250 ± 0.383	(2)	$(6.61 \pm 3.37) \times 10^{43}$
NGC 7371	0.184 ± 0.184	1.104 ± 0.341	2.679 ± 0.311	(3)	$(2.94 \pm 1.53) \times 10^{43}$
NGC 7787	0.177 ± 0.177	0.641 ± 0.058	1.846 ± 0.185	(2)	$(1.29 \pm 0.73) \times 10^{44}$
PGC 065981	_	_	_	_	$(1.10 \pm 0.87) \times 10^{44}$

Table 2.3 IR photometry data

Column I Galaxy name. Columns II–V IRAS flux densities for the 25, 60 and 100 μ m bands and the references. Column VI L(TIR) derived following the equations in Dale and Helou (2002). References (1) NED (2) IRAS faint source catalogue, version 2.0 (Moshir and et al. 1990). (3) IRAS faint source reject catalog (Moshir et al. 2008). For PGC 065981, we have estimated L(TIR) from the TIR/FUV ratio (Cortese et al. 2006)

In this case (galaxies with low specific SFR or dust-free galaxies), using these IR-based recipes can be problematic: the emission from the dust-heating of evolved stars may overestimate the IR luminosity, and therefore the corrected SFRs (see Kennicutt and Evans 2012 and references therein). As a consequence, the corrected luminosities from Eqs. 2.4–2.6 should be understood as upper limits, and therefore the resulting SFRs. The real SFRs should be in between the dust-uncorrected and the dust-corrected SFRs using these equations.

Cortese et al. (2008) presented empirical relations that avoided these systematic errors. They estimated the UV attenuation A(FUV) using the age dependence in the relationship between the TIR/FUV ratio and A(FUV). If τ_{age} is the time at which the SFR reaches the highest value over the whole galaxy Gavazzi et al. (2002), long τ_{age} corresponds to star-forming (young) galaxies and a short τ_{age} refers to galaxies with older stellar populations. Cortese et al. (2008) propose using the FUV – H colour to compute τ_{age} :

$$\log(\tau_{\text{age}}) = -0.068(\text{FUV} - H) + 1.13 \tag{2.7}$$

and afterwards calculating A(FUV) or A(NUV) from their polynomial fit.

Alternatively, several proposals regarding dust corrections can be found in the literature. The constant value of $A(H\alpha) = 1.1$ mag proposed by Kennicutt and Kent (1983) has been proved to change with inclination or morphological type (see James et al. 2005). Helmboldt et al. (2004) propose computing $A(H\alpha)$ from the absolute R magnitudes of the galaxies (M_R) from Table 2.2 using the following equation:

$$\log[A(H\alpha)] = (-0.12 \pm 0.048)M_R + (-2.5 \pm 0.96) \tag{2.8}$$

2.4 Results 35

Galaxy name	$A(H\alpha)_{TIR}$ (mag)	$A(H\alpha)_R$ (mag)	A(FUV) _{TIR} (mag)	A(FUV) _{Cor} (mag)	A(NUV) _{TIR} (mag)	A(NUV) _{Cor} (mag)
NGC 160	0.60	1.30	1.24	1.45	0.82	1.09
NGC 262	1.09	0.86	2.07	1.93	1.68	1.63
NGC 4698	0.58	0.86	1.51	0.91	0.75	0.80
NGC 5173	0.31	0.94	0.93	1.70	0.58	1.46
NGC 5389	0.74	1.03	2.22	0.69	1.53	0.51
NGC 5982	0.15	1.65	1.29	0.36	0.44	0.52
NGC 6962	0.70	1.58	1.14	1.73	0.78	1.40
NGC 7371	0.51	1.05	1.04	1.95	0.67	1.66
NGC 7787	1.12	1.02	3.17	1.56	2.39	1.33
PGC 065981	1.50	1.49	1.15	1.15	0.81	0.87

Table 2.4 Column I Galaxy name

Column II Extinction coefficient for H α using L(TIR). Column III Extinction coefficient for H α using Eq. 2.8. Columns IV-V Extinction coefficients for FUV using L(TIR) and Cortese et al. (2008) to correct for internal dust extinction. Columns VI-VII The same as IV-V but for NUV

In Table 2.4 we present the resulting values for the dust extinction corrections using TIR, and the methods of Cortese et al. (2008) and Helmboldt et al. (2004). The advantages and disadvantages of each method will be discussed in Sect. 2.5.

Following Kennicutt et al. (2009) and Hao et al. (2011) we derive the dust-corrected SFR measurements from the dust-corrected luminosities using:

SFR(FUV)
$$(M_{\odot} \text{ yr}^{-1}) = 4.6 \times 10^{-44} L(\text{FUV}),$$
 (2.9)

SFR(NUV)
$$(M_{\odot} \text{ yr}^{-1}) = 6.8 \times 10^{-44} L(\text{NUV})$$
 and (2.10)

SFR(H
$$\alpha$$
) $(M_{\odot} \text{ yr}^{-1}) = 5.5 \times 10^{-42} L(H\alpha)$ (2.11)

Tables 2.5 and 2.6 show the resulting SFRs. The final error takes into account the uncertainties in the method, as well as uncertainties arising from the quality of the image, from the image reduction processes, or from the distance (see Sect. 4.4.3 for a detailed discussion).

Outer regions

As mentioned before, our goal is to study the outer parts of the galaxies. *I RAS* data does not enable to correct specific regions for dust attenuation due to its poor angular resolution, and therefore this method can only be applied to the global measurements of galaxies. Calzetti et al. 2012) summarizes the problems induced by inaccurate estimates of local SFRs, and we cannot use these IR-based recipes to correct for dust attenuation in specific regions such as the spiral arms or the rings.

Alternatively, we have computed the ratio of emission located in the specific feature (i.e., ring or spiral arm) as compared to the total emission from the galaxy, shown in Table 2.7. Note that NGC 5982 has not been included in this table as the

Galaxy name	$SFR(H\alpha)_{obs} (M_{\odot} yr^{-1})$	$SFR(FUV)_{obs} (M_{\odot} yr^{-1})$	$SFR(NUV)_{obs} (M_{\odot} yr^{-1})$
NGC 160	0.43 ± 0.17	0.24 ± 0.09	0.39 ± 0.15
NGC 262	1.01 ± 0.41	0.49 ± 0.19	0.66 ± 0.26
NGC 4698	0.06 ± 0.02	0.02 ± 0.01	0.06 ± 0.02
NGC 5173	0.24 ± 0.10	0.09 ± 0.01	0.16 ± 0.06
NGC 5389	0.16 ± 0.06	0.04 ± 0.01	0.07 ± 0.03
NGC 5982	0.59 ± 0.24	0.06 ± 0.02	0.25 ± 0.10
NGC 6962	0.96 ± 0.38	0.75 ± 0.30	1.16 ± 0.47
NGC 7371	0.64 ± 0.26	0.39 ± 0.16	0.63 ± 0.25
NGC 7787	0.94 ± 0.38	0.16 ± 0.06	0.30 ± 0.12
PGC 065981	0.49 ± 0.19	1.24 ± 0.49	1.81 ± 0.72

Table 2.5 Observed SFRs (i.e., not corrected for internal dust attenuation)

UV emission is only found in the central parts, not in outer features. The case of the other elliptical in our sample, NGC 5173 is the opposite: there is emission found in the outer parts, in the form of incomplete spiral arms.

Table 2.7 shows that the emission in the outer features is, in most cases, dominant compared to the total emission from the galaxy. Specifically, for NGC 160, NGC 6962 and NGC 7371, the outer emission is above three quarters of the total emission. In addition, when we include the emission of all the rings in NGC 4698, almost 100 % of the emission is located outside the central parts. On the contrary, the case of NGC 262 is different: the ratio is over 50 % in the UV, but the H α emission in the spiral arms is around 3 %. This means that most of the H α emission comes from the central parts, consistent with the fact that NGC 262 is a Seyfert 2 galaxy, where the nuclear emission is dominated by the AGN activity. Note that in this table, we have only taken into account the emission from the features, not the central emission.

2.5 Discussion

2.5.1 Morphology

As far as morphology is concerned, our sample galaxies show very similar morphologies in the H α and the UV. This is one of the first important results from this work, there is a direct correlation between the position of outer features in the UV images and the HII regions in the H α images. For instance, the outer rings present in NGC 160, NGC 7731 and NGC 7787 can be easily identified in all the images, also confirming the morphological classifications designated by (R) or (R'). As explained before, the emission of these outer features look more extended in the UV, and more patchy in H α due to the different angular resolution and ages.

 Table 2.6
 Global SFRs corrected for dust absorption

Galaxy name	Preferred corrections	suc		Alternative corrections	tions		
	$SFR(H\alpha)_R$	SFR(FUV)Cort	SFR(NUV)Cort	$SFR(H\alpha)_{1.1}$	$SFR(H\alpha)_{TIR}$	SFR(FUV) _{TIR}	SFR(NUV) _{TIR}
	$ (M_{\odot} \text{ yr}^{-1}) $	$ (M_{\odot} \text{ yr}^{-1}) $	$(M_{\odot} \text{ yr}^{-1})$	$ (M_{\odot} \mathrm{\ yr}^{-1}) $	$ (M_{\odot} \text{ yr}^{-1}) $	$(M_{\odot} { m yr}^{-1})$	$ (M_{\odot} \text{ yr}^{-1}) $
NGC 160	1.41 ± 0.63	0.89 ± 0.42	1.05 ± 0.50	1.18 ± 0.47	0.74 ± 0.24	0.74 ± 0.29	0.82 ± 0.26
NGC 262	2.24 ± 1.00	2.86 ± 1.23	2.94 ± 1.26	2.79 ± 1.12	2.77 ± 0.93	3.28 ± 1.37	3.10 ± 1.05
NGC 4698	0.12 ± 0.06	0.05 ± 0.03	0.11 ± 0.06	0.15 ± 0.06	0.10 ± 0.03	0.08 ± 0.04	0.11 ± 0.04
NGC 5173	0.58 ± 0.26	0.45 ± 0.20	0.60 ± 0.26	0.67 ± 0.27	0.32 ± 0.11	0.22 ± 0.09	0.27 ± 0.09
NGC 5389	0.41 ± 0.18	0.07 ± 0.04	0.11 ± 0.07	0.44 ± 0.18	0.32 ± 0.10	0.29 ± 0.12	0.29 ± 0.09
NGC 5982	2.71 ± 1.21	0.09 ± 0.07	0.40 ± 0.23	1.63 ± 0.65	0.68 ± 0.24	0.20 ± 0.08	0.37 ± 0.12
NGC 6962	4.11 ± 1.84	3.69 ± 1.63	4.24 ± 1.88	2.64 ± 1.06	1.83 ± 0.63	2.14 ± 0.85	2.38 ± 0.78
NGC 7371	1.69 ± 0.76	2.33 ± 1.00	2.94 ± 1.26	1.77 ± 0.71	1.03 ± 0.34	1.01 ± 0.39	1.18 ± 0.38
NGC 7787	2.40 ± 1.07	0.66 ± 0.30	1.01 ± 0.45	2.59 ± 1.03	2.64 ± 1.11	2.88 ± 1.69	2.67 ± 1.35
PGC 065981	1.92 ± 0.86	3.57 ± 2.23	4.01 ± 2.63	1.34 ± 0.54	1.94 ± 1.23	3.55 ± 2.01	3.83 ± 1.77

methods: for H α , Helmboldt et al. (2004); for FUV and NUV, the FUV/TIR relationship in Cortese et al. (2008). *Right* Alternative correction methods: for H α only, the constant value of $A(H\alpha) = 1.1$ mag (Kennicutt and Kent 1983); and for H α , FUV and NUV, the TIR correction using the empirical calibration factors These measurements have been derived using the luminosities corrected for dust extinction with the extinction coefficients in Table 2.4. Left Preferred correction from Kennicutt et al. (2009) and Hao et al. (2011)

Galaxy name	Feature	$L_{\rm H\alpha,feat}$	$L_{\rm FUV,feat}$	$L_{\text{NUV,feat}}$
		$L_{ m Hlpha,tot}$	$L_{ m FUV,tot}$	$L_{ m NUV,tot}$
NGC 160	Ring	0.95	0.86	0.78
NGC 262	Arms	0.03	0.71	0.60
NGC 4698	Ring 1	0.20	0.40	0.36
NGC 4698	Ring 2	0.80	0.60	0.64
NGC 5173	Arms	0.54	0.59	0.60
NGC 5389	Ring	0.57	0.56	0.45
NGC 6962	Arms	0.76	0.91	0.87
NGC 7371	Ring	0.99	0.98	0.72
NGC 7787	Ring	0.62	0.76	0.66
PGC 065981	Arms	0.80	0.81	0.77

Table 2.7 Ratios of the luminosities (not corrected for internal dust absorption) of the whole galaxy and of the outer feature

Column I Galaxy name. Column II Outer feature of the galaxy. Column III Ratio of the observed luminosity of the feature and the luminosity of the whole galaxy in $H\alpha$, written $L_{H\alpha,feat}/L_{H\alpha,tot}$. Columns IV and V As column III, but for FUV and NUV, respectively

A direct consequence of the presence of the $H\alpha$ emission in the outer features of this elliptical, S0 and ETS galaxies is that the UV emission arises from the massive star formation, excluding the possibility of the UV-upturn in the outer parts of these galaxies.

2.5.2 Star Formation Rates

Corrections for internal dust absorption

Thesecond important finding of this work is regards the derived SFRs. Modest SFRs are obtained after correcting for internal dust absorption. As mentioned in Sect. 2.4.3, the luminosities need to be corrected for internal dust absorption. The methods proposed in the literature present some advantages and disadvantages for the galaxies studied in this Section. It is important to take into account that these galaxies of earlier types may have less dust than later types, and therefore the same dust corrections should be use with caution. Additionally, these galaxies present different stellar masses and SFRs (star-forming and quiescent galaxies), which obstructs the adoption of one single equation.

The use of TIR luminosity to correct for internal dust absorption is common when dealing with spiral galaxies. I first use it following the equations from Kennicutt et al. (2009) and Hao et al. (2011). Nevertheless, old population stars may produce dust-heated IR light in galaxies with low specific SFR, therefore overestimating TIR and the derived SFRs. Consequently and without information about the specific SFR of our galaxies, the equations in Kennicutt et al. (2009) and Hao et al. (2011) (our Eqs. 2.4–2.6) cannot blindly be applied.

2.5 Discussion 39

In order to overcome the possible problems due to dust-heated IR, I have searched for other methods to compute the corrections coming from internal dust absorption. I have adopted for the UV the recipes by Cortese et al. (2008) based on the relationship between the TIR/FUV ratio and UV attenuation. These can be applied to systems with low specific SFRs and are independent of the age of the stellar populations.

Regarding H α , I prefer to use the recipes in Helmboldt et al. (2004) (Eq. 2.8) which relate M_R with $A(H\alpha)$. In Table 2.4 we see that $\langle A(H\alpha)_{TIR} \rangle = 0.73$ mag, lower than $\langle A(H\alpha)_R \rangle = 1.18$ mag, but still more reliable than adopting the single value of $A(H\alpha) = 1.1$ mag. All the attenuation coefficients are collected in Table 2.6.

Implications on the derived star formation rates

There is a very good agreement between the SFRs derived for $H\alpha$, FUV and NUV (within the uncertainties). Three implications can be derived from these results:

- I confirm that the global SFRs should include both direct and dust-processed light so it is necessary to correct the observed luminosities for internal dust attenuation.
 In Tables 2.5 and 2.6 we see the significant differences between the corrected and non-corrected SFRs, remarkably in the UV.
- 2. There is a very good agreement in the dust-corrected SFRs of the different wavelengths, confirming that the UV and H α emissions come from newly born population of hot stars (recent SF). Thus, the extra UV emission does not come from old stars (UV-upturn related), but to massive star formation. Additionally, the ellipticals of the sample present star formation levels above those typical of their type, but still below $1 M_{\odot} \text{ yr}^{-1}$.
- 3. The SFRs in the elliptical, S0 and ETS galaxies of our sample are comparable to those typical of later type spiral galaxies (e.g., James et al. 2004). In particular, SFR(H α) > 1 M_{\odot} yr⁻¹ for 7 out of 10 galaxies. These results agree with previous findings (e.g., Young et al. 1996; Usui et al. 1998; Hameed and Devereux 1999 or Hameed and Devereux 2005, see Sect. 2.1).

2.5.3 Origin of Star Formation

With this study, I confirm that the outer UV emission in a sample of elliptical, S0 and ETS galaxies is caused by massive SF, found in outer features such as rings and spiral arms. We now ask ourselves the reason why there is UV emission in the outer parts of these galaxies of early types. At first sight, the presence of rings may well be explained as a result of bar action, although the small sample size cannot prove this (there are only five galaxies with rings classified as SB [1], SAB [1] and SA [2]).

The origin of UV light in elliptical and S0 galaxies was studied in Carter et al. (2011). They suggested that the excess UV emission may be based on a recent minor merger event, e.g. in the shell elliptical NGC 5982 (Sikkema et al. 2007). Moderate levels of SF are found in this galaxy, and we agree that the origin of this excess star

formation may arise from a merging event. Additionally, this galaxy is a LINER and the nuclear emission may not be due to SF.

The case of NGC 5173 is exceptional. On the one hand, this galaxy appears perfectly elliptical in the R-band image. But on the other hand, there is a large amount of H α and UV emission (see Fig. 2.2), in the form of incomplete spiral arms. NGC 5173 belongs to a group of galaxies (Mahtessian 1998) with NGC 5169 (distance of 64.8 kpc and $\Delta v = 17$ km s⁻¹). It is very likely that the interaction between these galaxies enhance star formation.

The (FUV-NUV) colour can be used to discriminate against star-forming and quenched galaxies. Elliptical, S0 and ETS galaxies are expected to have (FUV-NUV) > 0.9 (Gil de Paz et al. 2007). In our case, only NGC 4698 and NGC 5982 have FUV-NUV> 0.9 (last column of Table 2.2). Thus, the other galaxies (FUV-NUV < 0.9) confirm the unexpected level of star formation for their morphological type, and these galaxies do not behave like read and dead galaxies, but star forming ones. The newest morphological classification of NGC 4689 (Buta et al. 2015) agrees with the idea that this galaxy behaves as an elliptical rather than a spiral galaxy, classifying the galaxy as S0/a-E2 (whereas the previous classification in the RC3 was Sab).

Due to the fact that our sample is reduced, our limited study does not allow to make firm conclusions regarding the origin of the formation of stars in our sample galaxies apart from the clear statements that some fraction of galaxies presents rings which form stars and that interaction may stimulate the formation of stars.

Taking everything into account, although the sample selection is biased towards star-forming galaxies, I have found SFRs ranging from a few tenths to a few M_{\odot} yr⁻¹, rates comparable to those found in disc galaxies. Thus, I have found some cases of ellipticals, S0s and ETSs confirming that these galaxies are not red and dead, but are actually forming stars at a rate comparable to that of later-type galaxies.

References

```
T.R. Bradley, J.H. Knapen, J.E. Beckman, S.L. Folkes, A&A 459, L13 (2006)
```

A. Bressan, C. Chiosi, F. Fagotto, ApJS 94, 63 (1994)

T.M. Brown, C.W. Bowers, R.A. Kimble, A.V. Sweigart, H.C. Ferguson, ApJ 532, 308 (2000)

D. Burstein, F. Bertola, L.M. Buson, S.M. Faber, T.R. Lauer, ApJ 328, 440 (1988)

R.J. Buta, K. Sheth, E. Athanassoula et al., ApJS 217, 32 (2015)

R.J. Buta, K. Sheth, M. Regan et al., ApJS 190, 147 (2010)

A. Buzzoni, in Astronomical Society of the Pacific Conference Series, vol. 374, eds. by A. Vallenari, R. Tantalo, L. Portinari, A. Moretti. From Stars to Galaxies: Building the Pieces to Build Up the Universe (2007), p. 311

N. Caldwell, R. Kennicutt, A.C. Phillips, R.A. Schommer, ApJ 370, 526 (1991)

N. Caldwell, R. Kennicutt, R. Schommer, AJ 108, 1186 (1994)

D. Calzetti, G. Liu, J. Koda, ApJ 752, 98 (2012)

J.A. Cardelli, G.C. Clayton, J.S. Mathis, ApJ 345, 245 (1989)

D. Carter, S. Pass, J. Kennedy, A.M. Karick, R.J. Smith, MNRAS 414, 3410 (2011)

A.D. Code, G.A. Welch, ApJ 228, 95 (1979)

References 41

- L. Cortese, A. Boselli, V. Buat et al., ApJ 637, 242 (2006)
- L. Cortese, A. Boselli, P. Franzetti et al., MNRAS 386, 1157 (2008)
- D.A. Dale, G. Helou, ApJ 576, 159 (2002)
- G. de Vaucouleurs, A. de Vaucouleurs, H.G. Corwin Jr., et al., Third Reference Catalogue of Bright Galaxies, eds. by G. de Vaucouleurs, A. de Vaucouleurs, H.G. Corwin Jr., R.J. Buta, G. Paturel, P. Fouque (1991)
- G. de Vaucouleurs, A. de Vaucouleurs, J.R. Corwin, in Second reference catalogue of bright galaxies, 1976 (University of Texas Press, Austin, 1976)
- J. Donas, J.M. Deharveng, M. Laget, B. Milliard, D. Huguenin, A&A 180, 12 (1987)
- B. Dorman, R.W. O'Connell, R.T. Rood, ApJ 442, 105 (1995)
- S. Erroz-Ferrer, J.H. Knapen, E.A.N. Mohd Noh Velastín, J.E. Ryon, L.M.Z. Hagen, MNRAS 436, 3135 (2013)
- G. Gavazzi, C. Bonfanti, G. Sanvito, A. Boselli, M. Scodeggio, ApJ 576, 135 (2002)
- A. Gil de Paz, S. Boissier, B.F. Madore et al., ApJS 173, 185 (2007)
- L. Greggio, A. Renzini, ApJ **364**, 35 (1990)
- S. Hameed, N. Devereux, AJ 118, 730 (1999)
- S. Hameed, N. Devereux, AJ **129**, 2597 (2005)
- C.-N. Hao, R.C. Kennicutt, B.D. Johnson et al., ApJ 741, 124 (2011)
- J.F. Helmboldt, R.A.M. Walterbos, G.D. Bothun, K. O'Neil, W.J.G. de Blok, ApJ 613, 914 (2004)
- L.C. Ho, A.V. Filippenko, W.L. Sargent, ApJS 98, 477 (1995)
- L.C. Ho, A.V. Filippenko, W.L.W. Sargent, ApJ 487, 591 (1997)
- E. Horch, P. Demarque, M. Pinsonneault, ApJ 388, L53 (1992)
- P.A. James, N.S. Shane, J.E. Beckman et al., A&A 414, 23 (2004)
- P.A. James, N.S. Shane, J.H. Knapen, J. Etherton, S.M. Percival, A&A 429, 851 (2005)
- S. Kaviraj, K. Schawinski, J.E.G. Devriendt et al., ApJS 173, 619 (2007)
- R.C. Kennicutt, N.J. Evans, ARA&A 50, 531 (2012)
- R.C. Kennicutt Jr, ARA&A 36, 189 (1998)
- R.C. Kennicutt Jr, C.-N. Hao, D. Calzetti et al., ApJ 703, 1672 (2009)
- R.C. Kennicutt Jr, S.M. Kent, AJ 88, 1094 (1983)
- J.H. Knapen, S. Stedman, D.M. Bramich, S.L. Folkes, T.R. Bradley, A&A **426**, 1135 (2004) J. Kormendy, in *Evolution of Galaxies and Stellar Populations*, ed. by B.M. Tinsley, R.B.G. Larson,
- D. Campbell (1977), p. 131
 J. Kormendy, D.B. Fisher, M.E. Cornell, R. Bender, ApJS 182, 216 (2009)
- P. Kroupa, MNRAS 322, 231 (2001)
- E. Laurikainen, H. Salo, R. Buta, J.H. Knapen, S. Comerón, MNRAS 405, 1089 (2010)
- J.C. Lee, A. Gil de Paz, R.C. Kennicutt Jr et al., ApJS 192, 6 (2011)
- R. Lupton, M.R. Blanton, G. Fekete et al., PASP 116, 133 (2004)
- A.P. Mahtessian, Astrophysics 41, 308 (1998)
- D.C. Martin, J. Fanson, D. Schiminovich et al., ApJ 619, L1 (2005)
- P. Morrissey, T. Conrow, T.A. Barlow et al., ApJS **173**, 682 (2007)
- P. Morrissey, D. Schiminovich, T.A. Barlow et al., ApJ 619, L7 (2005)
- M. Moshir et al., in IRAS Faint Source Catalogue, version 2.0 (1990)
- M. Moshir, G. Kopan, T. Conrow et al. in VizieR Online Data Catalog 2275 (2008)
- R.W. O'Connell, ARA&A 37, 603 (1999)
- R.W. Pogge, P.B. Eskridge, in Astronomical Society of the Pacific Conference Series, ed. by P. Carral,
- J. Cepa. Star Formation in Early Type Galaxies, vol. 163 (1999), p. 174
- M.S. Roberts, AJ 74, 859 (1969)
- M.S. Roberts, M.P. Haynes, ARA&A 32, 115 (1994)
- S. Salim, J.J. Fang, R.M. Rich, S.M. Faber, D.A. Thilker, ApJ 755, 105 (2012)
- J.R. Sánchez-Gallego, J.H. Knapen, C.D. Wilson et al., MNRAS 422, 3208 (2012)
- A. Sandage, J. Bedke, *The Carnegie Atlas of Galaxies*, vol. I–II (1994)
- M. Sarzi, J. Falcón-Barroso, R.L. Davies et al., MNRAS 366, 1151 (2006)
- M. Sarzi, J.C. Shields, K. Schawinski et al., MNRAS 402, 2187 (2010)

- K. Schawinski, S. Kaviraj, S. Khochfar et al., ApJS 173, 512 (2007)
- E.F. Schlafly, D.P. Finkbeiner, ApJ **737**, 103 (2011)
- D.J. Schlegel, D.P. Finkbeiner, M. Davis, ApJ 500, 525 (1998)
- F. Schweizer, P. Seitzer, AJ 104, 1039 (1992)
- M. Seibert, in GALEX Proposal (2007), p. 91
- G. Sikkema, D. Carter, R.F. Peletier et al., A&A 467, 1011 (2007)
- A. Toomre, J. Toomre, ApJ 178, 623 (1972)
- G. Trinchieri, S. di Serego Alighieri, AJ 101, 1647 (1991)
- T. Usui, M. Saito, A. Tomita, AJ 116, 2166 (1998)
- S. van den Bergh, AJ **81**, 797 (1976)
- B.A. Vorontsov-Vel'Yaminov, Extragalactic Astronomy (1987)
- S.K. Yi, in *Astronomical Society of the Pacific Conference Series*, vol. 392, ed. by U. Heber, C.S. Jeffery, R. Napiwotzki. Hot Subdwarf Stars and Related Objects (2008), p. 3
- S.K. Yi, S.-J. Yoon, S. Kaviraj et al., ApJ **619**, L111 (2005)
- J.S. Young, L. Allen, J.D.P. Kenney, A. Lesser, B. Rownd, AJ 112, 1903 (1996)

Chapter 3 $H\alpha$ Kinematics of S^4G Spiral Galaxies: The Data

3.1 Introduction

The development of observing instrumentation has yielded kinematical data with better quality (better angular and spectral resolution) requiring less and less observing time. The first radial velocity measurements and the first rotation curves (Pease 1916, 1918) were derived for M104 and M31, using absorption line spectra with 80 and 79 h of exposure time each. Later, improved observing techniques were used by the Burbidges when they carried out an extensive programme, obtaining emission-line spectra and deriving the rotation curves for a large set of spiral galaxies, with 10–20 h of exposure time per pointing [e.g., NGC 5128 (Burbidge and Burbidge 1959); NGC 2146 (Burbidge et al. 1959) or NGC 7479 (Burbidge et al. 1960); see Burbidge and Burbidge (1975) for a complete list].

In parallel, radio observations became important with the development of radio telescopes. The first detailed HI observations of M31 were carried out by van de Hulst et al. (1957), using the 25-m Dwingeloo radio telescope with an angular resolution of 0.6° . These observations showed a slowly falling rotation curve, whereas 2 years later, Volders presented a flat rotation curve for M33, in conflict with his thesis professor's Jan Oort constants. Albert Bosma's thesis (1978, 1981) and the review by van der Kruit and Allen (1978) played a fundamental role to establish the flatness of the rotation curves and its relation to the total mass distribution of disc galaxies. However, these neutral hydrogen observations had poor angular resolution. The highest angular resolution (\sim 6") 21-cm HI surveys of nearby galaxies to date have been carried out by the HI Nearby Galaxy Survey (THINGS; Walter et al. 2008), using the Very Large Array (VLA) of the NRAO.

To improve this resolution problem inherent in radio observations, optical observations using 3D spectroscopy (IFU, FP) have been used when detailed information is needed. H α FP surveys have been created to study the gas kinematics of galaxies.

Some parts of this chapter have been published in Erroz-Ferrer et al. (2015), MNRAS, 451, 1004.

[©] Springer International Publishing Switzerland 2016

S. Erroz-Ferrer, Morphology, Kinematics and Star Formation Across the Hubble Sequence of Galaxies, Springer Theses,

Chemin et al. (2006) presented $H\alpha$ PF data survey of the Virgo cluster galaxies. Daigle et al. (2006a) also presented an $H\alpha$ FP survey complementary to the SINGS (Kennicutt et al. 2003). One of the largest and most important FP surveys in $H\alpha$ is the Gassendi HAlpha survey of SPirals (GHASP; Garrido et al. 2002). The GHASP survey consists of a sample of 203 spiral and irregular galaxies that have been observed with a sampling about 16 Km s⁻¹ in velocity and an average 3" in angular resolution (see Epinat et al. 2008; GHASP VII hereafter, for a complete list of data and resolutions). $H\alpha$ FP spectrographs are being nowadays used for studying the kinematics of several kinds of galaxies, e.g., bulgeless galaxies (Neumayer et al. 2011), starburst galaxies (Blasco-Herrera et al. 2013), or interacting galaxies in compact dwarfs (Torres-Flores et al. 2014).

One of the lastest FP spectrographs is $GH\alpha FaS$, the Galaxy $H\alpha$ Fabry-Perot System, mounted in the Nasmyth focus of the William Herschel Telescope (WHT) in La Palma. Since 2007 (Fathi et al. 2007), it has been observing to study pattern speeds of bars and spiral arms (Fathi et al. 2009), analyse the kinematics of planetary nebulae (Santander-García et al. 2010), gas flow in interacting galaxies (Font et al. 2011b), star formation and the kinematics of interacting galaxies (Zaragoza-Cardiel et al. 2013, 2014) and starburst galaxies (Blasco-Herrera et al. 2013), or studying the resonance radii and interlocking resonance patterns in galaxy discs (Font et al. 2011a, 2014).

This thesis is based on a FP observing programme which has obtained FP data of spiral galaxies as part of the ancillary data of the S^4G survey. The programme has obtained FP data of 29 galaxies using the $GH\alpha FaS$ instrument. In this chapter, I present the observed FP and narrow-band imaging data. Chapter 4 discusses the first results from the observing programme, studying in particular the barred galaxy NGC 864. This study will be expanded to all the galaxies in the sample in Chap. 5. In Chap. 6 I will study the inner part of the rotation curves of the galaxies of the sample, and Leaman et al. (in preparation) will study the relationship between kinematics and dark matter by analysing the outermost parts of the discs of the galaxies of the sample.

This chapter is organized as follows: the sample selection is presented in Sect. 3.2. Section 3.3 describes the observations. The data reduction and results are explained in Sect. 3.4. Sections 3.5 and 3.6 present the derived rotation curves and non-circular motions maps respectively. These results will be discussed in Chaps. 5 and 6.

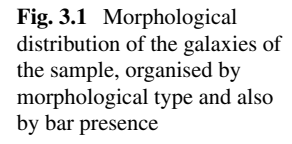
3.2 Target Selection

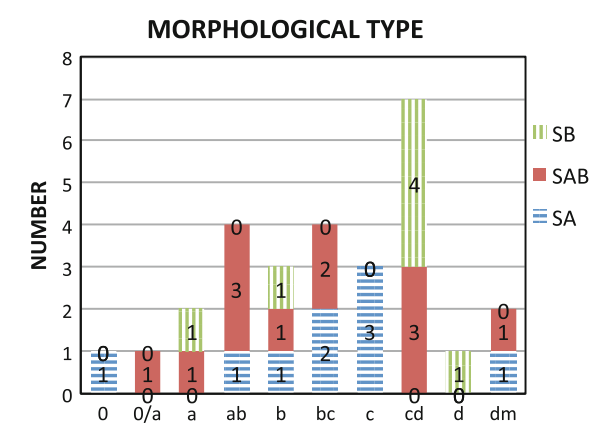
As mentioned before, this FP observational programme is part of the ancillary data of the S⁴G sample, and therefore all the 29 galaxies we observed are included in the S⁴G sample. To select the final sample we required a minimum of altitude in the sky at the time of the observations, leading to galaxies with inclinations

Table 3.1 General properties of the galaxies in the sample

Galaxy name	Mid-IR morphology (1)	d(Mpc) (2)	m _B (3)	M _B (4)	M _{3.6} (5)
NGC 428	SAB(s)dm	15.9 ± 3.2	11.95	-19.06	-19.20
NGC 691	(R)SA(rs,rl)ab	35.7 ± 7.1	12.28	-20.48	-21.36
NGC 864	SAB(rs)bc	20.9 ± 4.2	11.62	-19.98	-20.44
NGC 918	SAB(s)cd	20.5 ± 4.1	13.07	-18.49	-20.24
NGC 1073	SB(rs)cd	16.1 ± 3.2	11.68	-19.35	-19.75
NGC 2500	SAB(s)cd	9.8 ± 2.0	12.22	-17.73	-18.14
NGC 2541	SA(s) <u>d</u> m	10.4 ± 2.1	12.25	-17.84	-17.90
NGC 2543	SAB(s,bl)b	37.4 ± 7.5	12.94	-19.92	-20.96
NGC 2712	(R')SAB(rs,nl)a <u>b</u>	29.5 ± 5.9	12.78	-19.57	-20.67
NGC 2748	(R')SAB(<u>r</u> s)bc	25.1 ± 5.0	12.39	-19.61	-20.84
NGC 2805	(R)SA(s)c pec	28.7 ± 5.7	11.79	-20.50	-20.51
NGC 3041	SA(rs) <u>b</u> c	23.9 ± 4.8	12.30	-19.59	-20.52
NGC 3403	SA(rs)c:	22.8 ± 4.6	12.94	-18.85	-19.63
NGC 3423	SA(s)bc	14.3 ± 2.9	11.60	-19.18	-19.58
NGC 3504	(R ₁ ')SA <u>B</u> (<u>r</u> s,nl)a	27.8 ± 5.6	11.62	-20.60	-21.65
NGC 4151	SAB _a (l,nl)0/a	20.0 ± 4.0	11.36	-20.15	-21.40
NGC 4324	(L)SA(r)0 ⁺	13.6 ± 2.7	12.50	-18.17	-19.51
NGC 4389	SB(rs)a[d]	13.8 ± 2.8	12.55	-18.15	-19.11
NGC 4498	SB(rs)d	14.1 ± 2.8	12.77	-17.98	-18.51
NGC 4639	(R')SAB(rs,bl)ab	13.9 ± 2.8	12.19	-18.53	-19.39
NGC 5112	SB(s)cd	20.2 ± 4.0	12.63	-18.90	-19.49
NGC 5334	SB(rs,x ₁ r)cd	24.2 ± 4.8	12.88	-19.04	-20.03
NGC 5678	(R'L)SA(<u>r</u> s)b: pec	33.3 ± 6.7	12.02	-20.59	-21.87
NGC 5740	(RL)SAB(r)ab	27.0 ± 5.4	12.60	-19.56	-20.65
NGC 5921	SB(<u>r</u> s)b	26.2 ± 5.2	11.68	-20.41	-21.31
NGC 6070	SA(rs,nrl)c	33.6 ± 6.7	12.42	-20.21	-21.70
NGC 6207	SAB(rs)cd	18.5 ± 3.7	11.86	-19.48	-19.84
NGC 6412	SB(rs)cd	23.7 ± 4.7	12.38	-19.49	-20.07
NGC 7241	Scd sp/E(d)7	22.4 ± 4.5	13.23	-18.52	-20.51

Notes (1) Updated morphological classifications from Buta et al. (2010, 2015), where "double stage" galaxies are allowed (i.e., large-scale S0 or S0/a galaxies with smaller-scale inner spirals) (2) Adopted values of the distances, calculated after applying the Virgo, GA and Shapley corrections, with $H_0 = 73 \pm 5 \text{ km s}^{-1} \text{ Mpc}^{-1}$, from the NASA/IPAC Extragalactic Database (NED). The uncertainties in the distance measurements have been adopted as 20% of the value. (3) *B* magnitude from The Third Reference Catalogue of Bright Galaxies (RC3; de Vaucouleurs et al. 1991). (4) Absolute *B* magnitude measured using the distance and m_b of columns III and IV. (5) Absolute 3.6 μ m magnitude measured using the distance of column III and asymptotic magnitude at 3.6 μ m from the ellipse fitting to the 3.6 μ m S⁴G images (Muñoz-Mateos et al. 2015)





above -10° . Also, we required that the galaxies were not too inclined, and therefore we only selected galaxies with inclinations between 0° and 70° .

Additionally, some requirements resulted from the instrument specifications. Firstly, the size of the galaxy was constrained between 2 and 3.4 arcmin due to the GH α FaS FOV of 3.4 \times 3.4 arcmin. Also, we tried that the range in velocities of the galaxies was not higher than the free spectral range (FSR) of the instrument (see Sect. 3.3 for details) despite the fact that this information was not available beforehand for all the galaxies in the sample.

The final sample was randomly selected at the time of the observations, trying to reach a variety of morphologies and bar presence. The availability of some ancillary data was also a plus (interferometric CO, HI, ultraviolet, *Spitzer* mid-IR or *Herschel*).

Finally, the observed sample consists of 29 galaxies. The updated morphological classification has been obtained from the Comprehensive de Vaucouleurs revised Hubble-Sandage System (CVRHS, Buta et al. 2015), and presented in Table 3.1 along with other galaxy properties. Figure 3.1 represents the histogram of morphological classifications. NGC 7241 is an edge-on galaxy which ended up in the final sample because of its photometric inclination below 70°, which is biased much lower due to an optical companion in the line of sight. Thus, this galaxy is not studied in Chap. 5. In Leaman et al. (2015), we present a detailed analysis of the kinematics and structure of this galaxy (summarized in Appendix E.3).

3.3 Observations

We used the $GH\alpha FaS$ instrument mounted on the 4.2-m WHT in La Palma to perform the FP observations, during 24 nights between September 2010 and March 2013. $GH\alpha FaS$ is composed by a focal reducer, a filter wheel, a FP etalon, an image

¹From the table in http://www.iac.es/proyecto/S4G/pages/s4g-catalog.php?pn=5.

3.3 Observations 47

Table 3.2 Log of the observation

Galaxy name	Date	$FP t_{exp}(s)$	FP Hα filter ⁽¹⁾ (Å/Å)	ACAM Hα filter ⁽¹⁾ (Å/Å)	Seeing ⁽²⁾ (")
NGC 428	Sept. 2010	3840	6580/23	6589/24	1.0
NGC 691	Jan. 2012	11040	6623/23	6631/17	1.2
NGC 864	Sept. 2010	13920	6600.5/25	6589/24	0.9
NGC 918	Sept. 2010	2880	6600.5/25	6589/24	0.9
NGC 1073	Sept. 2010	20640	6580/23	6589/24	0.9
NGC 2500	Jan. 2012	10560	6580/23	6577/23	1.0
NGC 2541	Jan. 2012	10560	6580/23	6577/23	1.2
NGC 2543	Jan. 2012	12960	6623/23	6613/24	1.3
NGC 2712	Feb. 2012	10560	6600.5/25	6613/24	1.4
NGC 2748	Jan. 2012	9600	6600.5/25	6589/24	1.4
NGC 2805	Mar. 2013	9120	6597.5/17.6	6613/24	1.1
NGC 3041	Jan. 2012	10080	6600.5/25	6589/24	1.4
NGC 3403	Jan. 2012	10560	6580/23	6589/24	1.1
NGC 3423	Feb. 2012	9120	6580/23	6589/24	1.5
NGC 3504	Jan. 2012	15360	6600.5/25	6589/24	1.4
NGC 4151	Feb. 2012	13920	6580/23	6589/24	1.2
NGC 4324	Mar. 2013	8160	6597.5/17.6	6613/24	1.4
NGC 4389	Jan. 2012	12000	6580/23	6577/23	0.8
NGC 4498	Jun. 2011	10080	6598/18	6589/24	0.9
NGC 4639	Jun. 2011	8640	6583/15.5	6589/24	1.0
NGC 5112	Jun. 2011	9120	6583/15.5	6589/24	0.6
NGC 5334	Jun. 2011	11520	6598/18	6589/24	1.2
NGC 5678	Jan. 2012	10560	6600.5/25	6613/24	1.2
NGC 5740	Jun. 2011	11040	6598/18	6589/24	1.5
NGC 5921	Mar. 2013	7200	6597.5/17.6	6589/24	1.3
NGC 6070	Jun. 2011	9600	6608/16	6613/24	1.5
NGC 6207	Jun. 2011	8640	6583/15.5	6589/24	1.3
NGC 6412	Jun. 2011	13920	6598/18	6589/24	1.3
NGC 7241	Jun. 2011	7680	6598/18	6589/24	1.1

Notes (1) The adopted format for the filters is *central wavelength/FHWM*. (2) The seeing was measured from the ACAM images. To perform the continuum subtraction, the $H\alpha$ image or the R-band image were degraded to the same spatial resolution (the worst seeing of the two images), and this number has been adopted as the final seeing

photon-counting system (IPCS), and a calibration lamp (neon source). The interference order of the etalon was 765, leaving a FSR of $391.9\,\mathrm{km\,s^{-1}}$ (8.6 Å). We chose the high spectral resolution mode, with a velocity sampling of $\sim\!8\,\mathrm{km\,s^{-1}}$ and a pixel scale of 0.2". The exposure time per galaxy varied as a result of weather and instrumentation problems but, in general, each galaxy was observed for around 3 h,

corresponding to 22 cycles. Each observational cycle consists of 48 steps through the etalon, with 10 s of exposure in each step. In Table 3.2, we summarize the instrumental set-up used in the observations.

Hα narrow-band images were simultaneously observed with the goal to flux calibrate the kinematic data. For that, we used the Auxiliary port CAMera (ACAM; Benn et al. 2008) on the Cassegrain focus of the WHT. The instrument provides 0.25'' images with a circular FOV of 8 arcmin. Four different narrow-band filters were used according to different galaxy's redshift (6577/23, 6589/24, 6613/24 and 6631/17; central wavelength/FHWM, in Å). For calibration purposes, we also observed the galaxies in the *R*-band using a Bessel (6500/1360) and Sloan (6228/1322) filters. Each galaxy was observed $3 \times 20 \, \text{s}$ in the *R*-band and $3 \times 100 \, \text{s}$ in Hα. The seeing varied between 0.6'' to 1.6'', with a median seeing of 1.0''.

3.4 Data Reduction

3.4.1 Fabry-Perot: GH\alphaFaS

Hernandez et al. (2008) or Blasco-Herrera et al. (2010) present the customary reduction processes for $GH\alpha FaS$ data cubes. However, we have carried out some new reduction processes that we consider important for this kind of data, and all the data of all the galaxies have been re-reduced following these steps: de-rotation, phase correction, combination and wavelength calibration, astrometry calibration, spatial smoothing, continuum subtraction, removing sky lines, flux calibration and creation of the moment maps.

De-rotation, Phase-correction, combination and wavelength calibration

There is no proper de-rotator at the Nasmyth focus of the WHT. Hence, before reducing the FP data cubes, de-rotation must be performed. Following the procedures explained in Blasco-Herrera et al. (2010), two point sources were selected in each image (preferably stars) to be followed throughout the cube. Figure 3.2 (left) shows the integrated cube in wavelength for NGC 864 as an example, before de-rotation. Figure 3.2 (right) presents the final de-rotated integrated image of the galaxy.

Due to the nature of the FP data, de-rotation needs to be done in accordance with a transformation in the spectral dimension. Therefore, phase calibration is performed simultaneously with the de-rotation process. Wavelength calibration is also carried out at this step, using lamp exposures taken in between the FP observations (see Carignan et al. 2008). Then, we integrate all the observed cycles ending up with one 48-channel cube, already phase-corrected and wavelength-calibrated.

Astrometry calibration

The astrometry calibration was performed by direct comparison with the ACAM images (see Sect. 3.4.2 for the astrometry calibration of the ACAM images).

3.4 Data Reduction 49

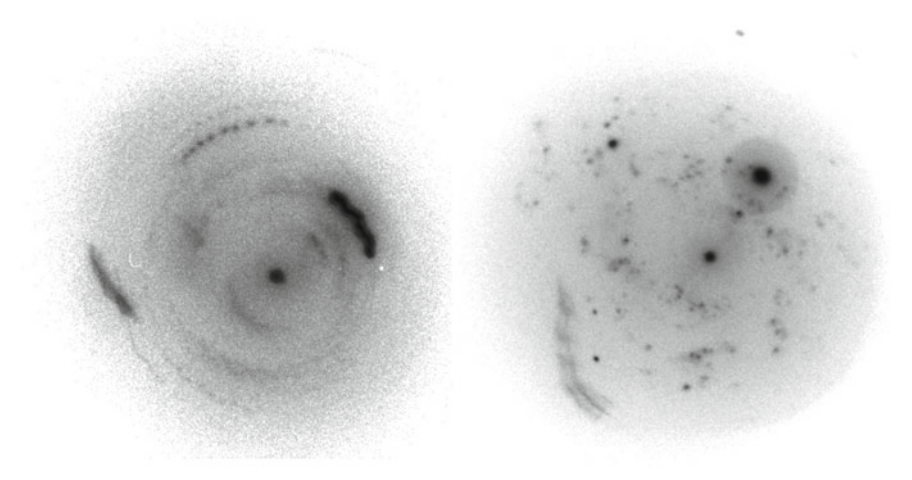


Fig. 3.2 *Left* This image shows the sum of all the planes of the raw cube of NGC 864 without de-rotating. Hence, it is possible to see the rotation that the galaxy presents in the CCD along the night. *Right* The sum image after de-rotation

Spatial smoothing

Although the pixel scale is 0.2"/pix, the spatial resolution is seeing limited. Additionally, if the de-rotation process is not perfectly performed, the spatial resolution might decrease. In order to improve the signal-to-noise ratio (S/N), we performed a 2D Gaussian smoothing with a 3 pixels FWHM, which does not degrade the spatial resolution significantly. For this purpose, the IDL task FILTER_IMAGE.PRO was used.

Continuum subtraction

The next step is to import the resulting cube into the program GIPSY (Groningen Image Processing System; van der Hulst et al. 1992). By using CONREM of GIPSY, it is possible to determine the channels free of line emission and remove the estimated continuum from all the channels in the cube. These channels have been identified with the visualization of the cube and also checking the spectra.

There are some cases where no channels are completely free of line emission. This can be for two reasons. The first one is what we call "peak intrusion": the $H\alpha$ line is broad enough to appear in more than two or three channels, and is located in the first or last channels. The line then appears in both the last and the first channels (two orders of interference appear at the same time in the interferometer, corresponding to a higher/lower wavelength than those allowed by the FSR). Specifically, we have found this effect in bright HII regions of NGC 691, NGC 2543, NGC 2712 and NGC 5740. The second reason is that the galaxy may emit in a wavelength range similar or higher than the FSR, and therefore the peak intrusion is inevitably present. This has been found in NGC 2748, NGC 5678 and NGC 6070.

When peak intrusion is present, we locate channels free of emission. If there are any, we redistribute the channels, moving the channels with "intruded peaks"

before or after the corresponding channel, resulting in a cube with channels free of emission at the beginning and at the end. If there are no channels free of emission (inevitably so when the galaxy velocity range is higher than the FSR), we divide the cube spatially in two parts (roughly corresponding to the areas where emission from the receding and approaching halves is seen). In these cases, the emission range is higher than the FSR, although for these selected two parts of the galaxy, there are channels free of emission (one should remember that the emission of an specific region is located in certain channels). Those channels containing emission from a peak intrusion are copied after or before the first or last channel, where they should really be, increasing the number of channels per cube. After that, the channels free of emission were identified separately for each sub-cube, and the continuum was calculated and subtracted separately in each sub-cube. After the continuum subtraction, the two cutouts have been combined again.

Sky line removal

In nearly half of the galaxies in our sample, there are stationary peaks (2–3 channels width) with a circular gradient peaking in the center of the image. The source of these sky lines (OH sky lines) is the airglow. They have been found peaking near the following velocities/wavelengths: 690 km s⁻¹/6577.3 Å (present in NGC 2500, NGC 2541, NGC 4389 and NGC 6207), 1080 km s⁻¹/6586.5 Å (NGC 428, NGC 1073, NGC 3403, NGC 4151, NGC 4639 and NGC 5112) and 1480 km s⁻¹/6596.7 Å (NGC 4498, NGC 5334 and NGC 6412). These stationary peaks have been treated as if they were gradients in images needed to be corrected for flat-fielding. The task FLAT of GIPSY, which fits a polynomial to the background, has been used in order to flatten the background and make the stationary peaks disappear.

Flux calibration

As mentioned before, the ACAM imaging has been obtained in order to calibrate in flux the FP data. Those data have been observed simultaneously so that the atmospheric conditions and airmass are similar. The procedure consists of selecting the same regions in both the ACAM and H α FP data, and measure the flux in those regions. Then, as the ACAM images are flux calibrated, it is possible to fit a linear relationship to the fluxes and calibrate the zeroth moment maps of the FP data. This procedure was first performed for NGC 864, explained in Chap. 4.

Moment maps

The MOMENTS task of GIPSY has been used to compute the velocity moment maps. They consist of the moment maps of order zero (intensity map), order one (velocity map along the line of sight) and order two (velocity dispersion maps). We required that the emission line should appear in three adjacent channels, but only the main peak should be taken into account. The moment maps have been created from the emission lines that are above a certain noise level σ , computed using the STAT task in GIPSY. Five sets of moment maps have been created from each cube: 1, 2, 3, 4 and 5σ maps. Throughout this thesis, we have derived our results from the 5σ moment maps, but all the data have been published with Erroz-Ferrer et al. (2015).

3.4 Data Reduction 51

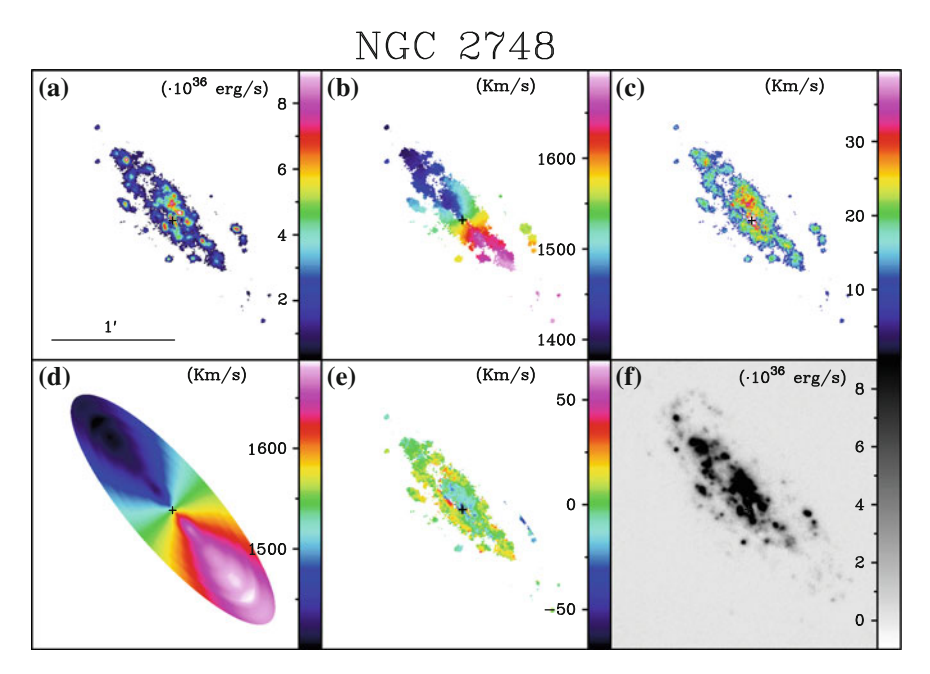


Fig. 3.3 Results from the analysis of the Fabry-Perot data cubes of the spiral galaxy NGC 2748. **a** Hα intensity map. **b** Velocity map. **c** Velocity dispersion map. **d** Velocity model map. **e** Noncircular motions map. **f** Hα narrow-band image from ACAM. In the images, North is up and East to the left. All the images have the same scale. Similar panels for all the sample galaxies are presented in Appendix A

The outputs from MOMENTS are checked afterwards, i.e. some residuals from saturated stars or central regions need to be masked. Concretely, the central emission is saturated in the AGN hosts NGC 4151 and NGC 4639 and in the central parts of NGC 4324, NGC 5740 and NGC 5921, where there was no line emission and some residuals were left.

We have created a six-plots figure for each of the 29 galaxies of our sample. Here, we present those of Fig. 3.3. The corresponding figures for all the galaxies can be found in Appendix A.

3.4.2 Ha Imaging: ACAM

All the images observed with ACAM (R-band and H α narrow-band) have been reduced in a similar way than the images in Chap. 2: first, basic reduction was performed using IRAF (bias and flat corrections, sky subtraction, combination of different exposures). Then, the astrometry in the DSS images has been copied to that of our images using KOORDS in KAPPA. To subtract the continuum to the H α images,

we have aligned the *R*-band and $H\alpha$ and followed the procedures in Knapen et al. (2004) and Sánchez-Gallego et al. (2012). Flux calibration was finally performed using observations from spectrophotometric stars.

The ACAM H α continuum-subtracted image of NGC 2748 can be found in panel (f) of Fig. 3.3. In Appendix A, I present the images for all the galaxies in the sample.

3.5 Rotation Curves

To study the rotation of the ionised gas from the HII regions, we extract the rotation curves from the velocity maps. To do that, we have used the ROTCUR task in GIPSY, which is based on the tilted ring method described in Begeman (1989). This method explains that each ring is defined by these parameters: inclination (i), position angle (PA), centre (x_0 and y_0) and systemic velocity (v_{sys}). Here we assume that the vertical and radial velocities are negligible, and we can express our observed velocity as $v_{obs}(R, \theta, i) = v_{sys} + v_{rot}(R, \theta) \cos\theta \sin i$, where θ is the azimuthal angle in the plane of the galaxy and depends on i, PA, x_0 and y_0 .

This process is not trivial and presents some difficulties. In the first place, there may be deviations from the circular motion (non-circular motions) which are not easy to remove. Secondly, some of the galaxies have low inclinations and thirdly, due to the nature of the $H\alpha$ data, some regions are not well sampled. The procedures have been carefully checked in order to minimize the errors and obtain the true rotation curve.

Some values from the literature have been used as initial conditions of i, PA, x_0 , y_0 and $v_{\rm sys}$: RC3, de Vaucouleurs et al. (1991); HyperLeda, Paturel et al. (2003); GHASP VII; and Muñoz-Mateos et al. (2015). The next step has been to extract position-velocity diagrams (PV diagrams) along the kinematic major axis of the galaxies. These diagrams allow to see the rotation in the spatial direction (presented as supplementary material in the Appendix C). PV diagrams along the minor axis have also been derived to see the possible deviations from the rotational motion (non-circular motions, thoroughly studied in Chap. 5).

With these initial conditions, these steps are followed until a final rotation curve is adopted:

- 1. In the first fit, we leave all the parameters free.
- 2. The first parameter to find is the kinematic centre. Then, the other parameters are fixed (PA, inclination, and systemic velocities) and the centre is left free. Some cases are unsuccessful because of the patchiness of the H α data. The cases where the centre is photometrically evident (i.e., point source), we chose the nucleus as centre. In the cases where the fits are not satisfactory and the centre is not distinguishable, we adopted the centre from the coordinates of the galaxy in NED. In one way or another, the differences between the adopted centre positions and the coordinates in NED are not higher than 0.8" (which is less than the angular resolution and the exactitude of the astrometry in our images).

3.5 Rotation Curves 53

3. The second parameter to find is the systemic velocity. Then, we fix the other coordinates (centre, PA and inclination) and let the systemic velocity as a free parameter.

- 4. Then, we leave free the PA and inclination, fixing the other parameters, and we try to find the inclination and PA.
- 5. Finally, the rotation curve is obtained when the program is executed with all the parameters fixed.

The sector under 30° from the minor axis was not included in the fits and we applied a $|\cos(\theta)|$ weight to the line-of-sight velocities during the fittings. The reason for these is to avoid the points near the minor axis, where projection effects may lead to more errors and where the circular velocity term is fitted with difficulty $[\cos(\theta) \to 0]$. Before deciding the final parameter in the fits, we took the mean of all the values from the rings that satisfied these requirements:

- A sufficient number of points should be in each ring, usually 20–50 (20 would correspond to the minimum number of points that fit in a region with the size of our angular resolution, ~1").
- The values which differ more than $15 \,\mathrm{km}\,\mathrm{s}^{-1}$ for the mean $v_{\rm sys}$ and 15° for the mean PA and i are rejected ($15 \,\mathrm{km}\,\mathrm{s}^{-1}$ is our spectral resolution, which is the double of the velocity sampling).
- The uncertainty linked to the fit (i.e., v_{sys} and the rotational velocity in step 2) should not be higher than 10° for the PA and i, and $10 \, \text{km s}^{-1}$ for the velocities.

Normally, these requirements coincide in the unsatisfactory fits and the corresponding values were not taken into account when computing the average.

A further step is to validate the true rotation curve by analysing the residual map (see the following section) and look for systematic errors. For instance, if the adopted systemic velocity is too low, the residual map will tend to have positive values. Figure 8 of Warner et al. (1973) shows other possible systematic errors and their impact on the residual map.

Two sets of rotation curves have been created for each galaxy: one low-resolution curve (with a separation of 5" between points), and a high-resolution rotation curve, with a separation of 5". While the low-resolution rotation curve shows the averaged behaviour of the rotation of the galaxy, the high-resolution rotation curve traces better the small-scale effect of the features of the galaxy, albeit fewer pixels are included in each ring and consequently, the noise is higher.

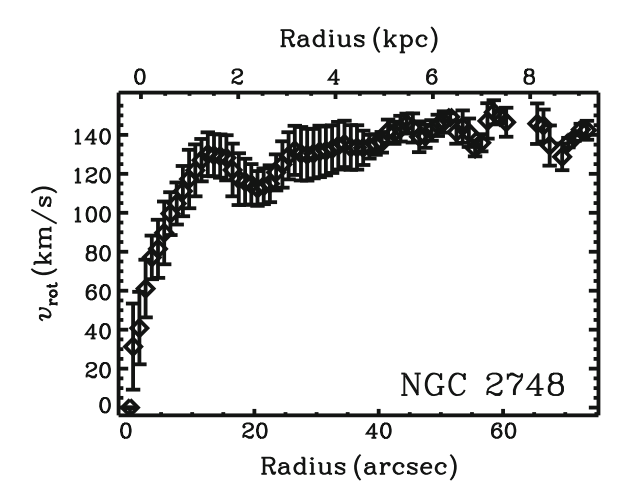
Table 3.3 presents the resulting parameters (i, PA and $v_{\rm sys}$) from the low-resolution fit. Figure 3.4 shows the high-resolution rotation curve of NGC 2748. All the high-resolution rotation curves are collected in the Appendix B.

Table 3.3 Results

Galaxy	$v_{\rm sys, Leda}$	$v_{ m sys,H}\alpha$	i _{3.6μm} (°)	<i>i</i> _{Hα} (°)	PA _{3.6μm} (°)	PA _{Hα} ⁽¹⁾ (°)
name	(km s^{-1})	(km s ⁻¹)			3.0μm	Πα
NGC 428	1162.4	1150 ± 6	40.3	45 ± 9	113.9	120 ± 4
NGC 691	2665.0	2712 ± 5	41.3	41 ± 10	93.7	91 ± 4
NGC 864	1558.9	1550 ± 4	44.6	43 ± 5	22.0	25 ± 6
NGC 918	1502.4	1507 ± 3	54.6	57 ± 4	157.4	160 ± 2
NGC 1073	1209.0	1203 ± 2	27.3	29 ± 1	180.5(2)	165 ± 5
NGC 2500	479.0	540 ± 8	29.9	41 ± 2	62.7	85 ± 5
NGC 2541	530.0	575 ± 3	57.0	57 ± 4	165.0	172 ± 3
NGC 2543	2469.8	2483 ± 6	59.2	61 ± 8	37.0	30 ± 3
NGC 2712	1815.0	1858 ± 2	57.9	58 ± 5	3.6	1 ± 3
NGC 2748	1461.3	1544 ± 6	52.9	74 ± 2	38.9	41 ± 2
NGC 2805	1730.3	1766 ± 4	36.0	36 ± 2	144.2	123 ± 3
NGC 3041	1400.2	1424 ± 4	50.7	50 ± 5	94.0	90 ± 5
NGC 3403	1239.5	1282 ± 5	66.9	66 ± 4	74.9	67 ± 4
NGC 3423	1000.8	1019 ± 4	28.4	28 ± 6	45.4	45 ± 5
NGC 3504	1523.5	1550 ± 6	20.9	39 ± 5	138.3	165 ± 8
NGC 4151	927.7	1000 ± 5	48.1	21 ± 7	150.6	20 ± 3
NGC 4324	1639.1	1689 ± 5	63.3	65 ± 2	55.0	57 ± 2
NGC 4389	712.9	718 ± 9	47.3	45 ± 2	98.9	100 ± 3
NGC 4498	1656.0	1541 ± 8	57.0	58 ± 8	140.3	132 ± 7
NGC 4639	1003.3	1025 ± 2	50.2	39 ± 4	128.4	126 ± 4
NGC 5112	979.1	1017 ± 5	49.2	49 ± 5	120.4	123 ± 5
NGC 5334	1372.0	1411 ± 5	41.5	42 ± 3	11.9	10 ± 6
NGC 5678	1898.5	1932 ± 5	56.4	60 ± 4	4.1	3 ± 3
NGC 5740	1566.1	1600 ± 3	56.8	57 ± 5	162.5	162 ± 2
NGC 5921	1409.4	1472 ± 3	33.2	40 ± 5	146.7	150 ± 6
NGC 6070	2000.1	2030 ± 4	63.8	60 ± 5	60.0	57 ± 3
NGC 6207	848.4	869 ± 3	50.5	57 ± 7	19.4	20 ± 3
NGC 6412	1330.4	1342 ± 2	18.4	20 ± 5	76.9	115 ± 5
NGC 7241	1447.0	1407 ± 8	63.5	65 ± 8	18.5	23 ± 4

Column I Galaxy name. Column II Systemic velocity from optical observations (HyperLEDA). Column III Systemic velocity derived from our FP data. Columns IV and VI Disc inclination and PA obtained from the 25.5 mag/arcsec² isophote from the ellipse fitting to the S⁴G 3.6 μ m image (Muñoz-Mateos et al. in preparation). Columns V and VII The same as columns IV and VI but derived from our FP data. Notes (1) PA of the major axis is defined as the angle, taken in anticlockwise direction between the North direction on the sky and the kinematical major axis of the galaxy, defined from 0° to 180°. (2) For NGC 1073, 180° have been added to PA_{3.6 \(\mu\mathcar{m}\) for a direct comparison with PA_{H\(\alpha\)}}

Fig. 3.4 High-resolution rotation curve derived from the 5- σ velocity map of NGC 2748. The rotation curves for all the galaxies of the sample are presented in the Appendix B



3.6 Non-circular Motion Maps

The circular rotation of galaxies is showed via the rotation curve. Nevertheless, deviations from the circular motion may locally appear. They can be caused by features of galaxies (i.e., presence of a bar), streaming motions in spiral arms or even past interactions with companions. As a matter of fact, I am interested in analysing the nature of these deviations from the circular motion, what we know as non-circular motions.

As mentioned before, the rotation of the galaxy is shown through the rotation curve. If we want to translate this rotation curve into a 2D velocity map, we need to translate the rotation curve and assume kinematic symmetry. Thus, I have used the VELFI task in GIPSY, which creates a velocity model map from the rotation curve and the values of i, PA, x_0 , y_0 and $v_{\rm sys}$. The non-circular motions would be the deviations from the circular rotation, and therefore it is straightforward to create a map of deviations/residuals by subtracting the observed velocity map to the velocity model. The residual map can be understood and interpreted as a non-circular motions map. Thus, throughout the thesis, I will use both terms (residual map and non-circular map) as synonyms. In each of the galaxy plots, I have included the velocity model and non-circular map in panels (d) and (e) respectively. Those corresponding to NGC 2748 are presented in Fig. 3.3. In A, the corresponding plots are presented for all the galaxies of the sample.

3.7 Data Release

With the publication of Erroz-Ferrer et al. (2015), all the data mentioned in this chapter will be released publicly. Specifically, those data will be: raw data cubes (derotated, phase corrected and wavelength calibrated cubes), continuum-subtracted

cubes, 0th, 1st and 2nd order moment maps and continuum-subtracted $H\alpha$ images. These data will be ready to download in FITS format from the NED and the Centre de Données Stellaires (CDS).

3.8 Discussion: Data Quality

3.8.1 Effects from the Nature of the H\alpha Data

The detailed analysis of the inner parts of the rotation curve is one of the scientific goals of this thesis. Thus, I want to exploit the high spatial resolution data that the $GH\alpha FaS$ instrument deliver. As a consequence, the reduction processes have been chosen not to degrade this high angular resolution and do not include large smoothing kernels and no adaptive binning methods have been applied. Thanks to the publication of the data, the user can download the raw data and reduce them following his/her specific interests.

Due to the nature of the $H\alpha$ emission, these data are patchy: this emission comes from the HII regions, which may be separated and present blank spaces among them. Our reduction processes have hardly smoothed the data spatially, and therefore the patchy appearance is present in most of out data. Our data set contains both galaxies with high signal (such as NGC 2748 and NGC 5678) and galaxies with lower signal and as a consequence, present patchy appearance (e.g., NGC 691 or NGC 918). There are, therefore, regions which are not fully sampled and from which it is not possible to derive any kinematical information. One example of unsampled radial regions are the centres of NGC 428, NGC 4151, NGC 4324, NGC 4639, NGC 5334, NGC 5740 and NGC 5921, which can not be studied with these data.

3.8.2 Kinematical Parameters Versus Photometric Parameters

Related to the previous subsection, determining the kinematical parameters can also be understood as a caveat in our study. In Sect. 3.5, I explained the procedures to obtain a rotation curve using ROTCUR in GIPSY. However, due to the patchiness of the FP data, the fits are not always satisfactory in all the rings and more data would be needed to determine the kinematical parameters (such as i, PA or $v_{\rm sys}$) more reliably. These other data would ideally present fully spatial coverage and be fully sampled, resulting in more accurate and reliable parameters. In this case, HI data in the literature of some of the galaxies in our sample have been used whenever possible as initial conditions in the fits. Additionally, the photometric information derived from the mid-IR data from the S⁴G survey published in Muñoz-Mateos et al. (2015) is also valid and have been used in this study. There are, however, discrepancies between the output from our H α FP kinematic data and that from the photometry (see Table 3.3 and Fig. 3.5).

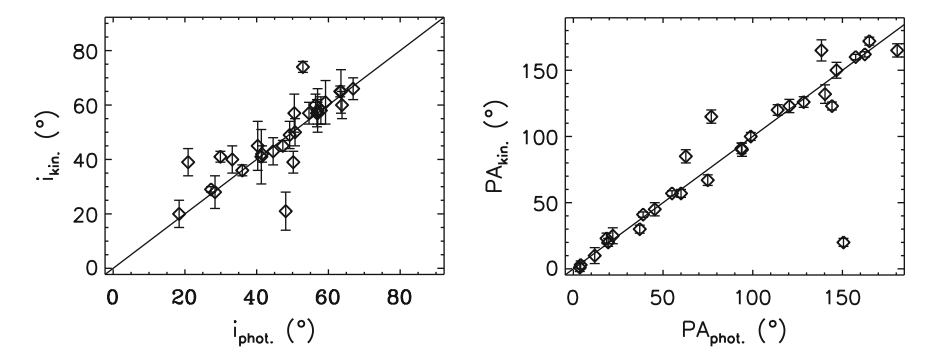


Fig. 3.5 Comparison between the parameters inclination and position angle derived from the S^4G 3.6 μm images (i.e., photometric) and derived with the tilted-ring method to our H α FP data (i.e., kinematical). *Left* Comparison of the inclinations derived photometrically and kinematically. *Right* Comparison between the position angles derived photometrically and kinematically. *Note* Due to our definition of the position angles ($0^{\circ} \leq PA < 180^{\circ}$), the difference between PA= 0° and PA= 179° is not 179° , but 1°

As far as the PA is concerned, the position of the minor axis and the PV diagrams are good tracers of the kinematical PA, and therefore the gas motion is better characterized with the kinematical results rather than with the photometric ones. NGC 4151 presents high discrepancy between the photometric (PA_{3.6}=150.6°) and kinematical (PA_{H α}=20°±3°) position angles. Note that the real difference is 49.4° (PA_{H α}=180°+20°=200°). After checking the continuum-subtracted cube and the velocity map (panel b of Fig. A.8 bottom), I conclude that the real PA is closer to 0°, thus not closer to the photometric result. The first HI synthesis maps of NGC 4151 and deep photograph by Arp showing the outer spiral arms were discussed in Bosma et al. (1977), finding that PA_{kin}=19°±4°, in agreement with our PA_{H α}=20°±3°. The photometric PA_{3.6} only takes into account the oval distribution of the galaxy.

Similarly, there are other cases where our PA_{kin} does not coincide with the mid-IR PA_{phot} , but are in agreement with other values of PA_{kin} found in the literature. These cases, collected and presented in Table 3.4, correspond to barred galaxies (including NGC 2805, which was classified as SA in CVRHS but claimed to have a bar in Salo

Table 3.4 TAIR	ili diliciciit soui	ccs, measured in de	gices and defined if	om Norm to East
Galaxy	PA _{phot}	PA _{kin,this} study	PA _{kin,lit}	References
NGC 1073	180.5	165 ± 4	164.6	England et al. (1990)
NGC 2500	62.7	85 ± 5	85	GHASP VII
NGC 2805	144.2	123 ± 3	114	GHASP VII
NGC 3504	138.3	165 ± 8	163	GHASP VII
NGC 5921	146.7	150 ± 6	147	Fathi et al. (2009)
NGC 6412	76.9	115 + 5	115	GHASP VII

Table 3.4 PA from different sources, measured in degrees and defined from North to East

Column I PA_{phot} from the ellipse fitting to the 3.6 μ m S⁴G images. Column II PA_{kin} from our H α FP data. Column III PA_{kin} values found in the literature. Column IV References

et al. 2015). Consequently, the difference between PA_{kin} and PA_{phot} may indicate that the bar that, depending on its orientation, has an influence on the bar kinematics and provoke non-circular motions (see Chap. 5).

Regarding the inclination, the largest differences are found in NGC 2748, NGC 3504 and NGC 4151 (explained before). In these cases, $i_{\rm phot}$ are systematically lower than $i_{\rm kin}$. This may well be explained from the non-uniformity in the HII regions distribution compared to that of the dust and stars as seen in the S⁴G 3.6 μ m images. Moreover, NGC 2748 and NGC 3504 have outer rings (R' and R'₁, respectively) which are not seen in H α .

3.8.3 Comparison with Literature Data

In Sect. 3.1, some $H\alpha$ FP kinematic follow-ups from different surveys were presented: GHASP (Garrido et al. 2002), SINGS (Daigle et al. 2006a) and VIRGO (Chemin et al. 2006). Analogous FP instruments to GH α FaS were used: Cigale and FaNTOmM (Fabry-Perot de Nouvelle Technologie de l'Observatoire du mont Mégantic²), mounted at three different locations: the 3.6-m Canada–France–Hawaii Telescope at the European Southern Observatory (VIRGO and SINGS), 1.93-m Observatoire de Haute-Provence telescope (VIRGO, SINGS and GHASP), and 1.60-m Observatoire du mont Mégantic telescope (VIRGO and SINGS). These instruments deliver seeing-limited data. However, the observing conditions were most of the time worse than ours (i.e., seeing up to 12"). Table 3.5 compares measurements of the quality of our survey with those of GHASP and VIRGO.

Regarding to the reduction techniques used in VIRGO and GHASP surveys, they are collected in Daigle et al. (2006b) and presented in the webpage University of Montréal Improved 3D Fabry-Perot Data Reduction Techniques. Spectral and spatial smoothing are the critical steps that differ from our reduction techniques. VIRGO and GHASP use a three-channel or Hanning-filtering spectral smoothing, whereas I do not smooth GH α FaS data spectrally. Moreover, the Voronoi adaptive binning method (Cappellari and Copin 2003) was applied to smooth spatially. This method highlights the emission of low-emission regions, with the drawback of degrading the spatial resolution in these low-emitting regions. The spatial resolution is not degraded in the regions with enough signal-to-noise ratio (chosen by the user). Contrarily, a 3×3 pixels median spatial smoothing was applied to the GH α FaS data in order to keep as high spatial resolution as possible. Our reduction techniques have been chosen according to our scientific goals.

Figure 3.6 compares the resulting moment maps of the overlapping galaxies between GH α FaS, GHASP and VIRGO surveys; reduced following the same procedures (here, the techniques explained in this thesis have been selected). In Figs. 3.7 and 3.8, this comparison has been made more carefully to a reduced sample

²http://www.astro.umontreal.ca/fantomm.

³http://www.astro.umontreal.ca/~odaigle/reduction/.

Parent survey	VIRGO	SINGS	GHASP	S ⁴ G (this thesis)
Sample size	30	28	203	29
Seeing < 1.5"	11	_	_	29
$2''$ < Seeing $\lesssim 4''$	19	_	143	_
$4''$ < Seeing $\lesssim 6''$	_	_	45	_
Seeing > 6.0"	_	_	15	_
Angular sampling	0.42"-1.61"	0.42"-1.61"	0.68"-0.96"	0.2"
Spatial smoothing	Voronoi S/N=5	Voronoi S/N=5	Voronoi S/N=5	Median 3×3 pix
	Gaussian $3'' \times 3''$			
Spectral sampling* (km s ⁻¹)	7–14	7–14	~10	~8

Table 3.5 Quality characteristics of the data published in Garrido et al. (2002) (GHASP), Daigle et al. (2006a) (SINGS sample) and Chemin et al. (2006) (VIRGO sample), compared to those of the data from $GH\alpha FaS$

Note The '–' denotes that there are no galaxies with that criteria (VIRGO, GHASP and $GH\alpha FaS$), or that the paper lacks of information about the observing conditions (SINGS). *Before the reduction (i.e., before smoothing)

galaxies, but can be easily extended to the rest sample galaxies. Figure 3.7 shows the comparison of the velocity maps of NGC 864, NGC 2500 and NGC 2543 (overlap between our survey with GHASP), and Fig. 3.8 shows the corresponding comparison for NGC 4498 and NGC 4639 (VIRGO). I show the results obtained by reducing GH α FaS data as explained in Sect. 3.4.1, and also using the reduction techniques used for GHASP data (three-channel spectral smoothing and Voronoi adaptive binning). With these figures, it is possible to directly compare the advantages and disadvantages of each reduction procedure. On the one hand, we see that one drawback of following the reduction steps of Sect. 3.4.1 is that the spatial coverage is limited to the location of the HII regions, resulting in patchy maps. But on the other hand, Voronoi smoothing reduces the angular resolution to that typical of HI data (6"-10"). With the results from the adaptive binning, it is very difficult to perform studies inside the structures of the galaxies (such as bars or spiral arms), as they cannot be resolved any more. This includes the study of the streaming motions (Chap. 5), and of the inner parts of the rotation curves (Chap. 6).

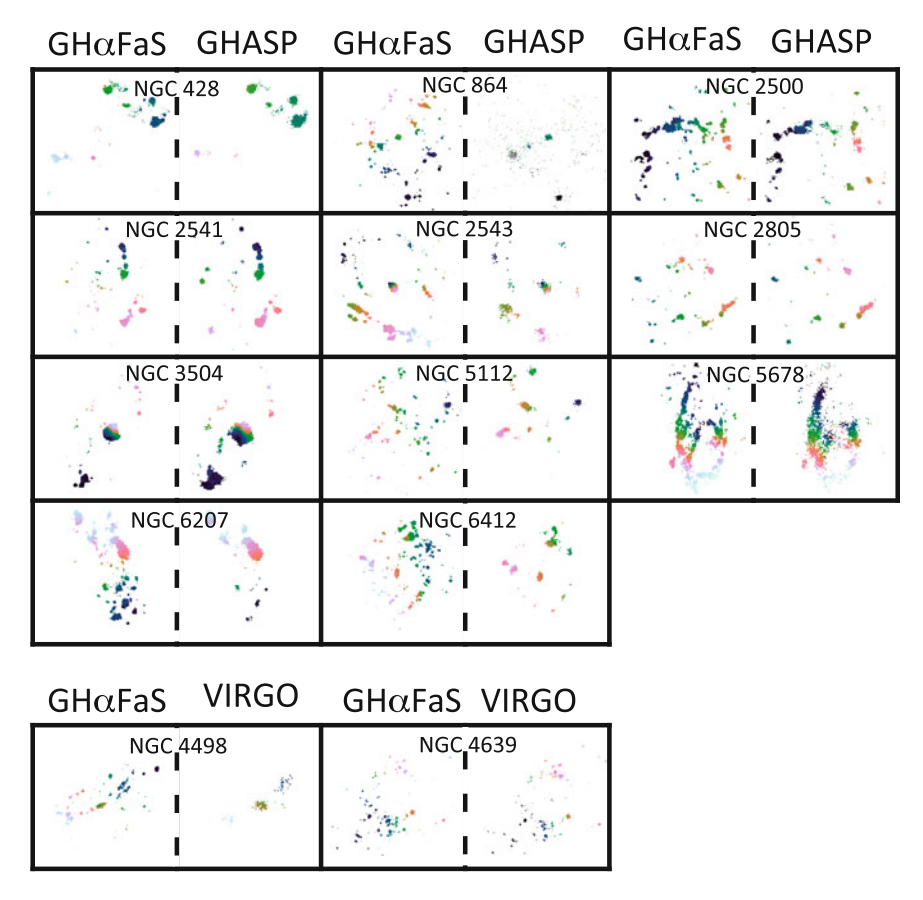


Fig. 3.6 Direct comparison of the moment maps from our FP data with those of GHASP (*top*) and VIRGO (*bottom*). These correspond to the overlapping galaxies in the samples. Both data samples have been reduced using the techniques explained in this thesis, and in this figure I compare the resulting velocity maps

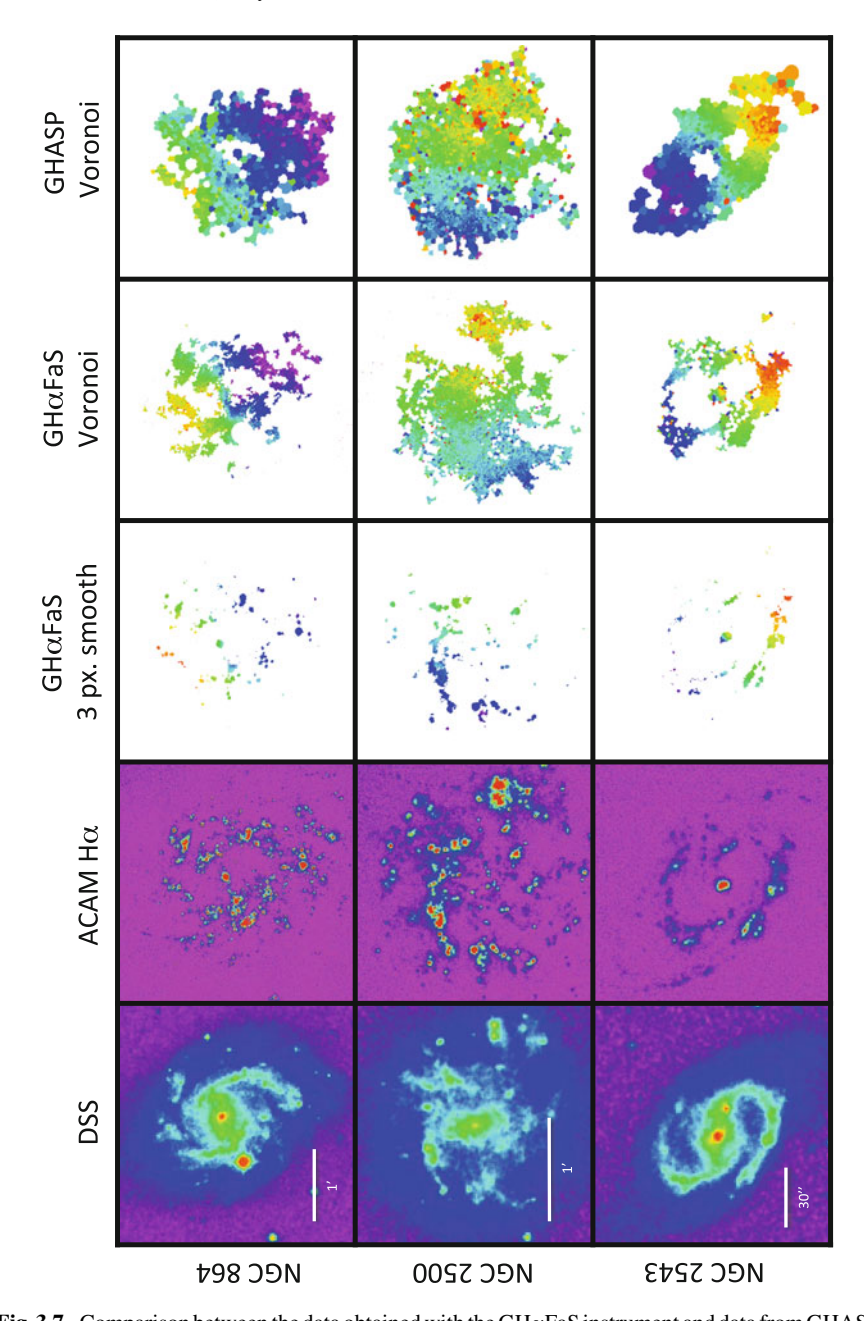
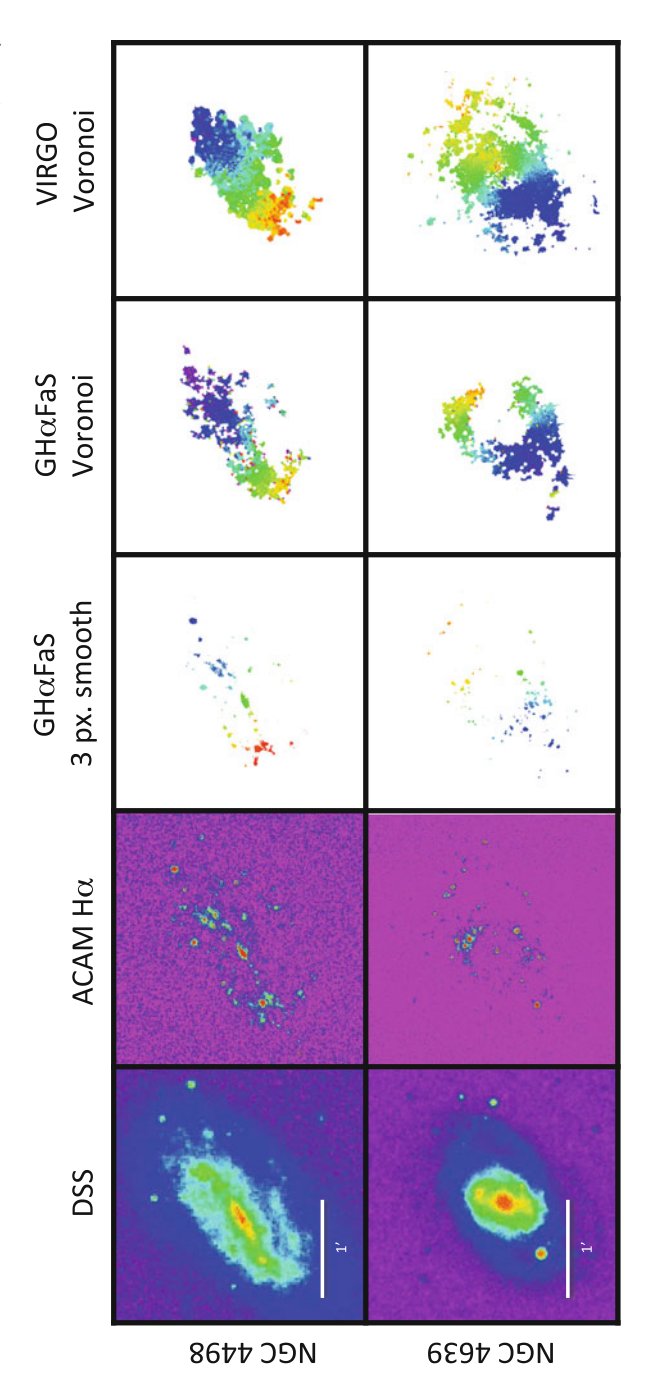


Fig. 3.7 Comparison between the data obtained with the GH α FaS instrument and data from GHASP for NGC 864 (top), NGC 2500 (middle) and NGC 2543 (bottom). Column I DSS image. Column II ACAM H α image. Column III Velocity field from GH α FaS observations, obtained following the reduction procedures described in Sect. 3.4.1. Column IV Velocity field from GH α FaS observations following the reduction processes of GHASP data (three-channel spectral smoothing and Voronoi adaptive binning). Column V Data from GHASP (Epinat et al. 2008)

Fig. 3.8 As Fig. 3.7, now for NGC 4498 (*top*) and NGC 4639 (*bottom*) from the VIRGO sample (Chemin et al. 2006)



References 63

References

- K.G. Begeman, A&A 223, 47 (1989)
- C. Benn, K. Dee, T. Agócs, in *Presented at the Society of Photo-Optical Instrumentation Engineers (SPIE) Conference*, vol. 7014, Society of Photo-Optical Instrumentation Engineers (SPIE) Conference Series (2008)
- J. Blasco-Herrera, K. Fathi, J. Beckman et al., MNRAS 407, 2519 (2010)
- J. Blasco-Herrera, K. Fathi, G. Östlin, J. Font, J.E. Beckman, MNRAS 435, 1958 (2013)
- A. Bosma, Ph.D. Thesis, Groningen University (1978)
- A. Bosma, AJ 86, 1791 (1981)
- A. Bosma, R.D. Ekers, J. Lequeux, A&A 57, 97 (1977)
- E.M. Burbidge, G.R. Burbidge, ApJ **129**, 271 (1959)
- E.M. Burbidge, G.R. Burbidge, in *The Masses of Galaxies*, ed. by A. Sandage, M. Sandage, J. Kristian (The University of Chicago Press, Chicago, 1975), p. 81
- E.M. Burbidge, G.R. Burbidge, K.H. Prendergast, ApJ 130, 739 (1959)
- E.M. Burbidge, G.R. Burbidge, K.H. Prendergast, AJ 65, 342 (1960)
- R.J. Buta, K. Sheth, E. Athanassoula et al., ApJs 217, 32 (2015)
- R.J. Buta, K. Sheth, M. Regan et al., ApJs 190, 147 (2010)
- M. Cappellari, Y. Copin, MNRAS **342**, 345 (2003)
- C. Carignan, O. Hernandez, J.E. Beckman, K. Fathi, in Astronomical Society of the Pacific Conference Series, vol. 390, Pathways Through an Eclectic Universe, ed. by J.H. Knapen, T.J. Mahoney, A. Vazdekis, p. 168 (2008)
- L. Chemin, C. Balkowski, V. Cayatte et al., MNRAS **366**, 812 (2006)
- O. Daigle, C. Carignan, P. Amram et al., MNRAS 367, 469 (2006a)
- O. Daigle, C. Carignan, O. Hernandez, L. Chemin, P. Amram, MNRAS 368, 1016 (2006b)
- G. de Vaucouleurs, A. de Vaucouleurs, H.G. Corwin Jr et al., in *Third Reference Catalogue of Bright Galaxies*, ed. by G. de Vaucouleurs, A. de Vaucouleurs, H.G. Corwin Jr, R.J. Buta, G. Paturel, P. Fouque (1991)
- M.N. England, S.T. Gottesman, J.H. Hunter Jr, ApJ 348, 456 (1990)
- B. Epinat, P. Amram, M. Marcelin, MNRAS 390, 466 (2008)
- S. Erroz-Ferrer, J.H. Knapen, R. Leaman et al., MNRAS 451, 1004 (2015)
- K. Fathi, J.E. Beckman, C. Carignan, O. Hernandez, in *JENAM-2007*, "Our Non-Stable Universe" (2007)
- K. Fathi, J.E. Beckman, N. Piñol-Ferrer et al., ApJ **704**, 1657 (2009)
- J. Font, J.E. Beckman, B. Epinat et al., ApJ 741, L14 (2011a)
- J. Font, J.E. Beckman, M. Querejeta et al., ApJs 210, 2 (2014)
- J. Font, J.E. Beckman, M. Rosado et al., ApJ 740, L1 (2011b)
- O. Garrido, M. Marcelin, P. Amram, J. Boulesteix, A&A 387, 821 (2002)
- O. Hernandez, K. Fathi, C. Carignan et al., PASP 120, 665 (2008)
- R.C. Kennicutt Jr, L. Armus, G. Bendo et al., PASP 115, 928 (2003)
- J.H. Knapen, S. Stedman, D.M. Bramich, S.L. Folkes, T.R. Bradley, A&A 426, 1135 (2004)
- R. Leaman, S. Erroz-Ferrer, M. Cisternas, J.H. Knapen, MNRAS 450, 2473 (2015)
- J.C. Muñoz-Mateos, K. Sheth, M. Regan et al., ApJs 219, 3 (2015)
- N. Neumayer, C.J. Walcher, D. Andersen et al., MNRAS 413, 1875 (2011)
- G. Paturel, C. Petit, P. Prugniel et al., A&A **412**, 45 (2003)
- F.G. Pease, Proc. Natl. Acad. Sci. 2, 517 (1916)
- F.G. Pease, Proc. Natl. Acad. Sci. 4, 21 (1918)
- H. Salo, E. Laurikainen, J. Laine et al., ApJs 219, 4 (2015)
- J.R. Sánchez-Gallego, J.H. Knapen, C.D. Wilson et al., MNRAS 422, 3208 (2012)
- M. Santander-García, P. Rodríguez-Gil, O. Hernandez et al., A&A 519, A54 (2010)
- S. Torres-Flores, P. Amram, C. Mendes de Oliveira et al., MNRAS 442, 2188 (2014)
- H.C. van de Hulst, E. Raimond, H. van Woerden, Bull. Astron. Inst. Netherlands 14, 1 (1957)

J.M. van der Hulst, J.P. Terlouw, K.G. Begeman, W. Zwitser, P.R. Roelfsema, in Astronomical Society of the Pacific Conference Series, vol. 25, Astronomical Data Analysis Software and Systems I, ed. by D.M. Worrall, C. Biemesderfer, J. Barnes, p. 131 (1992)

P.C. van der Kruit, R.J. Allen, ARA&A 16, 103 (1978)

L.M.J.S. Volders, Bull. Astron. Inst. Netherlands 14, 323 (1959)

F. Walter, E. Brinks, W.J.G. de Blok et al., AJ 136, 2563 (2008)

P.J. Warner, M.C.H. Wright, J.E. Baldwin, MNRAS 163, 163 (1973)

J. Zaragoza-Cardiel, J. Font-Serra, J.E. Beckman et al., MNRAS 432, 998 (2013)

J. Zaragoza-Cardiel, J. Font, J.E. Beckman, et al., MNRAS 445, 1412 (2014)

Chapter 4 Streaming Motions in the Spiral Galaxy NGC 864

4.1 Introduction

The dynamics and morphology of current galaxies is a result from an evolutionary process driven externally and by secular evolution (see Sect. 1.1). Although studying these processes is difficult for distant galaxies, nearby galaxies are the ending product of the evolution of the Universe and can be understood as the final record of it.

In order to understand the influence of the evolutionary processes, the combination of morphology and kinematic studies is fundamental. Traditionally, the 21-cm atomic hydrogen line has been observed to create 2D velocity maps of spiral galaxies, taking the advantage of the full spatial coverage of this line, usually tracing three or four times the visible disc. Rots (1975), van der Hulst (1979), Bosma (1981), Gottesman (1982) and others established the importance of these studies by deriving the distribution of mass in disc galaxies. Because of the low angular resolution inherent to HI observations, little small scale studies could be done.

On the contrary, $H\alpha$ observations have been carried out to provide detailed information at sufficient angular resolution. This line is usually the brightest line of a galaxy's spectrum due to the high abundance of this element in the Universe. The $H\alpha$ emission is produced when the HII regions are energetically excited by hot and young stars, and the hydrogen is ionized. Thus, this line traces the formation of massive young stars.

In the previous chapter, I have introduced the FP survey to study the kinematics of 29 spiral galaxies included in the S⁴G sample. In this chapter, I provide a thorough explanation of the observations and analysis of one of the first observed galaxies of the programme, NGC 864.

4.2 Target Selection

The criteria explained in Sect. 3.2 yielded a sample of 29 S⁴G observed galaxies. The galaxies observed in the first observing run were NGC 428, NGC 864, NGC 918, NGC 1073 and NGC 7479. This chapter will focus on the spiral galaxy NGC 864.

The general characteristics of NGC 864 have been collected in Table 4.1. According to the galaxy environment, it belongs to the Catalog of Isolated Galaxies [(CIG); Karachentseva 1973]. Although it is well isolated from nearby companions of similar size, it was included in a radial-velocity group (Fouque et al. 1992), composed by NGC 864 (v=1562 km/s), UGC 1670 (v=1601 km/s; $\Delta M=3.12$ mag; \sim 84 arcmin or \sim 5.7 Mpc away from NGC 864) and UGC 1803 (v=1624 km/s; $\Delta M=3.0$ mag; \sim 89 arcmin or \sim 6.1 Mpc away from NGC 864); all these values taken from the NED. Regarding the morphological properties, it is classified as SAB(rs)bc in the CRVHS (Buta et al. 2015). The bar has been classified as strong in Buta et al.

Name	NGC 864	Comments	
$\alpha_{J2000.0}$	$2^h 15^m 27.6^s$	(1)	
$\delta_{J2000.0}$	+06°00′09.1″	(1)	
$v_{\rm sys}~({\rm kms^{-1}})$	1561.6	(2)	
D (Mpc)	20.9 ± 1.5	(3)	
Туре	SAB(rs)bc	(4)	
m _B (mag)	11.62 ± 0.21	(5)	
Q_b	0.321	(6)	
Q_s	0.134	(6)	
i_{RC3}	43°	(7)	
<i>i</i> _{3.6μm}	44.6°	(8)	
$i_{H\alpha}$	$28.2^{\circ} \pm 20.4^{\circ}$	(9)	
PA _{RC3}	20°	(7)	
PA _{3.6μm}	22.0°	(8)	
PA _{Hα}	25.3° ± 6.7°	(9)	
$L(H\alpha)$ (erg s ⁻¹)	$(4.0 \pm 1.6) \times 10^{41}$	(10)	
$\overline{SFR} (M_{\odot} \text{ yr}^{-1})$	2.19 ± 0.88	(10)	

Table 4.1 General characteristics of NGC 864

(1) The centre position has been chosen to be the optical centre presented in Leon and Verdes-Montenegro (2003). (2) The systemic velocity is listed as the central velocity of the HI spectrum measured at the 20 % level, from Espada et al. (2005). (3) Distance calculated after applying the Virgo, GA and Shapley corrections, with $H_0 = 73 \pm 5\,\mathrm{km~s^{-1}~Mpc^{-1}}$, from NASA/IPAC Extragalactic Database (NED). (4) Morphological type from the CRVHS (Buta et al. 2015). (5) *B* magnitude from *The Third Reference Catalogue of Bright Galaxies* (RC3; de Vaucouleurs et al. 1991). (6) Bar and Spiral Arm torques, from Buta et al. (2005). (7) Disc inclination and position angle (PA) of the kinematic major axis, from the RC3. (8) Disc inclination and PA obtained from the 25.5 mag/arcsec² isophote with the S⁴G 3.6 μ m image, from Muñoz-Mateos et al. (2015). (9) Disc inclination and PA from our $H\alpha$ FP data (Sect. 4.4.2). (10) Luminosity and SFR of the whole galaxy measured from our $H\alpha$ images (Sect. 4.4.3)

(2005), with a bar strength of $Q_b = 0.321$, despite its apparent weakness in the blue light.

NGC 864 has been previously analysed in the literature (Martini et al. 2003; Epinat et al. 2008; Buta and Zhang 2009; Comerón et al. 2010). The most thorough kinematic study of the galaxy was presented in Espada et al. (2005), measuring large-scale features from HI observations. These outer features are beyond the coverage of our optical data, providing information about the environment or possible previous companion.

4.3 Observations and Data Reduction

In this chapter, I use data from three different instruments on the WTH: the $GH\alpha FaS$ instrument, the ACAM camera and the Spectrographic Areal Unit for Research on Optical Nebulae (SAURON) integral field spectrograph. Additionally, mid-IR data from the S^4G survey have been used.

4.3.1 ACAM

As explained in the previous chapter, $H\alpha$ imaging of the galaxy has been obtained in order to calibrate the FP data. Thus, the galaxy was observed with an $H\alpha$ filter (6589/15; CW/FWHM in Å) for 300s on 2010 September 4, together with 30s R-band observations (6228/1322) to perform the continuum subtraction (R-band image scaled by 0.0109). The basic reduction of the ACAM images was explained in Sect. 3.4.2. The resulting R-band and $H\alpha$ images are shown in Fig. 4.1.

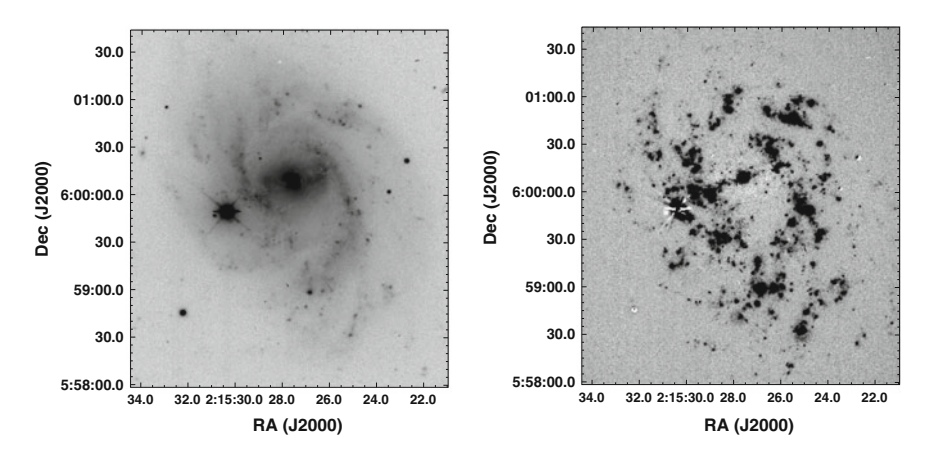


Fig. 4.1 R-band (left) and continuum-subtracted H α (right) images of NGC 864, taken with ACAM

4.3.2 GH\alphaFaS

4.3.2.1 Observations and Data Reduction

NGC 864 was observed with the FP instrument during 4 h, corresponding to 29 cycles composed of 48 channels each.

The data reduction steps for GH α FaS data are fully explained in Sect. 3.4.1. Here, we will present the particularities in the reduction of NGC 864. Specifically for this galaxy, the saturated star near the centre (at approximately RA $2^h15^m30^s$ and DEC $+05^\circ59'49''$) was masked out using the GIPSY task BLOT.

Although the worst seeing measurement in that night was 1.2'', the final FWHM after the de-rotation process corresponds to $1.56'' \times 1.4''$. With the GIPSY task SMOOTH, the FP data have been degraded to two different spatial resolutions: high-resolution (slightly smoothing kernel, final FWHM of $1.65'' \times 1.56''$) and low-resolution (final FWHM of $3'' \times 3''$ with the goal of highlight regions with low-emission). The velocity maps obtained using the two spatial resolution modes are presented in Fig. 4.2.

This chapter presents the first case of flux-calibration in our survey. In Fig. 4.3, the fluxes from HII regions in both the GH α FaS cube and the ACAM image are compared and fitted to a linear relationship.

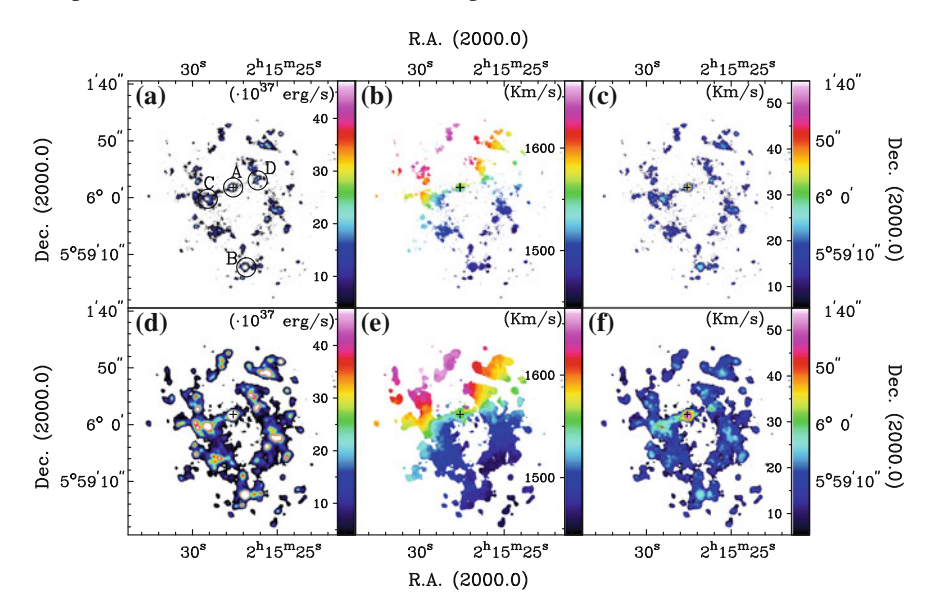
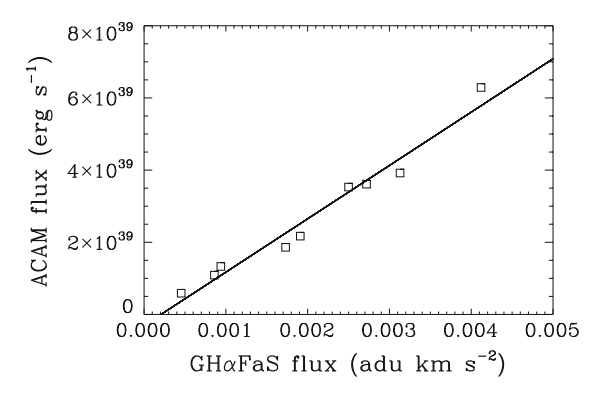


Fig. 4.2 a Intensity map for the high-resolution data. The *centre* is marked with *A*. *B* is the brightest HII region, located at the end of the western arm. *C* and *D* refer to other regions of massive star formation, found at the ends of the bar, and near the beginning of the arms. **b** Velocity map for the high-resolution data. **c** Dispersion velocity map for the high-resolution data. **d** Intensity map for the low-resolution data. **e** Velocity map for the low-resolution data. **f** Dispersion velocity map for the low-resolution data. The centre of the galaxy is indicated with a cross, calibrated colours are labelled in the *vertical colour* bars

Fig. 4.3 Comparison between the fluxes from the narrow-band imaging and the FP data. The *straight line* corresponds to the line fitted to the data and used to perform the flux calibration

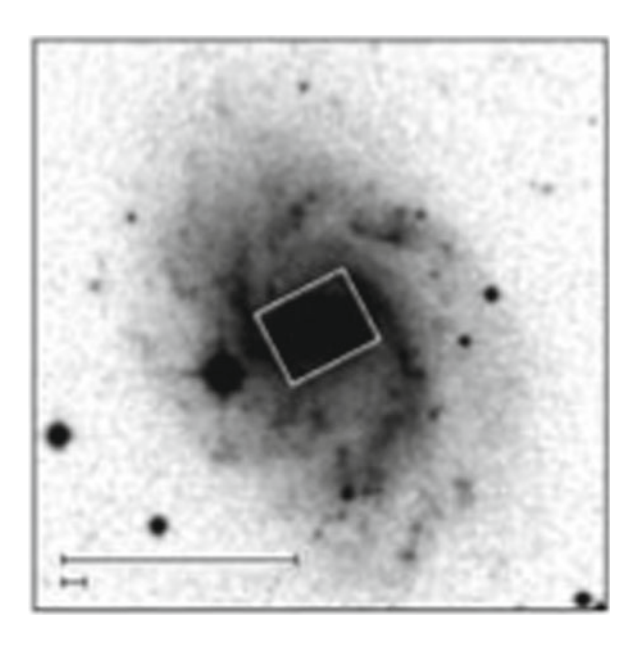


4.3.3 SAURON

I use here the stellar and gas kinematics moment maps of NGC 864 observed with SAURON and published in Ganda et al. (2006). Information about the instrument and data reduction processes can be found in Ganda et al. (2006). Although the FOV of SAURON (33 \times 41 arcsec²) is reduced to the central parts of the galaxy (see Fig. 4.4 for a comparison between the FOV of SAURON compared to the galaxy size), information about the gas and stellar kinematics is simultaneously provided using absorption (e.g. H β , Fe, Mgb) and emission lines (H β , [OIII], [NI]).

The resulting velocity moment maps for the gas and stars are shown in Fig. 4.5.

Fig. 4.4 The FOV of SAURON extends to the *white rectangle* in the image, showing the central part of the galaxy



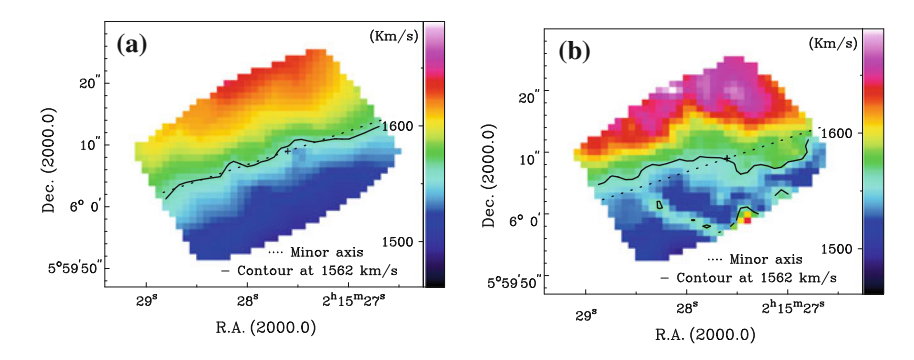


Fig. 4.5 a Velocity map of the stars in NGC 864, observed with SAURON. b Velocity map of the gas $(H\beta)$ observed with SAURON. The kinematic minor axis $(PA = 110^{\circ})$ is plotted with a *dotted line*, whereas the *solid line* shows the derived systemic velocity (see Sect. 4.4.2). The centre is indicated with a cross

4.3.4 S^4G image

I have used the mid-IR 3.6 μm from the S⁴G survey (Fig. 4.6) in order to obtain information about the stellar mass distribution and morphological features in the mid-IR (i.e., the bar). This galaxy was observed with *Spitzer* in the warm mission of the telescope. Information about the S⁴G, the images and reduction pipelines can be found in Sheth et al. (2010) and Muñoz-Mateos et al. (2015).

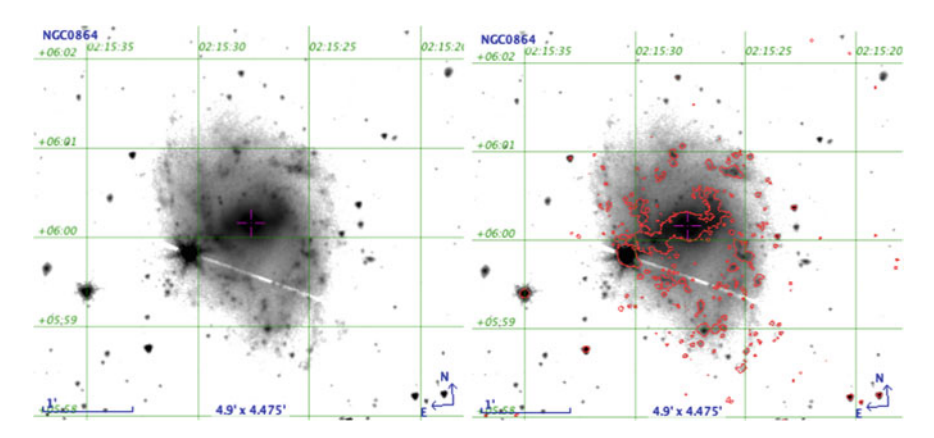


Fig. 4.6 Left 3.6 μ m S⁴G image. Right the same with H α contours at 1.1 \times 10³⁶ erg/s, taken from the ACAM image

4.4 Results 71

4.4 Results

4.4.1 Morphology

NGC 864 is a late-type barred spiral galaxy. According to its morphological classification, it can be classified as Sc in the blue light (*The de Vaucouleurs Atlas of Galaxies*; Buta et al. 2007). Looking at the mid-IR images, the classification is more Sb or bc. Focusing on the bar, it looks stronger in the mid-IR images (<u>B</u>, see Fig. 4.6) than in the blue light (AB).

In the ACAM *R*-band image image, we can distinguish the dust lanes. The spiral arms do not start at the same location where the bar ends. Indeed, the eastern arm starts at 0.89 ± 0.07 kpc away from the eastern end of the bar, whereas the western arm arises 0.96 ± 0.07 kpc from the western end of the bar.

According to the arm class, the galaxy was classified as a *grand design* galaxy with *Arm class* 5 (i.e., two symmetric, short arms in the inner regions and irregular outer arms) in Elmegreen and Elmegreen (1987). Certainly, the two outer arms are more flocculent than the inner spirals.

The bar has a skewed appearance. The PA of the flat outer part is between 90° and 100° (counter clockwise from North), whereas that of the inner part is about 70° – 80° . The reason for this skewness may well be explained by projection effects, where the inner thickened part would correspond to a box/peanut bulge (Athanassoula and Beaton 2006). However, Erroz-Ferrer et al. (2012) explains how the skewed appearance might be real. In this paper, we find that the bar has a flat light distribution, which fits the scenario of the strong bar with a flat light profile in a two-armed spiral. The flat-light distribution is also in accordance with the gap between the bar and the start of the spiral arms (Elmegreen and Elmegreen 1985). These results are further discussed in Erroz-Ferrer et al. (2012).

If we analyse the galaxy according to the $H\alpha$ emission as seen in the intensity map (left plots in Fig. 4.2) and the ACAM $H\alpha$ image (Fig. 4.1), four high emission regions can be distinguished (labelled with letters in Fig. 4.2a): (A) The emission in the central part is very strong, although not all this emission comes from the formation of stars (see Sect. 4.4.3). (B) A bright HII region where the western arm ends. (C) and (D) The regions where the bar ends and the start arms arise. In Sect. 5.2 I will explain the 2D decomposition used to define the bar region.

4.4.2 Kinematics

In this section, I am presenting the results from the $GH\alpha FaS$ gas kinematic data as well as the gas and stellar kinematics results from SAURON data. Due to the intrinsic patchiness of the $GH\alpha FaS$ FP moment maps, both the high- and low-resolution velocity maps have been studied. Thus, it is possible to analyse the overall kinematics of the galaxy as well as detailed information when there is enough good signal.

4.4.2.1 Rotation Curve

Rotation curves from the GH α FaS and SAURON data have been obtained with ROTCUR procedure in GIPSY, following the Begeman (1989) method. The initial entry values to fit the rotation curve were obtained from the literature. Specifically, the rotation velocities have been taken from the HI rotation curves in Espada et al. (2005). To compute the rotation curve as well as the galaxy parameters (centre position, PA and inclination), the steps described in Sect. 3.5 were followed. Table 4.1 presents the adopted values for PA and i.

I have followed the same steps to recover the rotation curves from SAURON observations, adopting the PA and i derived with GH α FaS data. The resulting gas and stellar velocity maps are presented in Fig. 4.5. The final rotation curves from GH α FaS and SAURON data are presented in Fig. 4.7.

First of all, I am going to discuss the different kinematic features as derived from the rotation curves in the literature, comparing those to our rotation curves. Note that it is not possible to compare the rotation curves from the gas with those from the stars, because asymmetric drift corrections are needed (see Sect. 6.4.2).

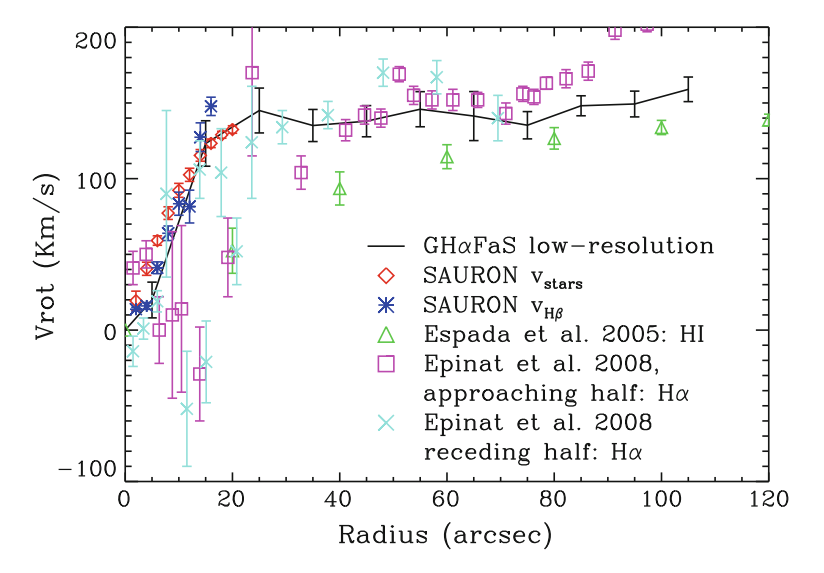


Fig. 4.7 Rotation curves for NGC 864. The *black line* corresponds to the rotation curve derived from the GHαFaS data, using the low-resolution velocity map. The *dark blue plus* signs show the rotation curve derived from the SAURON H β velocity map, whereas the *red diamonds* show the rotation curve derived from the SAURON stellar velocity map. The *green triangles* correspond to the rotation curve from HI observations taken from Espada et al. (2005). The *pink squares* and *light blue crosses* represent the rotation curves for the approaching and receding halves of NGC 864 derived in Epinat et al. (2008). Note that the FOV of SAURON covers only the inner part of the galaxy

4.4 Results 73

On the one hand, the HI rotation curve from Espada et al. 2005 is affected by beam smearing inherent to the low spatial resolution of the HI data, and the steep rise of the rotation curve is smoothed. But on the other hand, this HI rotation curve extends to larger radii than the optical data (Fig. 4.7 only represents the first 120''). The complete HI rotation curve (Fig. 7 in Espada et al. 2005) represents the typical behaviour of a disc galaxy: constant velocity in the outer parts. The rotation curve is flat after $\sim 100''$ (corresponding to ~ 10 kpc from the centre), with a constant velocity around $130 \, \mathrm{km \, s^{-1}}$ until the end of the observed disc is reached ($\sim 40.5 \, \mathrm{kpc}$).

The H α rotation curves from Epinat et al. (2008) (receding and approaching halves separately) agree with our H α rotation curve from GH α FaS observations: the typical solid body rise in the central parts and constant velocity in the outer parts. The inner parts of the rotation curve are also reproduced by the SAURON rotation curves, showing solid-body rotation in the first 20".

4.4.2.2 Velocity Models and Residual Maps

The presence of streaming motions in spiral galaxies affect on the shape of the rotation curve. Thus, it is important to remove those from the rotation curve in order not to derive a wrong amount of dark matter from the rotation curve. Also, the deviations from the circular motion provide crucial information about the galaxy features that influence on the galaxy's kinematics. The most important case is the non-circular motions caused by the non-axisymmetric gravitational potential of the bar. The effects of non-circular motions on the gas flow in galaxies were studied by e.g. Duval and Athanassoula (1983) under the beam scheme; by Lindblad et al. (1996) using the FS2 code presented in van Albada and Roberts (1981), van Albada et al. (1982) and van Albada (1985), or by Salo et al. (1999) using the sticky-particle method. The spiral structure can also provoke shocks and streaming motions in the gas (e.g., Bosma 1978; Visser 1980; Marcelin et al. 1985; Rots et al. 1990; Knapen et al. 1993, 2000; Fresneau et al. 2005; Shetty et al. 2007; Tamburro et al. 2008; Meidt et al. 2013).

Following the procedures explained in the previous chapter, a velocity model map is created using the GIPSY task *VELFI* (Fig. 4.8). This model is subtracted to the velocity map and the resulting residual map can be considered as the non-circular motions map (Fig. 4.9). In these figures we see that the highest non-circular motions, of \sim 50 km/s in absolute value (one third of the rotational velocity) are found along the bar. The amplitude of these non-circular motions is negative in the eastern part of the bar, and positive in the western one. There are also non-circular motions along the spiral arms, although the amplitude of those in the spiral arms is less (up to \pm 30 km/s) than those in the bar (\pm 50 km/s). The origin and implication of these will be studied in Sect. 4.5.

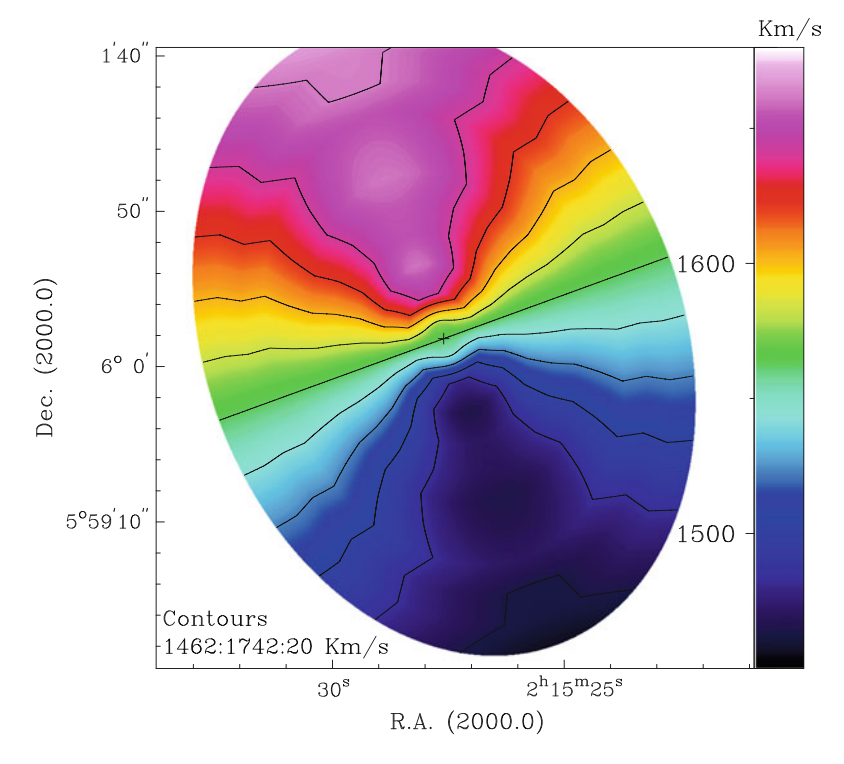


Fig. 4.8 Velocity model map

4.4.2.3 Position-Velocity Diagrams

It is possible to study the streaming motions via the residual map, as in the previous section. However, the rotation curve can be influenced by the non-circular motions and it is very important to distinguish the true rotation curve from the overall kinematics of the galaxy. As a consequence, position-velocity (PV) diagrams have been used as they reproduce the kinematic information without assumptions on galaxy parameters and are not azimuthally averaged (as the rotation curves).

The GIPSY task *SLICE* has been used to extract the PV diagram along three different angles: kinematic major axis (25°) , kinematic minor axis (115°) and along an intermediate angle of 70° (wedges of $\pm 5^{\circ}$ were used in all cases). These PV diagrams have been extracted from the low-resolution cube, and presented in Fig. 4.10.

In the absence of streaming motions, the PV diagram along the kinematic minor axis should be completely flat. Nevertheless, we see here the deviations from the circular rotations. The central emission is very strong and shows a clear extent in velocities, probably caused by strong gradients. Also, the central emission may come from a not perfect continuum-subtraction and star formation. At $2^h 15^m 29^s$ and $\sim 1660 \, \text{km/s}$, the [NII]-6548 line leaks and shows up in these PV diagrams. However, this leakage

4.4 Results 75

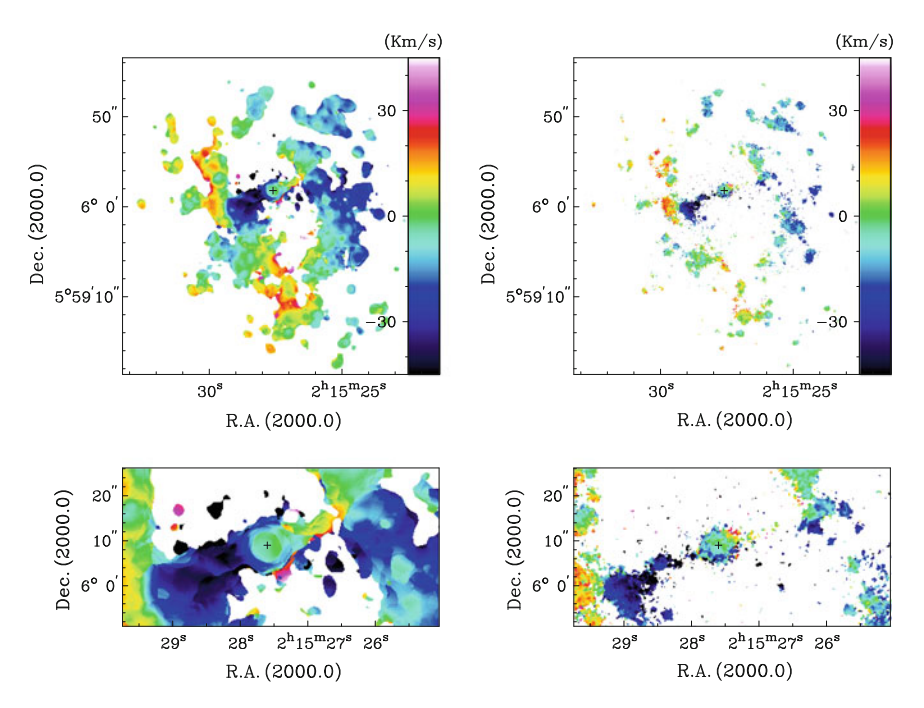


Fig. 4.9 Non-circular motions maps obtained from the low-resolution map (*left*) and from the high-resolution map (*right*). *Bottom* the bar zone for both maps is highlighted

do not appear in the moment maps as secondary peaks were not taken into account in the computation of the velocity maps (see Sect. 3.4.1).

4.4.2.4 Velocity Gradients

Residual velocities along the bar allow studies of the influence of the bar on the rotating gas. Huntley et al. (1978) and Athanassoula (1992) discussed the dynamical effects of a stellar bar on the gas motions. Most of these studies were classically carried out using HI or CO observations, and not in $H\alpha$ for a number of reasons, such as the patchy emission of $H\alpha$ or because slit spectroscopy needs more time for different position angle exposures. However, FP observations can provide 2D maps with great angular resolution that compensates for the intrinsic patchiness of the observed field, and that is the reason why we are using $GH\alpha$ FaS observations.

Analysing the residual velocity map, evidence of rapid velocity changes can be found. The analysis of these steep gradients in the residual velocity map motivates the creation of a velocity gradient map. The study of the velocity gradients can provide crucial information about the kinematics and its relation with the galaxy features, as pointed out by Zuritaet al. (2004). The first step to produce velocity gradient maps

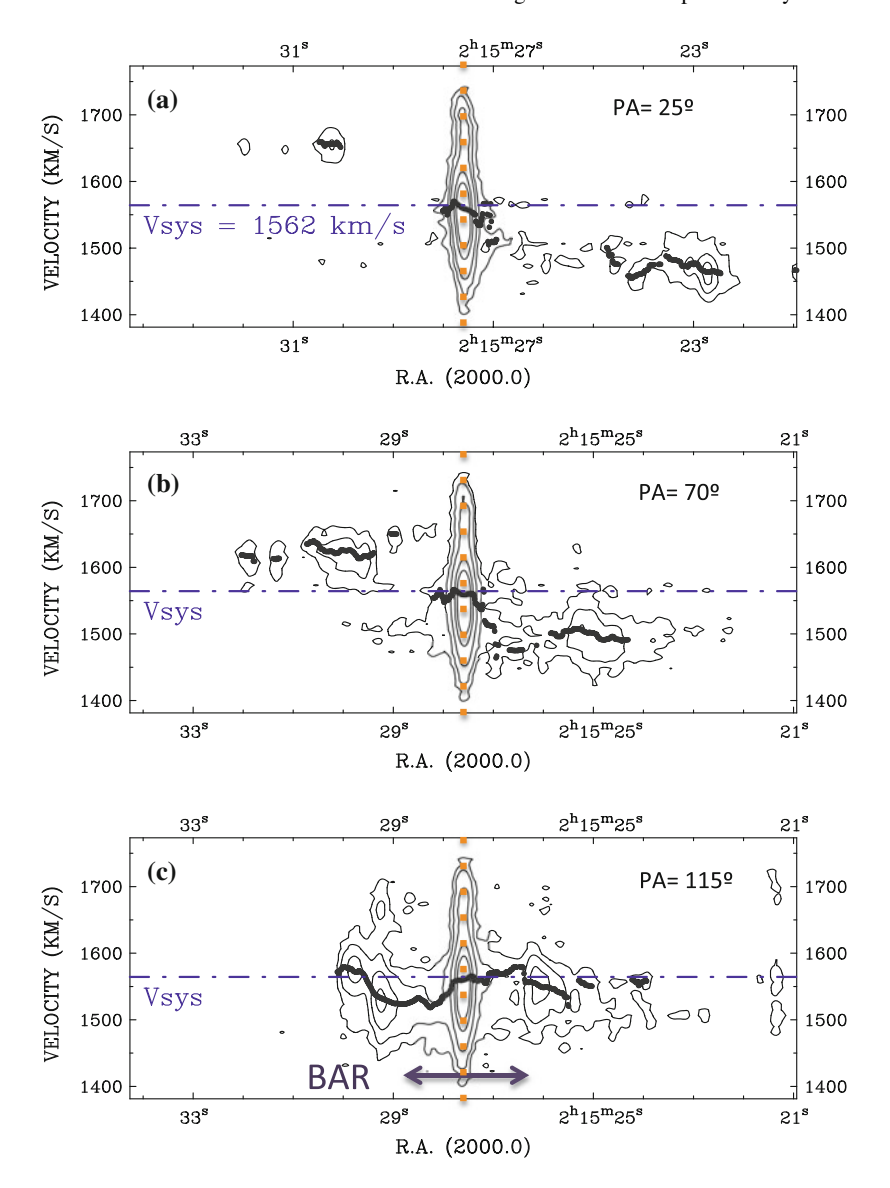


Fig. 4.10 PV diagrams for NGC 864 from the low-resolution GHαFaS velocity data. a PV along the kinematic major axis (PA = 25° , counter-clockwise from N); b PV along an intermediate angle (70°) and c PV along the kinematic minor axis (PA = 115°). Contour levels are at 0.5, 1.5, 4.5, 13.5 and 25σ . Overlaid (*grey dots*) is the velocity profile for the whole disc at the corresponding angle and the systemic velocity (*dash-dot-dash line*) corresponding to a velocity of $1562 \, \text{km/s}$

4.4 Results 77

is to create the non-circular motions map as described before. Subsequently, certain other steps are followed:

- The non-circular velocity map is displaced forward in one pixel in the direction parallel to the bar major axis.
- The displaced map is subtracted from the original map.
- The non-circular velocity map is displaced backward one pixel in the same parallel direction.
- The new displaced map is also subtracted from the original map.
- The absolute values of both subtractions are added and normalized.

The same steps are followed to create a gradient velocity map in the direction perpendicular to the bar. This decomposition in parallel and perpendicular directions is not to be taken into account when analysing the intrinsic dynamical effects, mainly due to the fact that the observations give the projected components along our line of sight, and projection effects are not removed. In general, there is a correlation between the zones with high velocity gradients in both parallel and perpendicular directions (Figs. 4.11, 4.12 and 4.13).

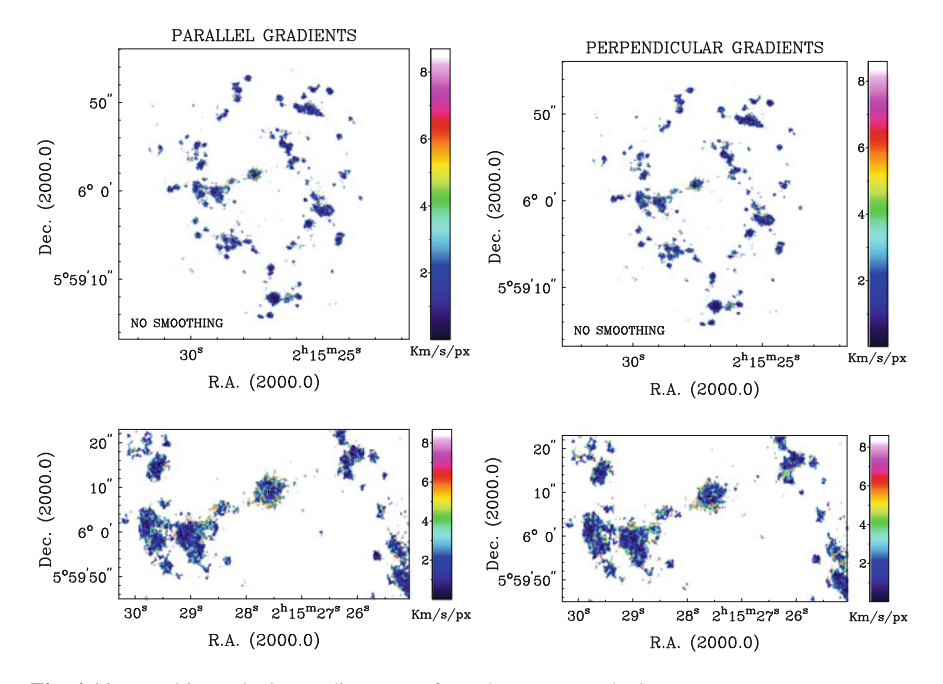


Fig. 4.11 Resulting velocity gradients map from the non-smoothed map

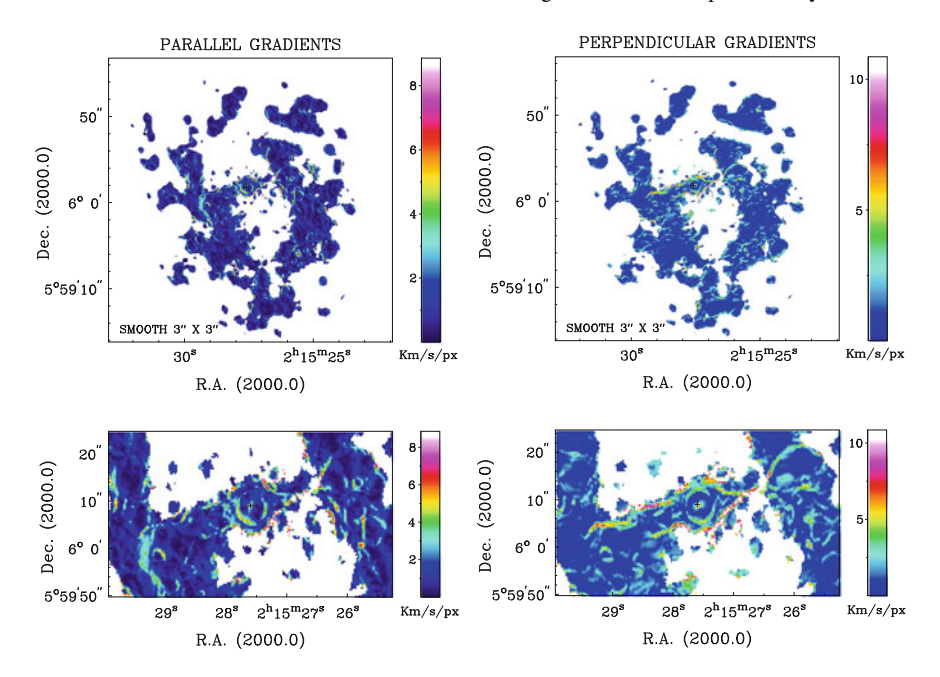


Fig. 4.12 Resulting velocity gradients maps from the 3" × 3" smoothed velocity map

4.4.3 Star Formation Rate

To compute the star formation rate, I use the equations presented in Sect. 1.4.2 (from Kennicutt et al. 2009), leading to

$$SFR(M_{\odot}yr^{-1}) = 5.5 \times 10^{-42} L(H\alpha)$$
 (4.1)

where $L(H\alpha)$ is the luminosity, calculated as

$$L(H\alpha)[erg/s] = 4\pi D^2 (3.086 \times 10^{24})^2 F_{H\alpha}^*,$$
 (4.2)

with D is the distance to the galaxy in Mpc (Table 3.1) and $F_{\rm H\alpha}^*$ the flux corrected for Galactic and internal absorption. Here, the Galactic absorption is A(R)=0.130 mag (based on the dust maps from Schlegel et al. 1998, from the NED). In Sánchez-Gallego et al. (2012), several procedures to correct for internal absorption are explained. Here, we adopt the constant value of $A(H\alpha)=1.1$ mag (Kennicutt and Kent 1983).

The SFR in the brightest regions in $H\alpha$ [those marked with letters in Fig. 4.2(a)] have been measured and presented in Table 4.2. Also, I have measured the SFR in the bar, in the spiral arms and in the whole galaxy. Note that not all the emission in the centre is due to star formation, and thus the SFR in the centre should be understood as

4.4 Results 79

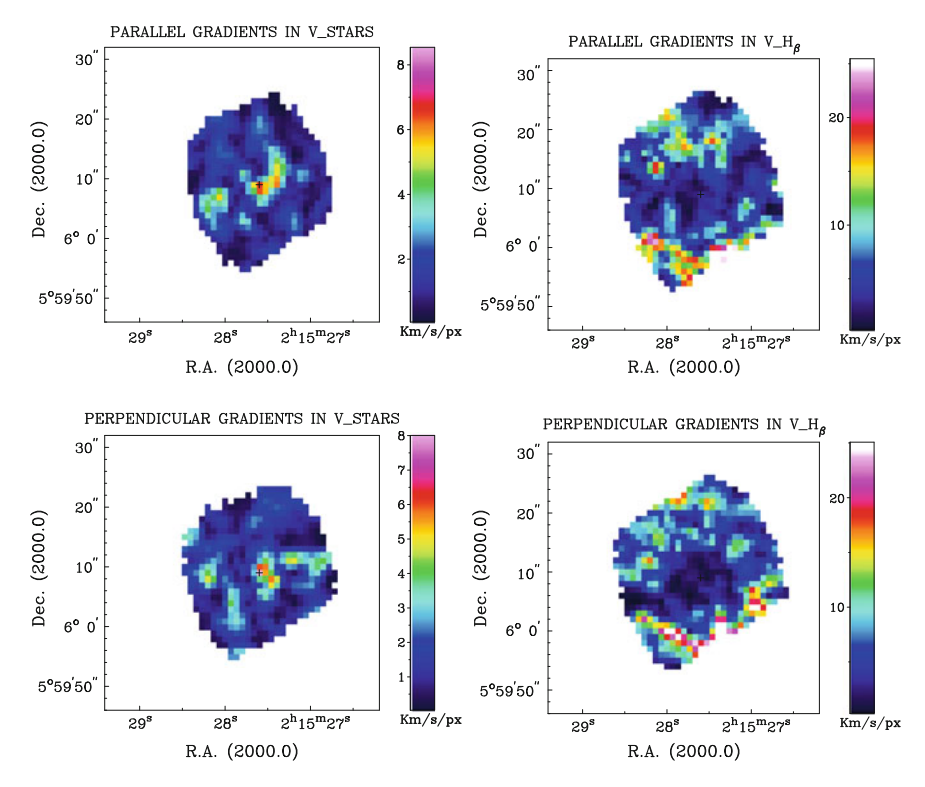


Fig. 4.13 Resulting velocity gradients maps from the SAURON stellar (left) and gas (right) velocity maps

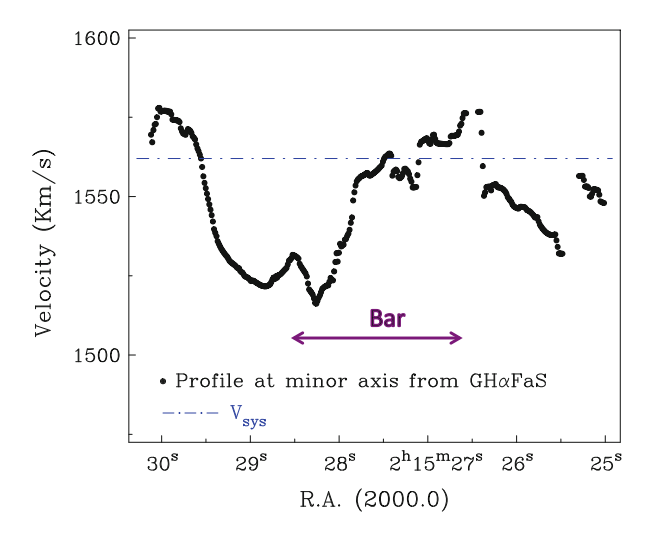
Table 4.2 $L(H\alpha)$ and SFR measured from the ACAM H α image for the whole galaxy, the eastern and western arms, for the bar region, and for the brightest regions named with A, B, C and D identified in panel (a) of Fig. 4.2 (the centre labelled with A; B in the south, at the end of the western arm, and C and D at the eastern and western ends of the bar, respectively)

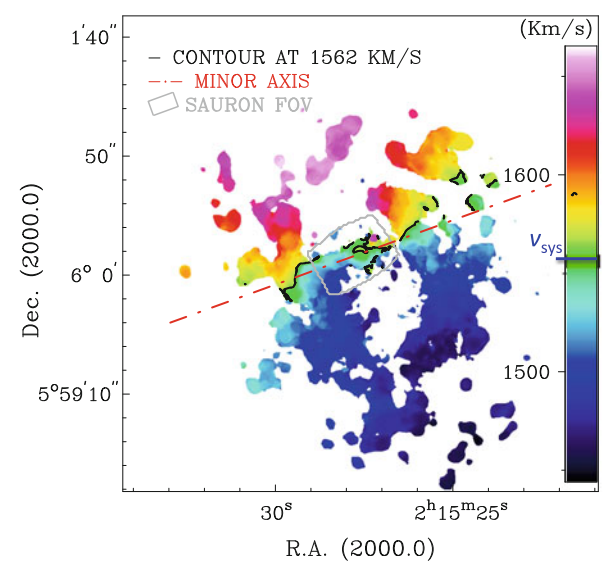
Region	$L(H\alpha)$ (erg s ⁻¹)	SFR $(M_{\odot} \text{ yr}^{-1})$
Whole galaxy	$(4.0 \pm 1.6) \times 10^{41}$	2.19 ± 0.88
Eastern arm	$(1.5 \pm 0.6) \times 10^{41}$	0.85 ± 0.34
Western arm	$(1.9 \pm 0.8) \times 10^{41}$	1.04 ± 0.41
Bar	$(5.3 \pm 2.1) \times 10^{39}$	0.03 ± 0.01
A (centre)	$(3.7 \pm 1.5) \times 10^{40}$	0.20 ± 0.08
B (End of western arm)	$(2.0 \pm 0.8) \times 10^{40}$	0.11 ± 0.04
C (start of eastern arm)	$(1.0 \pm 0.4) \times 10^{40}$	0.06 ± 0.02
D (start of western arm)	$(3.8 \pm 1.5) \times 10^{39}$	0.02 ± 0.01

an upper limit (and therefore that of the whole galaxy). The dominant old population in the bar can explain the low SFR of the region (0.03 M_{\odot} yr⁻¹). Finally, most of the star formation is located in the spiral arms.

Erroz-Ferrer et al. (2012) discuss the origin of the uncertainties on the measurements of the SFR. They come from the distance value, reduction processes and photometric accuracy. Taking all these into account, I estimate an uncertainty of about 17%, in agreement with the 14% presented in James et al. (2004), 16% in Kennicutt et al. (2008) and 18% in Sánchez-Gallego et al. (2012).

Fig. 4.14 Top the profile along the kinematic minor axis of NGC 864 in black dots: overlaid in a blue dash-dot-dash line the systemic velocity of 1562 km/s; in purple, the extent of the bar. Bottom velocity map obtained with GIPSY. The red dash-dot-dashed line shows the location of the kinematic minor axis, whereas the black contours trace a velocity of 1562 km/s, corresponding to the systemic velocity. In grey is shown the location of the SAURON image to compare the different scales





4.5 Discussion: Influence of the Bar on the Kinematics

In this chapter, we have found several ways of tracing the non-circular motions through kinematics: rotation curves (Fig. 4.7), PV diagrams (Fig. 4.10) and residual maps (Fig. 4.9). These streaming motions are mostly found in the bar region and are probably caused by the strong non-axisymmetric potential of the bar. Also, non-circular motions of high amplitude are found in the region where the arms start, meaning that the potential of the bar is also influencing the surrounding areas.

This idea can be supported with Fig. 4.14, where the velocity profile at the minor axis from the GH α FaS velocity map as well as the velocity contour at the systemic velocity of the galaxy are shown. We see that there are deviations from the systemic velocity, present as peaks and dips in the profile. These deviations, up to \sim 50 km/s in absolute magnitude, are positive in the western part of the bar and negative in the eastern one. The correspondence between peaks may indicate a flow to the central

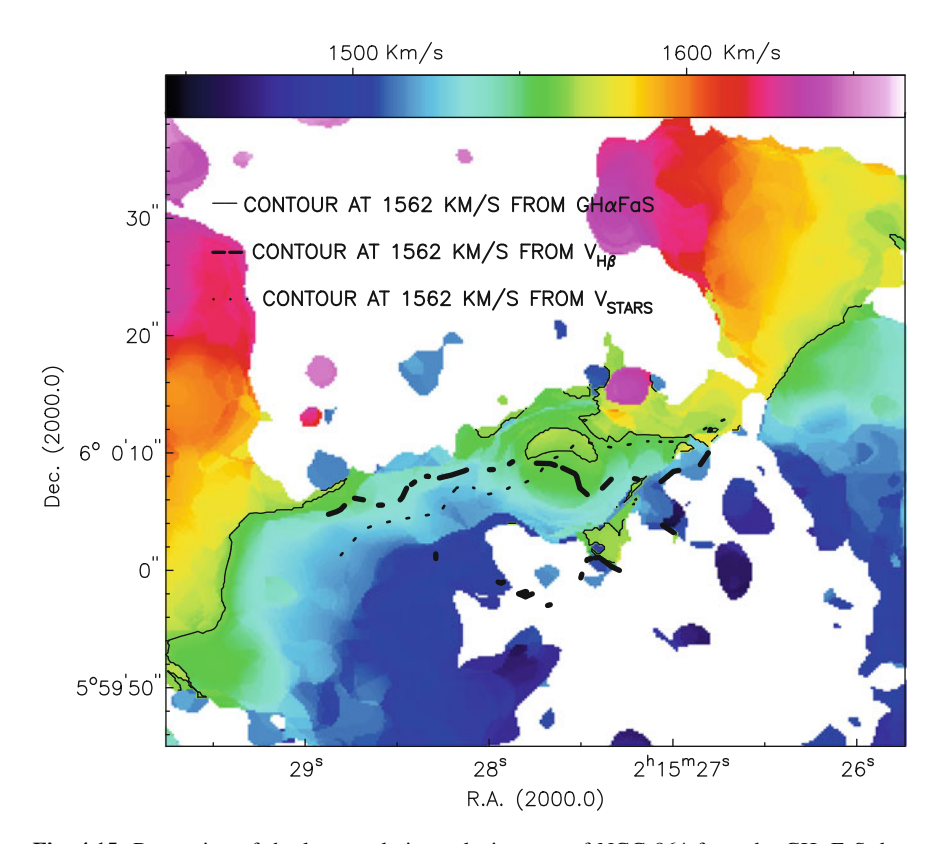


Fig. 4.15 Bar region of the low-resolution velocity map of NGC 864 from the GH α FaS data. Overlaid are contours from SAURON data: the *dashed thick line* corresponds to a velocity of 1562 km s⁻¹ in the H β velocity maps, whereas the *dotted line* corresponds to a velocity of 1562 km s⁻¹ in the stellar velocity map. The overlaid *black thin line* corresponds to 1562 km/s in GH α FaS data

parts. These streaming motions in the bar have been previously identified in some barred galaxies before, like M100 (Knapen et al. 2000).

Figure 4.15 shows the bar region of the velocity moment map from $GH\alpha FaS$ data. Overlaid, I have presented the isovelocity contour of the systemic velocity (1562 km/s) from $GH\alpha FaS$ data (straight line), SAURON stellar velocity map (dotted line) and SAURON gas velocity map (dashed line). We see here that the stellar kinematics are not as affected by the potential of the bar as the gas.

Taking everything into account, I have identified non-circular motions along the bar regions as shown by the velocity profiles, PV diagrams and residual maps. These streaming motions are likely to be produced by the non-axisymmetric potential of the bar, which is influencing on the kinematics on the galaxy and provoke deviations from the rotational, circular motion.

References

- E. Athanassoula, MNRAS 259, 345 (1992)
- E. Athanassoula, R.L. Beaton, MNRAS 370, 1499 (2006)
- K.G. Begeman, A&A 223, 47 (1989)
- A. Bosma, Ph.D. Thesis, University of Groningen, 1978
- A. Bosma, AJ 86, 1791 (1981)
- R. Buta, S. Vasylyev, H. Salo, E. Laurikainen, AJ 130, 506 (2005)
- R.J. Buta, H.G. Corwin, S.C. Odewahn, in *The de Vaucouleurs Altlas of Galaxies*, ed. by R.J. Buta, H.G Corwin, S.C. Odewahn (Cambridge University Press, Cambridge, 2007)
- R.J. Buta, K. Sheth, E. Athanassoula et al., ApJS 217, 32 (2015)
- R.J. Buta, X. Zhang, ApJS 182, 559 (2009)
- S. Comerón, J.H. Knapen, J.E. Beckman et al., MNRAS 402, 2462 (2010)
- G. de Vaucouleurs, A. de Vaucouleurs, H.G. Corwin, Jr., et al., in *Third Reference Catalogue of Bright Galaxies*, ed. by G. de Vaucouleurs, A. de Vaucouleurs, H.G. Corwin, Jr., R.J. Buta, G. Paturel, P. Fouque (1991)
- M.F. Duval, E. Athanassoula, A&A 121, 297 (1983)
- B.G. Elmegreen, D.M. Elmegreen, ApJ 288, 438 (1985)
- D.M. Elmegreen, B.G. Elmegreen, ApJ 314, 3 (1987)
- B. Epinat, P. Amram, M. Marcelin, MNRAS 390, 466 (2008)
- S. Erroz-Ferrer, J.H. Knapen, J. Font et al., MNRAS **427**, 2938 (2012)
- D. Espada, A. Bosma, L. Verdes-Montenegro et al., A&A 442, 455 (2005)
- P. Fouque, E. Gourgoulhon, P. Chamaraux, G. Paturel, A&A 93, 211 (1992)
- A. Fresneau, A.E. Vaughan, R.W. Argyle, AJ 130, 2701 (2005)
- K. Ganda, J. Falcón-Barroso, R.F. Peletier et al., MNRAS 367, 46 (2006)
- S.T. Gottesman, AJ 87, 751 (1982)
- J.M. Huntley, R.H. Sanders, W.W. Roberts Jr, ApJ 221, 521 (1978)
- P.A. James, N.S. Shane, J.E. Beckman et al., A&A 414, 23 (2004)
- V.E. Karachentseva, Astrofizicheskie Issledovaniia Izvestiya Spetsial'noj Astrofizicheskoj Observatorii 8, 3 (1973)
- R.C. Kennicutt Jr, C.-N. Hao, D. Calzetti et al., ApJ 703, 1672 (2009)
- R.C. Kennicutt Jr, S.M. Kent, AJ 88, 1094 (1983)
- R.C. Kennicutt Jr, J.C. Lee, J.G. Funes, S. Sakai, S. Akiyama, ApJS 178, 247 (2008)
- J.H. Knapen, J. Cepa, J.E. Beckman, M. Soledad del Rio, A. Pedlar, ApJ 416, 563 (1993)
- J.H. Knapen, I. Shlosman, C.H. Heller et al., ApJ 528, 219 (2000)

References 83

- S. Leon, L. Verdes-Montenegro, A&A 411, 391 (2003)
- P.A.B. Lindblad, P.O. Lindblad, E. Athanassoula, A&A 313, 65 (1996)
- M. Marcelin, J. Boulesteix, Y.P. Georgelin, A&A 151, 144 (1985)
- P. Martini, M.W. Regan, J.S. Mulchaey, R.W. Pogge, ApJS 146, 353 (2003)
- S.E. Meidt, E. Schinnerer, S. García-Burillo et al., ApJ 779, 45 (2013)
- J.C. Muñoz-Mateos, K. Sheth, M. Regan et al., ApJS 219, 3 (2015)
- A.H. Rots, A&A 45, 43 (1975)
- A.H. Rots, A. Bosma, J.M. van der Hulst, E. Athanassoula, P.C. Crane, AJ 100, 387 (1990)
- H. Salo, P. Rautiainen, R. Buta et al., AJ 117, 792 (1999)
- J.R. Sánchez-Gallego, J.H. Knapen, C.D. Wilson et al., MNRAS 422, 3208 (2012)
- D.J. Schlegel, D.P. Finkbeiner, M. Davis, ApJ 500, 525 (1998)
- K. Sheth, M. Regan, J.L. Hinz et al., PASP 122, 1397 (2010)
- R. Shetty, S.N. Vogel, E.C. Ostriker, P.J. Teuben, ApJ 665, 1138 (2007)
- D. Tamburro, H.-W. Rix, F. Walter et al., AJ 136, 2872 (2008)
- G.D. van Albada, A&A 142, 491 (1985)
- G.D. van Albada, W.W. Roberts Jr, ApJ 246, 740 (1981)
- G.D. van Albada, B. van Leer, W.W. Roberts Jr, A&A 108, 76 (1982)
- J.M. van der Hulst, A&A 75, 97 (1979)
- H.C.D. Visser, A&A 88, 159 (1980)
- A. Zurita, M. Relaño, J.E. Beckman, J.H. Knapen, A&A 413, 73 (2004)

Chapter 5 Non-circular Motions and Star Formation in S⁴G Galaxies

5.1 Introduction

One of the goals of this thesis is the analysis of the non-circular motions and its influence on the galaxy kinematics and evolution. Since the first studies of the rotation of galaxies were performed, studies of the deviations of the circular motion have also been carried out. Bosma (1978), Visser (1980) and Rots et al. (1990) performed the first studies of streaming motions induced by the spiral density wave using HI data. Ichikawa et al. (1985), Clemens (1985) and Cepa et al. (1992) also studied them using CO data, and van der Kruit (1976) and Marcelin et al. (1985) using H α data. The first studies of non-circular motions provoked by the bar were carried out by Peterson et al. (1978), Duval and Athanassoula (1983) and Pence et al. (1988) using optical data; and by Allen et al. (1973), Sancisi et al. (1979) and Gottesman et al. (1984) using HI data. This topic is still under debate and more studies are currently been carried out (e.g., Knapen et al. 2000; Fresneau et al. 2005; Spekkens and Sellwood 2007; Castillo-Morales et al. 2007; Shetty et al. 2007; Tamburro et al. 2008; García-Burillo et al. 2009; Sellwood and Sánchez 2010; Meidt et al. 2013; or Font et al. 2014).

In Sect. 3.6 I explained the procedure to obtain a map of the non-circular motions, what we usually denote as residual map. The first analysis of these maps were presented in last chapter for NGC 864. In this chapter, we expand the study to all the galaxies of the sample, now studying both non-circular motions caused by both the potentials of the bar (bar-induced non-circular motions hereafter) and spiral arms (spiral-induced non-circular motions).

5.2 Methodology

The procedure starts with the definition of the regions affected by the potential of the bar and those affected by the potential of the spiral arms. I have defined three regions: bar, spiral arms and start-of-arms-region (SAR hereafter, affected by both the potentials of the bar and spiral arms). This division has been done using images from the NED (mainly SDSS false-colour images by Baillard et al. 2011), 3.6 μm images from the S 4G and our H α ACAM images. Also, I have used the outputs from the 2D decomposition of the 3.6 μm images (Salo et al. 2015), used to determine the bar. Thus, this classification is not based on the star forming regions, i.e. bars are not perfectly traced in H α but in the mid-IR.

The first step is to define the stellar bars using the SDSS and mid-IR images, and also taking into account the length of the bar. Secondly, the SAR region have been defined by eye on the mid-IR images. Finally, the resulting parts of the galaxy are assumed to be spiral arms. In the grand design galaxies, it is easier to draw limits to the spiral arms, but not so for the more flocculent cases. All the three regions have been determined and defined astrometrically. Therefore, it is possible to extent the location of these regions to all the other wavelengths (i.e., to H α ACAM images and to the FP data).

The resulting regions for the barred galaxies are shown in Fig. 5.1: overlaid on the 3.6 μ m S⁴G images, the red contours correspond to the location of the bar, and the yellow one to the SAR regions. NGC 5678 has been added to the plot due to the fact that this galaxy may have a bar although it has been classified as an SA galaxy in Buta et al. (2015).

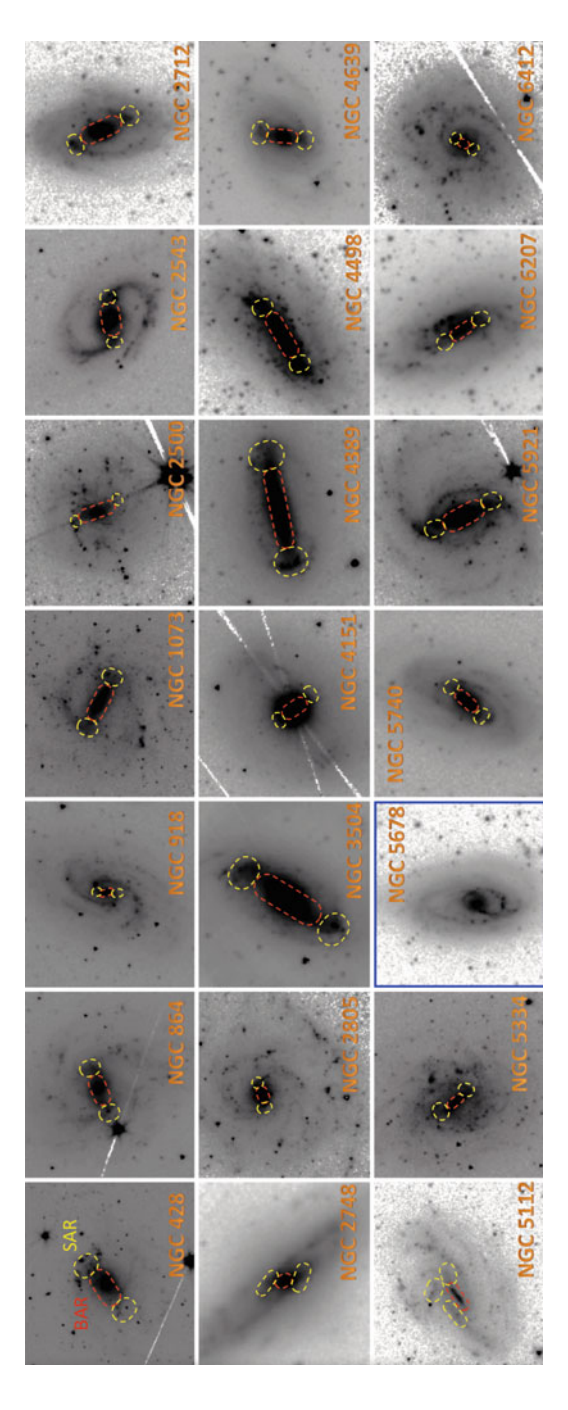
5.2.1 Non-circular Motions

To measure the amplitude of the non-circular motions and determine one fixed number for each region, I have adopted to use the cumulative distribution function (CDF) of the pixel values in the residual images. An histogram has not been chosen to avoid possible caveats, such as the bin or physical region size. Although i have used 95% as a representative value of the CDF, the correlations and trends do not change when adopting other quantities (such as 50, 70 or 90%), another advantage of the method.

I have estimated the uncertainties with Monte Carlo simulations, measuring the effect of a random noise on the velocity residual quantities which follows a Gaussian distribution being sigma the spectral resolution of the instrument. Figure 5.2 shows the resulting CDF of NGC 2748 arms region, compared also to the results from a histogram representation. The resulting values for the other galaxies of the sample are collected in Table 5.1.

5.2 Methodology 87

Fig. 5.1 Mid-IR images for all the barred galaxies in the sample, where the bar and SAR regions have been highlighted with red and yellow contours, respectively. Note that NGC 5678 has been included (into a blue square), as it is not classified as a barred galaxy in CVRHS but shows kinematic evidences to host one (see Sect. 5.3.3)



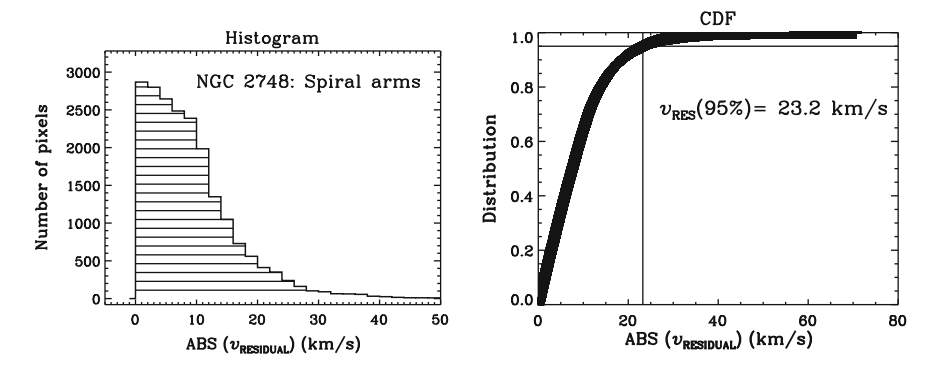


Fig. 5.2 Statistical distribution of the residual velocities of the spiral arm region of NGC 2748. *Left* Histogram distribution of the residual velocities found in the spiral arm region of the galaxy using a bin size of 1 km s^{-1} (in absolute value). *Right* Cumulative distribution function of the absolute values of the residual velocities for the spiral arm region of NGC 2748. We indicate the 95% value which we use as a representative overall measure of the residual velocities

5.2.2 Structural Parameters

The study of the non-circular motions in conjunction with the structural parameters of the galaxies may give the clues to understand the nature of these processes.

The strength of the bar can be measured using different methods. Here, we use the torque parameter Q_b which describes the maximum amplitude of the tangential forces normalised by the axisymmetric radial force (Combes and Sanders 1981; Buta and Block 2001). Q_b values have been obtained from a compilation of Q_b for the S⁴G sample (S. Díaz-García et al. in preparation). The computation of Q_b follows the method presented in Laurikainen and Salo (2002) and Salo et al. (2010). With this method, Q_b are affected by the presence of a bulge, and the higher the contribution to the bulge, the lower Q_b . Thus, a bar can be strong and have low values of Q_b due to a prominent bulge.

To study the role of the bulge on the kinematics, and also to remove the possible influence of the bulge on the computation of Q_b , we have used the bulge-to-total (B/T) ratios obtained from the decomposition to the 3.6 μ m S⁴G images (Salo et al. 2015). The values of Q_b and B/T are listed in Table 5.1.

To analyse the strength of the spiral arms, I have used the parameter called spiral arm class. D. Elmegreen has measured the arm classes for the galaxies in the S⁴G sample, and presented those in the CVRHS, classifying the arm classes into three categories: F (flocculent), M (multi-armed) and G (grand design). As NGC 4324 is a lenticular galaxy, it does not have an arm class classification. The arm classes for all the galaxies of our sample are also presented in Table 5.1.

Table 5.1 Non-circular motions as measured in the bar (Column II), SAR (Column III) and spiral arms (Column IV) of the galaxies of the sample

Galaxy name	v _{RES,BAR} (km s ⁻¹)	v _{RES,SAR} (km s ⁻¹)	VRES,ARMS (km s ⁻¹)	Qb	B/T	AC
NGC 428	35.8 ± 1.4	23.5 ± 2.7	18.8 ± 2.7	0.29 ± 0.03	0.002	F
NGC 691	_	_	19.1 ± 2.5	_	0.144	M
NGC 864	40.1 ± 1.8	45.0 ± 2.4	17.0 ± 2.9	0.47 ± 0.07	0.029	M
NGC 918	24.9 ± 2.3	26.7 ± 0.4	20.2 ± 2.3	0.23 ± 0.02	0.008	M
NGC 1073	14.6 ± 2.4	13.6 ± 3.3	12.8 ± 3.0	0.63 ± 0.08	0	M
NGC 2500	20.6 ± 2.4	16.3 ± 3.5	14.5 ± 3.0	0.28 ± 0.03	0.002	F
NGC 2541	_	_	18.9 ± 2.2	_	0	F
NGC 2543	63.2 ± 0.3	43.2 ± 0.4	30.8 ± 1.7	0.35 ± 0.08	0.166	G
NGC 2712	48.3 ± 1.5	23.3 ± 1.5	18.5 ± 2.6	0.28 ± 0.05	0.170	M
NGC 2748	44.6 ± 0.4	21.5 ± 2.7	23.2 ± 1.8	0.45 ± 0.03	0.035	M
NGC 2805	11.1 ± 3.3	13.9 ± 2.6	15.2 ± 2.7	0.19 ± 0.01	0.002	M
NGC 3041	_	_	22.6 ± 2.3	_	0.041	M
NGC 3403	_	_	19.9 ± 1.9	_	_	M
NGC 3423	_	_	13.0 ± 3.1	_	0.052	F
NGC 3504	41.4 ± 2.0	11.4 ± 3.7	12.6 ± 3.4	0.25 ± 0.06	0.372	G
NGC 4151	11.8 ± 3.1	10.1 ± 3.9	9.6 ± 4.3	0.09 ± 0.02	0.441	M ^(*)
NGC 4324	-	-	16.2 ± 3.2	-	0.291	_
NGC 4389	18.6 ± 2.6	26.3 ± 1.5	21.4 ± 3.0	0.52 ± 0.06	0	M ^(*)
NGC 4498	19.7 ± 2.6	16.2 ± 2.8	23.9 ± 1.3	0.46 ± 0.07	0	F
NGC 4639	_	17.7 ± 2.5	15.6 ± 3.0	0.26 ± 0.04	0.114	M
NGC 5112	14.0 ± 2.9	23.4 ± 2.7	19.9 ± 2.1	0.62 ± 0.06	0	M
NGC 5334	_	18.1 ± 2.9	15.3 ± 2.8	0.49 ± 0.08	0.001	F
NGC 5678	_	_	72.6 ± 0.1	_	0.037	F
NGC 5740	_	21.0 ± 2.4	21.1 ± 1.7	0.16 ± 0.03	0.128	M
NGC 5921	_	21.9 ± 1.7	16.5 ± 2.6	0.34 ± 0.06	0.118	M
NGC 6070	_	_	20.7 ± 1.7	_	0.045	M
NGC 6207	18.6 ± 2.6	15.5 ± 3.0	17.9 ± 2.3	0.21 ± 0.02	0	F
NGC 6412	12.7 ± 2.9	5.2 ± 6.7	15.0 ± 2.6	0.24 ± 0.02	0.005	M
NGC 7241	-	-	18.6 ± 2.3	-	0	M

We use the 95% value of the cumulative distribution function as a representative overall measure of the residual velocities. (Column V) Bar strength (Q_b) measured from the torque maps derived from the 3.6 μ m S⁴G images (S. Díaz-García et al. in preparation). (Column VI) B/T from the 2D decompositions to the 3.6 μ m images (H. Salo et al. in preparation). (Column VII) Arm class (AC) classification from CVRHS: F = flocculent, M = multi-armed, G = grand design. The "-" refers to non-barred galaxies, to those barred ones that do not have H α emission within the bar or to galaxies that do not have an arm classification. (*) These galaxies do not have an arm classification in the CVRHS, but as their arm classification in Elmegreen and Elmegreen (1987) was 5, we have classified them as multi-armed (M)

5.2.3 Star Formation Rates

Taking advantage of our $H\alpha$ images, it is also possible to relate the formation of stars to the galaxy's kinematics. Using Eqs. 4.1 and 4.2, I derive the SFRs, using the distances in Table 3.1. These SFRs are corrected for Galactic absorption. Table 5.2

Table 5.2 SFRs measured from the ACAM H α images, corrected for Galactic absorption (see text)

				1 '
Galaxy name	SFR _{tot}	SFR _{bar}	SFR _{SAR}	SFR _{arms}
	$(M_{\odot} \text{ yr}^{-1})$	$(M_{\odot} \text{ yr}^{-1})$	$(M_{\odot} \text{ yr}^{-1})$	$(M_{\odot} \text{ yr}^{-1})$
NGC 428	0.43 ± 0.17	0.019 ± 0.008	0.078 ± 0.031	0.334 ± 0.134
NGC 691	0.63 ± 0.25	_	_	0.628 ± 0.251
NGC 864	0.87 ± 0.35	0.082 ± 0.033	0.035 ± 0.014	0.750 ± 0.300
NGC 918	$0.48^{(*)} \pm 0.19$	0.006 ± 0.002	0.004 ± 0.002	0.465 ± 0.186
NGC 1073	0.73 ± 0.29	0.029 ± 0.011	0.018 ± 0.007	0.685 ± 0.274
NGC 2500	0.16 ± 0.06	0.002 ± 0.001	0.006 ± 0.002	0.154 ± 0.062
NGC 2541	0.19 ± 0.08	_	_	0.191 ± 0.076
NGC 2543	0.38 ± 0.15	0.060 ± 0.024	0.022 ± 0.009	0.297 ± 0.119
NGC 2712	0.21 ± 0.08	0.063 ± 0.025	0.021 ± 0.008	0.125 ± 0.050
NGC 2748	0.52 ± 0.21	0.018 ± 0.007	0.158 ± 0.063	0.345 ± 0.138
NGC 2805	1.04 ± 0.42	0.003 ± 0.001	0.017 ± 0.007	1.022 ± 0.409
NGC 3041	0.73 ± 0.29	_	_	0.730 ± 0.292
NGC 3403	0.23 ± 0.09	_	_	0.234 ± 0.094
NGC 3423	0.30 ± 0.12	_	_	0.298 ± 0.119
NGC 3504	0.93 ± 0.37	0.687 ± 0.275	0.148 ± 0.059	0.097 ± 0.039
NGC 4151	$0.25^{(*)} \pm 0.10$	0.025 ± 0.010	0.009 ± 0.003	0.217 ± 0.087
NGC 4324	0.05 ± 0.02	_	_	0.052 ± 0.021
NGC 4389	0.06 ± 0.02	0.035 ± 0.014	0.013 ± 0.005	0.013 ± 0.005
NGC 4498	0.11 ± 0.04	0.011 ± 0.004	0.021 ± 0.008	0.081 ± 0.032
NGC 4639	$0.17^{(*)} \pm 0.07$	0.003 ± 0.001	0.045 ± 0.018	0.122 ± 0.049
NGC 5112	0.54 ± 0.21	0.020 ± 0.008	0.099 ± 0.040	0.418 ± 0.167
NGC 5334	0.18 ± 0.07	0.002 ± 0.001	0.018 ± 0.007	0.157 ± 0.063
NGC 5678	0.80 ± 0.32	_	_	0.802 ± 0.321
NGC 5740	0.27 ± 0.11	0.005 ± 0.002	0.062 ± 0.025	0.206 ± 0.083
NGC 5921	0.97 ± 0.39	0.014 ± 0.006	0.107 ± 0.043	0.853 ± 0.341
NGC 6070	0.95 ± 0.38	_	_	0.946 ± 0.379
NGC 6207	0.41 ± 0.16	0.007 ± 0.003	0.113 ± 0.045	0.285 ± 0.114
NGC 6412	0.48 ± 0.19	0.030 ± 0.012	0.002 ± 0.001	0.452 ± 0.181
NGC 7241	0.11 ± 0.04	-	_	0.109 ± 0.044

Notes The "-" refers to non-barred galaxies or to those barred ones that do not have $H\alpha$ emission within the bar. (*) The AGN contribution has been excluded from the measurements

5.2 Methodology 91

presents the resulting SFRs for the three different regions (bar, SAR and arms), as well as the total SFR of the galaxy.

As mentioned in the previous section, not all the $H\alpha$ emission in the central parts may be due to SF. Thus, I have excluded the central emission from the AGNs of the sample: NGC 918 (no specific classification; Palumbo et al. 1983); NGC 4151 (Seyfert type 1.5; Khachikian and Weedman 1974) and NGC 4639 (Seyfert 1.0; Ho et al. 1997). On the other hand, NGC 3504 is a starburst galaxy (Balzano 1983) and the $H\alpha$ emission in the central part may well be explained by SF. In Erroz-Ferrer et al. (2015), a more detailed analysis of the total SFR distribution for the galaxies of the sample is presented.

5.3 Results

5.3.1 Bar-Induced Non-circular Motions

One of the goals of this chapter is to understand the effect of the secular evolution on the kinematics of the galaxies of the sample, and therefore the impact on the evolution of the galaxies. I start by studying the influence of the presence of a bar on the kinematics of the galaxy, concretely on the non-circular motions caused by the potential of the bar. I will first try to see the connection between the presence of a bar and the deviations from the rotational motion. Then, I will study the relationship between the presence of the bar and the formation of stars, although there is a caveat because our images only show the star forming regions.

Throughout this chapter, I will assume that the deviations from the circular velocity caused by turbulent motions or thermal broadening are negligible (see Sect. 6.2.4). However, a part of residual velocities may have their origin in the turbulent motions or thermal broadening, although I will not study them here.

Some bars do not show $H\alpha$ emission due to the dominant old-population stars and lack of formation of stars (e.g., in the SB galaxies NGC 4639, NGC 5334 or NGC 5921). Among all the barred galaxies (12 SAB and 7 SB) in our sample, the bar is seen in $H\alpha$ in 11 of them. In some of them (NGC 864, NGC 1073, NGC 2500, NGC 2748, NGC 2805, NGC 4151, NGC 4389, NGC 4498, NGC 5112, NGC 6207 and NGC 6412), this emission is obvious and it is easy to measure non-circular motions there. However, following the method explained before, as we define the regions astrometrically, there are some small SF regions that can not be distinguished by eye and that show little, but not negligible, $H\alpha$ emission in the bar. These cases are NGC 428, NGC 918 and NGC 3504 (Table 5.1). The other cases (NGC 2543, NGC 2712, NGC 5740 and NGC 5921) do not show $H\alpha$ emission in the bar but in the SAR, and indeed show large non-circular motions. For the lenticular NGC 4324, the residual velocities in the ring have been understood as spiral-induced non-circular motions, finding a value of $16.2 \pm 3.2 \text{ km s}^{-1}$.

As explained for NGC 864 in the previous section, the first clue to find the deviations from the circular motion are the PV diagrams along the minor axis. I have derived the PV diagrams along the minor axis for all the galaxies of the sample, and presented them in the Appendix C. I have also included the deprojected length of the bar in those plots. In most of the barred galaxies, there are deviations in the minor axis with peaks and dips, like in NGC 864, indicating a flow of gas to the central parts rather than being circular. These deviations are beyond the length of the bar in some cases such as NGC 864 (Fig. C.5), NGC 3504 (Fig. C.6) or NGC 5678 (Fig. C.7). This may indicate that there are bar-induced non-circular motions in the SAR region. Note, though, that in the SAR region there may well also be non-circular motions due to the potential of the spiral arms.

In Fig. 5.3 (left), i present the residual velocities of the three regions (bar, SAR and spiral arms) as a function of Q_b . In these plots, different symbols have been used

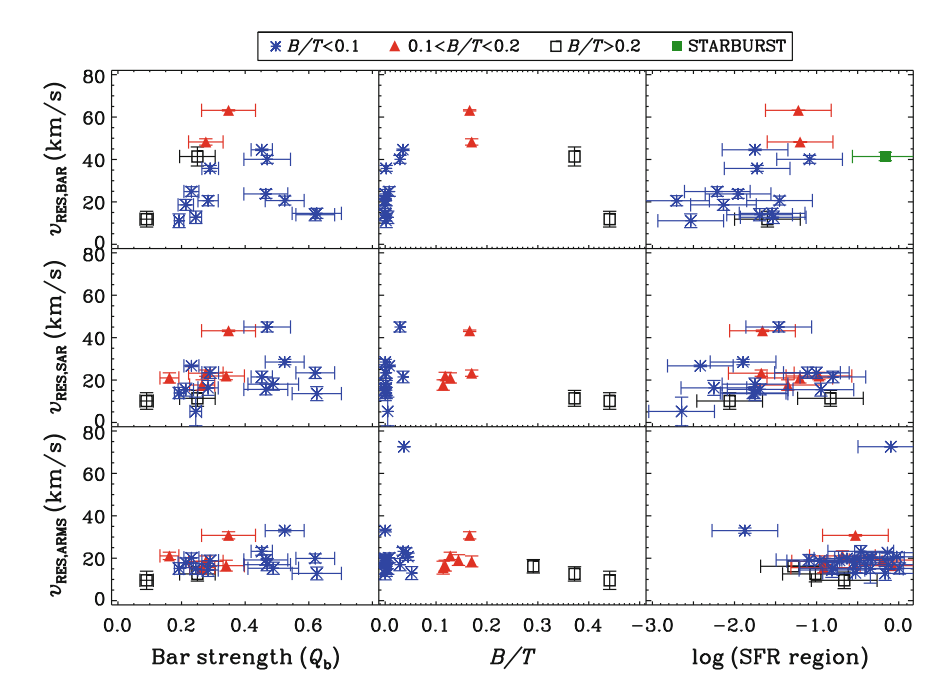


Fig. 5.3 Measurements of the non-circular motions. The *top panels* represent the non-circular motions (residual velocities from the 95 % level of the CDF) in the bar region, whereas the *middle* and *bottom plots* represent the residual velocities in the SAR and arms, respectively. *Left* Residual velocities as a function of the bar strength (represented by the parameter Q_b from Díaz-García et al. in preparation). The galaxies without a bar (i.e., $Q_b = 0$) have not been represented. *Middle* The same residual velocities as a function of *B/T. Right* The same residual velocities as a function of the SFR in each of the three regions. *Note* In all the plots, we have represented galaxies with B/T < 0.1 with *blue asterisks*, galaxies with 0.1 < B/T < 0.2 with *red triangles*, and galaxies with B/T > 0.2 (*bulge-dominated*) with squares. In the *top right plot*, we have highlighted with a filled *green square* the starburst nucleus (NGC 3504)

5.3 Results 93

depending on the B/T of the galaxy: blue asterisks for galaxies with B/T < 0.1, red triangles for the galaxies with 0.1 < B/T < 0.2 and squares for the galaxies with B/T > 0.2 (bulge dominated). Then, it is possible to distinguish the influence of the bulge on the relationships with Q_b . Also, I present the amplitude of the non-circular motions as a function of the B/T in the middle plots of Fig. 5.3 in order to see whether the bulge has a direct influence on the deviations from the circular motion. Note that in the Fig. 5.3 (left) plots and in all the plots for the bar and SAR regions, only the barred galaxies (i.e., $Q_b \neq 0$) have been included.

For completeness, we have normalized the residual velocities. To do so, we have computed the corresponding circular velocity at a radius equal to the bar length, to the extent of SAR, and to the last measured point (assuming that the spiral arms end there), following the universal rotation curve by Persic and Salucci (1991). The same plots as in Fig. 5.3 have been created for the normalized residual velocities, presented in Fig. 5.4. This method includes several uncertainties, such as assuming that the circular velocity in all the region is equal to that of the last radii, or that the region is circular with a radius the extent of the structure (bar, SAR or arms). However, it is useful to normalize our residual velocities. Note that the residual velocities have been deprojected.

Analysing the left hand plots of Figs. 5.3 and 5.4, we do not find a correlation between the amplitude of the non-circular motions and Q_b . However, the presence

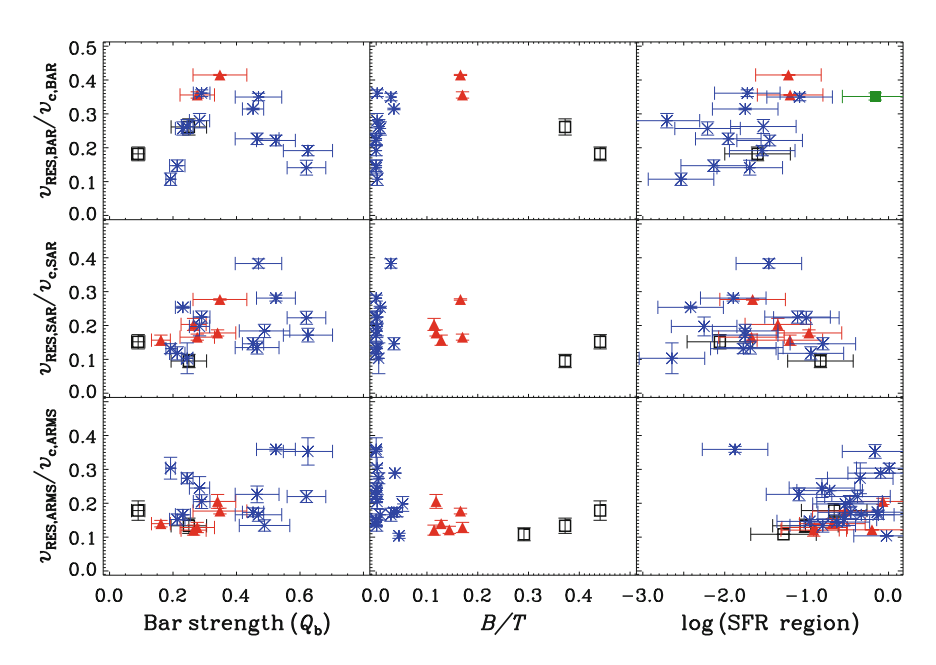


Fig. 5.4 As Fig. 5.3 but now for the residual velocities normalized by the circular velocity at the end of the bar region (*top plots*), end of SAR (*middle plots*) and end of spiral arms (*bottom plots*). These circular velocities have been estimated using the universal rotation curve from Persic and Salucci (1991)

of the bulge is important. Q_b varies inversely with B/T, so Q_b is strongly reacting to the bulge: a stronger bulge dilutes the tangential force from the bar and lowers Q_b . It is not necessarily true that the bar is weaker, just that motions are more influenced by the spherical potential of the bulge. In the bar region (residual velocity as a function of B/T, top middle plots of Figs. 5.3 and 5.4), we see that for galaxies with a significant bulge (B/T > 0.1), the residual velocities in the bar decrease as B/T increases. In these cases, we conclude that the bulge is constraining the velocities to remain circular, and the stronger the bulge (the lower Q_b in galaxies with bulges) the lower the residual velocities in the bar region.

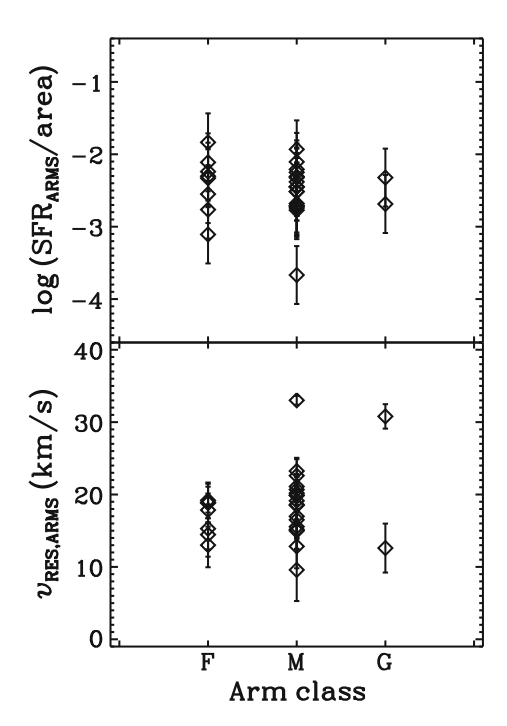
As noted previously in the literature (e.g., Athanassoula 1992), the high shear and shocks in the bar region prevent star formation, and therefore we might not see in $H\alpha$ those bars with higher non-circular motions. Consequently, we need to study more generally the role of bars in the formation of stars.

The SFRs of the three regions (bar, spiral arms and SAR) have been measured from the ACAM images. In Figs. 5.3 and 5.4 (left), i represent the amplitude of the non-circular motions as a function of the SFRs. I find that the bars with higher SFR show higher non-circular motions. On the contrary, Zurita et al. (2004) showed the example of the strong bar of NGC 1530, where SF is inhibited in the bar region and the non-circular motions anti-correlate with $L(H\alpha)$. This is probably related to shear prohibiting star formation, and one might thus expect to find lower SFR in regions of high non-circular motions, which would cause a bias in our study. Analysing also the middle and bottom right panels of Figs. 5.3 and 5.4, i find that the amplitude of the non-circular motions and the SFR do not correlate. Erroz-Ferrer et al. (2015) gives a thorough discussion about the relationship between the formation of stars and bar strength, out of the scope of this chapter.

5.3.2 Spiral-Induced Non-circular Motions

Now I analyse the relationship between the deviations from the circular motions caused by the potential of the spiral arms. In Fig. 5.5, I represent the amplitude of those non-circular motions as a function of the arm class. Also, I represent the SFR in the arms region (as measured from our ACAM images) as a function of the arm class. These parameters do not correlate. This result agrees with Elmegreen and Elmegreen (1986) (as they defended that the SFR per unit area does not depend on the arm class) and other studies that defended the idea that the SFR in the spiral arms did not correlate with the strength of the spiral arms (Dobbs and Pringle 2009; Foyle et al. 2010). On the contrary, this results disagree with other studies that defend the opposite (e.g., Seigar and James 2002; Clarke and Gittins 2006). In conclusion, the presence and magnitude of the non-circular motions in the spiral arms seem to be a local phenomenon.

Fig. 5.5 Top SFR in the arms per unit area as a function of the arm class classification from CVRHS. Bottom Amplitude of the non-circular motions within the spiral arms as a function of the arm class. We see that neither the SFR nor the amplitude of the non-circular motions correlate with the arm class. Note NGC 4324 has not been presented in the figure as it does not have an arm class classification. The value of NGC 5678 has not been presented either as the amplitude of the non-circular motion within its spiral arms presented in Table 5.1 is understood as caused by the bar (see Sect. 5.3.3)



5.3.3 Special Case: NGC 5678

The case of NGC 5678 is special, the residual velocities of this galaxy stand out in the bottom plots of Fig. 5.3. This galaxy was classified as SAB in de Vaucouleurs et al. (1991) and argued to be barred by Ganda et al. (2007), but Buta et al. (2015) reclassified it as SA from an S⁴G mid-IR image and it does not therefore have bar strength classification in Table 5.1. Epinat et al. (2008) (GHASP VII hereafter) found the signature of a bar in the centre in the form of an S shape of the isovelocity lines, also seen in our velocity map. We do not find clear evidence of a bar in NGC 5678 in the observed images of (H α , 3.6 μ m), but there is a reddish structure shown in the SDSS false-colour figure of the galaxy (Baillard et al. 2011) parallel to the major axis of the galaxy (see a compilation of images in Fig. 5.6).

If we analyse the residual velocity field [panel e, Fig. A.12 (top)], in the central part and where the spiral arm starts there is a region with very large deviations from the expected circular rotation, with values up to $130\,\mathrm{km\,s^{-1}}$ in absolute value. We find complex dust lanes when looking at broad-band images, tracing the places with high shear due to the spiral density wave. However, the high amplitude of the non-circular motions found here (representative value of \sim 70 km s⁻¹ above the average value of 20–30 km s⁻¹ for spiral-induced non-circular motions) leads us to conclude that a spiral cannot be the single cause, and that this galaxy could be barred.

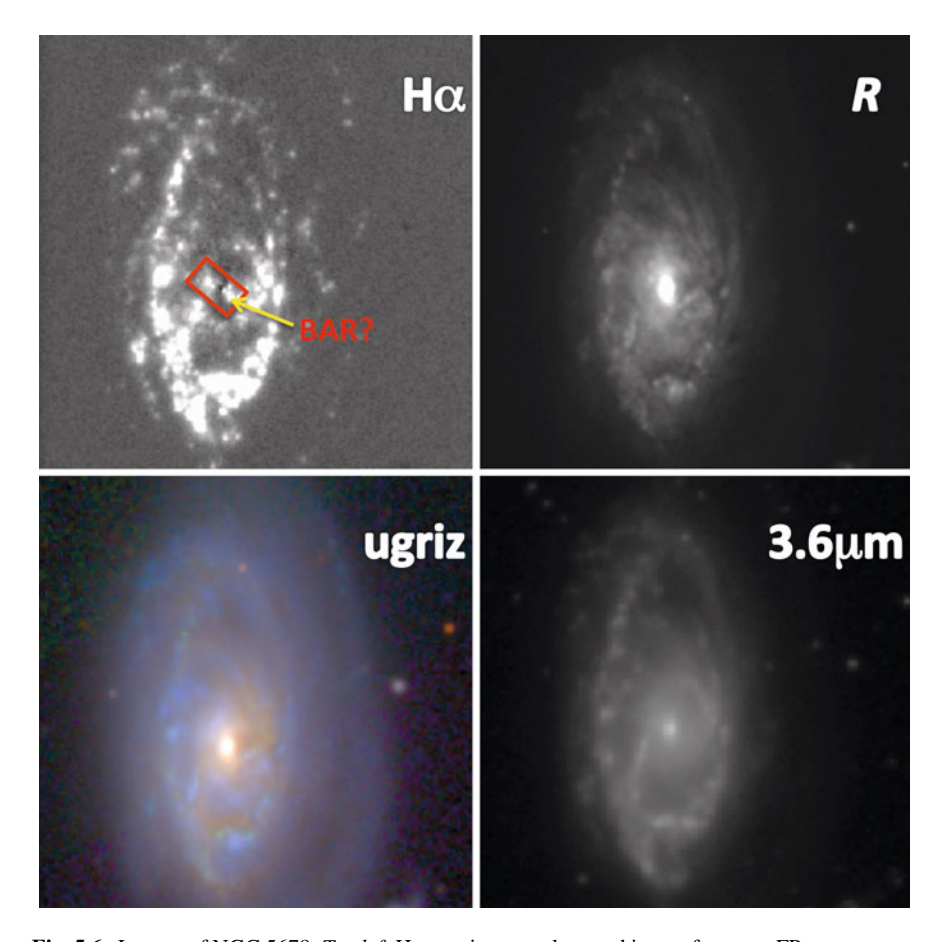


Fig. 5.6 Images of NGC 5678. Top left H α continuum subtracted image from our FP programme. Top right R-band image observed with ACAM at the same time as the H α image. Bottom left False colour image from the ugriz bands of SDSS, from (Baillard et al. 2011). Bottom right 3.6 μ m image from the S⁴G survey. Note that the bar cannot be clearly identified

To compare our data to that of GHASP VII, we represent the PV diagram along the kinematic major and minor axis of the galaxy in Fig. 5.7, derived from a 3" smoothed velocity map. If there is a bar, we expect to find a large effect in residual velocities only along the minor axis. In fact, the PV diagram along the major axis shows the rotation of the galaxy, and the PV diagram along the minor axis shows the deviations from the circular motions, very similar to those created by the potential of the bar in NGC 864 (Chap. 4).

The environment surrounding the galaxy must be also playing a role in this case. We have found that the galaxy has a companion (MCG +10-21-006, Δv =12 km/s; ΔM = 3.4 mag; \sim 1.9 arcmin or \sim 18.4 kpc away from NGC 5678; from de Vaucouleurs et al. 1976). Such a close companion could alter the kinematics

5.3 Results 97

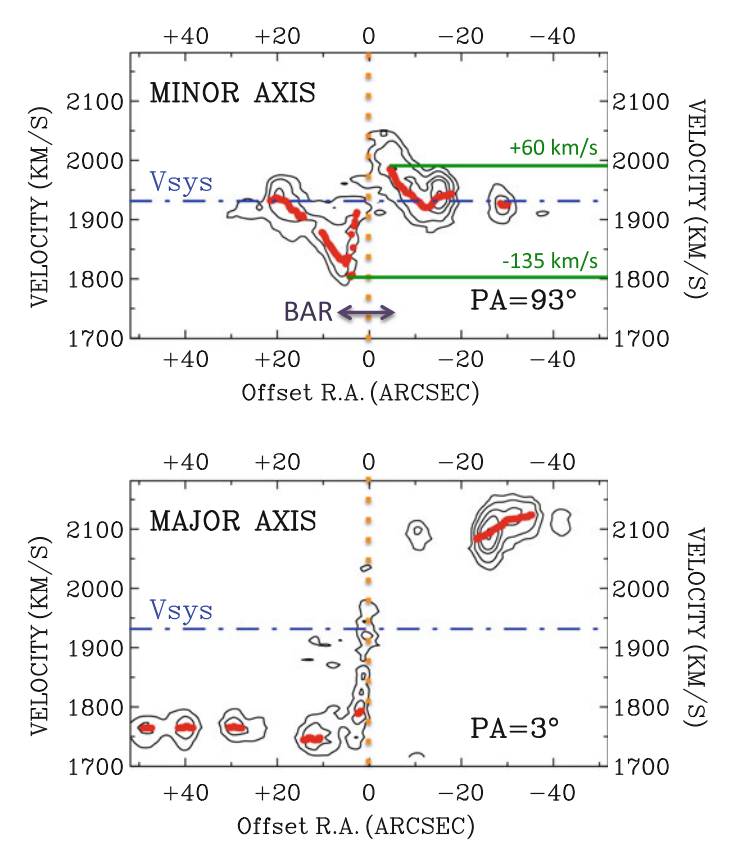


Fig. 5.7 PV diagrams of the SA galaxy NGC 5678. *Top* PV diagram along the minor axis. *Bottom* PV diagram along the major axis. Overlaid ($red\ dots$) is the velocity profile for the whole disc at the corresponding angle and the systemic velocity ($dash\-dot\-dash\ line$) corresponding to a velocity of 1932 km/s. If we agree that the bar is in the region marked in Fig. 5.6, the bar length is $\sim 13''$ (color online)

of the galaxy, and cause the gas at the begining of the spiral arm to have higher non-circular motions, although not as high as those found here.

Taking everything into account, I conclude that the non-circular motions in NGC 5678 are an evidence supporting the claim that NGC 5678 is a barred galaxy, and the high amplitude of those non-circular motions are bar-induced rather than only spiral-induced.

Although galactic discs are supported by rotation, there are regions that show deviations from this pure rotational motion. In particular, the potentials of the bar and spiral arms probably cause the non-circular motions found in the galaxies of our sample. These non-circular motions found in the bar region do not correlate with the bar strength $Q_{\rm b}$, although this parameter is influenced by the presence of a bulge. Also, for the galaxies with significant bulge (B/T over 0.1), the residual

velocities in the bar region decrease with *B/T*. This study, however, is biased because we only observe the streaming motions in the ionized gas, and there is a possibility that the non-circular motions with higher amplitude may not be observed (in the bar region). For NGC 5678, inspection of the PV diagram along the minor axis and the large residuals near the central parts indicate that there is a small bar there, whose potential cause the streaming motions. For the spiral arms, it seems that streaming motions is a local phenomena which is not correlated with the arm class.

References

- R.J. Allen, W.M. Goss, H. van Woerden, A&A 29, 447 (1973)
- E. Athanassoula, MNRAS **259**, 345 (1992)
- A. Baillard, E. Bertin, V. de Lapparent et al., A&A 532, A74 (2011)
- V.A. Balzano, ApJ 268, 602 (1983)
- A. Bosma, Ph.D. Thesis, Groningen Univ., 1978
- R. Buta, D.L. Block, ApJ 550, 243 (2001)
- R.J. Buta, K. Sheth, E. Athanassoula et al., ApJS 217, 32 (2015)
- A. Castillo-Morales, J. Jiménez-Vicente, E. Mediavilla, E. Battaner, MNRAS 380, 489 (2007)
- J. Cepa, J.E. Beckman, J.H. Knapen, N. Nakai, N. Kuno, AJ 103, 429 (1992)
- C. Clarke, D. Gittins, MNRAS 371, 530 (2006)
- D.P. Clemens, ApJ 295, 422 (1985)
- F. Combes, R.H. Sanders, A&A 96, 164 (1981)
- G. de Vaucouleurs, A. de Vaucouleurs, H.G. Corwin, Jr. et al., in *Third Reference Catalogue of Bright Galaxies*, ed. by G. de Vaucouleurs, A. de Vaucouleurs, H.G. Corwin, Jr., R.J. Buta, G. Paturel, P. Fouque (1991)
- G. de Vaucouleurs, A. de Vaucouleurs, J.R. Corwin, in Second Reference Catalogue of Bright Galaxies, Austin: University of Texas Press (1976)
- C.L. Dobbs, J.E. Pringle, MNRAS **396**, 1579 (2009)
- M.F. Duval, E. Athanassoula, A&A 121, 297 (1983)
- B.G. Elmegreen, D.M. Elmegreen, ApJ 311, 554 (1986)
- D.M. Elmegreen, B.G. Elmegreen, ApJ 314, 3 (1987)
- B. Epinat, P. Amram, M. Marcelin, MNRAS 390, 466 (2008)
- S. Erroz-Ferrer, J.H. Knapen, R. Leaman et al., MNRAS **451**, 1004 (2015)
- J. Font, J.E. Beckman, J. Zaragoza-Cardiel et al., MNRAS 444, L85 (2014)
- K. Foyle, H.-W. Rix, F. Walter, A.K. Leroy, ApJ 725, 534 (2010)
- A. Fresneau, A.E. Vaughan, R.W. Argyle, AJ 130, 2701 (2005)
- K. Ganda, R.F. Peletier, R.M. McDermid et al., MNRAS 380, 506 (2007)
- S. García-Burillo, S. Fernández-García, F. Combes et al., A&A 496, 85 (2009)
- S.T. Gottesman, R. Ball, J.H. Hunter Jr, J.M. Huntley, ApJ 286, 471 (1984)
- L.C. Ho, A.V. Filippenko, W.L.W. Sargent, ApJ 487, 591 (1997)
- T. Ichikawa, M. Nakano, Y.D. Tanaka et al., PASJ 37, 439 (1985)
- E.Y. Khachikian, D.W. Weedman, ApJ 192, 581 (1974)
- J.H. Knapen, I. Shlosman, C.H. Heller et al., ApJ 528, 219 (2000)
- E. Laurikainen, H. Salo, MNRAS 337, 1118 (2002)
- M. Marcelin, J. Boulesteix, Y.P. Georgelin, A&A 151, 144 (1985)
- S.E. Meidt, E. Schinnerer, S. García-Burillo et al., ApJ 779, 45 (2013)
- G.G.C. Palumbo, G. Tanzella-Nitti, G. Vettolani, Catalogue of radial velocities of galaxies (1983)
- W.D. Pence, K. Taylor, K.C. Freeman, G. de Vaucouleurs, P. Atherton, ApJ 326, 564 (1988)
- M. Persic, P. Salucci, ApJ 368, 60 (1991)

References 99

C.J. Peterson, N. Thonnard, V.C. Rubin, W.K. Ford Jr, ApJ 219, 31 (1978)

A.H. Rots, A. Bosma, J.M. van der Hulst, E. Athanassoula, P.C. Crane, AJ 100, 387 (1990)

H. Salo, E. Laurikainen, R. Buta, J.H. Knapen, ApJ 715, L56 (2010)

H. Salo, E. Laurikainen, J. Laine et al., ApJS 219, 4 (2015)

R. Sancisi, R.J. Allen, W.T. Sullivan III, A&A 78, 217 (1979)

M.S. Seigar, P.A. James, MNRAS **337**, 1113 (2002)

J.A. Sellwood, R.Z. Sánchez, MNRAS 404, 1733 (2010)

R. Shetty, S.N. Vogel, E.C. Ostriker, P.J. Teuben, ApJ 665, 1138 (2007)

K. Spekkens, J.A. Sellwood, ApJ 664, 204 (2007)

D. Tamburro, H.-W. Rix, F. Walter et al., AJ 136, 2872 (2008)

P.C. van der Kruit, A&A 49, 161 (1976)

H.C.D. Visser, A&A 88, 159 (1980)

A. Zurita, M. Relaño, J.E. Beckman, J.H. Knapen, A&A 413, 73 (2004)

Chapter 6 Inner Rotation Curves

6.1 Introduction

Rotation curves of spiral galaxies have been widely used to study the distribution of mass within galaxies. They provide information about the dynamics, evolution and formation of spiral galaxies.

Rotation curves have been extensively used in the literature as tracers of the distribution of mass in spiral galaxies. In particular, HI rotation curves extend to much larger radii than optical data, where dark matter (DM) is supposed to dominate the gravitational potential (Rogstad and Shostak 1972; Roberts and Whitehurst 1975; Bosma 1978, 1981). The relationship between the shape and amplitude of the rotation curve and the mass distribution is therefore more important and directly linked where baryonic mass is dynamically significant. On the contrary, if DM dominates the potential, this relationship between the main mass components and the shape of the rotation curve will be weaken. The flat part in the HI rotation curves was one of the first pieces of evidence for the presence of DM in galaxies (Bosma 1981; van Albada 1985; van Albada and Sancisi 1986; Begeman 1987). Therefore, the link between the shape of the rotation curve and the amount of luminous and DM provide important information about the formation and evolution of galaxies.

Several studies of the relationships between the shape of the rotation curve and the properties of individual galaxies have been carried out. Burstein and Rubin (1985) and Rubin et al. (1985) defended that the mass distribution did not depend on morphological type, luminosity, mass, bulge-to-disc ratio or other global properties of the galaxies, suggesting that the form of the gravitational potential is not correlated with the light distribution. Persic and Salucci (1991) and Persic et al. (1996) presented the idea of a universal rotation curve that only depends on the total luminosity of a galaxy.

In contrast, there are other studies which defend that the total luminosity of the galaxy is not the only component that influences on the shape of the rotation curve. Corradi and Capaccioli (1990) found that early-type galaxies with large bulges have

rotation curves that rise more rapidly in the central parts than galaxies with similar total luminosity but less or no bulge. Casertano and Gorkom (1991) showed that the shape of the outer part of the rotation curve depends on both the total luminosity and also the light distribution. Broeils (1992), Verheijen (1997), Swaters (1999), Verheijen (2001), Matthews and Gallagher (2002), Swaters et al. (2003) and Sancisi (2004), among others, also defended the importance of including other galaxy parameters that determine the rotation curve shape.

The shape of the rotation curve is the footprint of the dynamical evolution of a galaxy. In this sense, if the shape of the rotation curve does not correlate with the light distribution within the galaxy (Burstein and Rubin 1985; Rubin et al. 1985), the luminous matter plays a minor dynamical role, while DM dominates everywhere. If, on the contrary, the total luminosity is not the only parameter that determines the shape of the rotation curve, and other properties such as morphological type, surface brightness or presence of a bulge determine the shape of the rotation curve, the baryonic matter should contribute significantly to the gravitational potential.

There has recently been an important development in understanding the DM distribution inside galaxies, in part motivated by the difficulties of Cold Dark Matter (CDM) theory with regard to the DM profile in the central part of galaxies, the socalled *cusp vs core* problem. On the one hand, models based on the CDM scenario form galaxies using a universal DM density profile resulting in concentrated stellar bulges and a steep (cuspy) DM profile in the centre (e.g.; Barnes and Hernquist 1996; Moore et al. 1999; van den Bosch et al. 2001; Abadi et al. 2003; Governato et al. 2007). But on the other hand, observations of dwarf galaxies show that the rotation curves in the central parts rise almost linearly, interpreted as a sign of a shallow (cored) DM central profile (e.g.; Moore 1994; Salucci and Burkert 2000; de Blok et al. 2001, 2008; Swaters et al. 2003; Simon et al. 2005; Kuzio de Naray et al. 2008, 2009; Oh et al. 2011; Walker and Peñarrubia 2011). The cusp vs core problem has recently been addressed by many authors, creating simulations in which baryons erase the cuspy dark matter profile (Macciò et al., 2012), and developing simulations of bulgeless dwarf galaxies that present a shallower central DM distribution, which matches better with the measured rotation curves (e.g., Governato et al. 2010, 2012; Di Cintio et al. 2014a, b).

Several studies of HI rotation curves have analysed the shape of the rotation curve (e.g., de Blok et al. 1996; Swaters 1999; Côté et al. 2000; Verheijen 2001; Gentile et al. 2004; Noordermeer et al. 2007; Swaters et al. 2009, 2011, 2012), including all types of morphologies, luminosities (both high- and low-surface brightness galaxies) and galaxy properties. Nevertheless, few studies have performed a quantitative study of the shape of the rotation curve. Concretely, Swaters et al. (2009) parametrise the shape of the rotation curve with the logarithmic slope $S = \Delta \log v/\Delta \log R$, finding correlations for the logarithmic slope with the surface brightness and light distribution. They conclude that for both spiral and late-type dwarf galaxies, the correlation between the light distribution and the inner rotation curve shape suggests that galaxies with higher central light concentration also have higher central mass densities, which implies that the luminous mass dominates over the DM mass in the gravitational potential in the central regions.

6.1 Introduction 103

One of the most recent quantitative studies of the slopes of rotation curves was presented by Lelli et al. (2013, LFV13 hereafter). They found a scaling relation between the circular velocity gradient $d_RV(0)$ (what we refer to as slope of the circular velocity curve) and the central surface brightness μ_0 over more than two orders of magnitude in $d_RV(0)$ and four orders of magnitudes in μ_0 . This scaling relation for disc galaxies show a clear relationship between the central stellar density of a galaxy and the inner shape of the potential well, also for low-surface brightness galaxies where DM is supposed to dominate in the central regions.

Several systematic effects can change the shape of the rotation curve. In the first place, the most important is low angular resolution, which smooths the shape of the rotation curve, and can lead to an underestimation of the slope of the inner part of the rotation curve. Secondly, the velocities in the inner parts of high-inclined galaxies are underestimated (e.g., Sancisi et al. 1979; Swaters et al. 2003). In the third place, some methods to derive the velocity fields (such as adopting the intensity-weighted mean velocity of a profile) also underestimate the rotation curve (e.g., Bosma 1978; Swaters and Balcells 2002; de Blok et al. 2008). As a consequence, higher angular resolution data have been used in order to obtain detailed information on the shape of the rotation curves, especially in the innermost regions.

 $H\alpha$ observations using Fabry-Perot (FP) instruments have been used for some 40 years now (e.g., Tully 1974; Deharveng and Pellet 1975; Dubout et al. 1976 or de Vaucouleurs and Pence 1980), and have been employed to create high signal-to-noise ratio (S/N) rotation curves for many spiral galaxies (Marcelin et al. 1985; Bonnarel et al. 1988; Pence et al. 1990; Corradi and Capaccioli 1991; Amram et al. 1992; Cecil et al. 1992; Amram et al. 1994; Sicotte et al. 1996; Ryder et al. 1998; Jiménez-Vicente et al. 1999, and many more). With the purpose of obtaining the highest angular resolution possible for our sample of nearby galaxies, I have used H α FP data from the observational survey described in detail in Chap. 3 and introduced in Chap. 4. These data have very high angular (seeing limited, $\sim 1''$) and spectral $(\sim 8 \,\mathrm{km \, s^{-1}})$ resolution, higher than data from other FP studies such as those from the Virgo survey (Chemin et al. 2006) or the GHASP survey (see Epinat et al. 2008 for a complete description of the sample and data), or any other HI data (e.g., THINGS is one of the HI surveys with the highest angular resolution, of $\sim 6''$, Walter et al. 2008). The Plateau de Bure Interferometer Arcsecond Whirlpool Survey (PAWS; Schinnerer et al. 2013) is the first survey that targets molecular gas data combining high spatial resolution (\sim 1") with a wide enough field of view (FOV) (270" \times 170" in the inner disc of M51), but is so far limited to one galaxy. In a few of the HI studies mentioned before, either optical longslit data or beam smearing corrections have been used to overcome the low angular resolution in the central parts of the HI velocity fields (e.g., Noordermeer et al. 2005; LFV13), but 2D velocity fields provide full information about the central parts, not limited to the slit position.

This chapter is organised as follows: Sect. 6.2 gives a description of the sample selection, the observations and the data reduction. This section also describes the specialised data analysis. The derived results are presented in Sect. 6.3 and discussed in Sect. 6.4.

6.2 The Data

6.2.1 Sample, Observations and Data Reduction

The sample is explained in Chap. 3 and consists of 29 galaxies spread in morphological type and other characteristics such as bar presence. All these galaxies are part of the S^4G sample (Sheth et al. 2010). Information about the sample galaxies studied here can be found in Table 3.1.

The kinematic data have been obtained with the $GH\alpha FaS$ instrument mounted on the William Herschel Telescope (WHT) in La Palma. The velocity maps and derived rotation curves have been presented in Chap. 3. In that paper, the reader can find all the details about the observations and reduction processes that have been carried out. In this study, I will use the first and second-moment maps derived from the $GH\alpha FaS$ kinematic cubes (the velocity and velocity dispersion maps).

The FP data were observed along with H α narrow-band images observed using the Auxiliary port CAMera (ACAM) also at the WHT. The H α narrow-band images have two aims. Firstly, the kinematic cubes need to be flux calibrated, and the narrow-band images allow us to flux-calibrate the intensity maps from the GH α FaS cubes as explained in Chaps. 3 and 4. Secondly, we can compute star formation rates (SFRs) derived from the measured fluxes in these narrow-band images.

Furthermore, this study benefits from the products of the advanced data analysis of the S⁴G mid-IR images. The S⁴G survey has brought 3.6 and 4.5 μ m images of more than 2350 galaxies to the scientific community. I refer to Sheth et al. (2010) for a complete description of the survey goals and S⁴G sample selection. All the images have been processed using the S⁴G pipeline, and I use the products from these for our 29 galaxies (presented in Table 6.1): (i) results from the surface photometry (central surface brightness μ_0 , total stellar mass M_* from the 3.6 and 4.5 μ m absolute magnitudes and the calibration in Eskew et al. 2012, central light concentration index), from Muñoz-Mateos et al. in preparation; (ii) Bulge-total ratios (B/T) derived from the 2D structural decompositions (Salo et al. in preparation); (iii) bar torques Q_b and bar lengths from Díaz-García et al. and Herrera-Endoqui et al. (in preparation) (for the Q_b values, see Chap. 5, for a description of the method, see Salo et al. 2010 and Laurikainen and Salo 2002); and (iv) the stellar mass maps (Querejeta et al. 2015). In addition, I use the mid-IR morphological classifications and T-types from Buta et al. (2015).

6.2.2 Ha Luminosities and Star Formation Rates

The H α line is a tracer of recent massive star formation. Therefore, we can deduce the SFRs from calibrated H α narrow-band images, by measuring the H α luminosity ($L_{\text{H}\alpha}$) and following Eqs. 4.1 and 4.2. There are several uncertainties to consider when accounting for the errors in the measurements of the SFR: basic reduction

Table 6.1 General properties of the galaxies in the sample

Galaxy name	$\langle T \rangle (1)$	μ_0 (mag arcsec ⁻²) (2)	<i>Q</i> _b (3)	Bar length (kpc) (4)	<i>B/T</i> (5)	$\log(M_*)$ $(M_{\odot}) (6)$	f _* (7)
NGC 428	8.0	20.4 ± 0.2	0.29 ± 0.03	2.41	0.002	9.759	0.16
NGC 691	2.0	17.6 ± 0.7	0.00 ± 0.00	0.00	0.144	10.754	0.22
NGC 864	4.0	18.0 ± 0.5	0.47 ± 0.07	3.85	0.029	10.184	0.10
NGC 918	6.0	19.6 ± 0.4	0.23 ± 0.02	0.85	0.008	10.109	0.14
NGC 1073	5.5	19.4 ± 0.6	0.63 ± 0.08	4.14	0.000	9.972	0.53
NGC 2500	6.5	20.4 ± 0.3	0.28 ± 0.03	1.56	0.002	9.42	0.28
NGC 2541	7.5	21.0 ± 0.4	0.00 ± 0.00	0.00	0.000	9.443	0.17
NGC 2543	3.0	16.1 ± 0.8	0.35 ± 0.08	5.67	0.166	10.423	0.15
NGC 2712	2.5	16.0 ± 0.8	0.28 ± 0.05	4.00	0.170	10.43	0.27
NGC 2748	4.0	18.2 ± 0.5	0.45 ± 0.03	1.66	0.035	10.31	0.33
NGC 2805	5.0	19.7 ± 0.6	0.19 ± 0.01	2.13	0.002	10.392	0.66
NGC 3041	3.5	18.7 ± 0.3	0.00 ± 0.00	0.00	0.041	10.437	0.29
NGC 3403	5.0	19.4 ± 0.6	0.00 ± 0.00	0.00	0.000	10.14	0.23
NGC 3423	4.5	19.1 ± 0.5	0.00 ± 0.00	0.00	0.052	9.706	0.13
NGC 3504	1.0	14.5 ± 1.4	0.25 ± 0.06	4.59	0.372	10.404	0.30
NGC 4151	0.0	15.8 ± 1.1	0.09 ± 0.02	6.38	0.441	9.775	0.09
NGC 4324	-1.0	15.8 ± 0.9	0.00 ± 0.00	0.00	0.291	10.71	1.23
NGC 4389	1.0	18.3 ± 0.4	0.52 ± 0.06	2.81	0.000	9.844	0.28
NGC 4498	7.0	19.6 ± 0.4	0.46 ± 0.07	2.26	0.000	9.741	0.22
NGC 4639	2.0	16.4 ± 0.7	0.26 ± 0.04	2.09	0.114	10.317	0.28
NGC 5112	6.5	20.1 ± 0.4	0.62 ± 0.06	1.66	0.000	10.115	0.33
NGC 5334	6.0	20.4 ± 0.3	0.49 ± 0.08	2.36	0.001	10.409	0.27
NGC 5678	3.0	17.5 ± 0.4	0.00 ± 0.00	0.00	0.037	10.755	0.16
NGC 5740	2.0	16.0 ± 0.7	0.16 ± 0.03	3.05	0.128	10.456	0.33
NGC 5921	3.0	16.2 ± 1.0	0.34 ± 0.06	6.57	0.118	10.411	0.37
NGC 6070	5.0	17.9 ± 0.5	0.00 ± 0.00	0.00	0.045	10.725	0.18
NGC 6207	6.5	19.2 ± 0.2	0.21 ± 0.02	2.75	0.000	10.082	0.32
NGC 6412	6.0	18.8 ± 0.5	0.24 ± 0.02	1.08	0.005	10.117	0.21
NGC 7241	5.5	18.5 ± 0.4	0.00 ± 0.00	0.00	0.000	10.263	0.34

Notes (1) Mean T-types from the two independent morphological classifications in Buta et al. (2015). (2) Central surface brightness obtained following the procedure by LFV13 and measured from the light profiles derived with ellipse fitting to the $3.6\,\mu\mathrm{m}$ images (Muñoz-Mateos et al. in preparation). (3) Bar strengths derived from the torque maps obtained from the $3.6\,\mu\mathrm{m}$ images (Díaz-García et al. in preparation). (4) Bar lengths measured from the torque maps (Díaz-García et al. in preparation) The bar lengths are deprojected units, measured using the method explained in Salo et al. (2010), except when the fits do not have trustworthy quality, in which the bar lengths are measured visually [Herrera-Endoqui et al. (in preparation)]. (5) B/T ratios from the structural 2D decompositions to the $3.6\,\mu\mathrm{m}$ images (Salo et al. 2015). (6) Total stellar masses derived using the absolute magnitudes at 3.6 and $4.5\,\mu\mathrm{m}$ (from the ellipse fitting, Muñoz-Mateos et al. in preparation), and the calibration of Eskew et al. (2012). (7) Stellar mass fraction f_{\star} , defined as the ratio between the stellar mass and the total dynamical mass $M_{\rm dyn} = v_{\rm c}^2 r/G$ (see Sect. 6.4)

processes (i.e., flat-fielding correction, around 2%), the zero-point calibration (3%, in agreement with the value of 2% typical for photometric nights), uncertainty in the flux measurement (1%) and continuum-subtraction process (around 11%). Taking all these into account (without considering the uncertainties in the adopted value for the distance), I estimate an uncertainty of 17%, similar to previous studies (James et al. 2004: 14%, Kennicutt et al. 2008: 16%, Sánchez-Gallego et al. 2012: 18%, Chap. 2: 20% including internal dust extinction).

I have measured $L_{\text{H}\alpha}$ (and therefore the SFRs) in several regions: inner 0.5, 1.0, 1.5, 2.0 kpc, inside R_{90} (see Sect. 6.2.5) and across the whole galaxy.

6.2.3 Rotation Curves Derived from the Stellar Mass Maps

To understand the mass distribution, we have modelled the circular velocity from the observed photometric data. In particular, the starting point are the stellar mass maps that have been derived from the 3.6 and 4.5 μ m images by Querejeta et al. (2015), using the method explained in Meidt et al. (2012). The radial force map obtained to compute the bar strength following the method of Salo et al. (2010) is used to compute the circular velocity as

$$v_*^2 = r \frac{\partial \Phi}{\partial r} = r F_r. \tag{6.1}$$

Here I will refer to the circular velocity derived from the stellar mass maps as v_* , although it is also a circular velocity, leaving the notation v_c to the circular velocity derived from the FP kinematic data. Three different disc scale heights (h_z) have been used to compute the potential: $h_z = 0.05 \, \mathrm{R}_{K20}$, $h_z = 0.1 \, \mathrm{R}_{K20}$ and $h_z = 0.2 \, \mathrm{R}_{K20}$. The value of $h_z = 0.1 \, \mathrm{R}_{K20}$ is statistically the closest to reality, based on the observations of edge-on galaxies carried out by de Grijs and Peletier (1997) and the study of Speltincx et al. (2008). The other two disc thickness values give a margin of errors in our method and account also for the impact of the DM halo on the Q_b estimation.

I present in Fig. 6.1 the circular velocity curves derived from the uncorrected $3.6\,\mu m$ images and from the stellar mass maps (hereafter stellar mass-derived rotation curves) for one of the galaxies of our sample: NGC 4639. We see the importance of the scale height assumption in these velocity curves. Also, we see the difference between using the stellar mass maps and using the $3.6\,\mu m$ images. The non-stellar emission present in the raw $3.6\,\mu m$ images is traduced into an overestimate of the circular velocity. Although the shape of the rotation curve does not dramatically change, we see that several features change (e.g., the inner slope changes as well as the maximum rotational velocity). Therefore, importantly, for this study I use the circular velocity curves derived from the stellar mass maps.

6.2 The Data 107

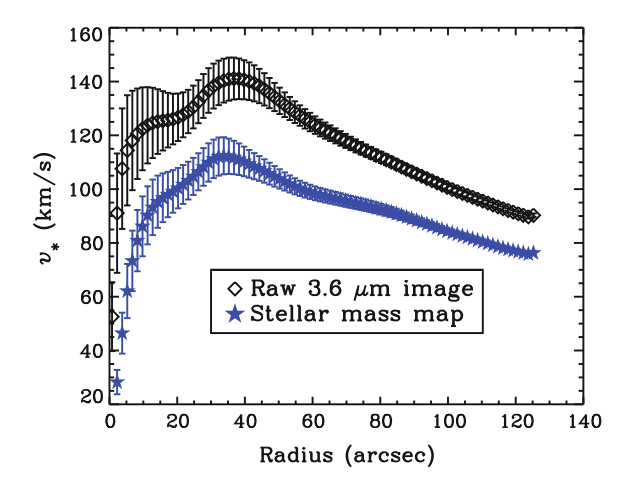


Fig. 6.1 Circular velocity curves derived from the uncorrected $3.6\,\mu\mathrm{m}$ image (diamonds), and from the stellar mass map (blue stars) for NGC 4639, assuming a scale height of $h_z = 0.1~\mathrm{R}_{K20}$. The uncertainties indicate the difference between assuming a scale height of $h_z = 0.05~\mathrm{R}_{K20}$ and $h_z = 0.2~\mathrm{R}_{K20}$. The non-stellar emission in the $3.6\,\mu\mathrm{m}$ images significantly overestimates the derived circular velocity

6.2.4 Asymmetric Drift Correction

The high angular resolution of $GH\alpha$ FaS allows us to derive a high-resolution rotation curve (\sim 1" sampling). We use the ROTCUR task in GIPSY, based on the tilted-ring method explained in Begeman (1989). All the details of the computation of the rotation curves can be found in Chap. 3.

The gravitational interactions caused by virial motions of the gas under a gravitational potential lower the observed velocity, and therefore we need to correct our observed velocity for this loss with the so-called asymmetric drift correction (ADC, see, e.g., Sect. 4.8.2 of Binney and Tremaine 2008). The gravitational interactions also show up in the velocity dispersion, and whenever this dispersion is significant, the ADC is not negligible. In such case, we need to measure the velocity dispersion and compute the true circular velocity including an ADC.

The circular velocity can be expressed as $v_c^2 = R(\partial \Phi/\partial R)$, and following Eq. 4-227 of Binney and Tremaine (2008):

$$v_{\rm c}^2 = v_{\phi}^2 + \overline{v_{\phi}^2} - \overline{v_{R}^2} - \frac{R}{v} \frac{\partial (v \overline{v_{R}^2})}{\partial R} - R \frac{\partial (\overline{v_{R}} \overline{v_{z}})}{\partial z}.$$
 (6.2)

If we neglect the $v_R v_z$ term by assuming relaxed objects, $\overline{v_\phi^2} = \sigma_\phi^2$, $\overline{v_R^2} = \sigma_R^2$ and we assume an exponential distribution of the density $v = v_0 e^{-R/R_{\rm exp}}$, we obtain:

$$v_{\rm c}^2 = v_{\phi}^2 + \sigma_{\phi}^2 \left[2 \left(\frac{R}{R_{\rm exp}} - \frac{\partial \ln \sigma_r^2}{\partial \ln R} \right) + 1 - \frac{\sigma_r^2}{\sigma_{\phi}^2} \right],\tag{6.3}$$

where v_{ϕ} is the deprojected rotation velocity (from the rotation curve), and σ_{ϕ} is the azimuthal velocity dispersion. We see that no change of the radial velocity dispersion is found along the radius (so $\partial \ln \sigma_r^2/\partial \ln R \approx 0$). If we define $\beta = \sigma_{\phi}^2/\sigma_R^2$, we arrive at the expression:

$$v_{\rm c}^2 = v_{\phi}^2 + \sigma_{\phi}^2 \left(2\frac{R}{R_{\rm exp}} + 1 - \frac{1}{\beta} \right).$$
 (6.4)

For a flat rotation curve $\beta=0.5$, whereas for a solid-body rotation $\beta=1$. Therefore, as we have both features in our galaxies, I have defined $1.0 > \beta > 0.5$, starting in the centre where $\beta=1$, decreasing with radius until the rotation curve is flat, where $\beta=0.5$. The observed velocity dispersion in the ionised gas results from three different phenomena: gravitational interaction between particles, thermal broadening and turbulent motions. The only effect that slows down the velocity is the gravitational interaction, and therefore we need to identify the other contributions and subtract them from the observed velocity dispersion. The thermal component is due to the thermal energy of the molecules in the HII regions, which amounts to $\sigma_{\text{thermal}} \approx 9\,\text{km}\,\text{s}^{-1}$ for electron temperatures of $10^4\,\text{K}$. Here, we also need to subtract the natural broadening of the line ($\sigma_{\text{N}} \approx 3\,\text{km}\,\text{s}^{-1}$), using

$$\sigma_{\text{obs}}^2 = \sigma_{\text{grav}}^2 + \sigma_{\text{thermal}}^2 + \sigma_{\text{turb}}^2 + \sigma_{\text{N}}^2. \tag{6.5}$$

Without information about the stellar kinematics (where there is no turbulent component), it is not possible to identify which fraction of σ is due to the gravitational or turbulent components. I have assumed that $\sigma_{turb} \approx 90 \% \sigma_{obs}$ in the central regions, until a constant σ is reached (Weijmans et al. 2008; Kalinova et al. in preparation). As an estimate of the uncertainty in our determination of σ_{grav} , I incorporate the difference between assuming $\sigma_{turb} \approx 90 \% \sigma_{obs}$ and $\sigma_{grav} = 0$.

The resulting circular velocity curves are therefore corrected for the slowdown caused by the velocity dispersion. I have implemented the ADC on our rotation curves and thus obtained the circular velocity curves. By definition, this correction is more significant in galaxies with higher σ . Also, in Eq. 6.4 we see that the higher the scalelength ($R_{\rm exp}$), the lower the correction. Therefore, the ADC is negligible in the central regions of some of the galaxies of our sample, like the extreme case of NGC 3041, where the resulting $v_{\rm c}$ curves are very similar to those inner regions in the rotation curves of most of the galaxies in our sample (Fig. 6.2). On the contrary, we see in Fig. 6.3 the other extreme case, NGC 4389, where the velocity dispersion is significant and the ADC is very important in the central parts of the rotation curve. In Appendix D, I present the rotation curves and the ADC-corrected (circular) velocity curves for all the galaxies of our sample. In general, the ADC is negligible for the inner parts of most of the galaxies of our sample, but gains importance at larger radii.

6.2 The Data 109

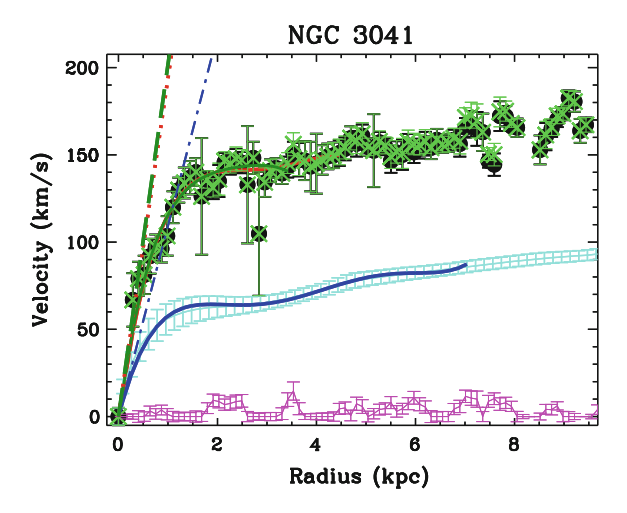
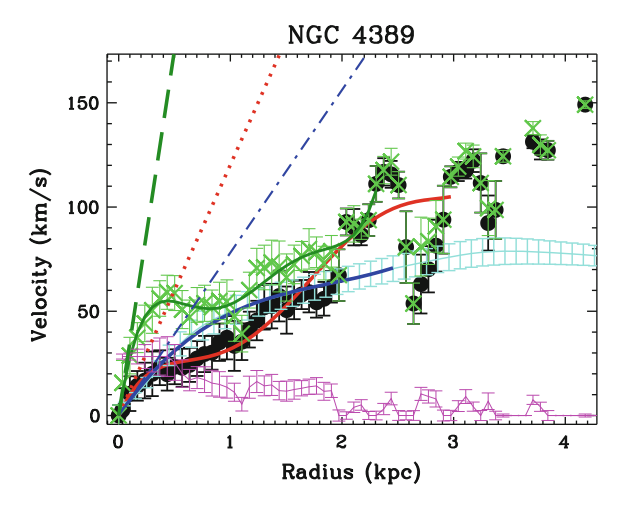


Fig. 6.2 High resolution (1") rotation curves for NGC 3041 derived from the FP data (circles), from the stellar mass maps (solid line with errormarks), and after the ADC (circular velocity, green crosses). Overlaid, the polynomial fitted to the observed curve. The slope of the curve has been highlighted with a dotted line for the FP data, with a dot-dash-dot line for the mass rotation curve and with a dashed line for the circular velocity curve. The lower pink line corresponds to the σ_{ϕ} . Note The polynomial is fitted to the points with radius below R_{90} . The ADC is not important in this galaxy, and the circular velocity curve is very similar to the observed rotation curve

Fig. 6.3 As Fig. 6.2, now for NGC 4389, where the ADC is not negligible in the inner part of the galaxy



6.2.5 Determination of the Rotation Curve Slopes

The motivation of this chapter is to study the inner part of the rotation curve. To characterise this, I proceed as LFV13 by measuring the slope of the curve, hereafter $d_RV(0)$. The method consists of fitting a polynomial function with the form

 $V(R) = \sum_{n=1}^{m} a_n \times R^n$ to the inner part of the circular velocity curve (up to the radius where the curve reaches 90% of the maximum velocity, R_{90}). The slope of the inner part is the term of the first order $a_1 = d_R V(0) = \lim_{R \to 0} dV/dR$, where the fit is forced to pass through R = 0 and V = 0. The extrapolated central surface brightness μ_0 is measured with a linear extrapolation of the surface brightness profile in the inner few arcseconds to R = 0. I refer the reader to LFV13 for more details about the method.

I have measured the slope of the observed rotation curves $d_R v_{rot}(0)$, of the circular rotation curves for the FP data $d_R v_c(0)$ and of the stellar mass-derived rotation curves $d_R v_*(0)$. In Fig. 6.2, we see the resulting fits for the observed, circular and mass rotation curves for our example galaxy NGC 3041, and the corresponding determination of the slopes, represented as the tangent line to the rotation curve at R = 0 kpc. In Fig. 6.3 we see the same fits for NGC 4639, and now we clearly see the differences between v_{rot} and v_c , due to the significant amount of σ_{grav} and ADC in the central parts. Again, the rotation curves and fits for all the galaxies of the sample are presented in the Appendix D.

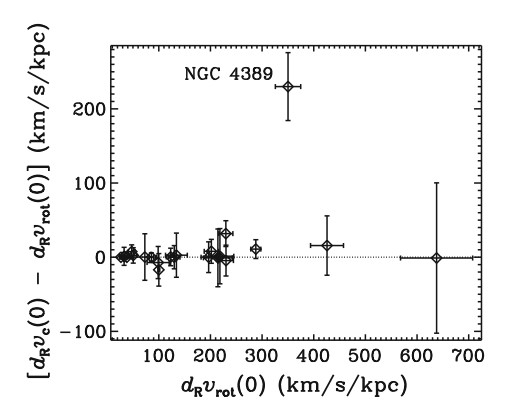
From our FP data, we have measured the slope in the circular velocity curve in all the galaxies of the sample. The central regions of the galaxies NGC 4151, NGC 4324, NGC 4639, NGC 5740 and NGC 5921 are not sampled. These galaxies are mostly early-type barred galaxies. I have analysed those data equally as in the other galaxies in the sample in order to obtain lower limit values of $d_R v_{rot}(0)$ and $d_R v_c(0)$, which are highlighted in the forthcoming correlations with red arrows. For completeness, I have computed the observed slope that LFV13 predict, from the μ_0 , for these lower limits, and these values are presented with red crosses in the forthcoming plots. The differences between the observed slopes and those predicted by Lelli's equation can be up to 30 % of $\log(d_R V(0))$, which means that the error in the predicted $d_R V(0)$ increases logarithmically as μ_0 increases in absolute value. NGC 4151 is a Seyfert 1.0 (Ho et al. 1997), and the central surface brightness yields an overestimate of $d_R V(0)$. We therefore estimate μ_0 as a linear extrapolation of the surface brightness profile to the centre, resulting in $d_R V(0) = 630 \,\mathrm{km \, s^{-1}}$, very similar to what would correspond to its morphological type (613 km s⁻¹, see Sect. 6.3.1). The H_I rotation curves of NGC 4151 in Bosma et al. (1977) and Bosma (1981) cannot provide further information in the central parts, as beyond their first measured point at 1 arcmin, the velocity curve is flat with a $v \sim 150 \, \mathrm{km \, s^{-1}}$.

6.3 Results

In the first place, I am going to present the relationships between the slopes measured using different velocity curves: $d_R v_{\rm rot}(0)$ derived from the rotation curves, $d_R v_{\rm c}(0)$ computed from the circular velocity curves after ADC correction, and $d_R v_*(0)$ as derived from the stellar mass-maps.

6.3 Results

Fig. 6.4 Comparison between the slopes derived from the FP rotation curve and those derived from the circular velocity. There are few differences except for NGC 4389, where a very high velocity dispersion in the centre, in combination with a low scalelength compared to the radius, produces a large ADC



We see in the rotation curves (figures of the Appendix D) that there are very few galaxies in which ADC is important in the central parts and therefore $d_R v_{\rm rot}(0) \neq d_R v_{\rm c}(0)$: NGC 864, NGC 2712, NGC 2748 and NGC 4389. In addition, in the cases of NGC 4498, although $R/R_{\rm exp}$ may be low in the central parts, it increases with R until the ADC is significant, changing the maximum velocity and therefore R_{90} and $d_R v_{\rm c}(0)$; and here $d_R v_{\rm rot}(0) \neq d_R v_{\rm c}(0)$ too. In the remaining galaxies of the sample, either the dispersion in the centre is very low (e.g., NGC 428, NGC 691 or NGC 3041) or the scalelength is very high compared with the radius (e.g., NGC 3043, NGC 5678 or NGC 6207). In those cases, the ADC is not important ($v_{rot} \approx v_{\rm c}$ in the central parts) and $d_R v_{\rm rot}(0) \approx d_R v_{\rm c}(0)$. In Fig. 6.4, I compare $d_R v_{\rm rot}(0)$ and $d_R v_{\rm c}(0)$. We see that the highest discrepancy is found in NGC 4389, where the ADC in the central part is most significant.

I now study the relationship between $d_R v_c(0)$ and $d_R v_*(0)$. To investigate what is causing the circular velocity curves to differ from the mass derived rotation curves, I plot $d_R v_c(0)$ as a function of $d_R v_*(0)$ in Fig. 6.5.

The circular velocity of the galaxy is defined from the gravitational potential, which takes into account the total mass of the galaxy. Therefore, we expect all the components that have mass to influence the gravitational potential of the galaxy, and therefore the derived circular velocity:

$$v_c^2 = v_{\text{gas}}^2 + v_*^2 + v_{\text{DM}}^2 \tag{6.6}$$

Taking this into account, we expect to find that $v_c^2 > v_*^2$. Therefore, as v_c is the sum of its components, v_* cannot be higher and therefore $d_R v_c(0) > d_R v_*(0)$. In Fig. 6.5, we see that the cases where $d_R v_c(0) < d_R v_*(0)$ are marked with arrows, indicating that they are lower limits and $d_R v_c(0)$ is probably larger than $d_R v_*(0)$ in all the cases. The only cases where $v_{c,\text{max}} \leq v_{*,\text{max}}$ are the starburst NGC 3504 and the AGN NGC 4151. Also, the only case where I find that $d_R v_c(0) < d_R v_*(0)$ is the predicted value for NGC 4151. Due to the fact that these galaxies have an excess of light in their centres, the rotation curve derived from the stellar mass may have

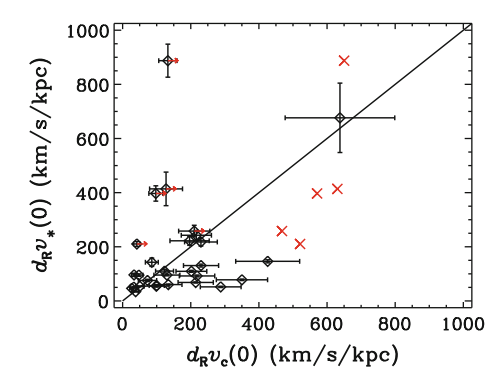


Fig. 6.5 Comparison between the slopes derived from v_c and those from the stellar mass-derived rotation curves. The *red arrows* indicate that those values are lower limits to the slopes, corresponding to the galaxies with bad sampling in their central parts. We see that $d_R v_c(0) \ge d_R v_*(0)$ except for the lower limits. For those cases, I have computed the predicted value of the slope given by the scaling relation presented in LFV13, which I represent with *red crosses* (color online)

been increased when we assume a single stellar M/L throughout all the galaxy. In other words, the excess light coming from the bright nucleus may have increased the derived stellar velocity curve, and therefore $d_R v_*(0)$.

6.3.1 Rotation Curve Slopes and Physical Properties of Galaxies

Relationship with central surface brightness and T-type

The aim of this study is to find possible relationships between the dynamics in the central parts of galaxies (by studying the slope of the rotation curve) and the formation, evolution and characteristics of those galaxies. First of all, I study the clearest scaling relation between the slopes of the rotation curve and one feature of the galaxy, the one presented in LFV13. They find that $d_RV(0)$ correlates with the extrapolated central surface brightness of the galaxies (μ_0), implying that regardless of the formation or evolution of the galaxy, the central stellar density closely relates to the inner shape of the potential well. The scaling relation for disc galaxies found by LFV13 is found for more than two orders of magnitude in $d_RV(0)$ and four orders of magnitudes in μ_0 , which means that this correlation is valid for both low- and high-surface brightness galaxies.

I reproduce this relationship, obtaining similar results despite the fact that the mass range (and therefore μ_0) in our galaxies is more reduced. In Fig. 6.6, we see that $d_R v_c(0)$ and $d_R v_*(0)$ correlate with μ_0 , although the relation is not as tight as that of LFV13. As in the previous Section, the points with the largest deviation from the slope predicted by LFV13 are the lower limits. As in LFV13, the scatter can come from observational uncertainties on the slopes, but can also be intrinsically

6.3 Results

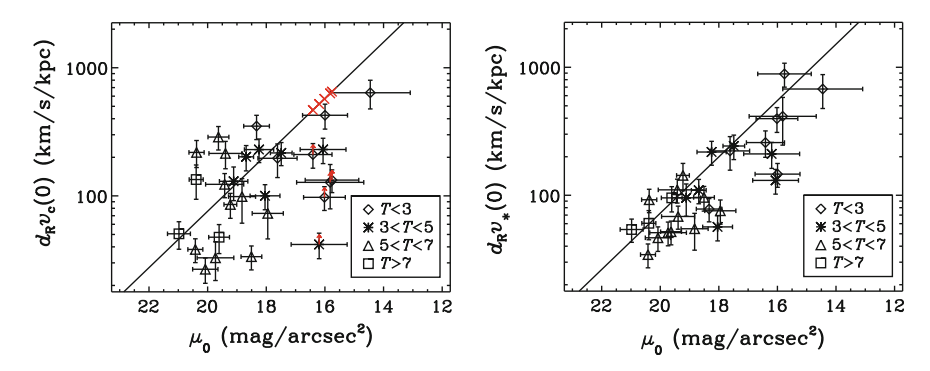


Fig. 6.6 Slopes derived from the circular velocity curves $(d_R v_c(0), left)$ and from the stellar-derived curve $(d_R v_*(0), right)$ as a function of the central surface brightness μ_0 . There is a correlation, although not as tight as that found by LFV13

linked to the determination of μ_0 (affected by the different structural components such as bars, bulges or nuclear activity). However, the fact that the scatter is higher when studying $d_R v_c(0)$ may imply that the scatter is due to observational constraints when determining $d_R v_c(0)$. The correlation with $d_R v_*(0)$ is expected, as the stellar mass maps have been derived from the photometric 3.6 μ m maps. Taking everything into account, I confirm the LFV13 scaling relation, which implies that there is a link between the stellar density and the steepness of the potential well in the centres of disc galaxies.

In the relationship between μ_0 and the slope of the rotation curve, μ_0 must be a secondary parameter, as it does not directly trace the stellar density in the centre. μ_0 correlates with the morphological T-type (Fig. 6.7), although T is not a physical quantity. One might expect to find a relation between a parameter that directly indicates the mass in the central parts and the slope of the rotation curve. Therefore, I compute the mass of the bulge (M_B) as $M_B = M_* \times B/T$, where M_* is the total stellar mass and a constant M/L is assumed. In Fig. 6.7, I represent the morphological T-type (bottom left) and μ_0 (bottom right) as a function of M_B . These plots show a clear correlation between M_B , T-type and μ_0 . In Sect. 6.3.1, I will study the relationship between the bulge and the slope of the rotation curve.

Due to the fact that there is a correlation between the morphological T-type and μ_0 , we also expect a correlation between the morphological T-type and the slope of the rotation curve (actually, following LFV13, with the logarithm of the slope). Therefore, following Eq.(8) in LFV13, if $\mu_0 \approx 0.65 * T + 15.53$ (see Fig. 6.7), we expect that $\log[d_R v_c(0)] \approx -0.14 * T$. I find (from Fig. 6.8):

$$\log[d_R v_c(0)] \approx -0.139 * T + 2.787$$
 and (6.7)

$$\log[d_R v_*(0)] \approx -0.123 * T + 2.596, \tag{6.8}$$

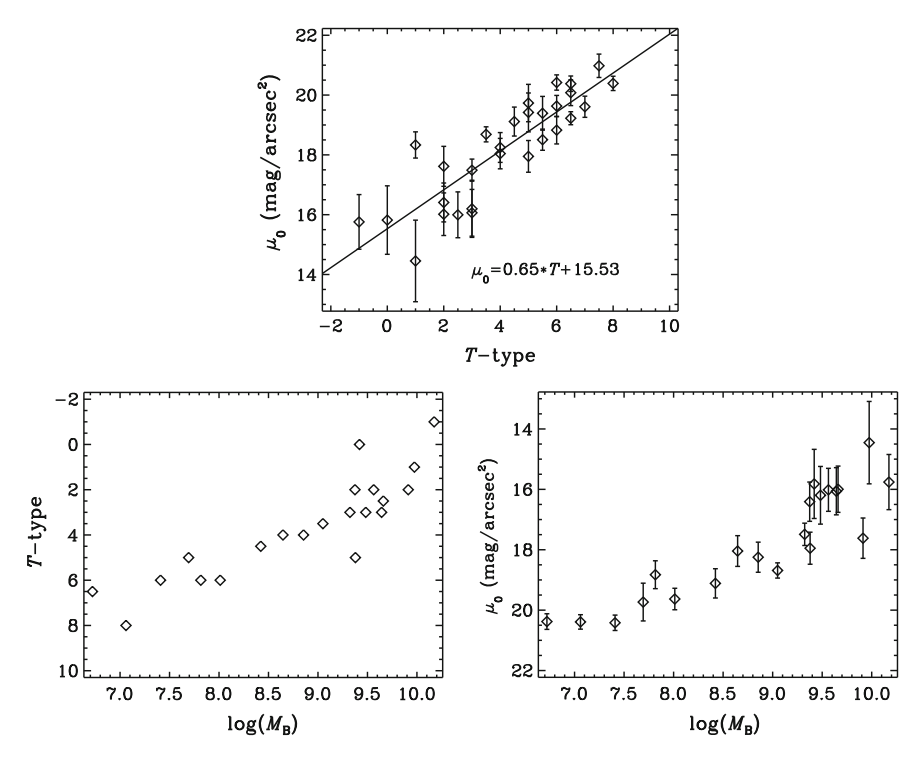


Fig. 6.7 Top Correlation between the morphological T-type and the central surface brightness. Bottom Correlations between the mass of the bulge (M_B) and the morphological T-type $(bottom\ left)$ and $\mu_0\ (bottom\ right)$. We see that these parameters are correlated among them. Note that the y-axes in the bottom panels have been inverted so that the correlations can be easily compared

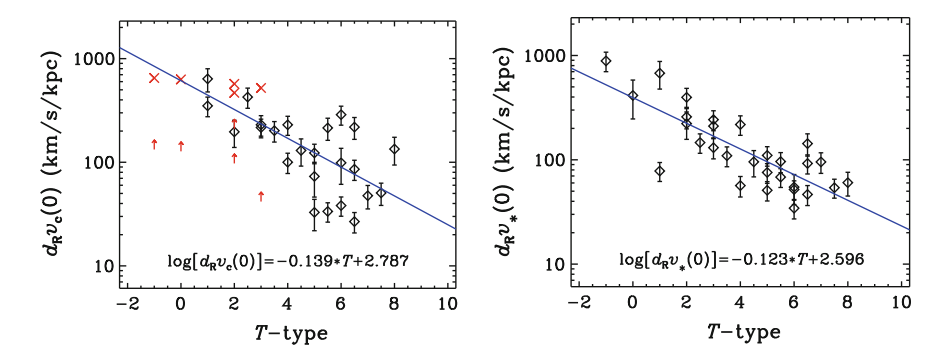


Fig. 6.8 Slopes $d_R v_c(0)$ and $d_R v_*(0)$ as a function of the morphological T-type. We expect these correlations as T-type correlates with μ_0 (Fig. 6.7), and μ_0 correlates with the logarithm of $d_R v_c(0)$ (LFV13; Fig. 2). This correlation may be useful to obtain a measurement of $d_R v_c(0)$ and $d_R v_*(0)$ where one does not have information on the central surface brightness but about the morphological T-type

6.3 Results 115

which can be understood as other scaling relations for disc galaxies. As expected, the scatter of this relationship is greater than that of LFV13, coming from both the scatter in their relationship and from the correlation between T and μ_0 . However, this relationship can also be a proxy for the computation of the slope of the inner rotation curve. Of course, the morphological type is not a measured physical quantity and is defined for galaxies with and without discs, but this relationship can be useful when one does not have information about the surface brightness and wants to estimate the slope of the rotation curve.

Relationships with stellar mass and maximum rotational velocity

In the previous Section we have seen that the extrapolated central surface brightness in the inner parts of galaxies correlates with the steepness of the inner rotation curve. We now want to know if there is also a relationship between the dynamics in the centres of galaxies and the potential in the whole galaxy. To do so, I compare the measured slopes with physical properties related with the *total* mass of a galaxy: total stellar mass M_* (which dominates the baryonic mass), and the maximum velocity. In Figs. 6.9 and 6.10 I represent $d_R v_c(0)$ and $d_R v_*(0)$ as a function of the total stellar mass (log M_*), the maximum circular velocity ($v_{c,max}$) and the maximum velocity from the stellar mass maps ($v_{*,max}$), respectively. Note that for NGC 2805, NGC 4324 and NGC 4389, $v_{c,max}$ is a lower limit as we do not see that the curve has reached a maximum or flat part.

I find no correlations, but I can identify some trends. The empty regions in the plots indicate that there are *forbidden* slopes that a certain galaxy cannot present. In this way, steeper slopes correspond to the more massive galaxies, with higher $v_{\text{rot,max}}$. Also, the total stellar mass and v_{max} limit the slope, and low mass galaxies only have slow-rising rotation curves. It is well known that the more massive a galaxy, the higher its maximum rotation velocity (Tully-Fisher relation, Tully and Fisher 1977). Here, we see that $d_R v_*(0)$ increases with $v_{*,\text{max}}$. Therefore, for the stellar component, we see a clear relationship between the mass and the dynamics of the central parts of

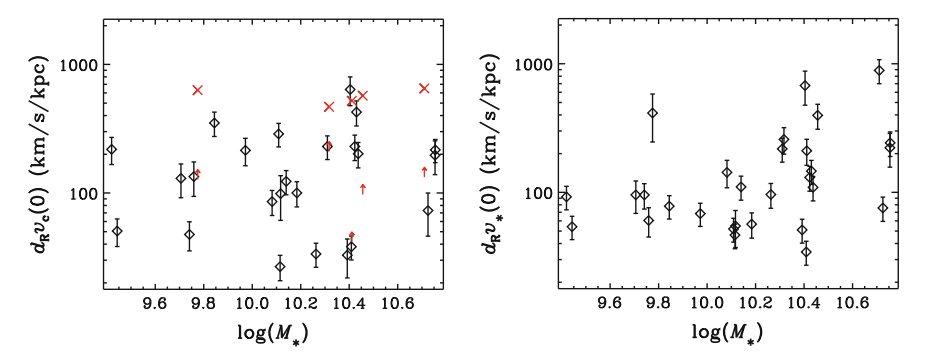


Fig. 6.9 Rotation curve slopes $d_R v_c(0)$ and $d_R v_*(0)$ as a function of the total stellar mass (log M_*). I find no correlation, but the total stellar mass limits the slope: steep slopes are found only in more massive galaxies, whereas lower mass galaxies present only low values of the slopes

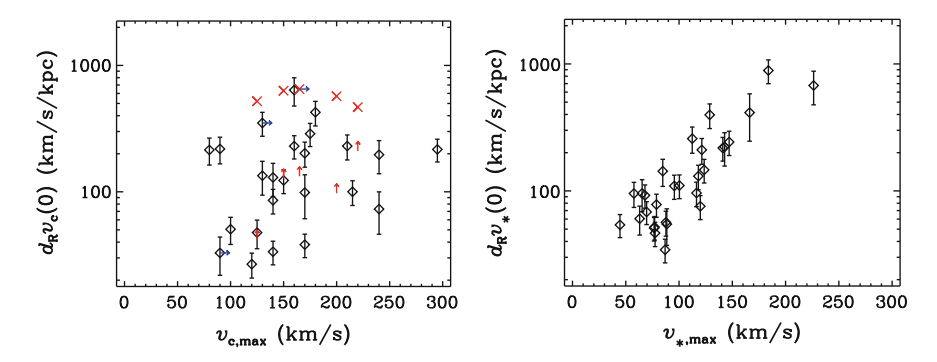


Fig. 6.10 Rotation curve slopes $d_R v_c(0)$ and $d_R v_*(0)$ as a function of the maximum circular velocity ($v_{c,max}$) and maximum velocity from the stellar-derived mass maps ($v_{*,max}$) respectively. We see no correlation between $d_R v_c(0)$ and $v_{c,max}$, but $d_R v_*(0)$ increases with $v_{*,max}$. As seen in the relationships with the total stellar mass, $v_{*,max}$ limits the slopes (steeper slopes are found for galaxies with higher $v_{*,max}$ and galaxies with low $v_{*,max}$ just have low-rising slopes). Note that for NGC 2805, NGC 4324 and NGC 4389, $v_{c,max}$ is a lower limit (marked with *blue arrow*) as we do not see that the curve has reached a maximum or flat part, but the opposite, the curve seems to keep rising

the galaxies. This relationship is less obvious in the circular velocity plot as the latter represents all the components of the galaxy, increasing the scatter of the correlation.

Relationships with bar and bulge parameters

In the previous section, we have seen that the total mass does not determine the slope of the rotation curve. Therefore, as the central surface brightness does correlate with the slope of the rotation curve, we need to investigate further the structural components of galaxies, mainly those that play a role in galaxy evolution and participate in the distribution of mass light, and thus, material within the galaxy.

I therefore explore whether the structural parameters (such as the presence of a bar or bulge) have an impact on the shape of the rotation curve, and more concretely, on its slope. If bars and bulges modify the mass distribution of a galaxy, the dynamics should be consistent with this new distribution. To study this, I represent in Figs. 6.11, 6.12, 6.13, $d_R v_c(0)$ and $d_R v_*(0)$ as a function of bar strength (as indicated by the Q_b parameter), bar length and bulge-to-total light ratio (B/T). The bar lengths are deprojected quantities, measured using the method explained in Salo et al. (2010), except when the results have flag >3 (not trustworthy), in which case the bar lengths are measured visually.

The presence of bars does not affect the rotation curve slope, as either Q_b and bar length do not correlate with $d_R v_c(0)$ or $d_R v_*(0)$ (Figs. 6.11 and 6.12). I find some limits, as in the relationships between slopes and mass: galaxies with high Q_b only present low-rising rotation curves, and steeper slopes tend to be found in galaxies with low Q_b .

On the contrary, when we represent $d_R v_c(0)$ and $d_R v_*(0)$ as a function of B/T (Fig. 6.13, top), we identify two different groups: those galaxies with a prominent

6.3 Results 117

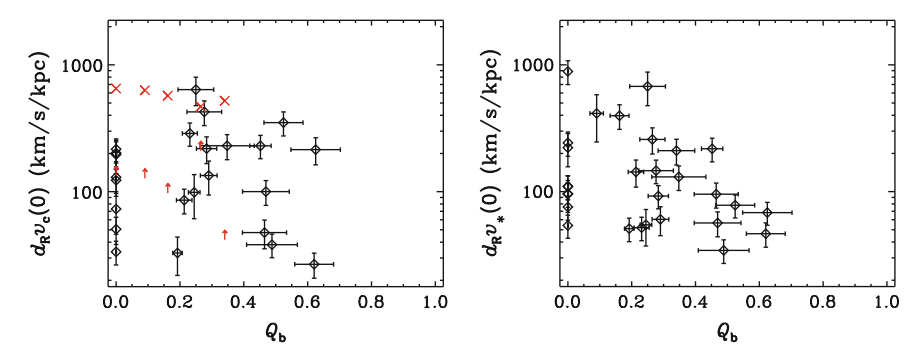


Fig. 6.11 Rotation curve slopes $d_R v_c(0)$ and $d_R v_*(0)$ as a function of Q_b , a parameter which accounts for the strength of the bar. We see no correlation among these parameters

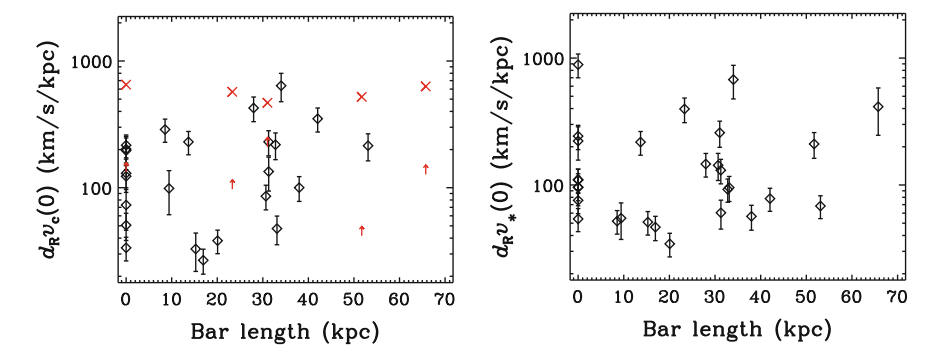


Fig. 6.12 As Fig. 6.11, but now for bar length

bulge ($B/T \gtrsim 0.2$) with steeper slopes, and those without bulges, with shallower slopes. Also, in the bottom panels of (Fig. 6.13) we see that the mass of the bulge is correlated with $d_R v_*(0)$, but not that clearly with $d_R v_c(0)$. In Sect. 6.4, I will discuss the physical consequences of this separation.

Relationships with star formation

Finally, we want to explore if the steepness of the rotation curve is influenced by the formation of stars. Star formation transforms gas into stars, and may lead to a redistribution of mass. Thus, we might expect changes in the dynamics of the central parts of galaxies. To check this, I measure the massive SFR as measured from the H α images, the total SFR(H α), using Eqs. 4.1 and 4.2. Furthermore, I measure the SFR densities (Σ SFRs) as the SFR divided by the physical area (in kpc²), and present them as a function of the slope.

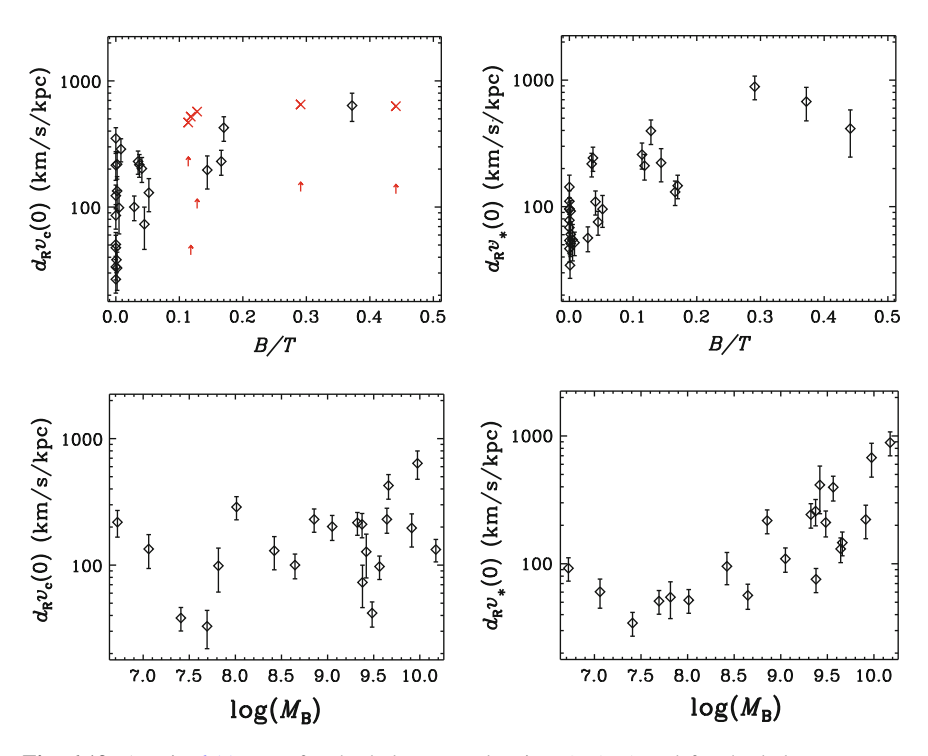


Fig. 6.13 As Fig. 6.11, now for the bulge-to-total ratio B/T (top) and for the bulge mass M_B (bottom). Bulge-dominated galaxies (B/T over 0.2) only have steep slopes, although more data would be needed to confirm this trend

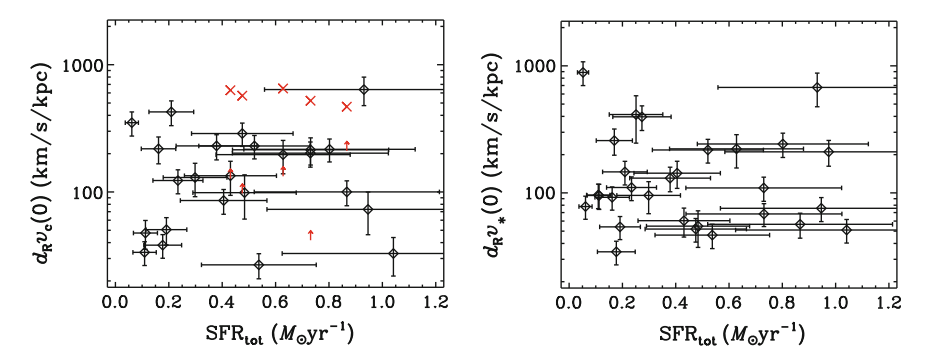


Fig. 6.14 Rotation curve slopes $d_R v_c(0)$ and $d_R v_*(0)$ as a function of the total SFR

In Figs. 6.14 and 6.15 I represent $d_R v_c(0)$ and $d_R v_*(0)$ as a function of the total SFR and total Σ SFR. There is no correlation between the star formation and the slope of the inner part of the rotation curve (as found in Lelli et al. 2014 for starburst galaxies). Because we want to explore the inner parts of the galaxy, I have in particular

6.3 Results 119

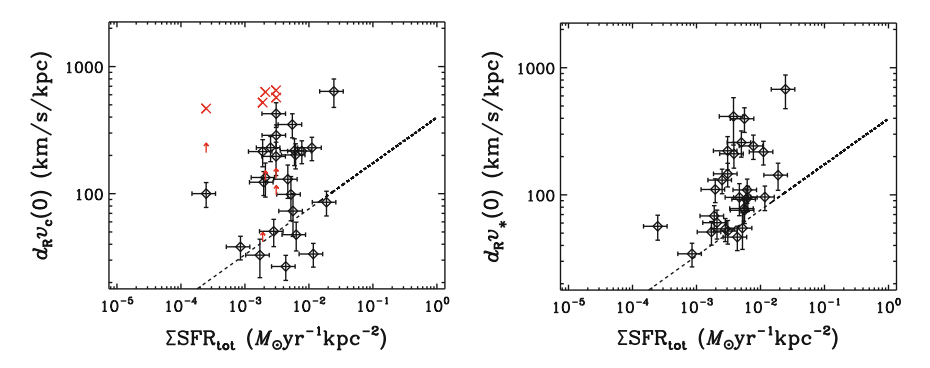


Fig. 6.15 As Fig. 6.14 but for Σ SFR_{tot}. The *dashed line* is the prediction for starbursts by Lelli et al. (2014). Our galaxies have systematically lower Σ SFR for the corresponding slopes (only one galaxy in our sample is a starburst)

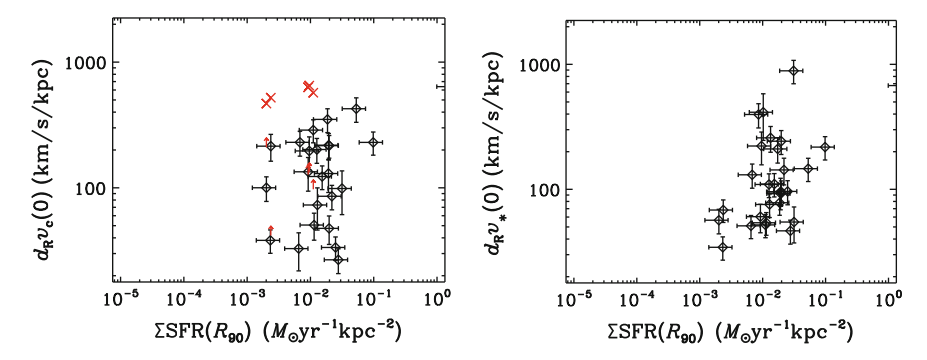


Fig. 6.16 Rotation curve slopes $d_R v_c(0)$ and $d_R v_*(0)$ as a function of the Σ SFR within R_{90} , which is defined as the radius where 90% of the maximum velocity is reached. I find no correlation among these parameters

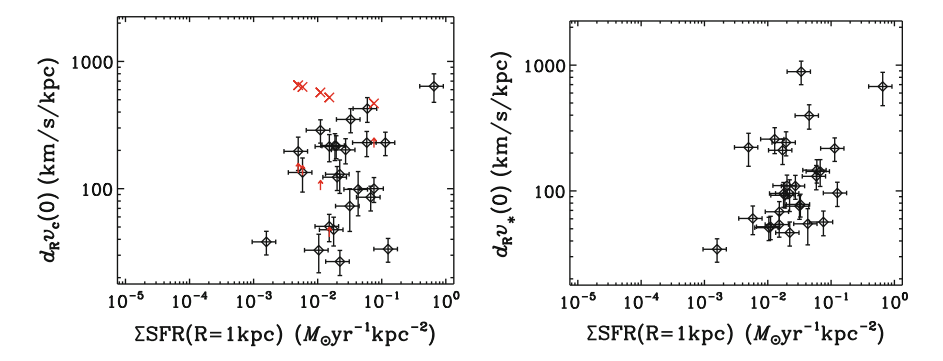


Fig. 6.17 As Fig. 6.16, but for the SFR density within 1 kpc from the centre, Σ SFR (1 kpc)

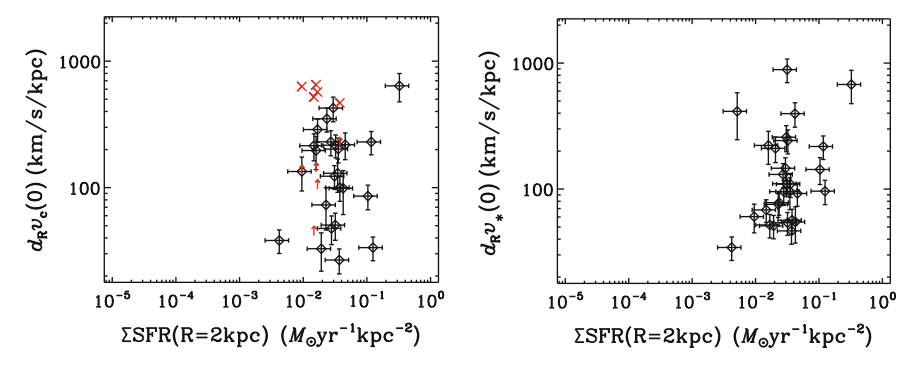


Fig. 6.18 As Fig. 6.17, but for Σ SFR(2 kpc)

studied the SFR inside R_{90} , 1 and 2 kpc. In Figs. 6.16–6.18 I represent $d_R v_c(0)$ and $d_R v_*(0)$ as a function of Σ SFR inside R_{90} , 1 and 2 kpc, respectively. There is no correlation between the formation of stars and the slope of the inner rotation curves.

6.4 Discussion: Cosmological Versus Secular

The Universe is evolving from an epoch in which hierarchical clustering and galaxy mergers took place (Eggen et al. 1962; Toomre 1977; Kormendy and Kennicutt 2004), to a time when internal secular evolution processes dominate galaxy evolution. Following Newton's classical laws, the circular velocity is determined by the enclosed mass within a certain radii if we assume axisymmetric distribution. Therefore, we expect the mass distribution to be reflected in the kinematics of the galaxy.

When secular evolution takes place or when the evolution of a galaxy is influenced by the environment, the mass distribution changes. We ask ourselves *can internal* (secular processes driven by bars, spirals or oval distortion) and external (gas infall, minor mergers) evolution processes change the "cosmological" backbone of the galaxies? And fast processes such as galaxy mergers or protogalactic collapse? We want to explore whether we can identify deviations from what classical laws predict (more enclosed mass is translated into a steeper rising rotation curve) in the galaxy's kinematics.

Here, the sample galaxies are spread in characteristics: we have barred and unbarred galaxies, galaxies with and without bulges, and galaxies hosting AGN. In Sect. 6.3 I have presented several plots that relate the results from the rotation curve analysis ($d_R v_c(0)$) and $d_R v_*(0)$) to a list of galaxy parameters (μ_0 , $v_{c,max}$, stellar mass, Q_b , bar length...). I now analyse and discuss the possible scientific reasons that explain why there are so few correlations between the slopes and many of the parameters.

6.4.1 Secular Evolution

First of all, I study the effect that the presence of the bar, or the growth of a pseudobulge can have on the rotation of the galaxy, specifically on the measurements of $d_R v_c(0)$ and $d_R v_*(0)$. Bars are the most important drivers of secular evolution in galactic discs. They get stronger, longer and thinner over time (Athanassoula 2003), and change the distribution of material in a galaxy, pushing the mass inside the corotation radius (CR) towards the centre, and the material outside the CR outwards.

This redistribution of material caused by the bar torque can result in a central region with higher density, often called disky bulges, disc-like bulges, disky pseudobulges or simply pseudobulges (Athanassoula 1992; Wada and Habe 1992, 1995; Friedli and Benz 1993; Heller and Shlosman 1994; Sakamoto et al. 1999; Sheth et al. 2003; Regan and Teuben 2004; Kormendy and Kennicutt 2004; Heller et al. 2007a, b; Athanassoula 2008; Fisher et al. 2009; Kormendy 2013). I will use the term disky bulges hereafter in the chapter, to avoid the confusing term pseudobulge and distinguish disky bulges from the boxy-peanut bulges (which are the inner parts of bars seen edge-on, see Athanassoula 2005).

Disky bulges would be able to form stars and be seen as young populated (Fisher et al. 2009; Fisher and Drory 2010), although they will also contain old stars (Grosbøl et al. 2004). I refer to the review by Kormendy and Kennicutt (2004) for a detailed explanation of these sub-structures. One should distinguish these *disky* bulges (which are thought to be formed through internal, secular evolution) from the *classical* bulges. The latter are similar to elliptical galaxies (Davies et al. 1983; Franx 1993; Wyse et al. 1997 and references therein), composed by old-population stars and probably formed by gravitational collapse or hierarchical merging of smaller objects.

I have in particular studied Q_b , a parameter which represents the bar strength. By definition, Q_b is influenced by the presence of the bulge. As explained in Sect. 5.3.1, Q_b decreases with the axisymmetric radial force. Therefore, Q_b anticorrelates with B/T by definition and as also expected, Q_b decreases with morphological T-type (e.g.; Buta et al. 2005; Laurikainen et al. 2007).

In Figs. 6.11 and 6.12, we see that Q_b and the length of the bar do not directly have an impact on the slope of the rotation curve. Whether the bar is strong or weak, or even when galaxies are unbarred, there is no specific trend for the slopes of the rotation curves. Nevertheless, the bar can be strong, have exchanged a large amount of angular momentum and moved material towards the centre of the galaxy, modifying the kinematics of the galaxy. But if a disky bulge has been formed because of the mass redistribution, Q_b will be lower. In other words, the bar may have created the disky bulge at a time when Q_b was larger than at present time, when Q_b may have diminished. Therefore, the next step is to study the role of the bulge in the dynamics of the central parts of the galaxies.

Corradi and Capaccioli (1990) found that in the bulge-dominated galaxies of their sample, the rise of the rotation velocities was faster than that in galaxies with similar luminosity but less concentration of central luminous matter. Also, Verheijen (1997) and Sancisi (2004) agree that for galaxies with similar total luminosity, a greater

concentration of material and light (as in systems with bulges) is translated into a steeper slope. They conclude that the correspondence between the shape of the rotation curve and the distribution of light indicates that the gravitational potential in the inner parts of the galaxies in their samples is dominated by luminous matter. Noordermeer et al. (2007) confirm this, finding that the rotation curves of the bulgedominated ETGs in their sample show an initial rise in the inner parts, followed by a decline and a final flat part, indicating that the baryonic matter is more determinant than the DM in the central parts. They conclude that although the stellar mass is the main factor that determines the shape of the rotation curve, there are other factors (e.g., bulges in ETGs) that influence the shape of the rotation curve.

Noordermeer (2008) studied the contribution of the bulge to the rotation curve. He found that both the flattening and the concentration of the bulge influence the steepness of the rotation curve in the inner parts: a flattened bulge has a higher rotational peak velocity than a spherical bulge (more accentuated for more concentrated bulges), reaching that peak velocity at smaller radius; in other words, a steeper slope. None of the previous studies have distinguished between classical or disky bulges. Therefore I will not make any assumption on the type of bulges they observe. We know that most Sa galaxies contain classical bulges, both classical and disky bulges are comparably common in Sb galaxies, most Sbc galaxies contain disky bulges, and galaxies with later types (Sc-Im) do not contain classical bulges (Kormendy and Kennicutt 2004). Some disky bulges have been found in lenticular galaxies (Laurikainen et al. 2007; Fisher and Drory 2008; Weinzirl et al. 2009; Fisher and Drory 2010; Vaghmare et al. 2013).

Analysing the possible influence of the bulge on the slope of the rotation curve, we see in Fig. 6.13 that the presence of the bulge does seem to matter, as when B/T and M_B increasee, $d_R v_c(0)$ and $d_R v_*(0)$ increase too. Furthermore, there is an apparent division in two families regarding the stellar mass-derived data: the galaxies with B/T > 0.2 have slopes steeper than $400 \, \text{km/s/kpc}$, whereas those with B/T < 0.2 have slopes lower than $400 \, \text{km/s/kpc}$. This duality cannot be explained from the point of view of the method to derive the radial force maps, as the force maps were not derived with assumptions about B/T. The bulge, in these cases, may be controlling the velocities and make the gas in the central parts to have steeper-rising rotation curves, because steep slopes are only found in galaxies with prominent bulges, confirming the previous studies presented before. Also, the correlation between M_B and $d_R v_*(0)$ indicates that the bulge mass plays a fundamental role in the dynamics of the stars. The less tight correlation between M_B and $d_R v_c(0)$ confirms that not only the stellar bulge, but also the gas and DM (the other components of the dynamic mass) determine $d_R v_c(0)$.

I have not analysed the nature of the bulges in our sample. From the 2D decompositions of the 3.6 μ m images, we have derived the brightness profiles of the bulges, which follow a Sérsic (1968) function brightness profile, and which can be a proxy to determine if a bulge is a classical or a disky bulge. Most disky bulges have Sérsic index n < 2 (although some disky bulges have been found to have $n \approx 4$), whereas almost all classical bulges have $n \gtrsim 2$. All the bulges in our sample have n < 2 except for those in NGC 691, NGC 4324 and NGC 4639. Another criterion to see if

a bulge is classical or disky is the B/T. Small B/T values do not imply that a bulge is disky, although a disky bulge cannot have B/T > 0.35, and large B/T > 0.5 only correspond to classical bulges (Kormendy and Kennicutt 2004). All the B/T values of our galaxies are below 0.5, so we cannot determine the type of bulge with this criterion. More data would be necessary to confirm the nature of our bulges, such as IFU to constrain the stellar populations in their central parts.

On the one hand, classical bulges may have been formed through a fast event in the evolution of a galaxy (such as a merger event that accumulates material in the central part of the galaxy). But on the other hand, disky bulges originate in the internal secular evolution of galaxies, which comes from the redistribution of material within the galaxy by the bar. This creates a higher density region from the disc, the disky bulge. I confirm that the highest slopes are found in the bulge-dominated (B/T > 0.2) galaxies, and that the slopes increase with B/T. However, regardless of the nature of the bulge, the greater concentration of material in the bulge significantly influences the central dynamics of the galaxies in our sample.

The bulge is a concentration of stellar mass in the centre of the galaxy. We are able to study the concentration of luminous material (gas and stars) by computing the concentration of light in the central parts of the galaxy. From the S⁴G images, we can measure the light concentration as the C_{31} parameter defined in de Vaucouleurs (1977) and the C_{82} parameter defined in Kent (1985):

$$C_{31} = \frac{r_{75}}{r_{25}},\tag{6.9}$$

$$C_{82} = 5\log\left(\frac{r_{80}}{r_{20}}\right),\tag{6.10}$$

where r_x is the semi-major axis of the ellipse enclosing x % of the total luminosity of the galaxy. I present $d_R v_c(0)$ and $d_R v_*(0)$ as a function of both C_{31} and C_{82} parameters in Figs. 6.19 and 6.20. I have obtained the parameters C_{31} and C_{82} from the ellipse fitting of the 3.6 μ m images from Muñoz-Mateos et al. (in. prep), although

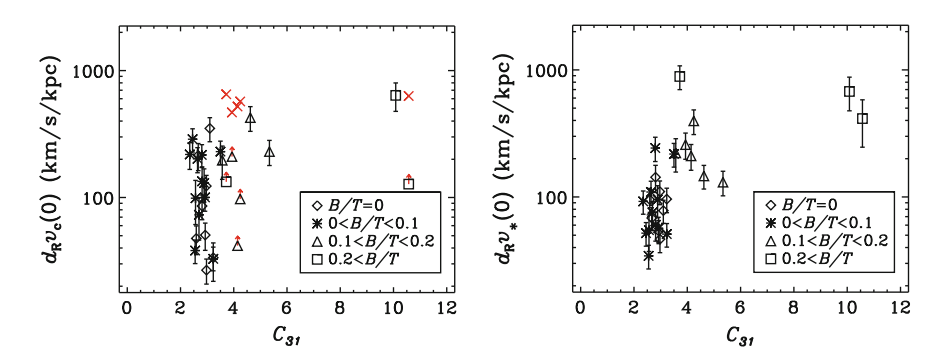


Fig. 6.19 Rotation curve slopes $d_R v_c(0)$ and $d_R v_*(0)$ as a function of C_{31} concentration index

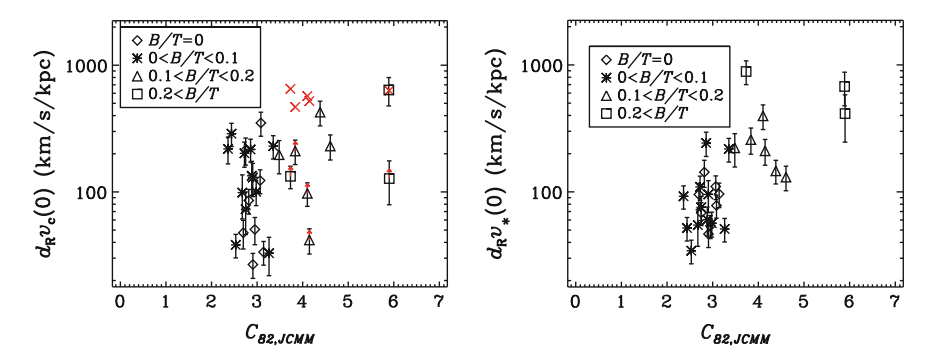


Fig. 6.20 As Fig. 6.19, but now for the C_{82} concentration index from Muñoz-Mateos et al. in preparation

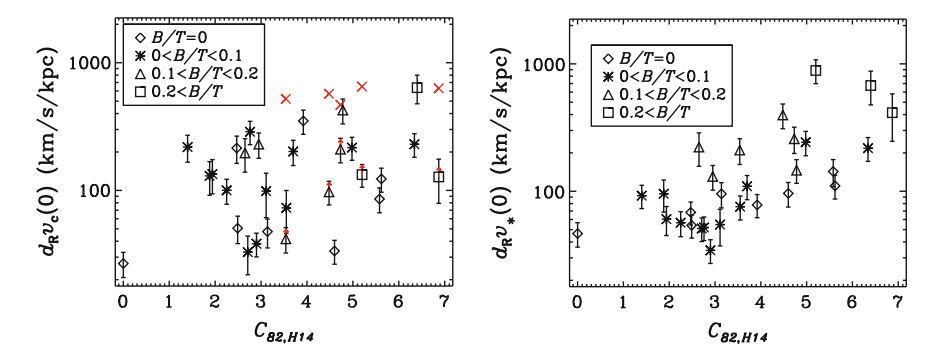


Fig. 6.21 As Fig. 6.19, but now for the C_{82} concentration index from Holwerda et al. (2014)

similar results are obtained when using $4.5 \,\mu\text{m}$ images from the same paper, or those results from Holwerda et al. (2014) (Fig. 6.21).

We see that there is a tendency that the higher the central light concentration, the steeper the slope. Also, we see that the central light concentration is related to galaxies with prominent bulges and with galaxies with intense central activity. We see in Fig. 6.19 that there are two galaxies (the starburst NGC 3504 and the AGN NGC 4151) that have higher C_{31} parameters than the others, and that have a steeper slope than the others. In de Vaucouleurs (1977) we see that C_{31} and C_{82} tend to decrease with T-type (de Vaucouleurs 1977; Holwerda et al. 2014), but not linearly and with some scatter. Therefore we do not expect a linear relationship between C_{31} and C_{82} with $d_R v_c(0)$. The absence of linear correlation between the light concentration and the slope of the rotation curve may be caused because of the differences between the luminous and dark matter. However, we see that this tendency, that the higher the central light concentration, the steeper the slope, indicates that the luminous matter may be dominating the gravitational potential in the central parts of our galaxies.

Another process that takes place within galaxies is the SF. To understand whether SF changes the dynamics of the galaxy (as extracted from the study of the slopes),

I represent the total SFR and Σ SFRs as function of $d_R v_c(0)$ and $d_R v_*(0)$ (Figs. 6.14, 6.15, 6.16, 6.17, 6.18). We see that there is no clear correlation among these parameters, implying that SF does not determine the slope of the rotation curve. The fact that our galaxies have systematically lower Σ SFR than the gas-rich dwarfs from Lelli et al. (2014) is expected. The galaxies in our sample are not characterised for being either dwarfs, starburst (except NGC 3504) or gas-rich. Lelli et al. argue that the starburst activity is related to the inner steepness of the potential well and the gas surface density, while the exact nature of the relationship between the slope of the circular velocity and Σ SFR is unclear. They give two possible explanations that are related to the nature of the dwarfs and irregulars, which do not apply to the galaxies in our sample: (i) the progenitors of BCDs are unusually compact Irrs with a steep potential well; or ii) a starburst is caused because of the concentration of mass (gas, stars, and dark matter) in typical Irrs.

6.4.2 Cosmological Parameters

Now I study the relationship between the global parameters of the galaxy, such as the total stellar mass and maximum rotation velocity, and the slope of the rotation curve. We see in Figs. 6.9 and 6.10 that there are no correlations between stellar mass or $v_{c,max}$ and $d_R v_c(0)$, but that there are limitations: less-massive galaxies have lower $d_R v_c(0)$ or $d_R v_*(0)$, and steep slopes are only found in the most massive galaxies. Also, a possible correlation of $v_{*,max}$ with $d_R v_*(0)$ is expected, as the velocities derived from the stellar-mass maps have been obtained from the light distribution, (a stellar M/L has been adopted, and M_* is correlated with $v_{*,max}$ throughout the Tully-Fisher relationship).

To estimate the quantity of stellar mass compared to the total mass within a certain radius, we estimate the enclosed total mass at a certain radius as $v_{\rm c}^2 r/G$. The stellar mass fraction, f_{\star} , is defined as the ratio between the stellar mass over the radial range of interest divided by the total mass enclosed within the same radial interval.

Therefore, I measure f_{\star} at the radii where the stellar masses were measured, assuming spherical distribution and that the circular velocity remains flat after the last measured point of the rotation curve. This last statement may be true except for NGC 2805, NGC 4324 and NGC 4389, whose rotation curves continue rising after the last point, and therefore the estimated f_{\star} is an upper limit (the enclosed mass would be a lower limit). The stellar fractions (presented in Table 6.1) are within a reasonable range, $0.1 < f_{\star} < 1$ for all galaxies, except for the upper limit on NGC 4324. This means that not all the mass that influences the gravitational potential is stellar mass, but that there are gas and DM to take into account. Although it is true that the gas component is sometimes negligible, the fact that $f_{\star} < 1$ indicates that not all the dynamic mass is stellar mass.

The idea that the stellar mass is not the only component determining the dynamics of the central parts of the galaxy is supported by the fact that the relationships between $d_R v_*(0)$ and the other parameters (concretely with μ_0 , T-type, $v_{*,\max}$ and M_B) are

always tighter than those of $d_R v_c(0)$ (see Figs. 6.6, 6.8, 6.10 and 6.13). In those figures we see more scatter in the relationships of $d_R v_c(0)$ with the other properties than in the relationships with $d_R v_*(0)$. This confirms that not only stellar, but gas and dark mass also contribute to the gravitational potential in the central parts.

Taking everything into account, I conclude that despite the fact that the stellar mass distribution in the central kpc of a galaxy dominates the gravitational potential there (as seen in the correlations of B/T, C_{31} and C_{82} with $d_R v_*(0)$), the scatter of these correlations may be due to other processes that deviate from Newton laws. This idea is supported by two facts: (i) all the correlations with $d_R v_*(0)$ have larger scatter than those with $d_R v_*(0)$ and (ii) not all the dynamical mass is luminous mass.

6.4.3 Implications on Dark Matter Distribution

As previously shown, the shape of the rotation curve is related to the gravitational potential of the galaxy, and therefore harbours information about the amount of DM present within the galaxy. Using pure baryonic slopes (e.g., those derived from the stellar-mass maps) may be a useful complement to the measurements of the slopes inferred from rotation curve decomposition, and help to determine whether the baryonic mass dominates over the DM or vice-versa.

Di Cintio et al. (2014b) find from simulations that the flattest inner DM profiles are expected for galaxies with rotational velocities of 50 Km s⁻¹, and increasing for more massive galaxies (cuspier profiles), eventually reaching the prediction at the Milky Way mass. They find that the most clear measurements of cored profiles are those found in low surface brightness galaxies with rotational velocities \$\leq 100 \text{ km s}^{-1}\$. Galaxies with more mass are baryon-dominated, and cusp/core DM profiles are more difficult to distinguish due to the larger uncertainties in the disc-halo decomposition of the rotation curves. In Leaman et al. (in preparation), we combine S⁴G IR data with FP data to decompose the rotation curves, obtaining separate information about the contributions by gas, stars and DM. Therefore, it is possible to derive accurate measurements of the DM profile parameters (more accurately than previously done in the literature). Also, for more massive (and luminous) galaxies, the baryonic mass determines the dynamics in the inner regions more than the DM (see references in the Introduction). The study of the DM profile parameters done by Leaman et al. will allow us to determine whether the DM profile in the central part is cuspy or cored.

References

M.G. Abadi, J.F. Navarro, M. Steinmetz, V.R. Eke, ApJ **591**, 499 (2003) P. Amram, E. Le Coarer, M. Marcelin et al., A&AS **94**, 175 (1992) P. Amram, M. Marcelin, C. Balkowski et al., A&AS **103**, 5 (1994)

References 127

E. Athanassoula, in *Astronomical Society of the Pacific Conference Series*, Vol. 396, ed. by J.G. Funes, E.M. Corsini. Formation and Evolution of Galaxy Disks (2008), p. 333

- E. Athanassoula, MNRAS 259, 345 (1992)
- E. Athanassoula, MNRAS **341**, 1179 (2003)
- E. Athanassoula, MNRAS **358**, 1477 (2005)
- J.E. Barnes, L. Hernquist, ApJ 471, 115 (1996)
- K.G. Begeman, Ph.D. thesis, Kapteyn Institute (1987)
- K.G. Begeman, A&A 223, 47 (1989)
- J. Binney, S. Tremaine, Galactic Dynamics, 2nd edn. (Princeton University Press, Princeton, 2008)
- F. Bonnarel, J. Boulesteix, Y.P. Georgelin et al., A&A 189, 59 (1988)
- A. Bosma, Ph.D. Thesis, Groningen University (1978)
- A. Bosma, R.D. Ekers, J. Lequeux, A&A 57, 97 (1977)
- A. Bosma, AJ 86, 1791 (1981)
- A.H. Broeils, Ph.D. thesis, University of Groningen (1992)
- D. Burstein, V.C. Rubin, ApJ 297, 423 (1985)
- R.J. Buta, K. Sheth, E. Athanassoula et al., ApJS 217, 32 (2015)
- R. Buta, S. Vasylyev, H. Salo, E. Laurikainen, AJ 130, 506 (2005)
- S. Casertano, J.H. van Gorkom, AJ 101, 1231 (1991)
- G. Cecil, A.S. Wilson, R.B. Tully, ApJ 390, 365 (1992)
- L. Chemin, C. Balkowski, V. Cayatte et al., MNRAS 366, 812 (2006)
- R.L.M. Corradi, M. Capaccioli, A&A 237, 36 (1990)
- R.L.M. Corradi, M. Capaccioli, A&AS 90, 121 (1991)
- S. Côté, C. Carignan, K.C. Freeman, AJ 120, 3027 (2000)
- R.L. Davies, G. Efstathiou, S.M. Fall, G. Illingworth, P.L. Schechter, ApJ 266, 41 (1983)
- W.J.G. de Blok, S.S. McGaugh, J.M. van der Hulst, MNRAS 283, 18 (1996)
- W.J.G. de Blok, S.S. McGaugh, A. Bosma, V.C. Rubin, ApJl **552**, L23 (2001)
- W.J.G. de Blok, F. Walter, E. Brinks et al., AJ 136, 2648 (2008)
- R. de Grijs, R.F. Peletier, A&A **320**, L21 (1997)
- G. de Vaucouleurs, in *Evolution of Galaxies and Stellar Populations*, ed. by B.M. Tinsley, R.B.G. Larson, D. Campbell (1977), p. 43
- G. de Vaucouleurs, W.D. Pence, ApJ 242, 18 (1980)
- J.M. Deharveng, A. Pellet, A&A 38, 15 (1975)
- A. Di Cintio, C.B. Brook, A.A. Dutton et al., MNRAS 441, 2986 (2014a)
- A. Di Cintio, C.B. Brook, A.V. Macciò et al., MNRAS 437, 415 (2014b)
- R. Dubout, A. Laval, A. Maucherat et al., Astrophys. Lett. 17, 141 (1976)
- O.J. Eggen, D. Lynden-Bell, A.R. Sandage, ApJ 136, 748 (1962)
- B. Epinat, P. Amram, M. Marcelin, MNRAS 390, 466 (2008)
- M. Eskew, D. Zaritsky, S. Meidt, AJ 143, 139 (2012)
- D.B. Fisher, N. Drory, M.H. Fabricius, ApJ 697, 630 (2009)
- D.B. Fisher, N. Drory, AJ **136**, 773 (2008)
- D.B. Fisher, N. Drory, ApJ 716, 942 (2010)
- M. Franx, in IAU Symposium, Vol. 153, ed. by H. Dejonghe, H.J. Habing. Galactic Bulges (1993), p. 243
- D. Friedli, W. Benz, A&A 268, 65 (1993)
- G. Gentile, P. Salucci, U. Klein, D. Vergani, P. Kalberla, MNRAS 351, 903 (2004)
- F. Governato, B. Willman, L. Mayer et al., MNRAS 374, 1479 (2007)
- F. Governato, C. Brook, L. Mayer et al., Nature 463, 203 (2010)
- F. Governato, A. Zolotov, A. Pontzen et al., MNRAS 422, 1231 (2012)
- P. Grosbøl, P.A. Patsis, E. Pompei, A&A 423, 849 (2004)
- C.H. Heller, I. Shlosman, E. Athanassoula, ApJl 657, L65 (2007a)
- C.H. Heller, I. Shlosman, E. Athanassoula, ApJ 671, 226 (2007b)
- C.H. Heller, I. Shlosman, ApJ **424**, 84 (1994)
- L.C. Ho, A.V. Filippenko, W.L.W. Sargent, ApJ 487, 591 (1997)

- B.W. Holwerda, J.-C. Muñoz-Mateos, S. Comerón et al., ApJ 781, 12 (2014)
- P.A. James, N.S. Shane, J.E. Beckman et al., A&A 414, 23 (2004)
- J. Jiménez-Vicente, E. Battaner, M. Rozas, H. Castañeda, C. Porcel, A&A 342, 417 (1999)
- R.C. Jr Kennicutt, J.C. Lee, J.G. Funes, S.J. Sakai, S. Akiyama, ApJS 178, 247 (2008)
- S.M. Kent, ApJS **59**, 115 (1985)
- J. Kormendy, in Secular Evolution in Disk Galaxies, ed. by J. Falcón-Barroso, J.H. Knapen (2013), p. 1
- J. Kormendy, R.C. Kennicutt Jr, ARA&A 42, 603 (2004)
- R. Kuzio de Naray, S.S. McGaugh, W.J.G. de Blok, ApJ 676, 920 (2008)
- R. Kuzio de Naray, S.S. McGaugh, J.C. Mihos, ApJ 692, 1321 (2009)
- E. Laurikainen, H. Salo, R. Buta, J.H. Knapen, MNRAS 381, 401 (2007)
- E. Laurikainen, H. Salo, MNRAS 337, 1118 (2002)
- F. Lelli, F. Fraternali, M. Verheijen, MNRAS 433, L30 (2013)
- F. Lelli, F. Fraternali, M. Verheijen, A&A 563, A27 (2014)
- A.V. Macciò, G. Stinson, C.B. Brook et al., ApJ 744, L9 (2012)
- M. Marcelin, J. Boulesteix, Y.P. Georgelin, A&A 151, 144 (1985)
- L.D. Matthews, J.S. Gallagher III, ApJS 141, 429 (2002)
- S.E. Meidt, E. Schinnerer, J.H. Knapen et al., ApJ 744, 17 (2012)
- B. Moore, Nature 370, 629 (1994)
- B. Moore, T. Quinn, F. Governato, J. Stadel, G. Lake, MNRAS 310, 1147 (1999)
- E. Noordermeer, J.M. van der Hulst, R. Sancisi, R.A. Swaters, T.S. van Albada, A&A 442, 137 (2005)
- E. Noordermeer, J.M. van der Hulst, R. Sancisi, R.S. Swaters, T.S. van Albada, MNRAS **376**, 1513 (2007)
- E. Noordermeer, MNRAS 385, 1359 (2008)
- S.-H. Oh, W.J.G. de Blok, E. Brinks, F. Walter, R.C. Kennicutt Jr, AJ 141, 193 (2011)
- W.D. Pence, K. Taylor, P. Atherton, ApJ 357, 415 (1990)
- M. Persic, P. Salucci, F. Stel, MNRAS 281, 27 (1996)
- M. Persic, P. Salucci, ApJ **368**, 60 (1991)
- M. Querejeta, S.E. Meidt, E. Schinnerer et al., ApJS 219, 5 (2015)
- M.W. Regan, P.J. Teuben, ApJ 600, 595 (2004)
- M.S. Roberts, R.N. Whitehurst, ApJ 201, 327 (1975)
- D.H. Rogstad, G.S. Shostak, ApJ 176, 315 (1972)
- V.C. Rubin, D. Burstein, W.K. Ford Jr, N. Thonnard, ApJ 289, 81 (1985)
- S.D. Ryder, A.V. Zasov, O.K. Sil'chenko, V.J. McIntyre, W. Walsh, MNRAS 293, 411 (1998)
- K. Sakamoto, S.K. Okumura, S. Ishizuki, N.Z. Scoville, ApJ 525, 691 (1999)
- H. Salo, E. Laurikainen, R. Buta, J.H. Knapen, ApJ 715, L56 (2010)
- P. Salucci, A. Burkert, ApJ **537**, L9 (2000)
- J.R. Sánchez-Gallego, J.H. Knapen, C.D. Wilson et al., MNRAS 422, 3208 (2012)
- R. Sancisi, in IAU Symposium, Vol. 220, ed. by S. Ryder, D. Pisano, M. Walker, K. Freeman. Dark Matter in Galaxies (2004), p. 233
- R. Sancisi, R.J. Allen, W.T. Sullivan III A&A, 78, 217 (1979)
- E. Schinnerer, S.E. Meidt, J. Pety et al., ApJ 779, 42 (2013)
- K. Sheth, M.W. Regan, N.Z. Scoville, L.E. Strubbe, ApJ 592, L13 (2003)
- K. Sheth, M. Regan, J.L. Hinz et al., PASP 122, 1397 (2010)
- V. Sicotte, C. Carignan, D. Durand, AJ **112**, 1423 (1996)
- J.D. Simon, A.D. Bolatto, A. Leroy, L. Blitz, E.L. Gates, ApJ 621, 757 (2005)
- T. Speltincx, E. Laurikainen, H. Salo, MNRAS 383, 317 (2008)
- R.A. Swaters, Ph.D. thesis, Rijksuniversiteit Groningen (1999)
- R.A. Swaters, B.F. Madore, F.C. van den Bosch, M. Balcells, ApJ 583, 732 (2003)
- R.A. Swaters, R. Sancisi, T.S. van Albada, J.M. van der Hulst, A&A 493, 871 (2009)
- R.A. Swaters, R. Sancisi, T.S. van Albada, J.M. van der Hulst, ApJ 729, 118 (2011)
- R.A. Swaters, R. Sancisi, J.M. van der Hulst, T.S. van Albada, MNRAS 425, 2299 (2012)

References 129

- R.A. Swaters, M. Balcells, A&A 390, 863 (2002)
- A. Toomre, in Evolution of Galaxies and Stellar Populations, ed. by B.M. Tinsley, R.B.G. Larson,
 - D. Campbell (1977), p. 401
- R.B. Tully, ApJS 27, 415 (1974)
- R.B. Tully, J.R. Fisher, A&A 54, 661 (1977)
- K. Vaghmare, S. Barway, A. Kembhavi, ApJ 767, L33 (2013)
- G.D. van Albada, A&A 142, 491 (1985)
- T.S. van Albada, R. Sancisi, R. Soc. Lond. Philos. Trans. Ser. A 320, 447 (1986)
- F.C. van den Bosch, A. Burkert, R.A. Swaters, MNRAS 326, 1205 (2001)
- M.A.W. Verheijen, Ph.D. thesis, University of Groningen, The Netherlands (1997)
- M.A.W. Verheijen, ApJ **563**, 694 (2001)
- K. Wada, A. Habe, MNRAS 258, 82 (1992)
- K. Wada, A. Habe, MNRAS 277, 433 (1995)
- M.G. Walker, J. Peñarrubia, ApJ 742, 20 (2011)
- F. Walter, E. Brinks, W.J.G. de Blok et al., AJ 136, 2563 (2008)
- A.-M. Weijmans, D. Krajnović, G. van de Ven et al., MNRAS 383, 1343 (2008)
- T. Weinzirl, S. Jogee, S. Khochfar, A. Burkert, J. Kormendy, ApJ 696, 411 (2009)
- R.F.G. Wyse, G. Gilmore, M. Franx, ARA&A 35, 637 (1997)

Chapter 7 Conclusions and Future Work

7.1 Conclusions

This thesis contains studies regarding the morphology, kinematics and star formation across the Hubble sequence of galaxies. With the goal of understanding the secular evolution processes that take part in nearby galaxies, we have designed an observational kinematic programme. Within this programme, I have observed 29 spiral galaxies with a H α Fabry-Perot, reduced the data and derived results of morphology, kinematics and star formation. In particular, I have studied the non-circular motions in the galaxy substructures (bar, SAR and arms), as well as the rotation curve in the inner regions. These kinematic studies have been related to properties of the galaxies, such as star formation, bulge or bar presence. The star formation distribution of the observed sample has been analysed, as well as studies of unexpected star formation in early-type galaxies and early-type spirals.

The most important conclusions are the following:

Massive star formation in galaxies with excess UV emission

Galaxies with morphological types between E and Sab are generally characterized by low gas content and low SFR. However, observational evidences that prove the opposite have been found in the last decades. I have obtained deep $H\alpha$ imaging of ten of those galaxies that showed unusual excess ultra-violet (UV) emission from beyond their optical extent (R_{25}). The goal was to understand the nature of the excess UV emission. From the analysis, I conclude the following:

- From *GALEX* images of 1899 elliptical, S0, and ETS galaxies, excess UV emission beyond R_{25} is found in 28% of them. Concretely, 8% of the elliptical galaxies, 28% of the S0s and 45% of the ETSs.
- From deep H α imaging of a subsample of 10 of these UV-excess galaxies, H α emission is located accordingly to that of the UV light for all galaxies except for

- one. There is a good correlation between the $H\alpha$ and UV morphologies of the outer features of these galaxies.
- From the above, the origin of the excess UV light is the massive SF, confirmed by the Hα counterparts and excluding the possibility of the UV-upturn in these outer parts. This SF mostly occurs in spiral arms and outer rings.
- The dust-corrected SFRs in $H\alpha$, FUV and NUV agree within the uncertainties, ranging from a few tenths to a few M_{\odot} yr⁻¹. These rates are typical of later type galaxies. The SFRs of the elliptical galaxies of our sample are, however, well below $1 M_{\odot}$ yr⁻¹.

$H\alpha$ Kinematics of S^4G Spiral Galaxies: The data

This chapter presents the complete set of Fabry-Perot (FP) and narrow-band imaging data for the 29 galaxies in our kinematical study, reaching the following conclusions:

- I have completed the observations of our kinematical study of 29 S⁴G spiral galaxies of all morphological types using the GH\$\alpha\$FP instrument (field-of-view of 3.4 × 3.4 arcmin). The data have seeing limited angular resolution (typical values between 0.6" and 1.4") sampled with 0.2" pixels and a spectral resolution \sim 8 km s⁻¹. These FP data have been observed together with H\$\alpha\$ flux-calibrated images.
- To reach our scientific objectives, I have followed specific data reduction and analysis procedures which guarantee high angular resolution (~1") kinematic cubes and data products. The images and data described in this chapter are publicly released.
- I flux-calibrate the $GH\alpha$ FaS data cubes. I conclude that the flux calibration cannot be automatized, and no standard calibration factors can be extracted for any particular $GH\alpha$ FaS filter. Instead, flux calibration is specific to each galaxy and needs to be performed by comparison with calibrated $H\alpha$ images, such as our ACAM images.
- I have applied the tilted-ring method to our velocity maps to extract the rotation curves. Some caveats arising in the nature of these FP data need to be taken into account (e.g., intrinsic patchiness of the line emission).

Streaming motions in the spiral galaxy NGC 864

This chapter presents the first results of the kinematic programme to observe a sample of S^4G spiral galaxies of all morphological types with the $GH\alpha FaS$ FP instrument, studying in detail the spiral galaxy NGC 864. Data sets obtained with three different WHT instruments have been studied, resulting in rotation curves and intensity, velocity, residual and gradient maps. From this, I reach the following conclusions:

• The bulge/disc/bar two-dimensional decomposition of the S⁴G 3.6 μm image of NGC 864 using BUDDA yields a flat-profile bar, which is typical of strong bars (Athanassoula and Misiriotis 2002) and of two-armed grand design spirals (Elmegreen and Elmegreen 1985). Flat-profile bars are linked to a higher degree

7.1 Conclusions 133

of exchange of angular momentum with the halo than exponential bars (Athanassoula 2003). Such bars can result from sharply rising rotation curves, as observed in NGC 864, and are most likely connected to the observed spatial offset between the ends of the bars and the onset of the spiral arms.

- The rotation curves obtained from the $GH\alpha FaS$ velocity maps are similar to those obtained by Epinat et al. (2008), both using $H\alpha$ observations. However, these curves do not cover all the disc and the intrinsic patchiness linked to the line emission prejudices the analysis and the derived results. Due to the high angular and spectral resolution, our new rotation curve shows considerable detail in the central $2 \, \text{kpc}$ radius.
- I have found non-circular motions along the bar in the residual maps, in the position-velocity (PV) diagram along the kinematic minor axis, and in the velocity profile along the kinematic minor axis. These velocity patterns are typical of a barred galaxy behaviour, with streaming motions along the bar.

Non-circular motions and star formation in S⁴G spirals

This chapter deals with the deviations from pure rotational motion (non-circular motions) and the relationship with SFRs, arriving at the following conclusions:

- I have created non-circular motion maps for all the galaxies of the sample. I confirm the presence of these non-circular motions created by the non-axisymmetric potential of the bar along the bar region and at the start of the spiral arms, with a tendency that the more star-forming bars induce higher non-circular motions.
- I find that the bar strength (as denoted by the parameter Q_b) does not correlate with the amplitude of the non-circular motions, but these decrease with B/T because the bulge constrains the velocities to remain more nearly circular. However, our data is biased towards bars with recent star formation, where strong shocks and shear may take place and star formation may be inhibited.
- Also, I confirm the presence of non-circular motions along the spiral arms, but there is no correlation of the amplitude of these non-circular motions with the arm class, a parameter that is related to the arm strength.
- The high non-circular motions (up to \sim 135 km s⁻¹) along the spiral arms of NGC 5678 cannot be due to the spiral arms. They may well be caused by a small bar that cannot be easily identified photometrically. Also, the interaction with its close companion may induce the deviations from the pure circular motion.

Inner rotation curves

In this chapter I present a detailed analysis of the inner parts of the rotation curves which have been derived for the set of galaxies in the kinematic survey. In particular, I study the relationship between the kinematics in the innermost parts of galaxies and several key galaxy parameters, and reach the following conclusions:

• I study the innermost parts of the rotation curves of 29 spiral galaxies with very high angular (seeing limited, \sim 1") and spectral (\sim 8 km s⁻¹) FP data, which allow

to quantify the slope of the rotation curves with higher precision than with HI data or other literature data for a galaxy sample of this size.

- I compare the slopes obtained from the circular velocity curves (rotation curves corrected for ADC), $d_R v_c(0)$, with those obtained from the velocity curves derived from the stellar-mass maps, $d_R v_*(0)$. I confirm that because the circular velocity is composed by subcomponents (stars, gas and DM), $d_R v_*(0)$ is never higher than $d_R v_c(0)$.
- The total stellar mass and the maximum rotational velocity do not correlate with the slopes of the rotation curve, although there are some limits: steep slopes are only found in more massive galaxies, and low-mass galaxies only have shallow slopes.
- I confirm that the extrapolated central surface brightness (μ_0) correlates with $d_R v(0)$. I also find a resulting scaling relation for disc galaxies, a relationship between the morphological T-type and $d_R v(0)$. This implies that for galaxies from early-type to late-type spirals, the morphological type of a galaxy is related to the dynamics in the central parts of galaxies.
- Although the bar should affect the distribution of material in the central parts of the galaxies, the bar strength (Q_b) does not correlate with $d_R v(0)$. On the contrary, due to the fact that as higher B/T, bulge mass and light concentration is correlated with steeper slopes, bulges play a role in the dynamics of the central parts of galaxies. In this sense, and regardless of the formation process of a bulge (classical or disky), the resulting concentration of material in the centres of galaxies is translated into steeper slopes, confirming Newton's classical laws.
- DM plays a dynamical role in the centres of some of the galaxies in our sample, as the gravitational potential is not exclusively determined by the stellar component. This idea comes from the fact that the stellar mass fraction is less than unity, and also because the relationships of $d_R v_*(0)$ are always tighter than those of $d_R v_c(0)$.

7.2 Future Work

The topics studied in this thesis (secular evolution, morphology, kinematics and star formation) are very broad subjects, and of course no one is completely solved. Many things need to be discovered or studied in more detail regarding these matters.

In the first place, this thesis is based on $H\alpha$ observations. Due to the nature of the $H\alpha$ emission, our study is biased towards regions with recent star formation. As a consequence, we have not been able to fully sample the bar region of all the barred galaxies of the sample. Therefore we might have lost the highest non-circular motions, or information in the central parts to derive the rotation curve there. We know that the bar potential influences the kinematics of the bar region and produces the non-circular motions. We have been able to study those in regions of star formation. Therefore and to complete the study, other tracers of atomic or molecular gas would help to fully sample the bar region and the non-circular motions there. IFU data would

7.2 Future Work 135

also help to do this, as these data also includes information about the kinematics of the stars as well as about the stellar populations.

Secondly, the galaxies observed in the kinematical survey are not sufficient in number for a well-based statistical study. More galaxies will be added to this study. In particular, $H\alpha$ FP data from the Virgo cluster (Chemin et al. 2006) and from the GHASP survey will be analysed. The overlap between these surveys and the S^4G is nearly 130 galaxies, which is a significant number that will allow a more complete kinematical study. The objective is to expand the study of the non-circular motions to this set of galaxies. One possible drawback arises from the rather bad spatial resolution and seeing of the data from the surveys cited above, where spiral arms or bars cannot be distinguished.

As the inner rotation curve analysis is concerned, more data would also be helpful, although the same angular resolution problem is found here if we use the FP data presented in the literature. The uncertainties in the measurements of the slope of the inner rotation curve would be higher, but always less than when using HI data. In this context, the upcoming surveys (MaNGA, MUSE, WEAVE, KMOS, SAMI...) will bring new kinematical 3D data to the scientific community. These data would also help to achieve the kinematical goals proposed here by providing kinematic data cubes for samples of $\sim 10^4$ galaxies, although an overlap with the S⁴G sample will not be always present (as for MaNGA).

The inner rotation curve study has shown that the bulge plays a major role in the dynamics of the central parts. However, we have not been able to determine the relationship of the slope of the rotation curve with the bar strength itself. We have used Q_b , which is a parameter that is influenced by the bulge. We would need another parameter that accounts for the bar strength without being influenced by other structure. It would be nice to have spiral arm *strength maps* similar to those we have for the bar strength, in order to obtain the spiral strength too.

The scientific goals proposed in the thesis outline (Sect. 1.6) have not been totally reached in this thesis. Specifically, I have not studied the outer disc kinematics with our FP data. This will be done in Leaman et al. (in preparation). This paper will include the relationships between the dark matter halo properties, the total mass of the galaxy and the gravitational potential, but HI data is required and we do not have those for the galaxies of the sample.

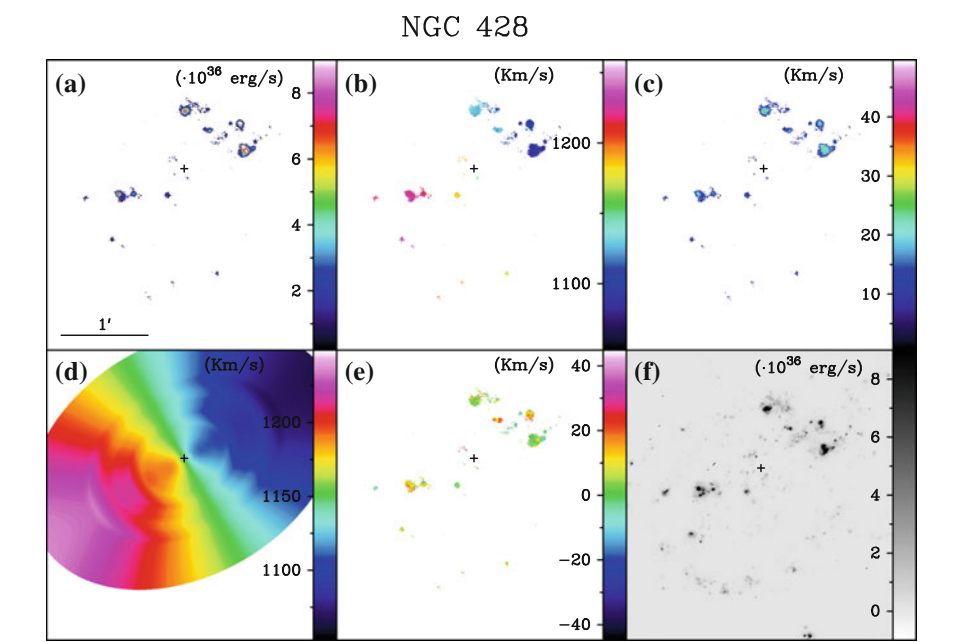
In addition, there are several scientific topics to be studied that have been mentioned along this thesis, and that are not completely understood by the scientific community. Some examples are the star formation within bars, the kinematics of disc-like bulges, or the link between the inner slope of the rotation curve and the DM profile (the *cusp vs. core* problem, see Sect. 6.4.3).

References

- E. Athanassoula, MNRAS 341, 1179 (2003)
- E. Athanassoula, A. Misiriotis, MNRAS 330, 35 (2002)
- L. Chemin, C. Balkowski, V. Cayatte et al., MNRAS 366, 812 (2006)
- B.G. Elmegreen, D.M. Elmegreen, ApJ 288, 438 (1985)
- B. Epinat, P. Amram, M. Marcelin, MNRAS 390, 466 (2008)

Appendix A Figures: Individual Maps

See Figs. A.1, A.2, A.3, A.4, A.5, A.6, A.7, A.8, A.9, A.10, A.11, A.12, A.13, A.14 and A.15



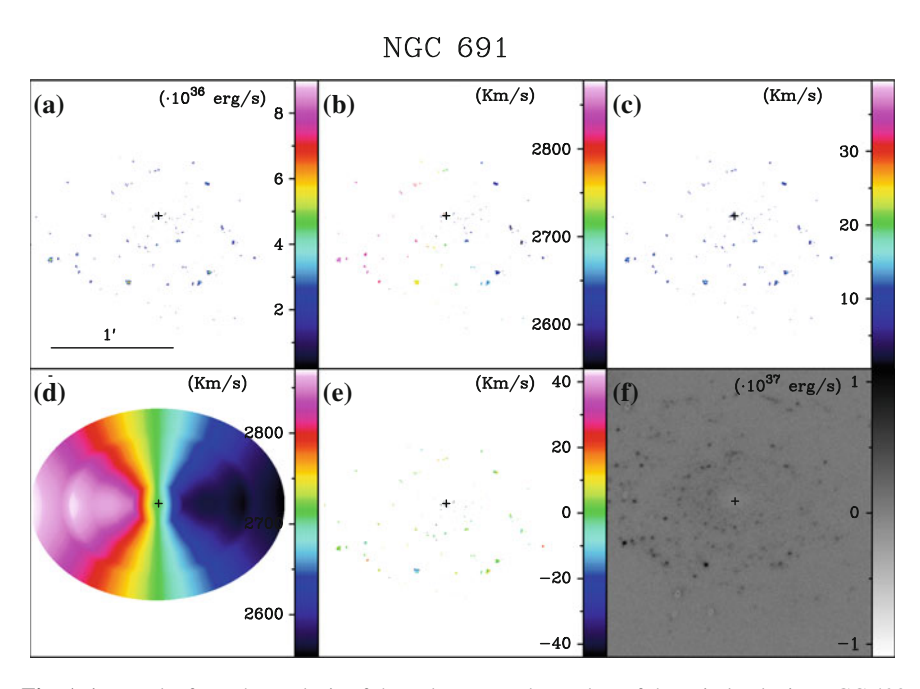


Fig. A.1 Results from the analysis of the Fabry-Perot data cubes of the spiral galaxies NGC 428 (top) and NGC 691 (bottom). For each galaxy, **a** $H\alpha$ intensity map. **b** Velocity map. **c** Velocity dispersion map. **d** Velocity model map. **e** Non-circular motions map. **f** $H\alpha$ narrow-band image from ACAM. In the images, North is up and East to the left. All the images have the same scale

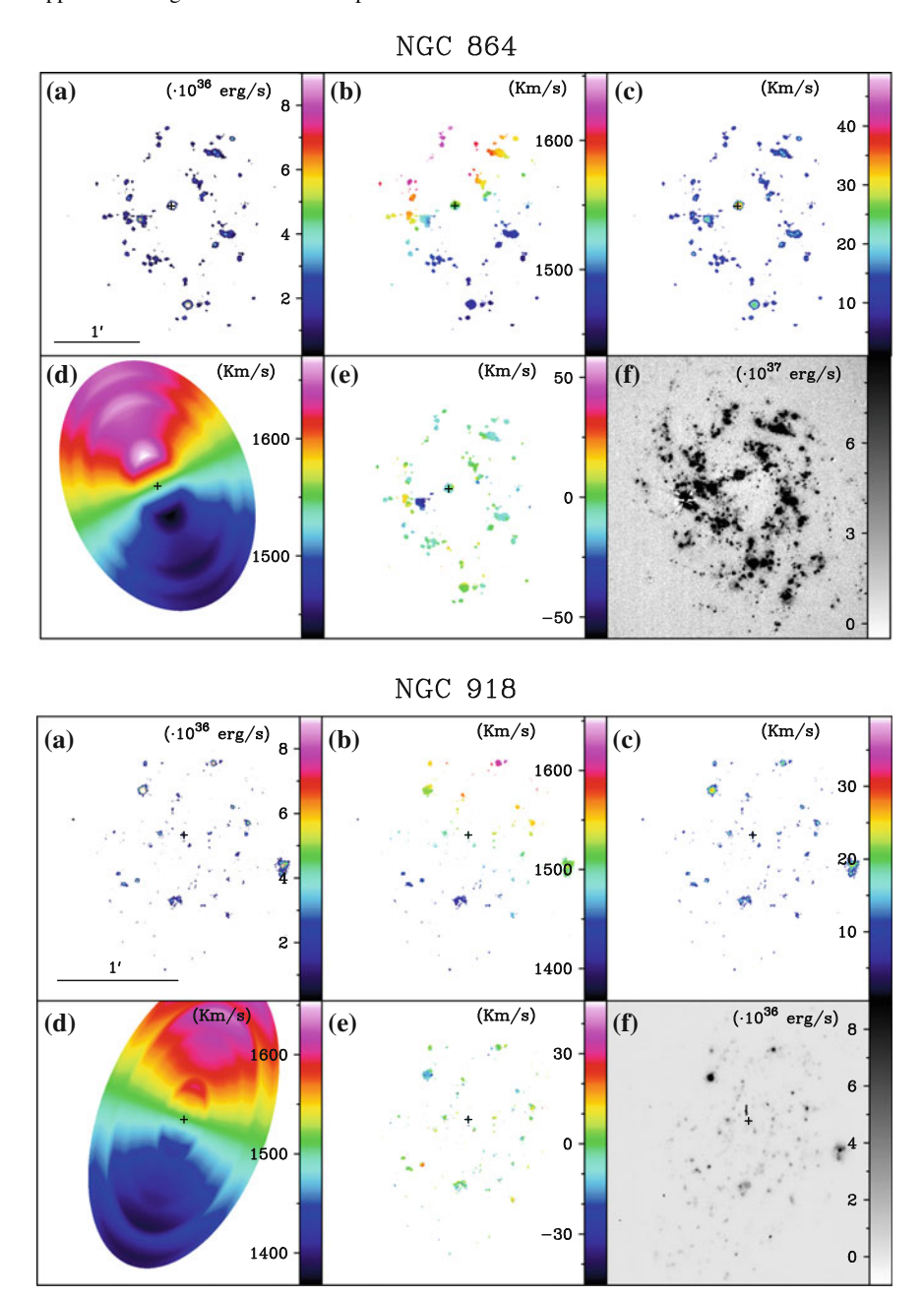


Fig. A.2 Same as Fig. A.1 but for NGC 864 (top) and NGC 918 (bottom)

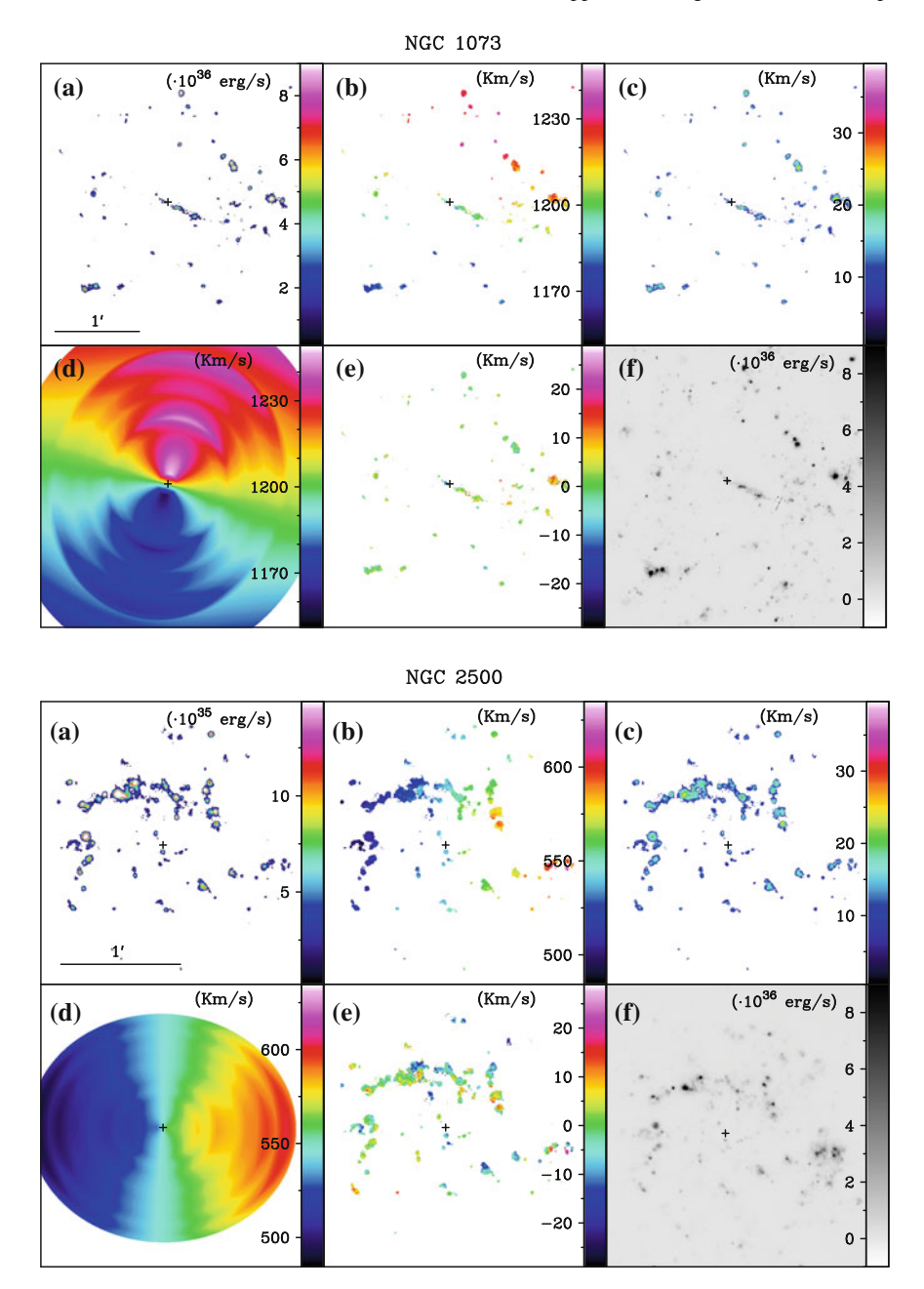


Fig. A.3 Same as Fig. A.1 but for NGC 1073 (top) and NGC 2500 (bottom)

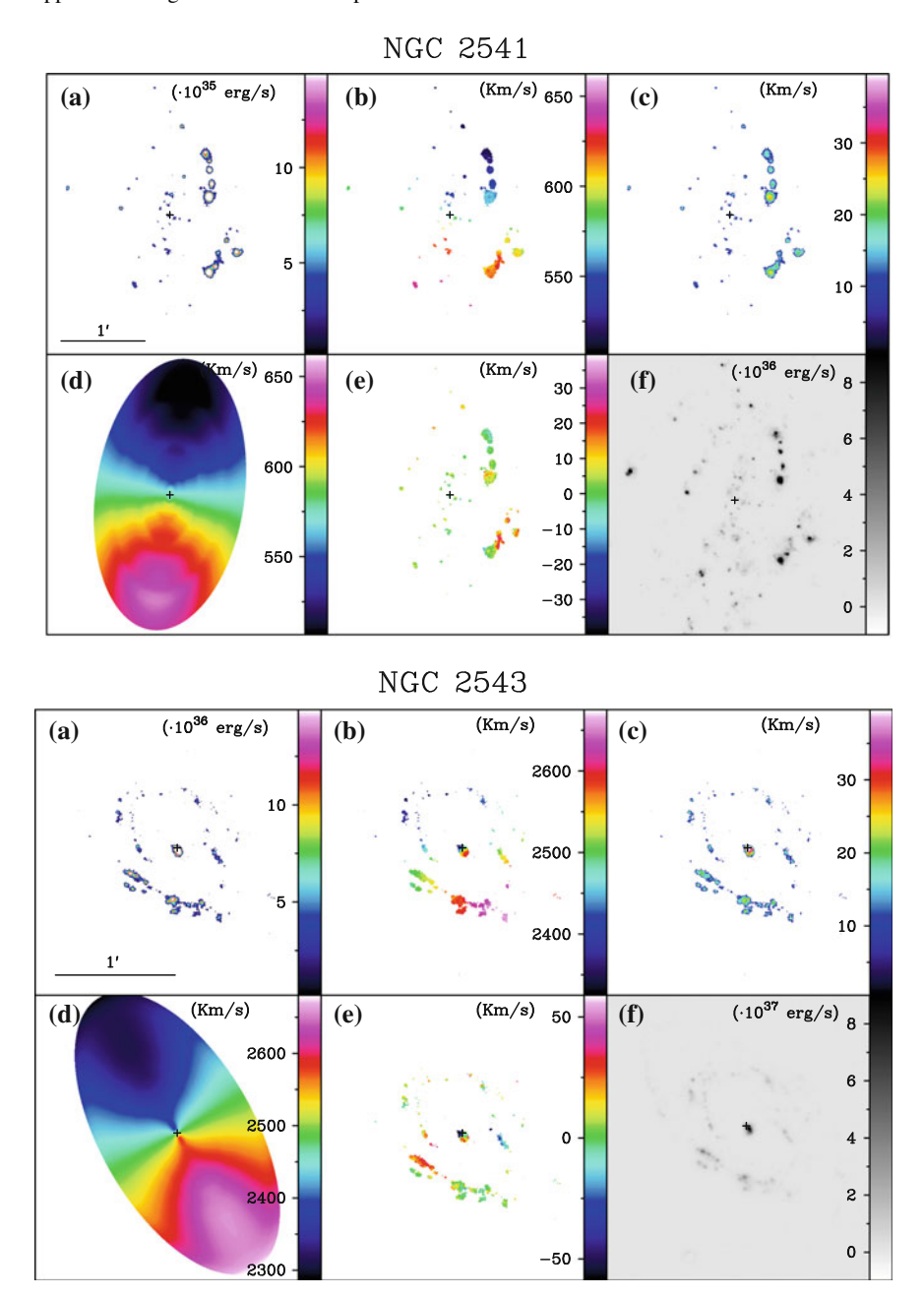


Fig. A.4 Same as Fig. A.1 but for NGC 2541 (top) and NGC 2543 (bottom)

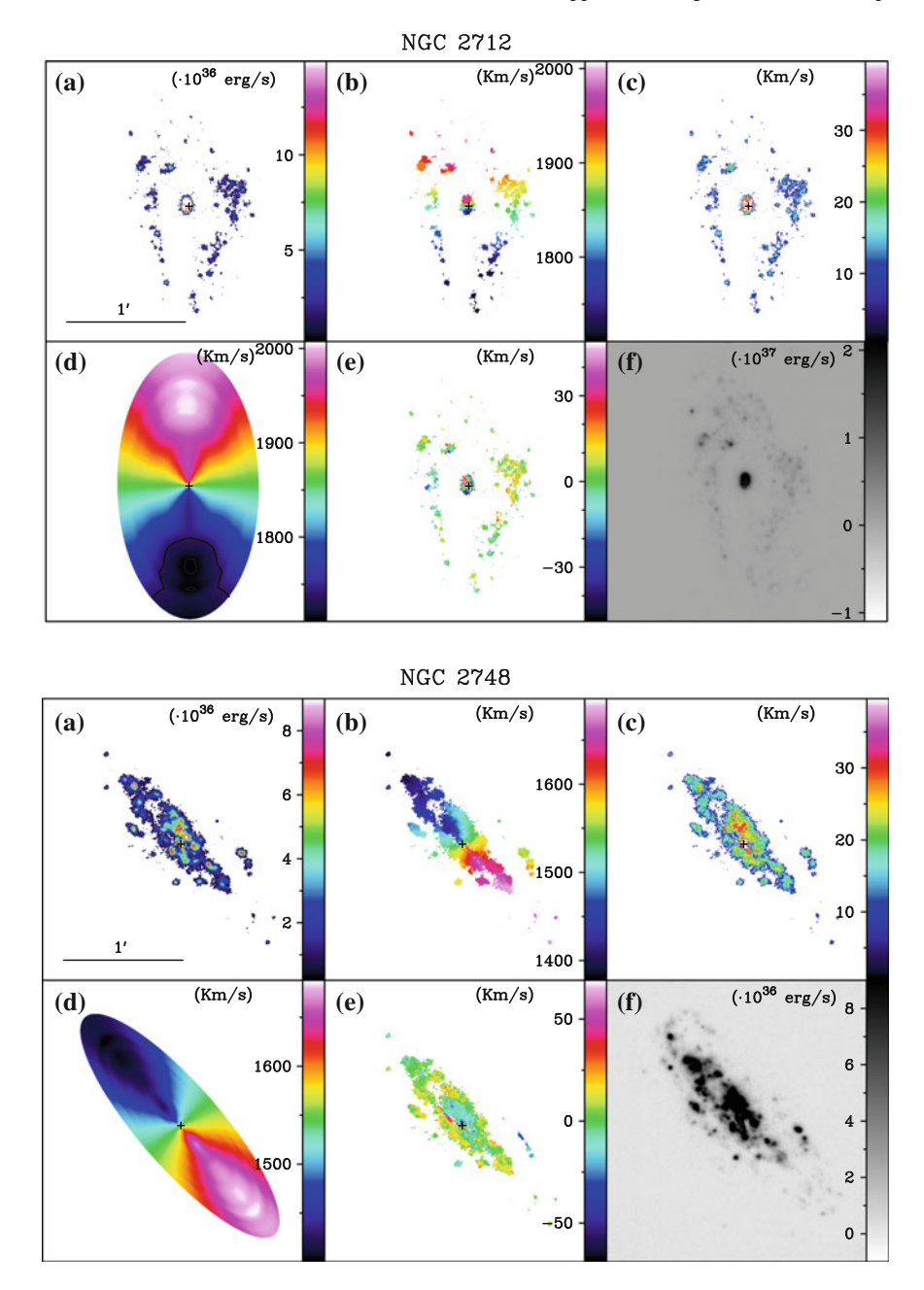
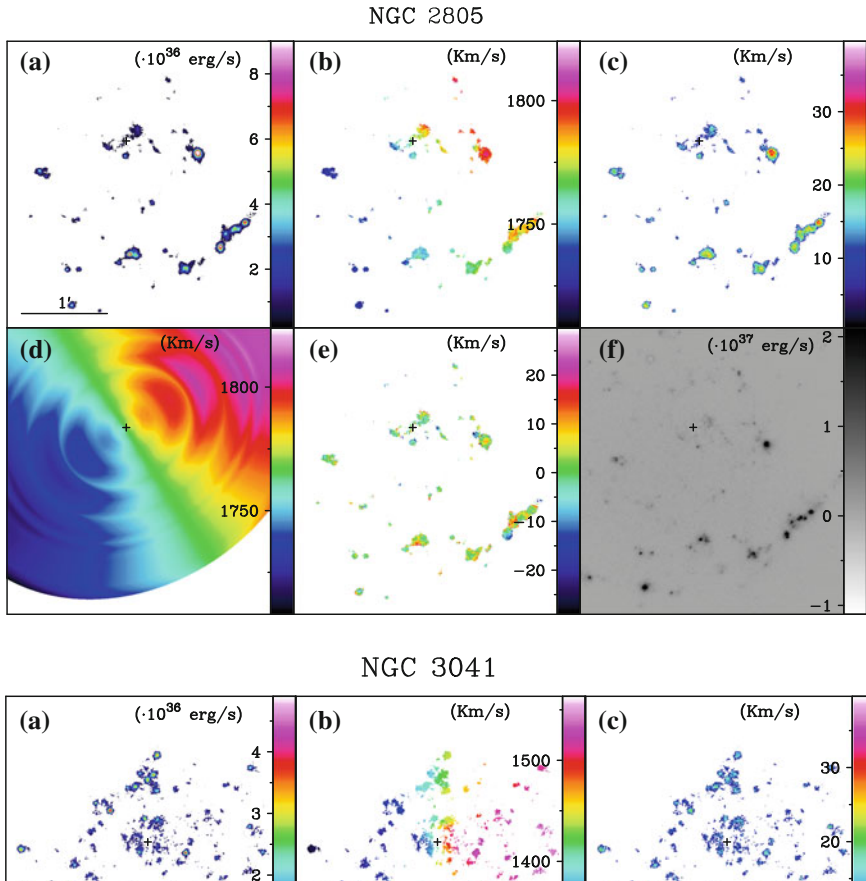


Fig. A.5 Same as Fig. A.1 but for NGC 2712 (top) and NGC 2748 (bottom)



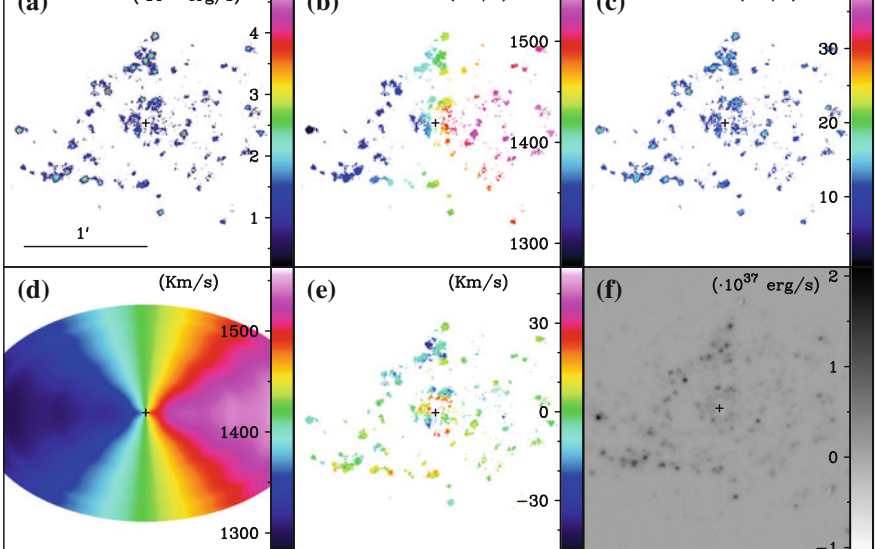


Fig. A.6 Same as Fig. A.1 but for NGC 2805 (top) and NGC 3041 (bottom)

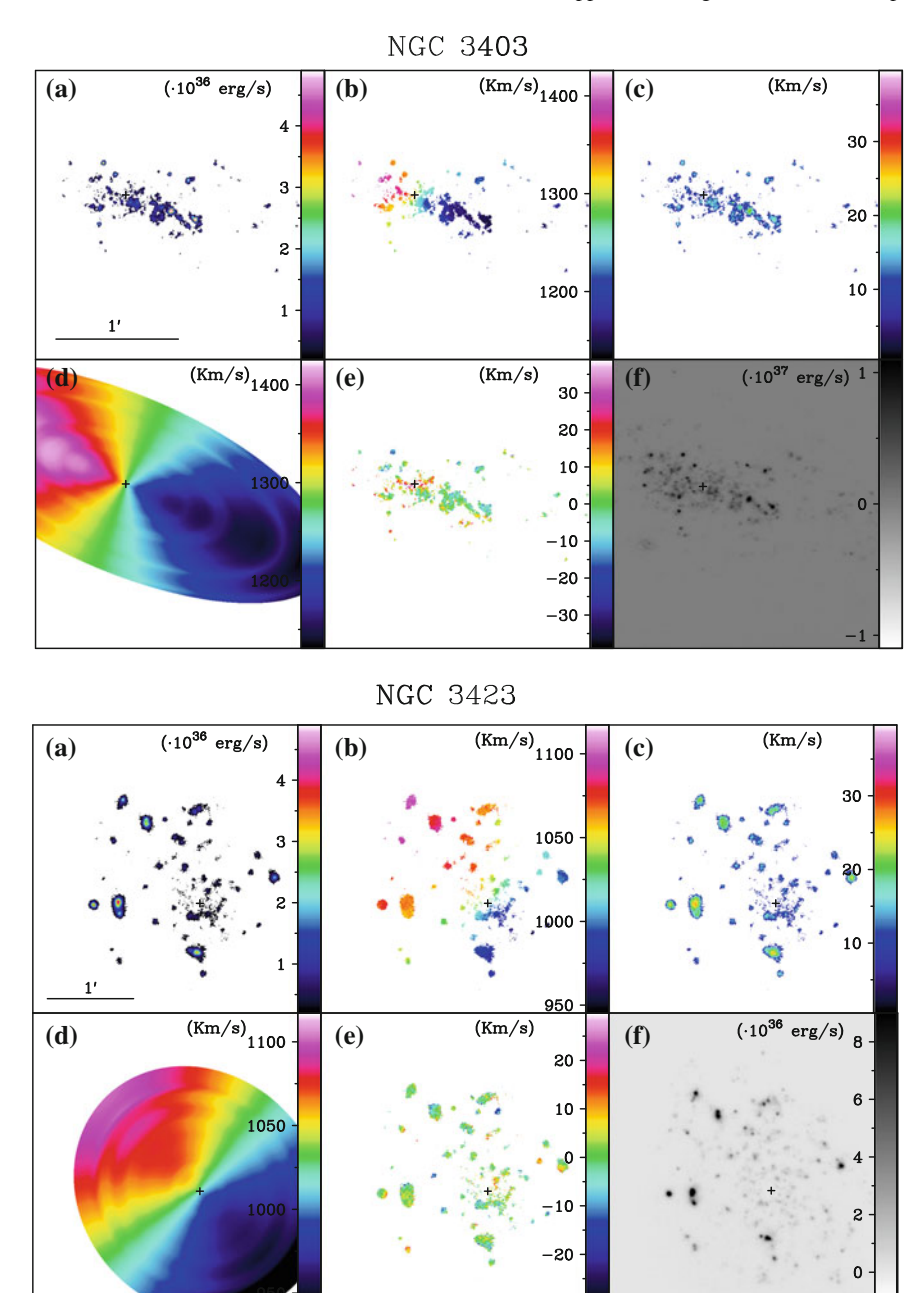
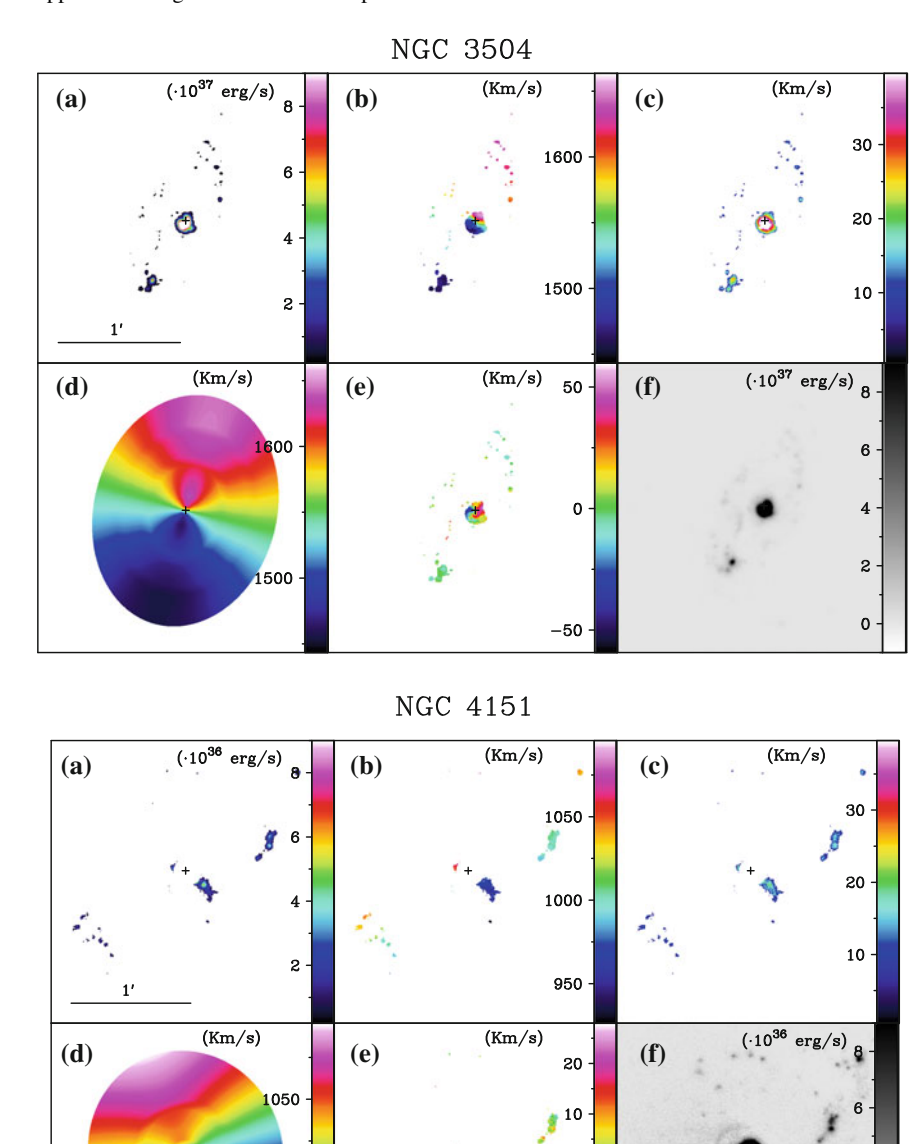


Fig. A.7 Same as Fig. A.1 but for NGC 3403 (top) and NGC 3423 (bottom)

2



0 · -10 ·

-20

Fig. A.8 Same as Fig. A.1 but for NGC 3504 (top) and NGC 4151 (bottom)

950

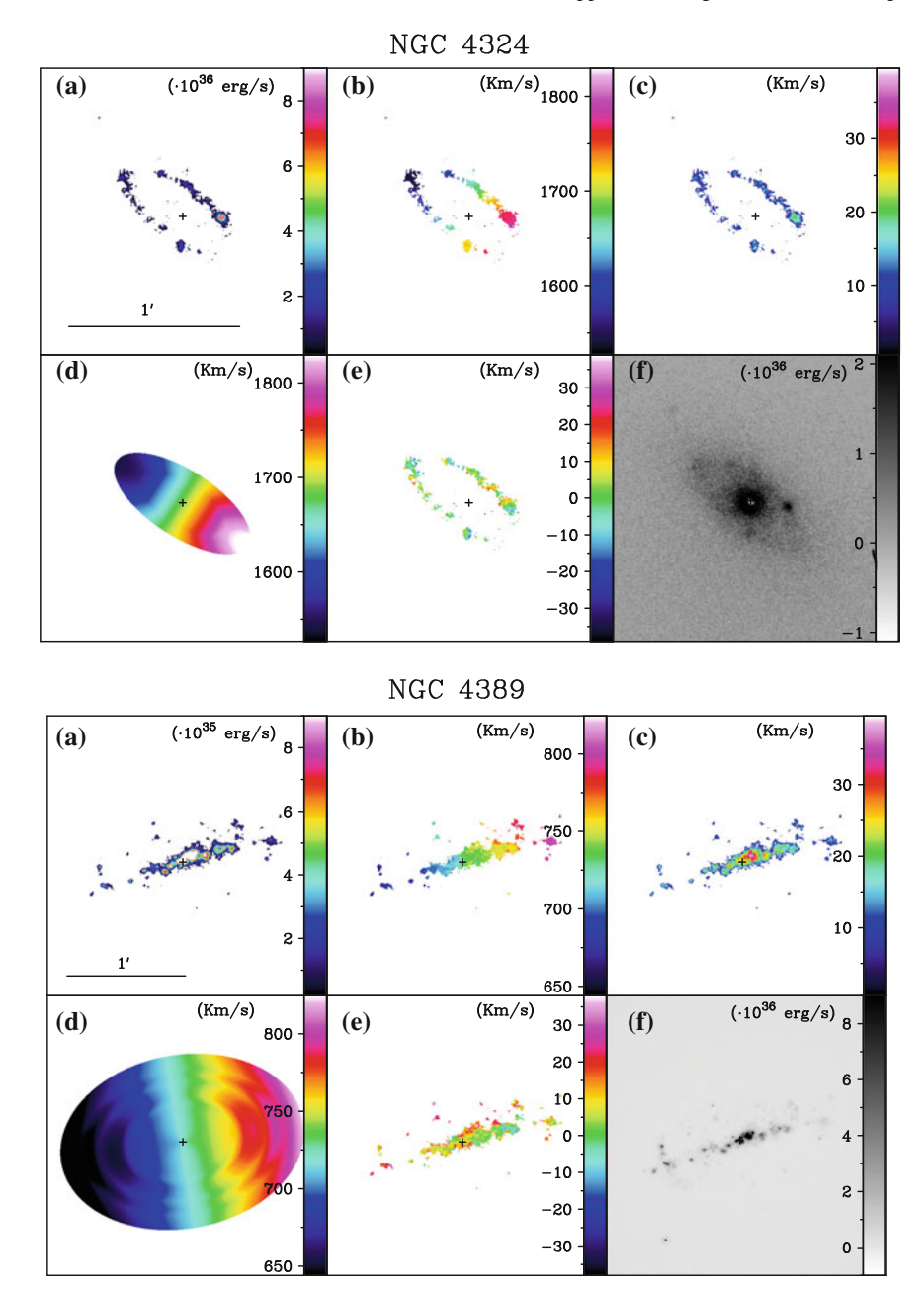


Fig. A.9 Same as Fig. A.1 but for NGC 4324 (top) and NGC 4389 (bottom)

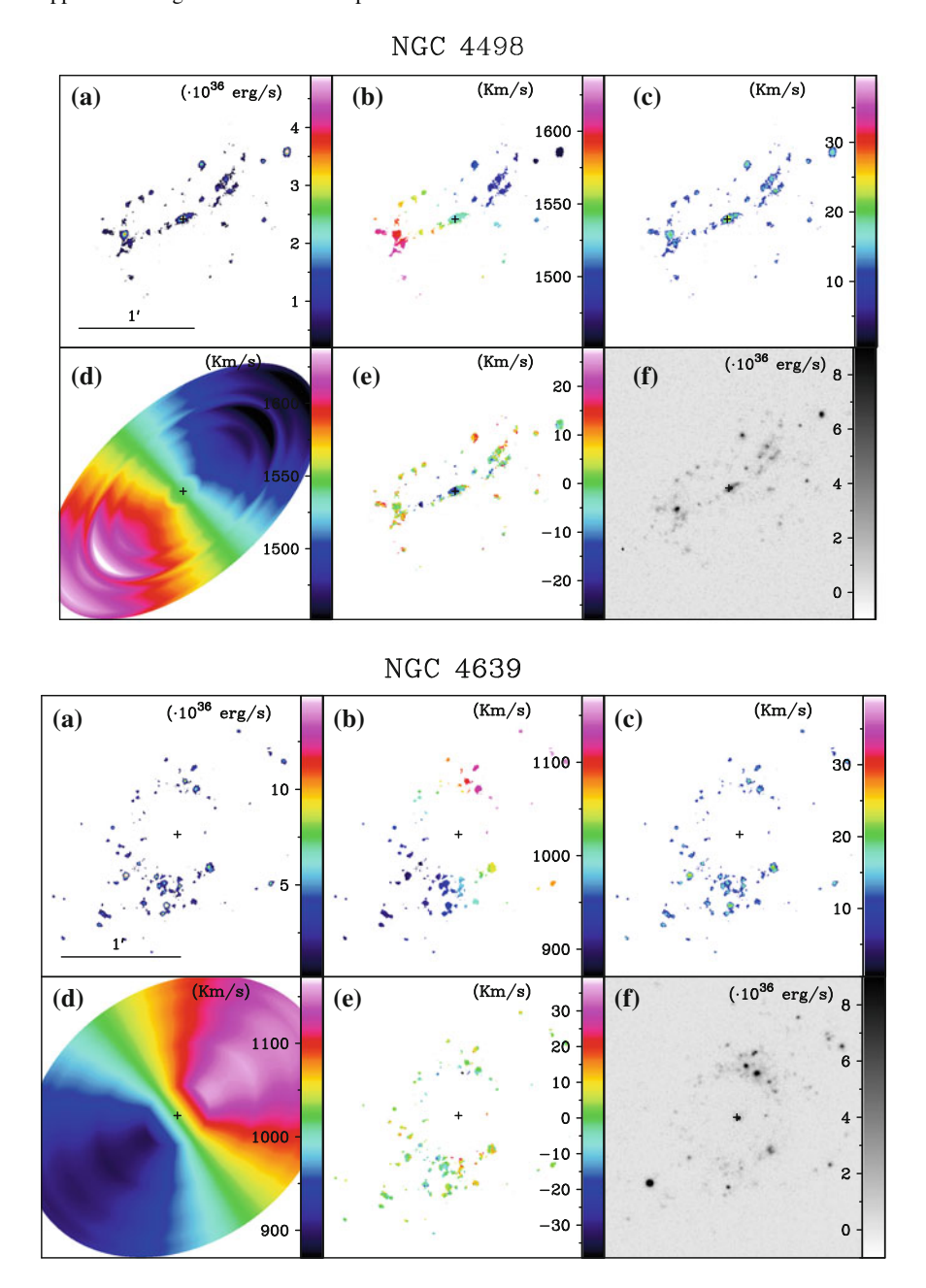


Fig. A.10 Same as Fig. A.1 but for NGC 4498 (top) and NGC 4639 (bottom)

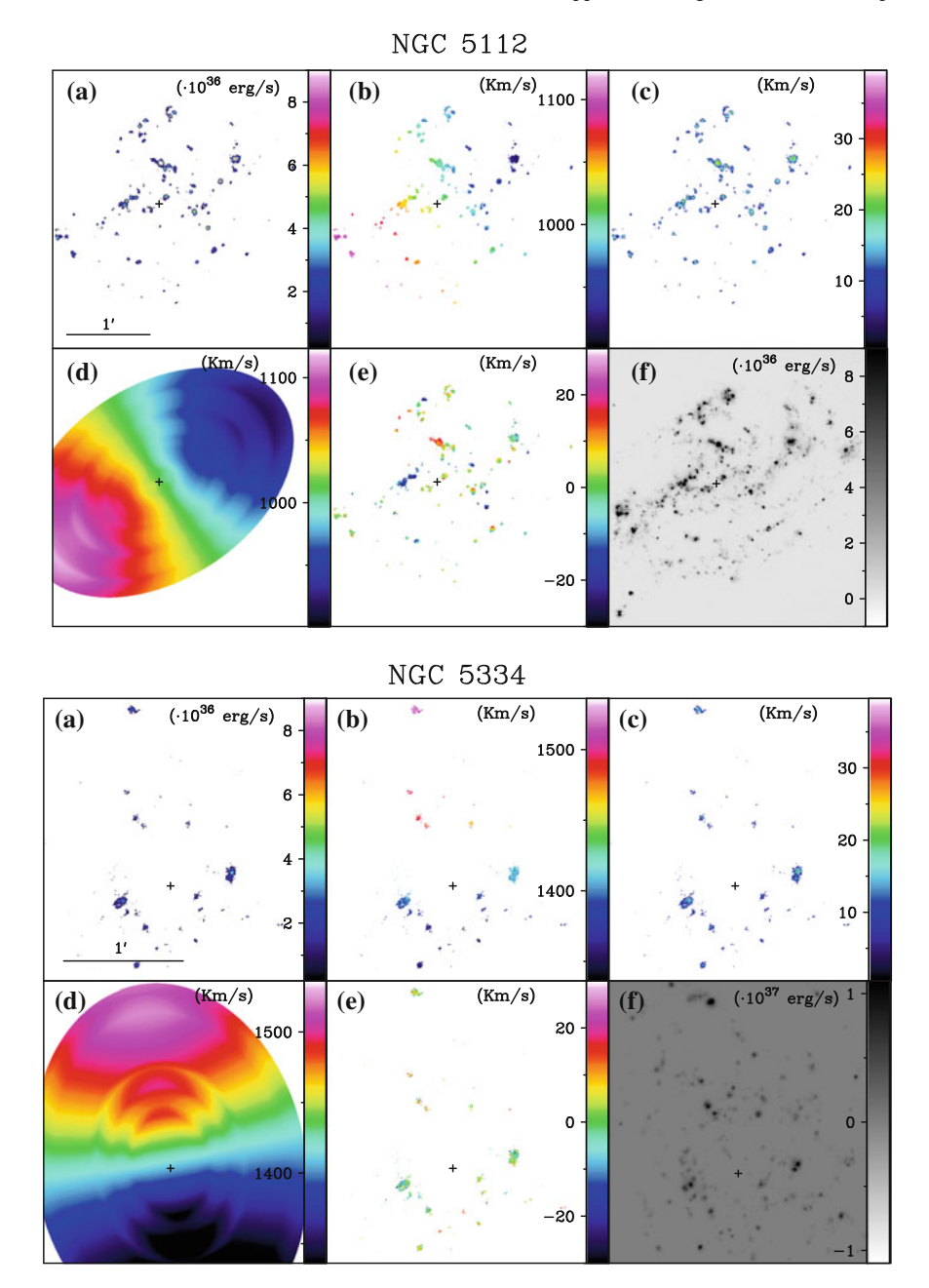


Fig. A.11 Same as Fig. A.1 but for NGC 5112 (top) and NGC 5334 (bottom)

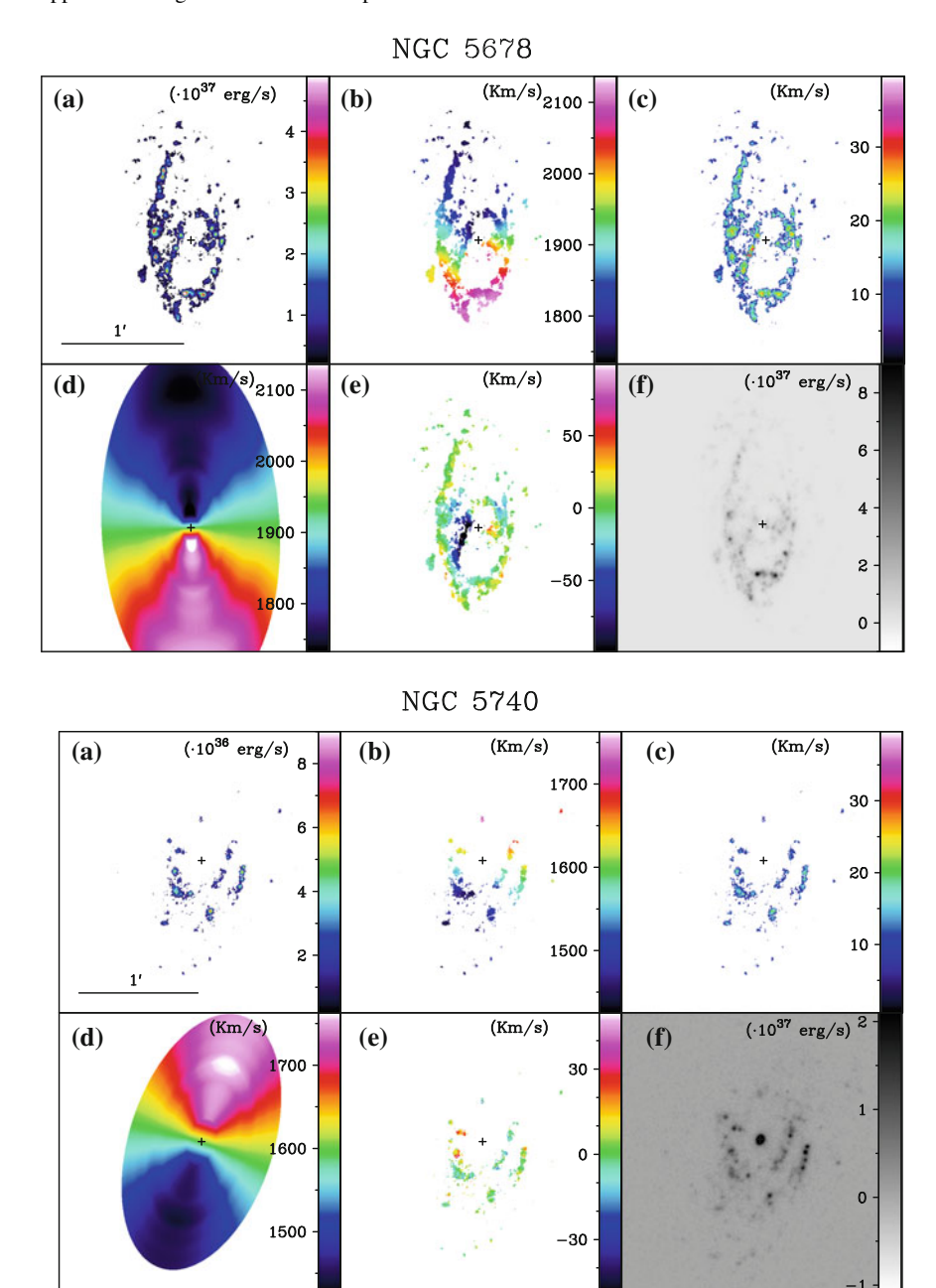


Fig. A.12 Same as Fig. A.1 but for NGC 5678 (top) and NGC 5740 (bottom)

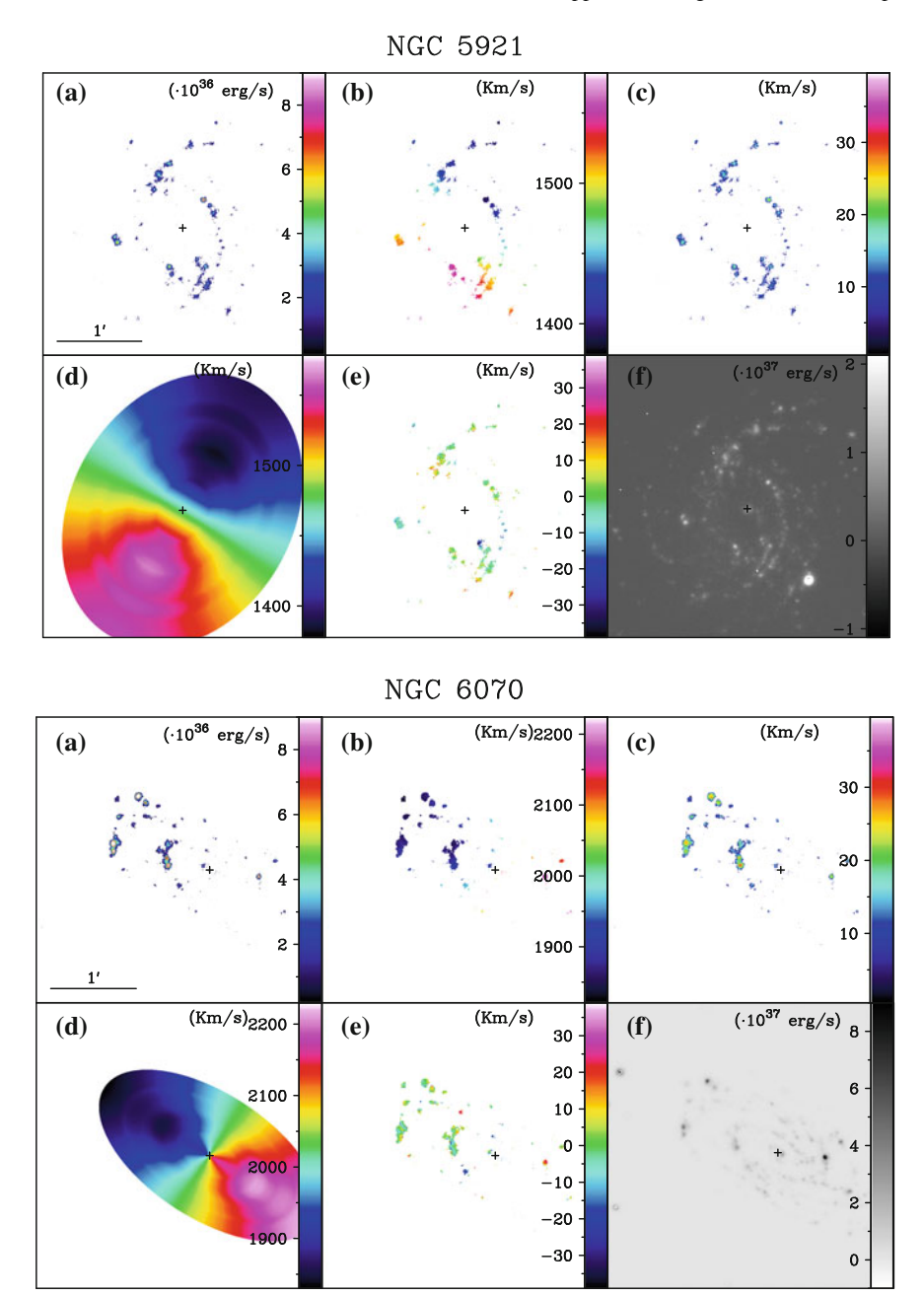


Fig. A.13 Same as Fig. A.1 but for NGC 5921 (top) and NGC 6070 (bottom)

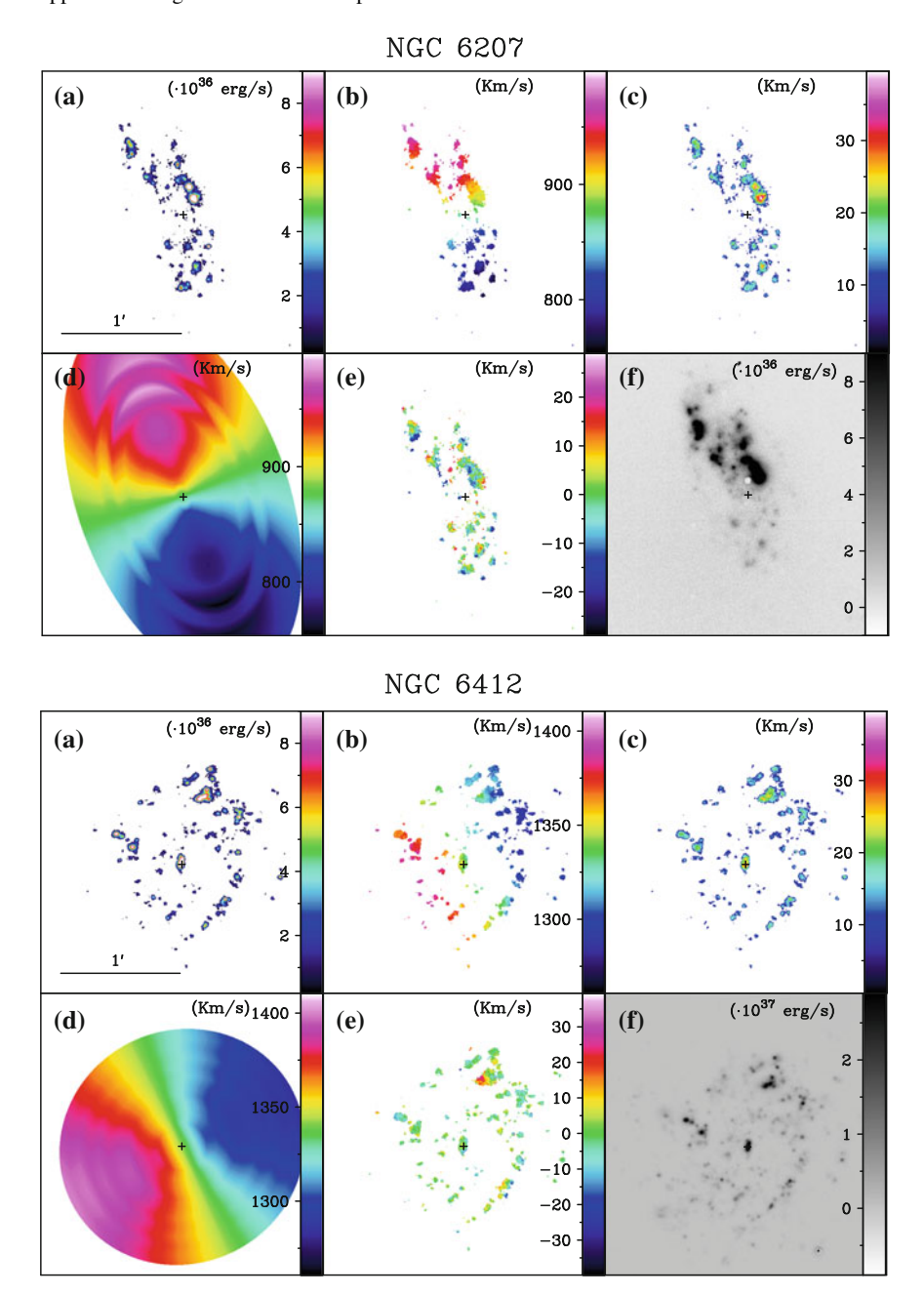


Fig. A.14 Same as Fig. A.1 but for NGC 6207 (top) and NGC 6412 (bottom)

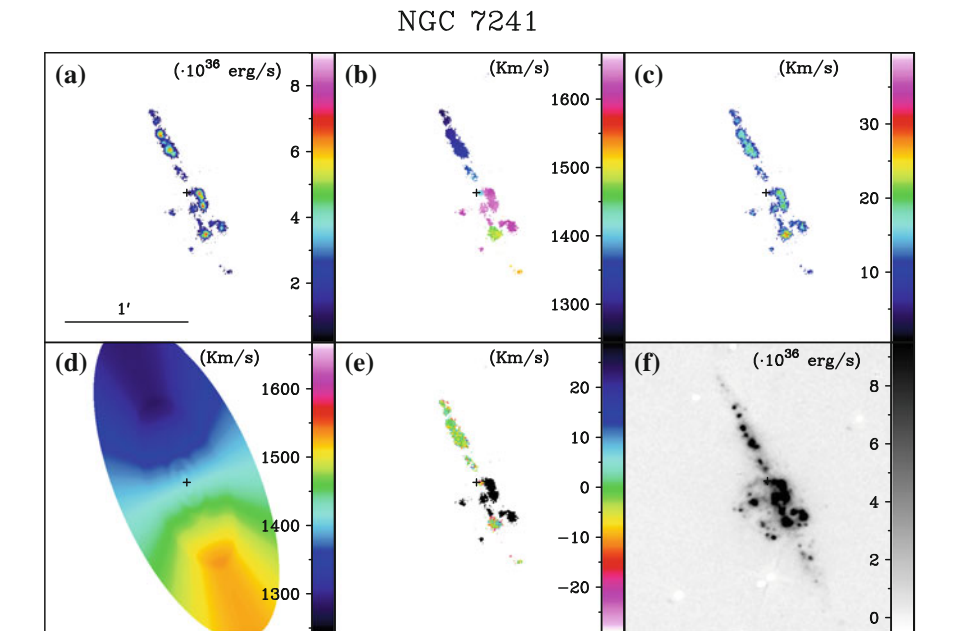


Fig. A.15 Same as Fig. A.1 but for NGC 7241

Appendix B Rotation Curves

See Figs. B.1, B.2, B.3 and B.4

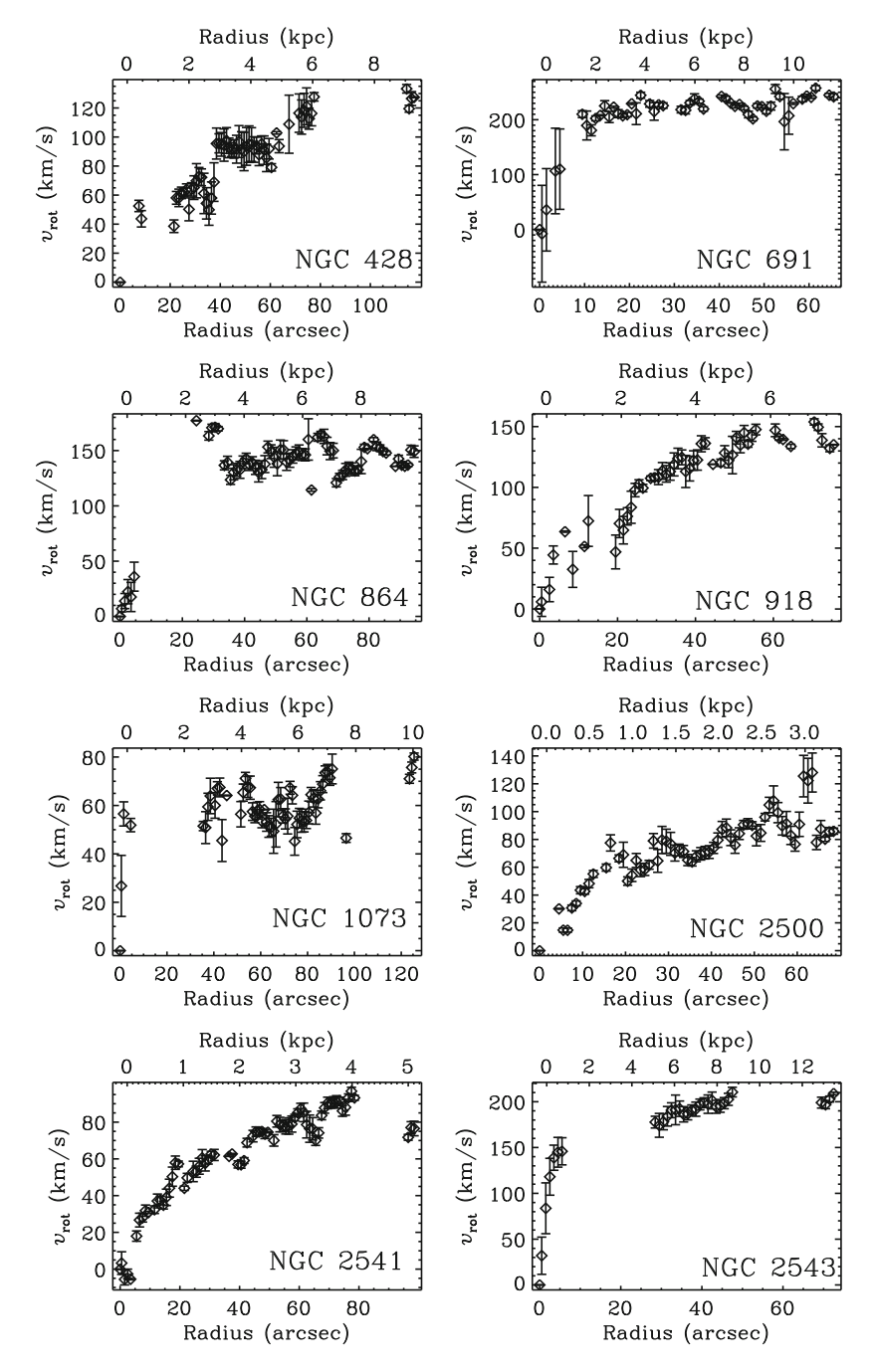


Fig. B.1 High-resolution rotation *curves* for NGC 428, NGC 691, NGC 864, NGC 918, NGC 1073, NGC 2500, NGC 2541 and NGC 2543

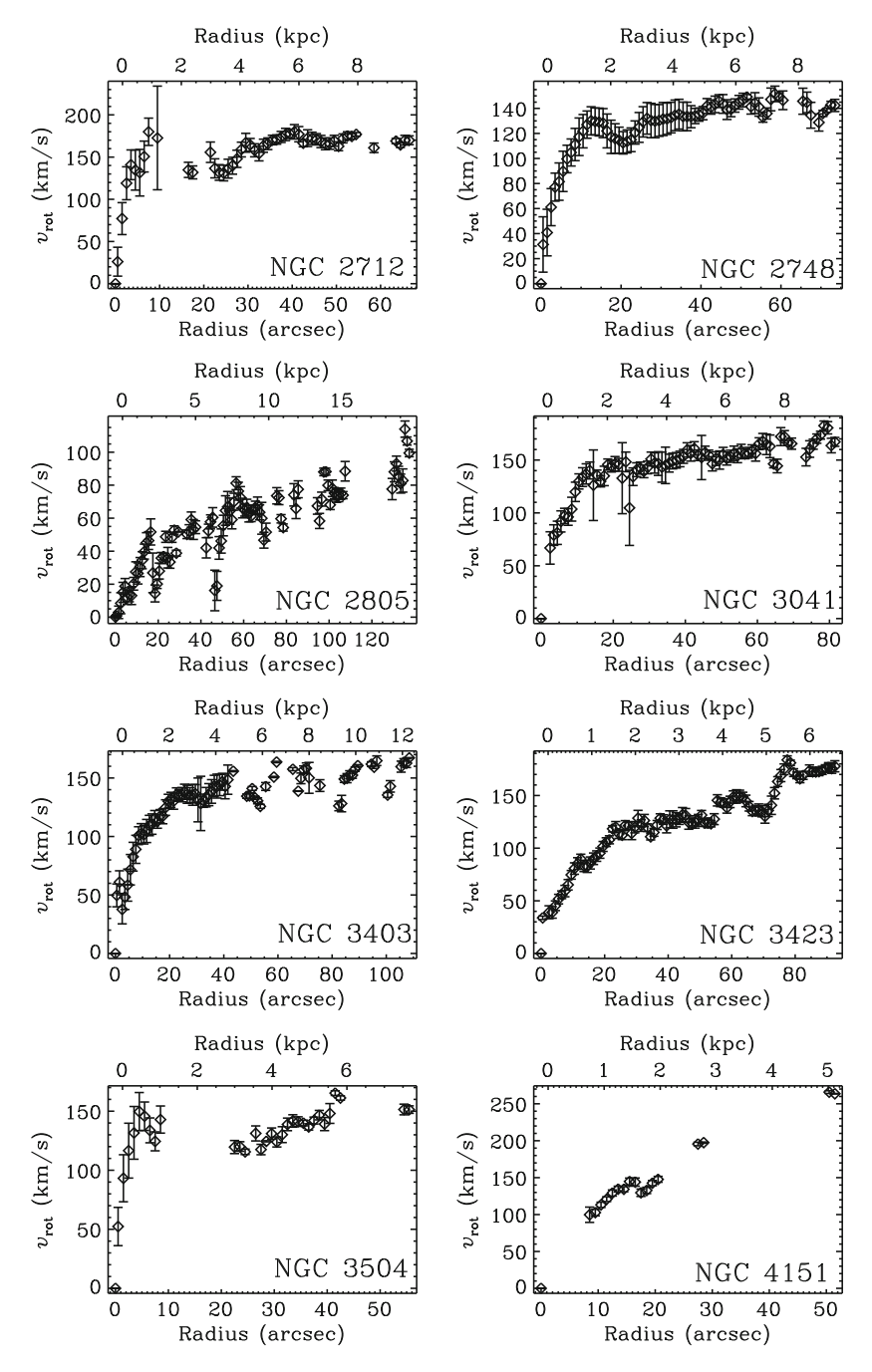


Fig. B.2 High-resolution rotation *curves* for NGC 2712, NGC 2748, NGC 2805, NGC 3041, NGC 3403, NGC 3423, NGC 3504 and NGC 4151

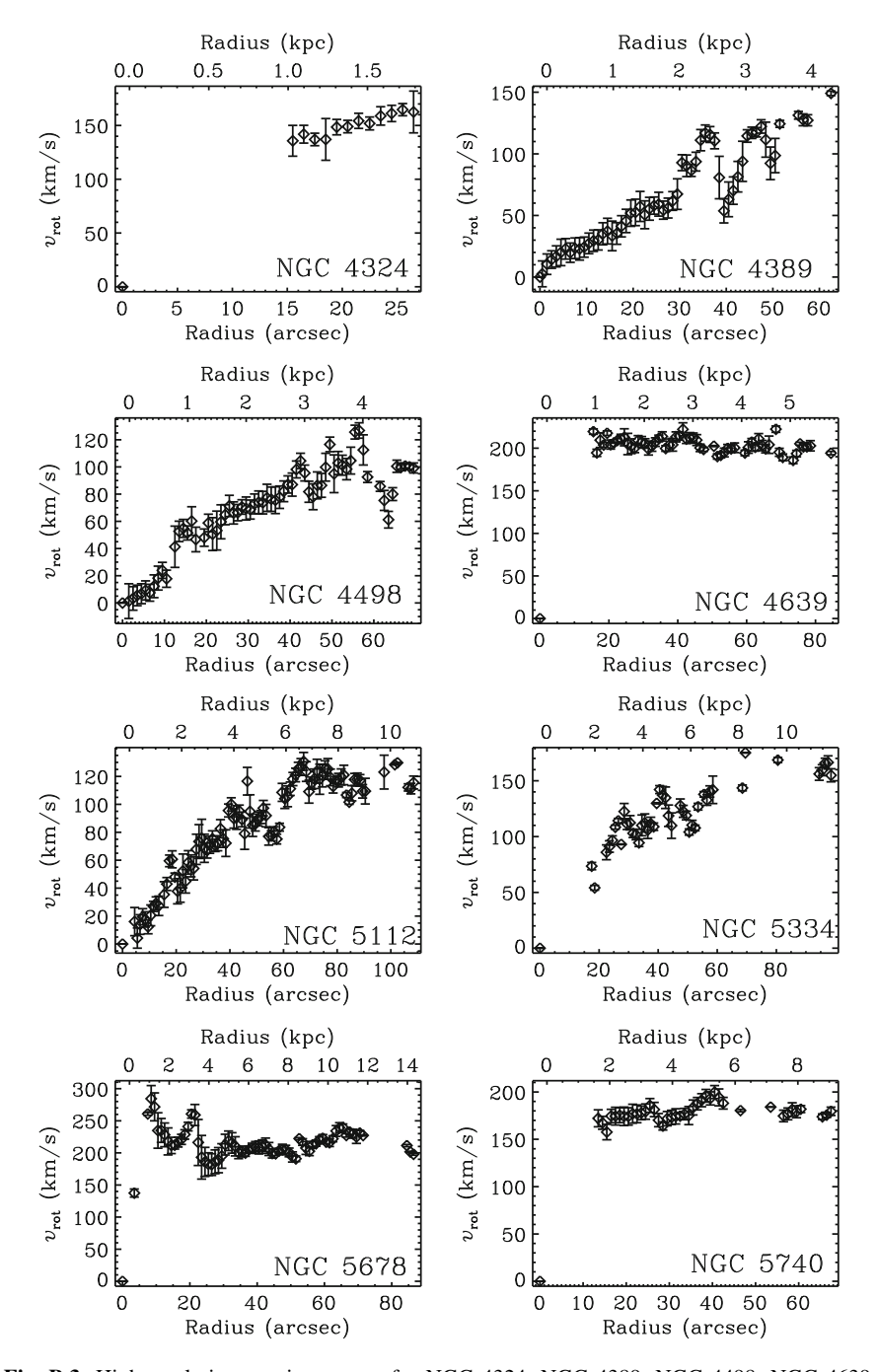
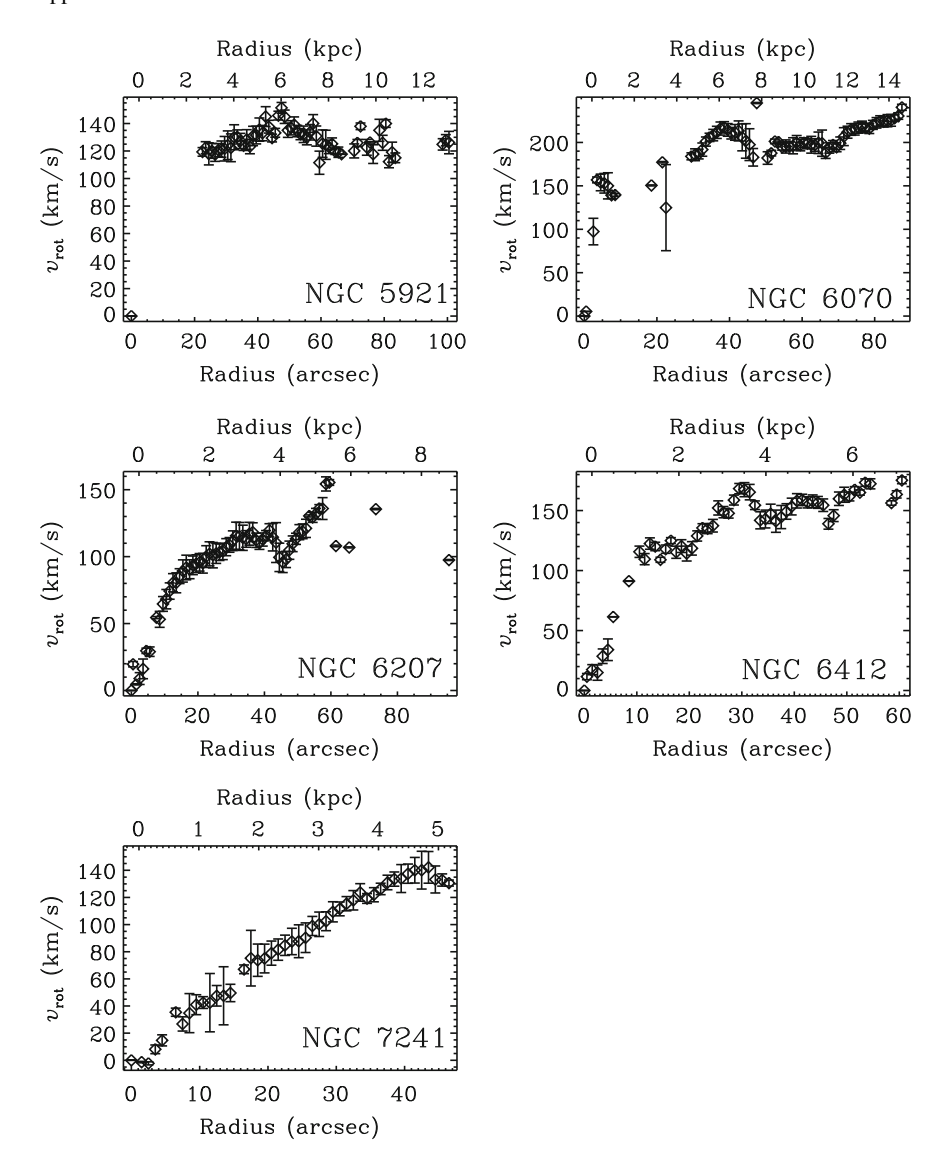


Fig. B.3 High-resolution rotation *curves* for NGC 4324, NGC 4389, NGC 4498, NGC 4639, NGC 5112, NGC 5334, NGC 5678 and NGC 5740



 $\textbf{Fig. B.4} \quad \text{High-resolution } \textit{curves} \text{ for NGC 5921, NGC 6070, NGC 6207, NGC 6412 and NGC 7241}$

Appendix C Position-Velocity Diagrams

See Figs. C.1, C.2, C.3, C.4, C.5, C.6, C.7 and C.8

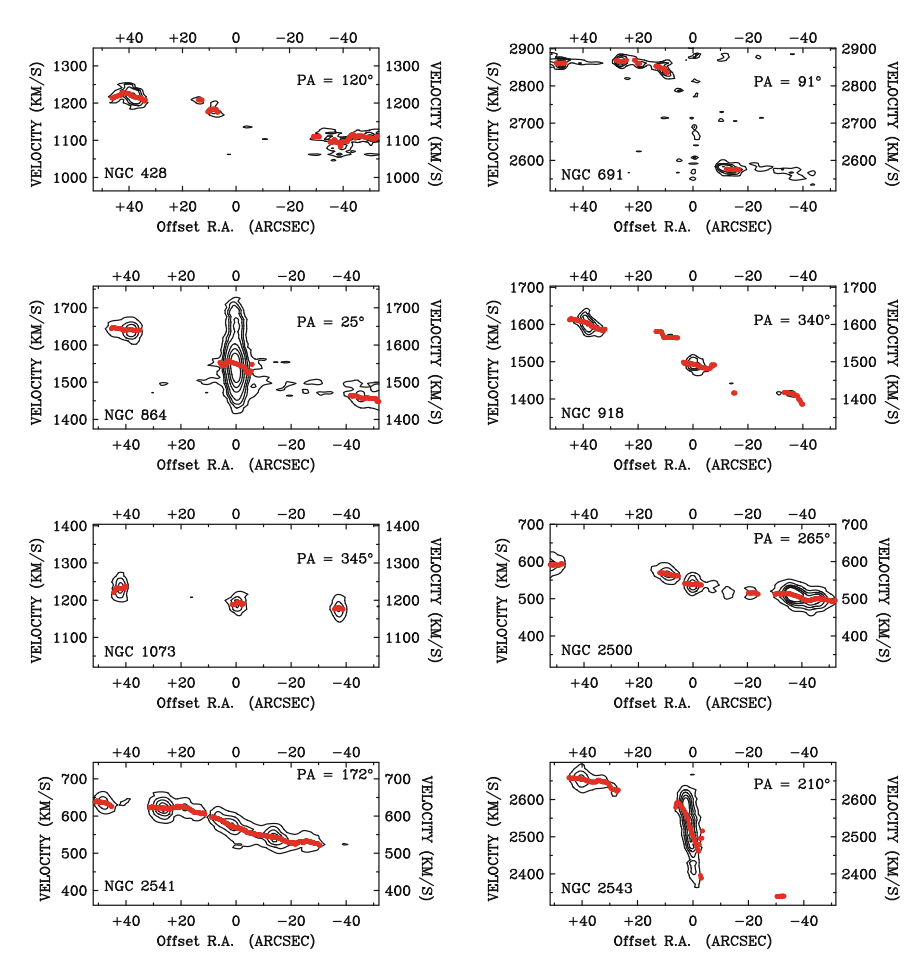


Fig. C.1 Position-Velocity (PV) diagrams along the kinematical major axis for NGC 428, NGC 691, NGC 864, NGC 918, NGC 1073, NGC 2500, NGC 2541 and NGC 2543. In each plot, overlaid (*red dots*) is the velocity profile for the whole disc at the corresponding angle (color online)

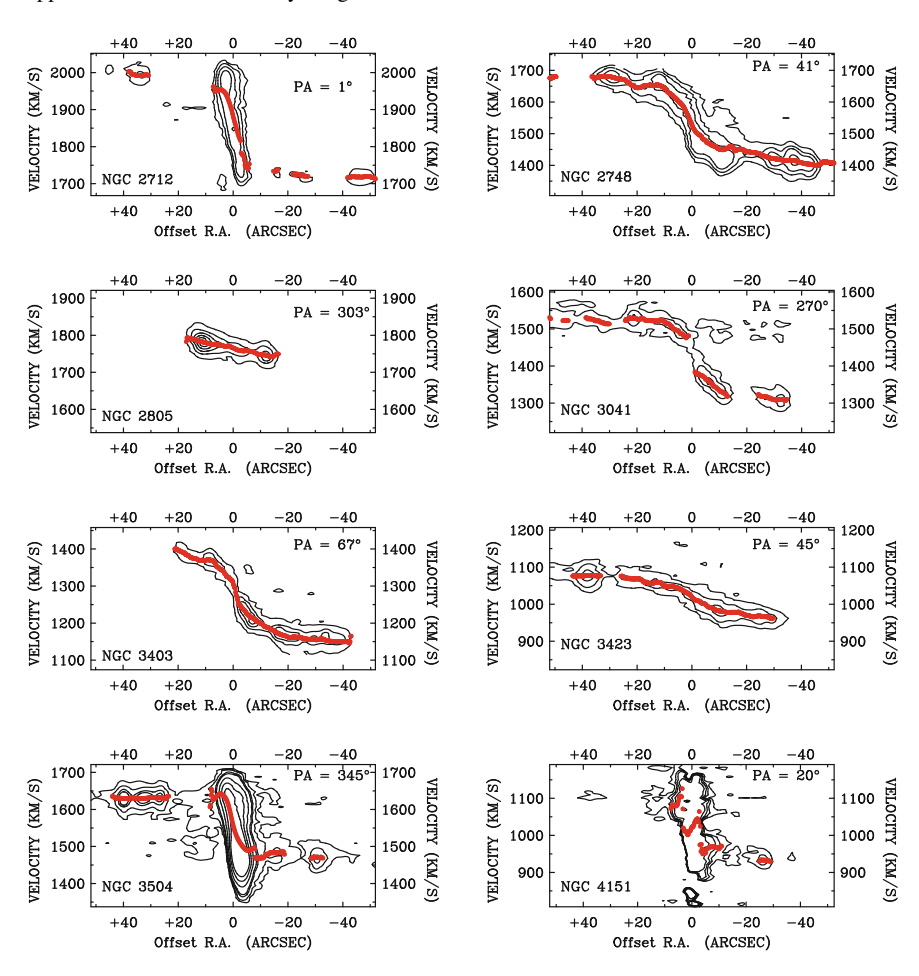


Fig. C.2 As Fig. C.1 but for NGC 2712, NGC 2748, NGC 2805, NGC 3041, NGC 3403, NGC 3423, NGC 3504 and NGC 4151

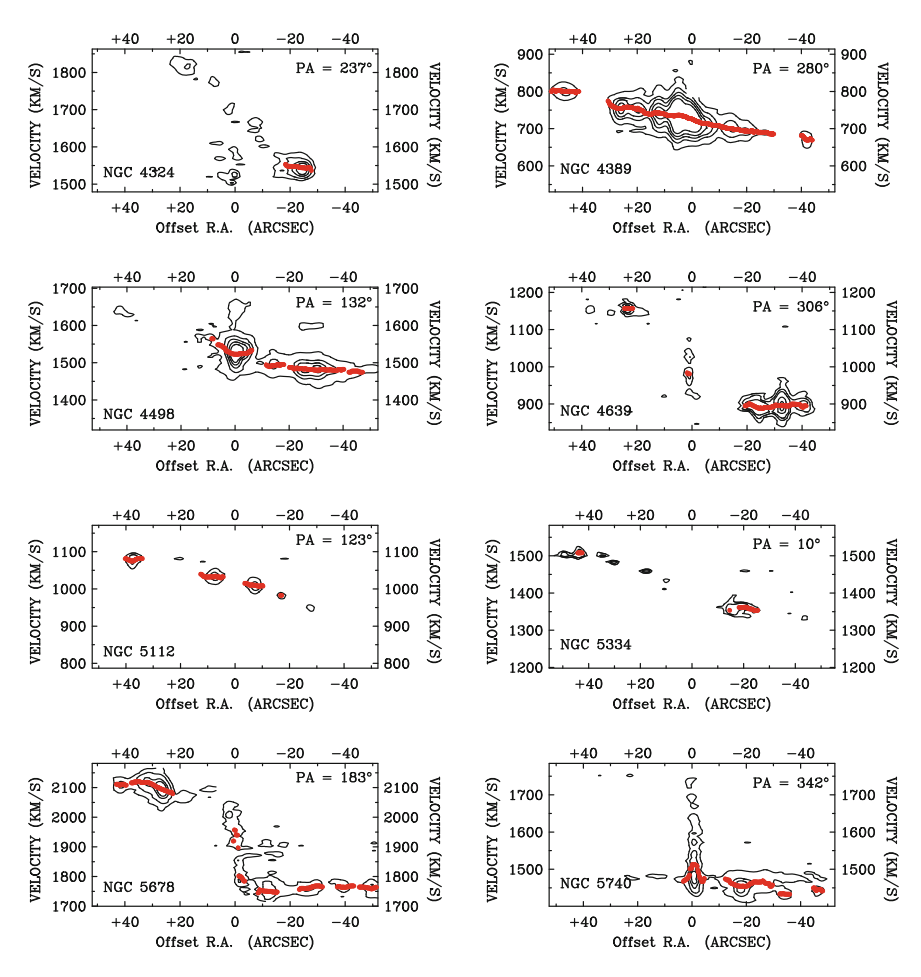


Fig. C.3 As Fig. C.1 but for NGC 4324, NGC 4389, NGC 4498, NGC 4639, NGC 5112, NGC 5334, NGC 5678 and NGC 5740

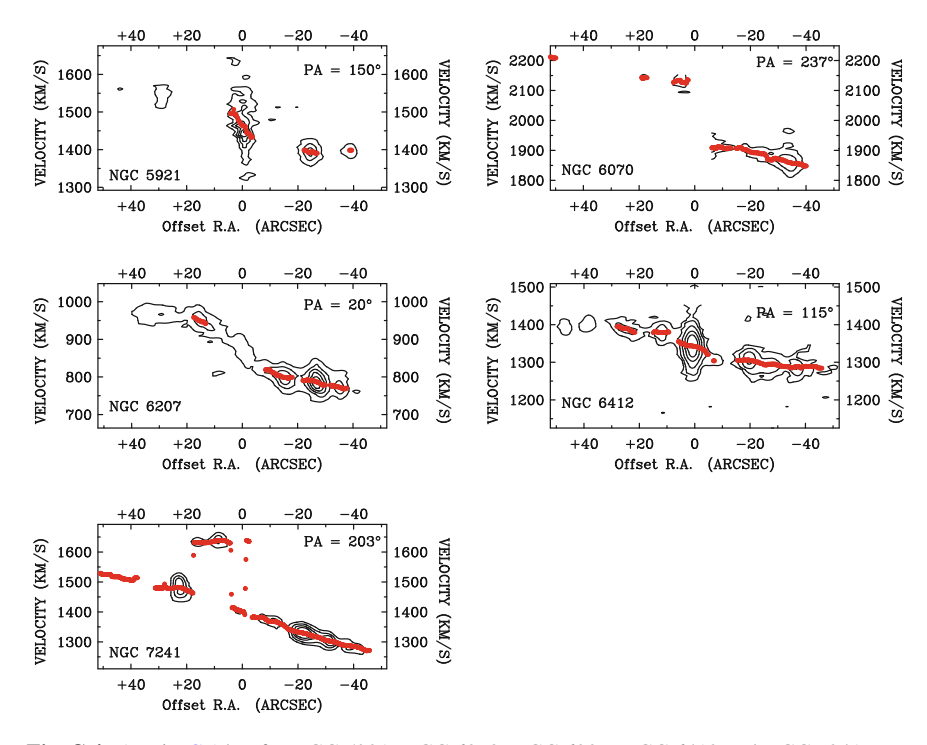


Fig. C.4 As Fig. C.1 but for NGC 5921, NGC 6070, NGC 6207, NGC 6412 and NGC 7241

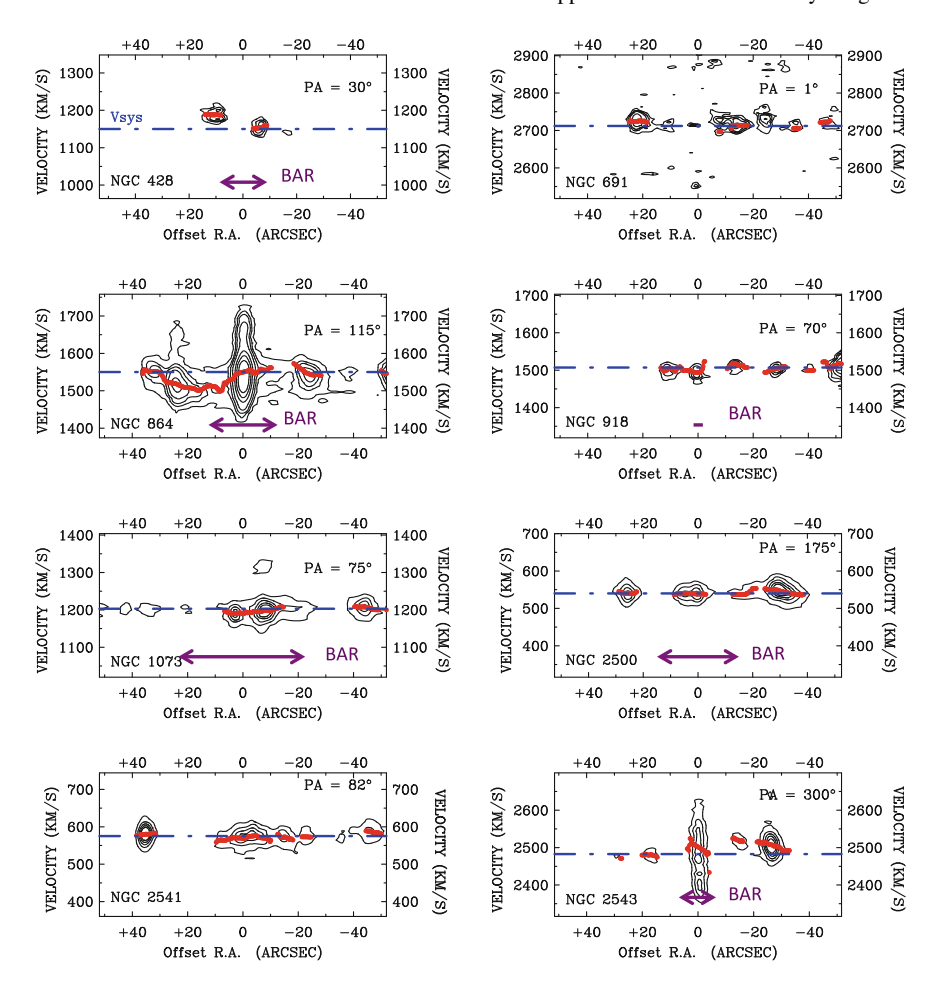


Fig. C.5 PV diagrams along the kinematical minor axis for NGC 428, NGC 691, NGC 864, NGC 918, NGC 1073, NGC 2500, NGC 2541 and NGC 2543. In each plot, overlaid (*red dots*) is the velocity profile for the whole disc at the corresponding angle. Also, the systemic velocity is presented with a *horizontal blue dashed line*. For the barred galaxies, the deprojected length of the bar has also been presented (color online)

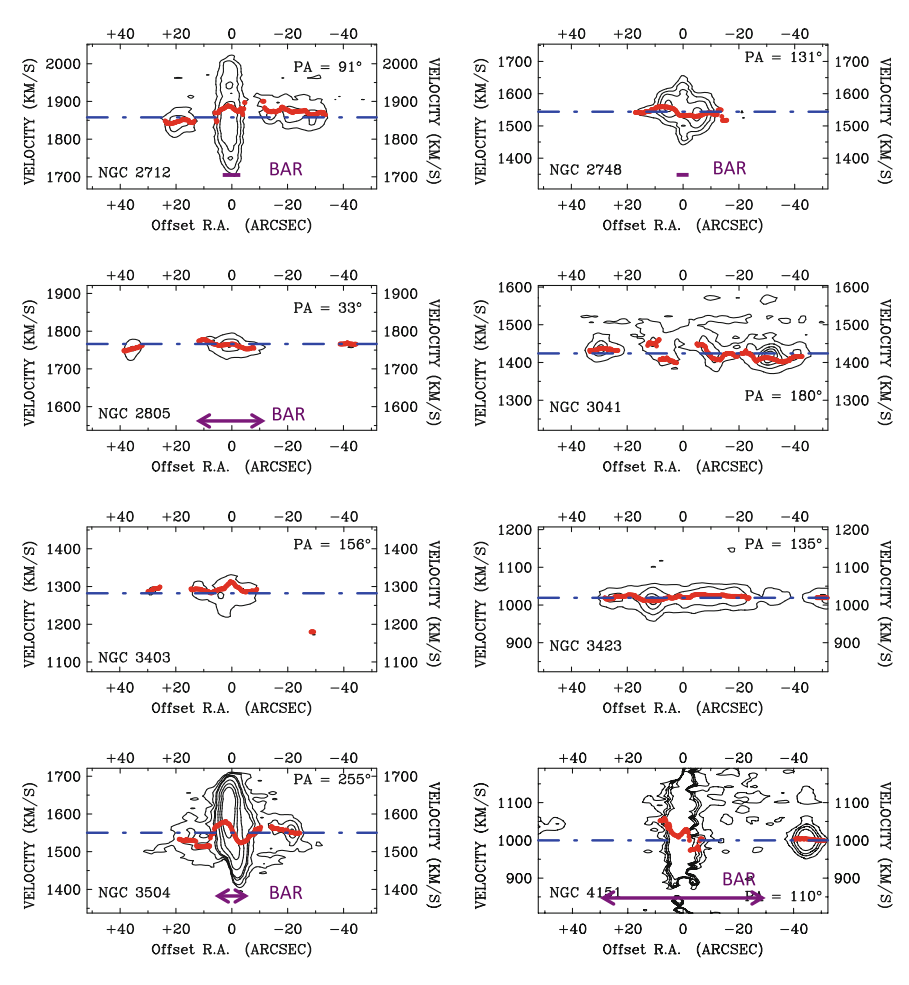


Fig. C.6 As Fig. C.5 but for NGC 2712, NGC 2748, NGC 2805, NGC 3041, NGC 3403, NGC 3423, NGC 3504 and NGC 4151

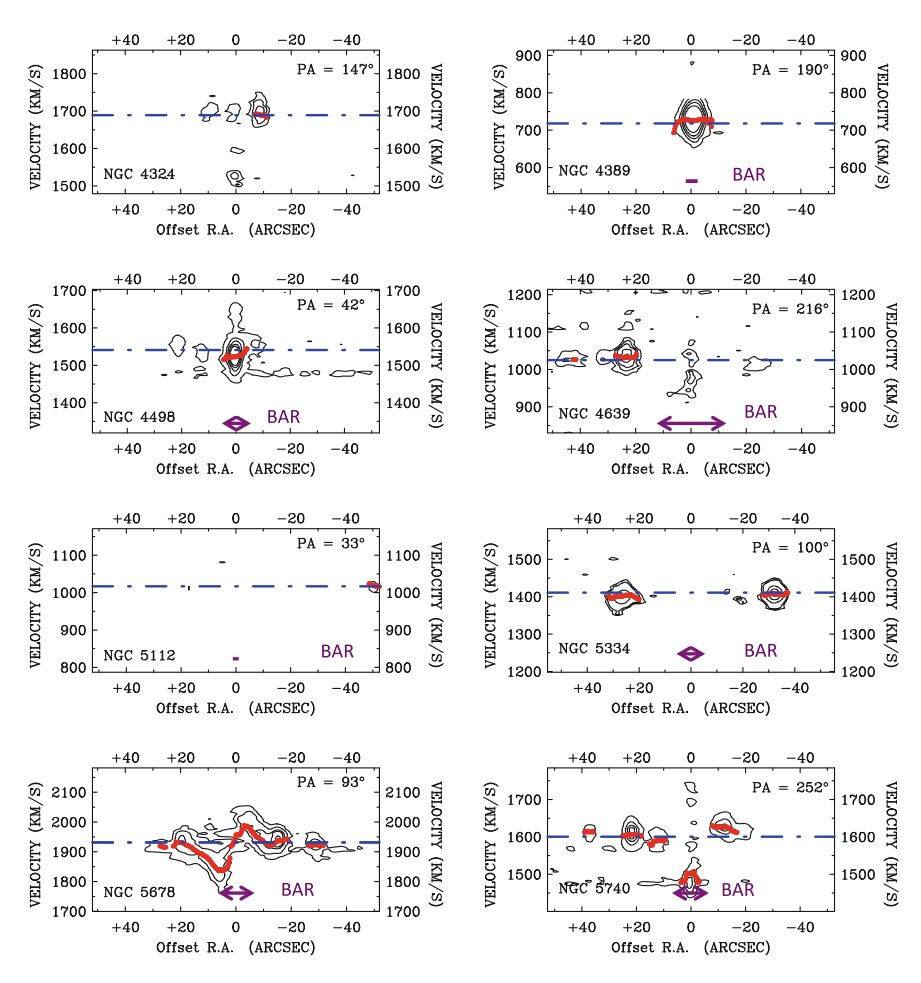


Fig. C.7 As Fig. C.5 but for NGC 4324, NGC 4389, NGC 4498, NGC 4639, NGC 5112, NGC 5334, NGC 5678 and NGC 5740

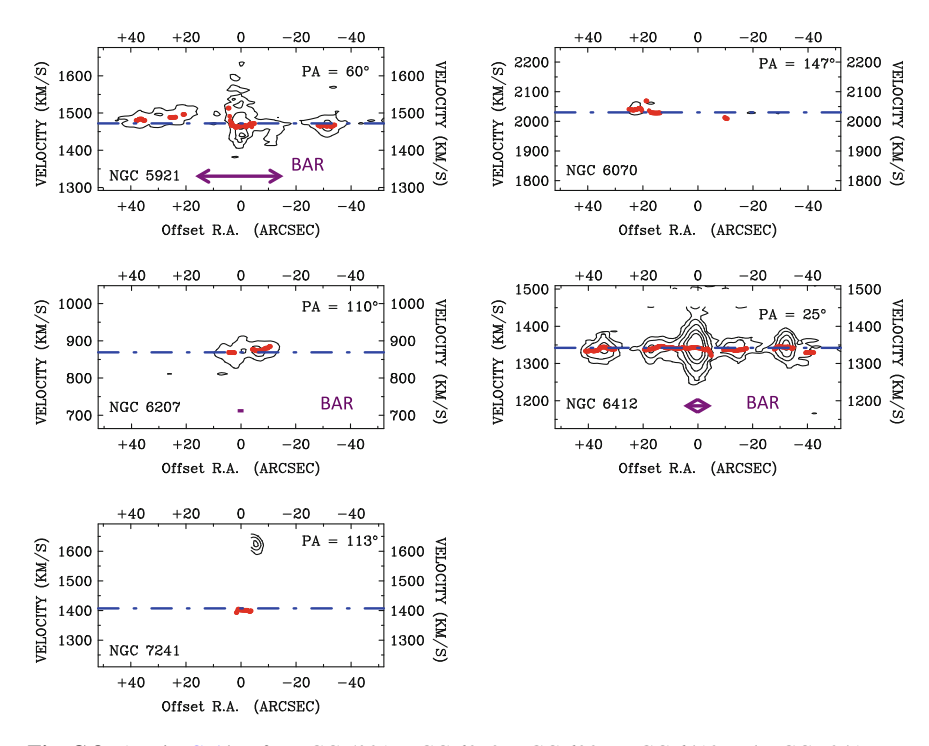


Fig. C.8 As Fig. C.5 but for NGC 5921, NGC 6070, NGC 6207, NGC 6412 and NGC 7241

Appendix D Rotation Curve Fits

See Figs. D.1, D.2, D.3 and D.4

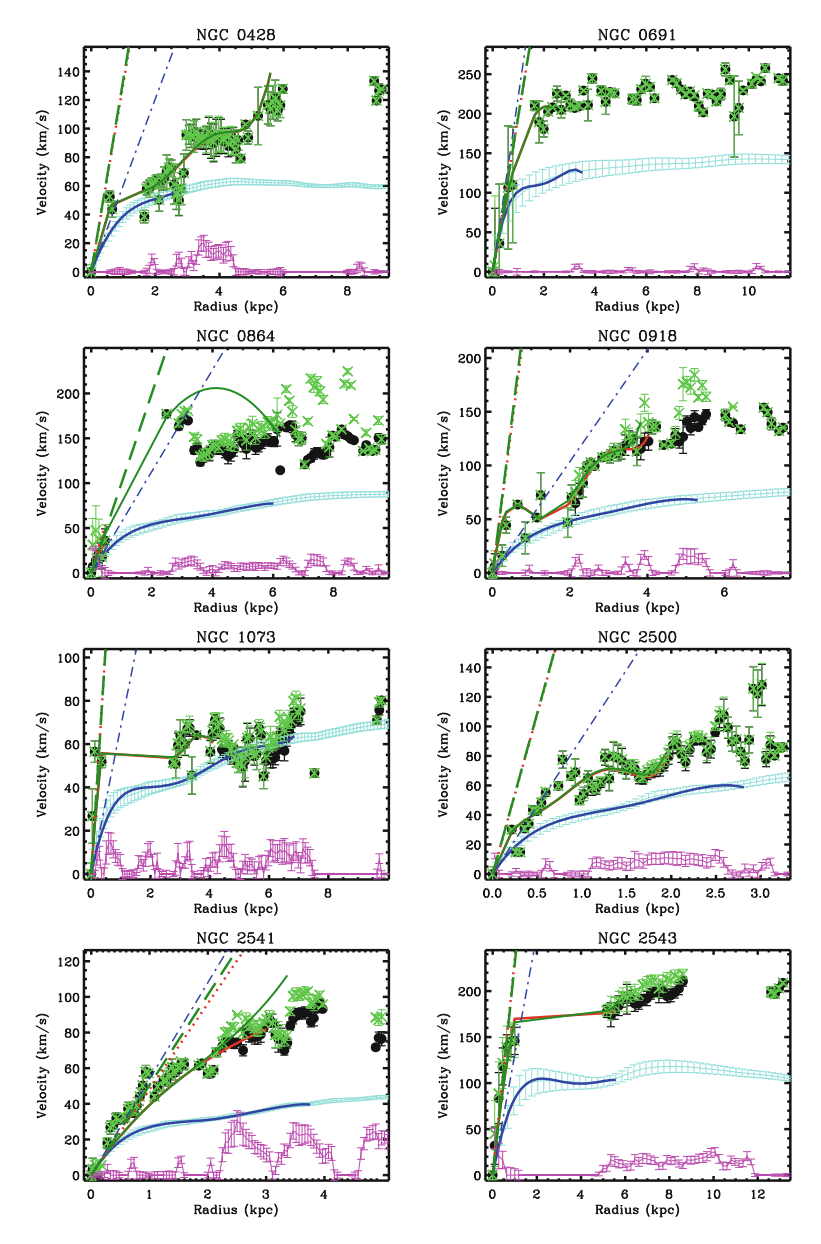
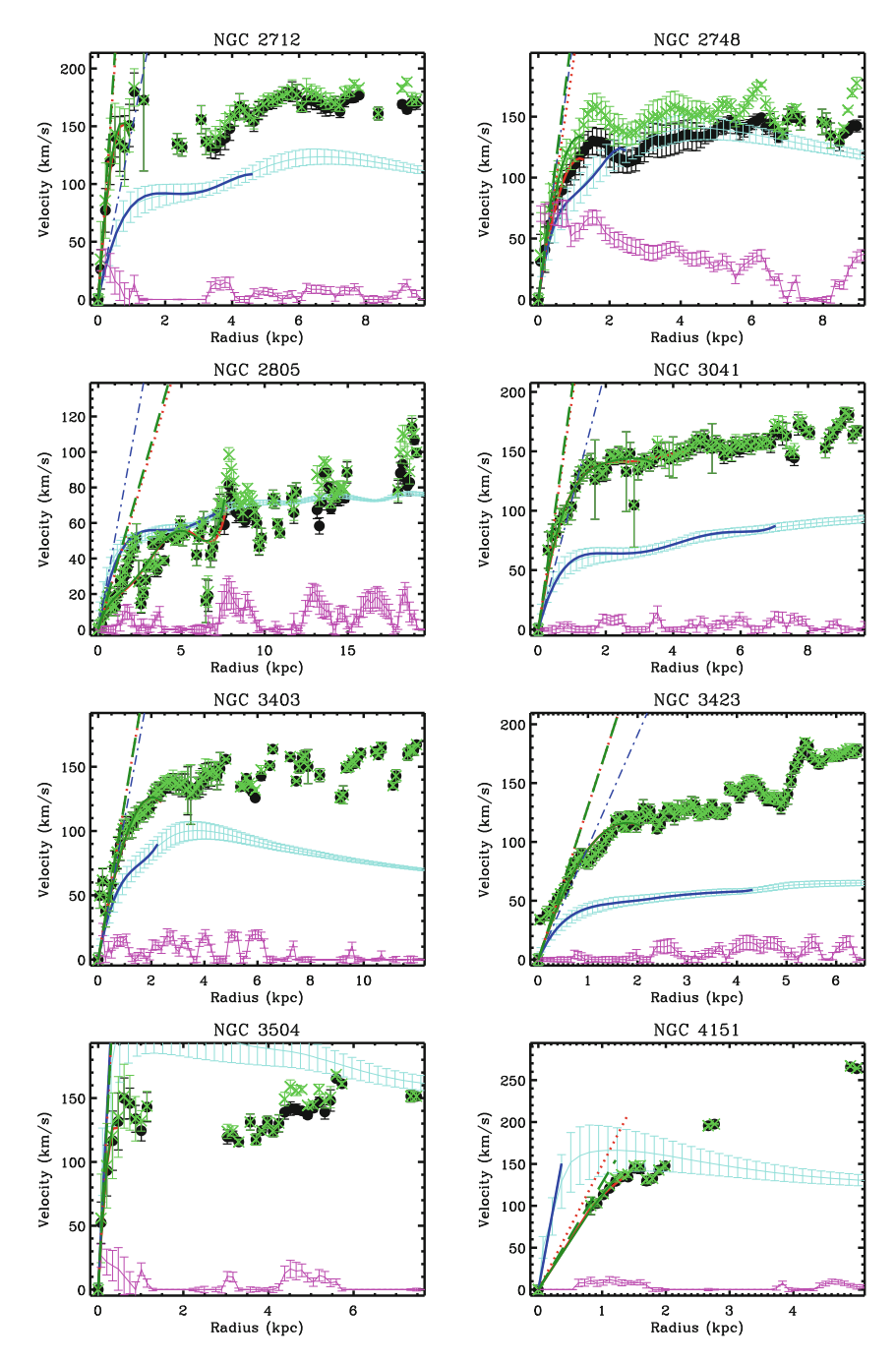
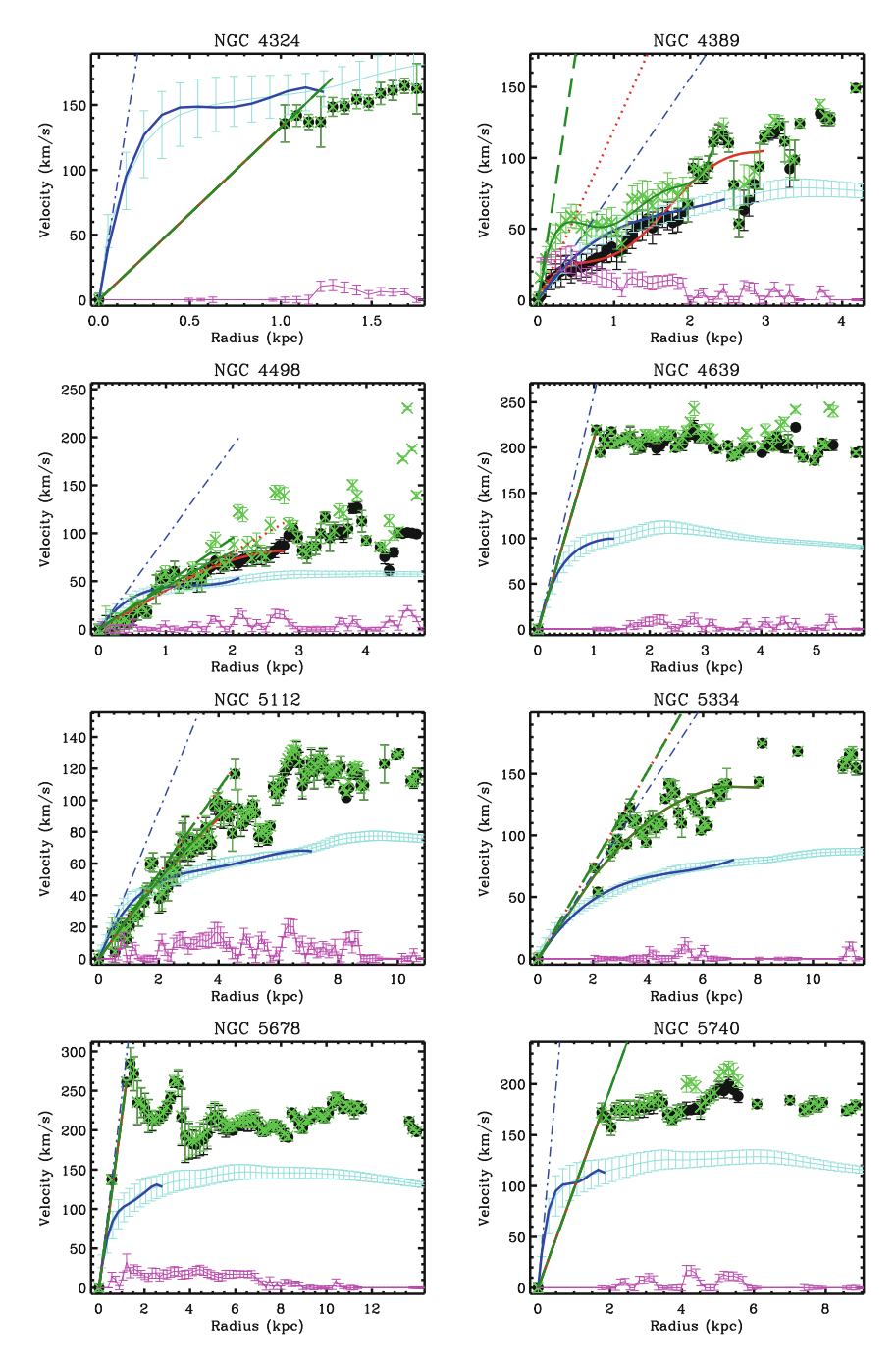


Fig. D.1 High-resolution rotation *curves* for NGC 428, NGC 691, NGC 864, NGC 918, NGC 1073, NGC 2500, NGC 2541 and NGC 2543. The rotation *curves* derived from the FP data are represented with *black circles*. The velocity *curves* derived from the stellar mass maps are represented with a *solid light-blue line* with error marks. The circular velocity *curves* are represented with *green* crosses. Overlaid with solid lines are the polynomials fitted to the *curves*. The slopes of the *curves* are indicated with a *dotted line* for the FP data, with a *dot-dash-dot line* for the mass rotation *curve* and with a *dashed line* for the circular velocity *curve*. The lower *pink line* corresponds to σ_{ϕ} . Polynomials are fitted to the points with radius below R_{90}



 $\label{eq:Fig.D.2} \textbf{Fig. D.1}, but for NGC 2712, NGC 2748, NGC 2805, NGC 3041, NGC 3403, NGC 3423, NGC 3504 and NGC 4151$



 $\textbf{Fig. D.3} \quad \text{As Fig. D.1, but for NGC 4324, NGC 4389, NGC 4498, NGC 4639, NGC 5112, NGC 5334, NGC 5678 and NGC 5740}$

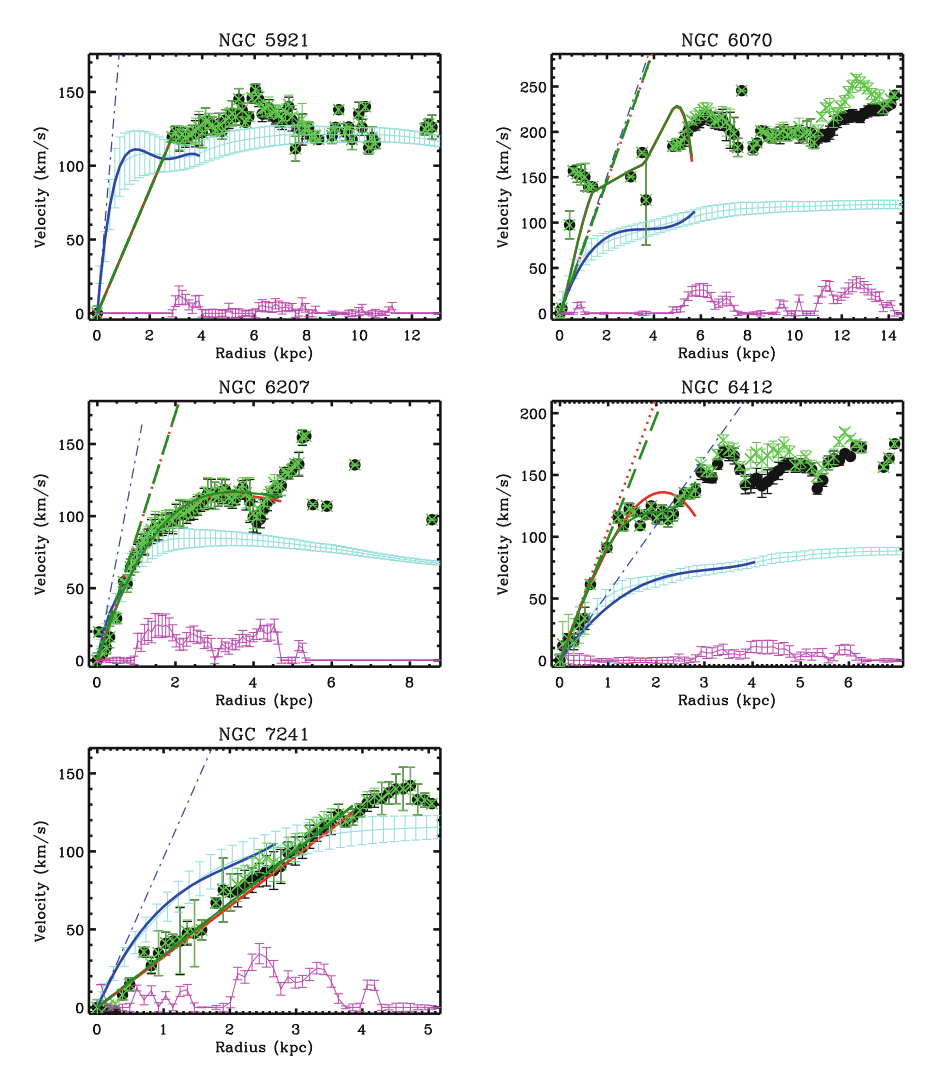


Fig. D.4 As Fig. D.1, but for NGC 5921, NGC 6070, NGC 6207, NGC 6412 and NGC 7241

Appendix E Other Relevant Studies

In this chapter I will explain the contributions that I have made to three works in which I have been involved but not as first author. Here I will describe me concrete input to these papers, rather than reproduce the papers entirely. The papers are Elmegreen et al. (2014) (E14 hereafter), Knapen et al. (2014) (K14 hereafter) and Leaman et al. (2015) (L15 hereafter), where I am second or third author.

E.1 Embedded Star Formation in S⁴G Galaxy Dust Lanes

Debra M. Elmegreen, Bruce G. Elmegreen, Santiago Erroz-Ferrer, et al., 2014, ApJ, 780, 32

E.1.1 Introduction

Star formation triggered in spiral arms has been studied since the density waves were firstly identified by Fujimoto (1968) and Roberts (1969) (see E14 and references therein). In E14, we explore the conditions of this star formation in the case of regions embedded in dust lanes. To do so, we study the most opaque regions in the optical bands of five galaxies which present emission at 3.6 μ m and show star formation (as seen in H α images). My contribution to this paper is the study of the star formation in these regions as derived from the H α images.

E.1.2 Methodology

We have selected five galaxies (Table E.1) with similar size, luminosity and Hubble Type, but representing different spiral arm classes to study the star-forming regions

[©] Springer International Publishing Switzerland 2016 S. Erroz-Ferrer, *Morphology, Kinematics and Star Formation Across the Hubble Sequence of Galaxies*, Springer Theses,

Galaxy name	Distance (Mpc)	Hα images			
		λ (Å)	Δλ (Å)	Scale ("/px)	References
NGC 4321	20.9	6572.62	66.2	0.305	(1)
NGC 5055	7.54	6572.62	66.2	0.305	(1)
NGC 5194	7.54	6572.62	66.2	0.305	(1)
NGC 5248	15.4	6594	44	0.241	(2)
NGC 5457	4.94	6570	55	0.241	(2)

Table E.1 Galaxies observed for embedded sources and information about the H α images

The assumed distances come from the NED. Regarding the $H\alpha$ images: $H\alpha$ filter central wavelength (Column III), $H\alpha$ filter bandwidth (Column IV) and pixel scale of the $H\alpha$ image (Column V). References (1) Spitzer infrared nearby galaxies survey (SINGS) legacy project¹; (2) Knapen et al. (2004)

embedded in dust lanes. To do so, we have used u,g,r,i,z images from the Sloan Digital Sky Survey (SDSS; York et al. 2000), with 0.396" pixels. Also, we have used ground-based observations with $H\alpha$ narrow-band filters. Those images have been compared to the corresponding Spitzer 3.6 μ m images from the S⁴G survey to search for sources without optical counterparts. NGC 4321, NGC 5055, NGC 5194 $H\alpha$ continuum-subtracted images have been obtained from The Spitzer Infrared Nearby Galaxies Survey (SINGS) Legacy Project. 1 $H\alpha$ continuum-subtracted images of NGC 5248 and NGC 5457 have been obtained from Knapen et al. (2004). All the information regarding the $H\alpha$ observations, data reduction and data products can be found in the SINGS webpage and in Knapen et al. (2004).

In Figs. E.1, E.2, E.3, E.4 and E.5, we compare four images of each galaxy in order to identify the star-forming regions embedded in dust lanes: H α (top left), SDSS i-band (top right), SDSS g-band (bottom left) and 3.6 μ m (bottom right). We have identified embedded star-forming complexes on the *Spitzer* 3.6 μ m images by blinking these with the SDSS g images, searching those in the most opaque regions in the optical bands. In Fig. E.6 we have presented the H α images of the five galaxies, where the star-forming regions have been highlighted and numbered.

We have measured the fluxes for the same regions used to define the 3.6 μ m sources. Due to the width of the filter, the neighbouring NII lines contribute to these fluxes. We have estimated this contribution using (i) for NGC 4321 and NGC 5194: integrated spectrophotometry of the galaxies from Moustakas and Kennicutt (2006); and (ii) for NGC 5055, NGC 5248 and NGC 5457: an empirical scaling relation between the NII/H α ratio and M $_B$ described in Appendix B of Kennicutt et al. (2008). The resulting NII/H α ratio for the galaxies of the sample is 0.430 (NGC 4321); 0.486 (NGC 5055); 0.590 (NGC 5194); 0.369 (NGC 5248) and 0.389 (NGC 5457). After correcting for the NII contamination, the H α fluxes, F(H α), are converted to H α luminosities using Eq. 4.2 and to H α intensities (also known as intrinsic H α emission), defined as:

¹http://irsa.ipac.caltech.edu/data/SPITZER/SINGS/.

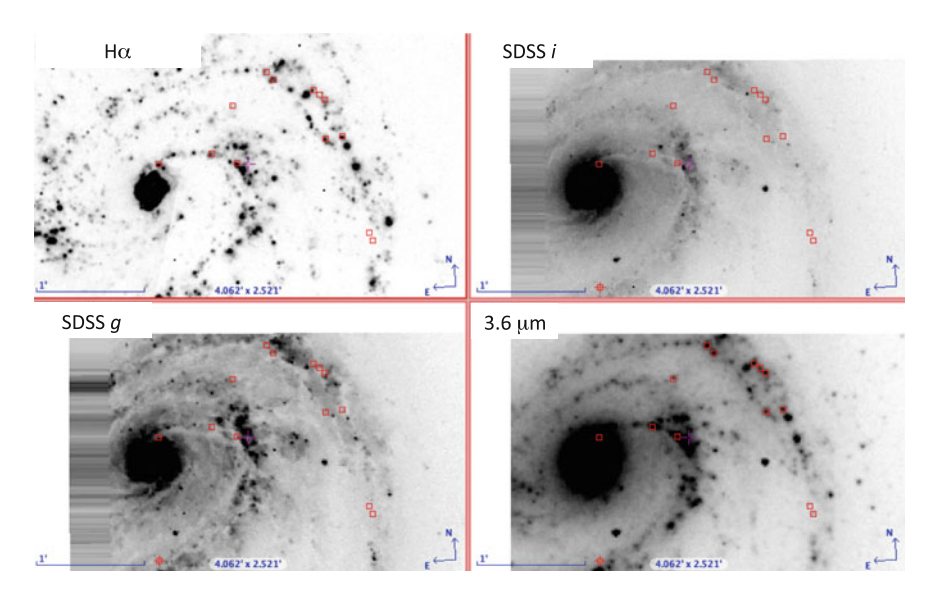


Fig. E.1 H α (top left), SDSS i-band (top right), SDSS g-band (bottom left) and 3.6 μ m (bottom right) images for NGC 4321. All the images have the same scale. Overlaid the regions subject to study

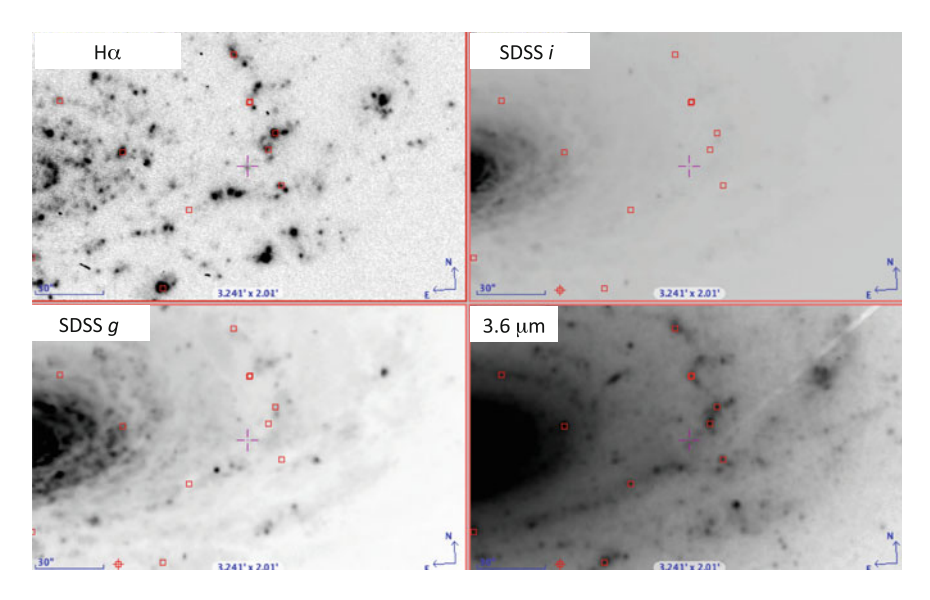


Fig. E.2 The same as Fig. E.1 but for NGC 5055

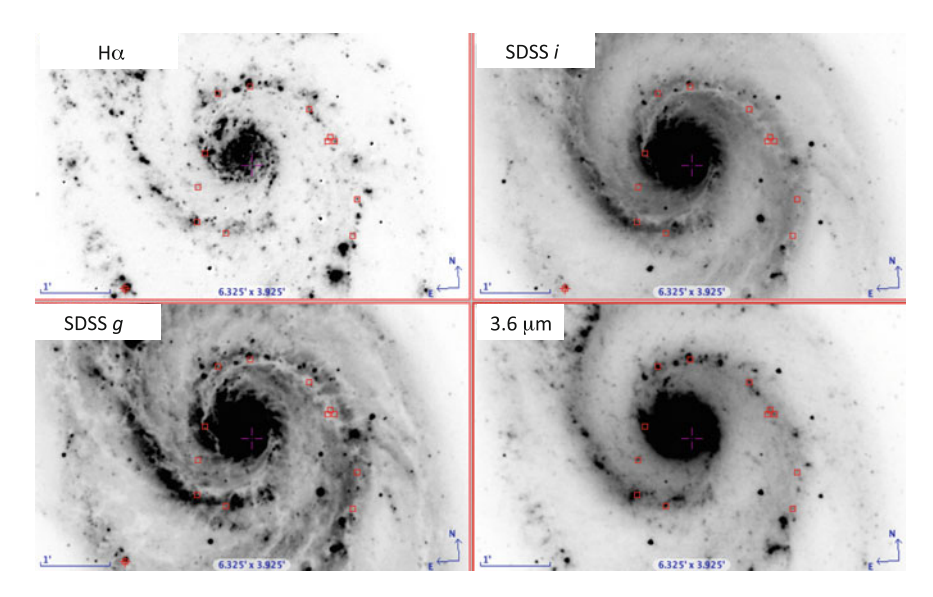


Fig. E.3 The same as Fig. E.1 but for NGC 5194

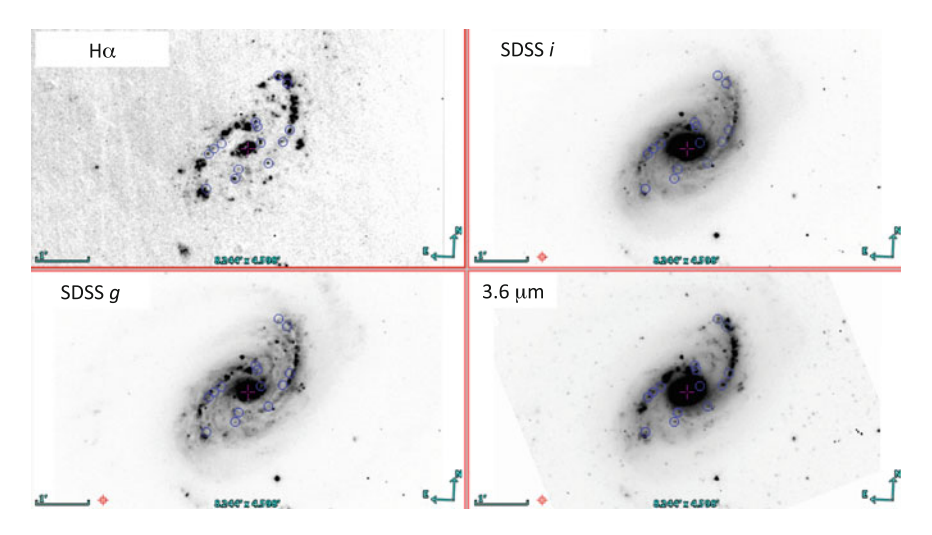


Fig. E.4 The same as Fig. E.1 but for NGC 5248

$$I(H\alpha) = \frac{f_{\nu}}{\Omega} = \frac{F(H\alpha)\lambda^2}{\Omega c \Delta \lambda},$$
 (E.1)

being f_{ν} the flux density (in units of frequency, e.g. Jy) and Ω the solid angle. Images from the Two Micron All Sky Survey (2MASS) at J band (1.25 μ m; Skrutskie et al. 2006) have been used to apply Mentuch et al. (2010) technique to estimate the underlying old stellar population. This technique assumes that the old

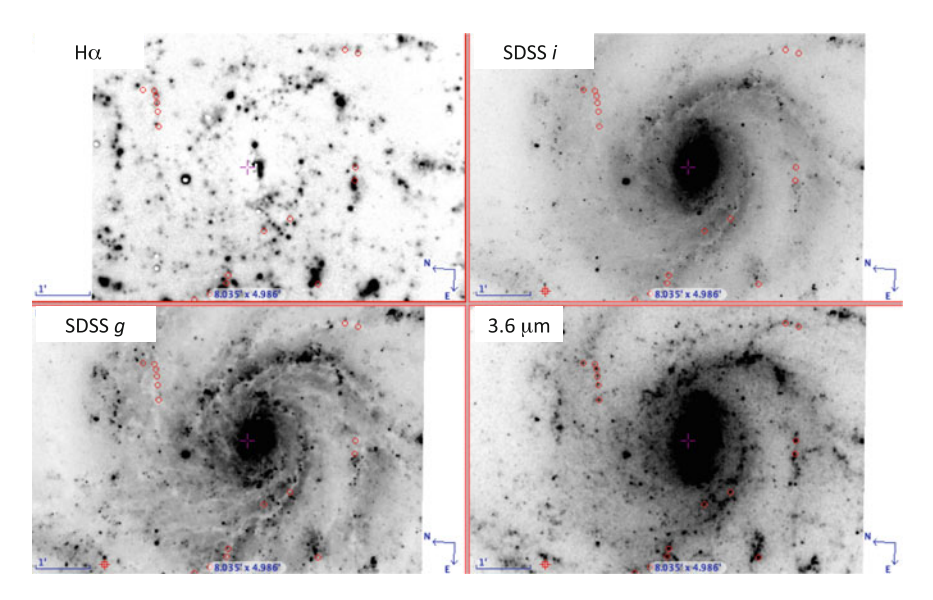


Fig. E.5 The same as Fig. E.1 but for NGC 5457

stellar population in the galaxy disc has a flux density at 1.25 μm that is typically about twice the flux density at 3.6 μm , and that there is also a correlation of those quantities with H α intensity:

$$I_{\rm IR}(H\alpha) = (I[3.6\,\mu\text{m}] - 0.5I[1.25\,\mu\text{m}])/0.043$$
 (E.2)

Both $I(H\alpha)$ and $I_{IR}(H\alpha)$ were converted to luminosities and to ionization rates using $S_{obs} = 7.3 \times 10^{11} L_{H\alpha}$ from Kennicutt (1998). Then, these observed ionization rates have been compared to the stellar evolution models in Bruzual and Charlot (2003) to determine the intrinsic properties of the embedded regions. The resulting model magnitudes in all five SDSS bands are subtracted from the observed ones to obtain the minimum extinction in each band (lower limits), and converted to *g*-band extinction using the extinction curve in Cardelli et al. (1989). All the details about this process can be found in Sect. 3 of E14.

E.1.3 Results

We have presented the observed H α fluxes, luminosities and intensities in Table E.2. With the observed 3.6 and 1.25 μ m fluxes, we have estimated the intrinsic H α emission following Mentuch et al. (2010). The stellar luminosities determined assuming an age in the range 1–10 Myr have been combined with the upper limits from the SDSS images, obtaining lower limits to the extinction and stellar mass. In particular,

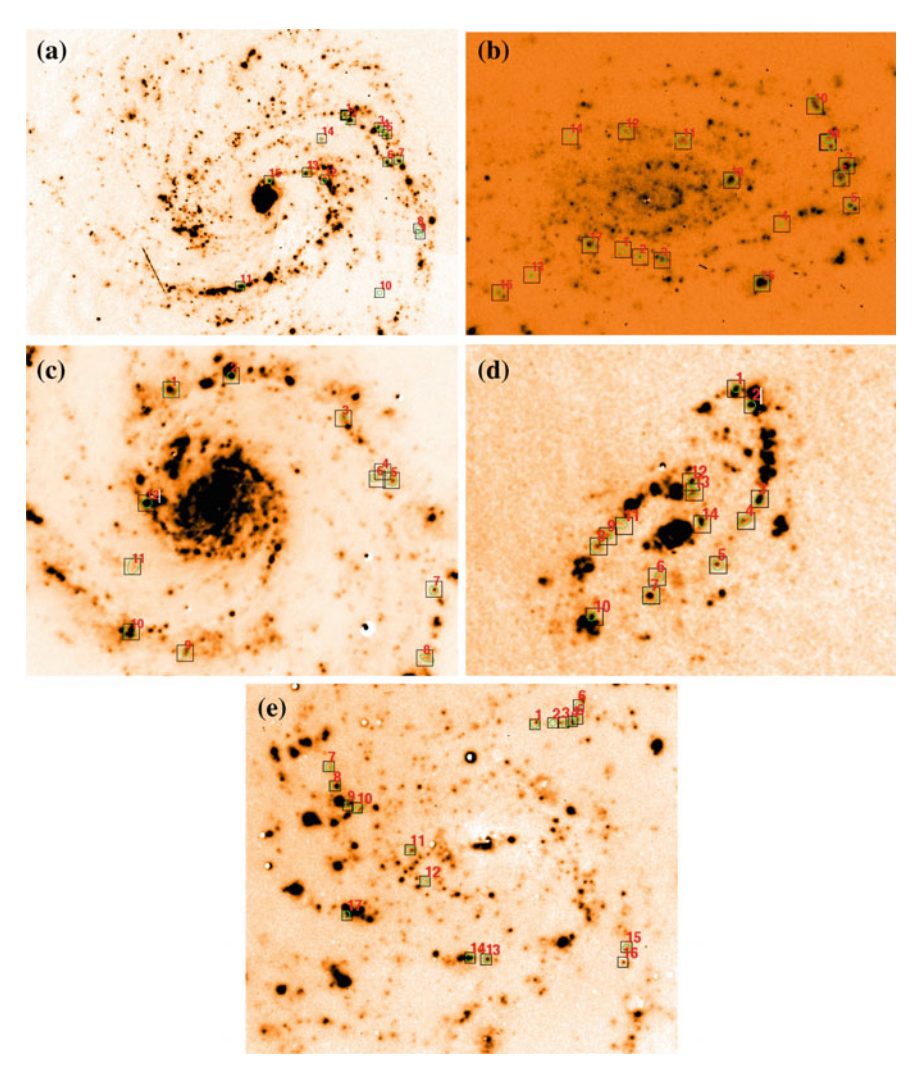


Fig. E.6 H α images of (a) NGC 4321, (b) NGC 5055, (c) NGC 5194, (d) NGC 5248 and (e) NGC 5457. Overlaid with *rectangles* and labelled with numbers the location of the regions for which we have measured the fluxes and luminosities presented in Table E.2

Table 3 of E14 shows the derived properties of the embedded sources for assumed ages of 3 Myr: columns 3 and 4 contain the masses and g-band-equivalent extinction for the H α measurements; columns 5 and 6 contain the masses and average g-band-equivalent extinction from the 3.6 μ m measurements. In column 7, the extinction coefficient of the HII regions needed to produce the observed H α fluxes measured at g-band.

Table E.2 Photometry of the star-forming regions from the H α images

Galaxy	Region ID	RA	DEC	$F(H\alpha)$ (erg/s/cm ²)	$Log[L(H\alpha)]$ (erg/s)	I(Hα) (MJy/sr)
NGC4221	1	12 22 50 400	15 50 24 02	_		-
NGC4321	1	12:22:50.498	15:50:24.03	5.72E-15	38.47	0.40
	2	12:22:50.238	15:50:19.91	8.87E-15	38.66	0.62
	3	12:22:48.705	15:50:14.28	2.95E-15	38.19	0.77
	4	12:22:48.471	15:50:11.66	<1.03E-15	< 37.73	<0.27
	5	12:22:48.263	15:50:9.03	2.36E-15	38.09	0.59
	6	12:22:48.238	15:49:47.28	2.68E-15	38.14	0.72
	7	12:22:47.614	15:49:48.78	4.19E-15	38.34	0.93
	8	12:22:46.575	15:48:55.15	<1.09E-16	<36.75	<0.01
	9	12:22:46.445	15:48:50.65	<1.67E-16	<36.94	<0.01
	10	12:22:48.654	15:48:4.53	<5.20E-16	<37.43	< 0.04
	11	12:22:56.241	15:48:10.16	1.05E-14	38.74	0.99
	12	12:22:51.642	15:49:33.41	7.11E-15	38.57	1.17
	13	12:22:52.603	15:49:39.04	4.66E-15	38.38	0.55
	14	12:22:51.797	15:50:5.66	1.03E-15	37.73	0.19
	15	12:22:54.656	15:49:33.04	4.79E-15	38.40	0.79
NGC5055	1	13:15:50.565	42:1:16.91	<1.91E-15	<37.11	< 0.14
	2	13:15:49.657	42:1:12.78	2.66E-15	37.26	0.37
	3	13:15:48.512	42:1:10.91	1.14E-14	37.89	0.91
	4	13:15:42.286	42:1:31.89	8.93E-16	36.78	0.13
	5	13:15:38.651	42:1:42.75	9.72E-15	37.82	0.84
	6	13:15:39.155	42:1:58.50	1.99E-14	38.13	0.81
	7	13:15:38.886	42:2:5.63	3.69E-14	38.40	1.60
	8	13:15:39.861	42:2:19.51	8.78E-15	37.77	0.46
	9	13:15:39.895	42:2:19.13	5.67E-15	37.58	0.41
	10	13:15:40.534	42:2:40.14	2.50E-14	38.23	0.67
	11	13:15:47.401	42:2:19.91	1.45E-14	37.99	0.40
	12	13:15:50.364	42:2:25.53	5.79E-15	37.59	0.35
	13	13:15:53.326	42:2:22.53	<4.40E-16	<36.47	< 0.03
	14	13:15:43.330	42:0:57.40	7.86E-14	38.73	1.68
	15	13:15:56.958	42:0:52.14	3.85E-15	37.42	0.33
	16	13:15:52.281	42:1:19.53	1.86E-14	38.10	0.77
NGC5194	1	13:29:54.725	47:12:36.45	4.70E-14	38.50	0.86
	2	13:29:52.038	47:12:42.82	4.82E-14	38.51	2.82
	3	13:29:46.997	47:12:23.32	1.57E-14	38.03	1.05
	4	13:29:45.231	47:11:58.94	6.71E-15	37.66	0.29
	5	13:29:44.864	47:11:55.18	1.30E-14	37.94	0.51
	6	13:29:45.489	47:11:55.56	4.75E-15	37.51	0.32
	7	13:29:42.953	47:11:5.30	9.85E-15	37.82	0.49
	8	13:29:43.359	47:10:33.80	9.41E-15	37.80	0.40

(continued)

Table E.2 (continued)

Galaxy	Region ID	RA	DEC	$F(H\alpha)$ (erg/s/cm ²)	$Log[L(H\alpha)]$ (erg/s)	I(Hα) (MJy/sr)
	9	13:29:54.098	47:10:36.07	1.45E-14	37.99	0.72
	10	13:29:56.526	47:10:45.82	5.67E-14	38.58	1.09
	11	13:29:56.453	47:11:15.82	1.84E-14	38.09	0.33
	12	13:29:55.828	47:11:44.70	5.38E-14	38.56	2.07
NGC5248	1	13:37:29.691	8:54:30.29	9.75E-15	38.44	0.82
	2	13:37:29.033	8:54:20.91	1.21E-14	38.53	1.09
	3	13:37:28.780	8:53:27.66	3.05E-14	38.93	0.99
	4	13:37:29.286	8:53:14.91	1.42E-14	38.60	0.36
	5	13:37:30.374	8:52:50.16	8.25E-15	38.37	0.51
	6	13:37:32.601	8:52:43.41	6.07E-15	38.23	0.21
	7	13:37:32.930	8:52:32.54	3.66E-14	39.02	0.53
	8	13:37:34.929	8:53:0.29	1.57E-14	38.65	0.39
	9	13:37:34.575	8:53:6.29	1.02E-14	38.46	0.35
	10	13:37:35.106	8:52:20.54	1.11E-14	38.50	0.83
	11	13:37:33.967	8:53:12.29	1.46E-15	37.61	0.10
	12	13:37:31.386	8:53:37.04	2.00E-14	38.75	0.57
	13	13:37:31.285	8:53:31.41	1.25E-14	38.55	0.43
NGC5457	1	14:3:7.750	54:22:43.86	1.42E-14	37.62	0.39
	2	14:3:5.818	54:22:45.35	<3.71E-15	<37.03	< 0.14
	3	14:3:4.745	54:22:45.73	<1.58E-14	<37.66	< 0.28
5	4	14:3:3.843	54:22:47.22	<1.97E-14	<37.76	< 0.40
	5	14:3:3.285	54:22:49.09	<9.70E-15	<37.45	< 0.30
	6	14:3:3.198	54:23:1.84	5.68E-16	36.22	0.07
	7	14:3:29.293	54:22:2.54	8.79E-15	37.41	0.33
	8	14:3:28.604	54:21:44.92	4.55E-14	38.12	0.73
	9	14:3:27.230	54:21:27.31	5.15E-14	38.18	0.68
	10	14:3:26.243	54:21:25.07	2.34E-14	37.83	0.45
	11	14:3:20.620	54:20:47.22	2.22E-14	37.81	0.46
	12	14:3:19.032	54:20:18.73	7.65E-15	37.35	0.21
	13	14:3:12.514	54:19:7.87	2.97E-14	37.94	0.41
	14	14:3:14.186	54:19:8.99	1.05E-13	38.49	0.86
	15	14:2:57.854	54:19:20.93	1.13E-14	37.52	0.19
	16	14:2:58.199	54:19:7.06	1.50E-14	37.64	0.34
	17	14:3:27.177	54:19:46.81	6.04E-14	38.24	1.09

Upper limits on the $H\alpha$ flux result when the HII region is not seen at the position of the 3.6 μm source

We conclude that the observed $H\alpha$ luminosities, compared to those estimated from the technique by Mentuch et al. (2010) using 3.6 and 1.25 μ m, give a consistent value for the extinction, near the estimated lower limit (otherwise these regions would not be observed). The star-forming complexes are understood as parts of regular strings that form stars that include embedded sources. In E14 we discuss the possible star formation mechanisms: gravitational collapse of gas that accumulates behind the shock front in a spiral arm and compression and collapse of pre-existing clouds that hit these shock fronts.

E.2 Optical Imaging for the *Spitzer* Survey of Stellar Structure in Galaxies—Data Release and Notes on Interacting Galaxies

Johan H. Knapen, Santiago Erroz-Ferrer, et al., 2014, A & A, 569, 91

E.2.1 Sample Selection

In K14, we provide with optical images for some of the original S⁴G sample and its extension,² which makes a final list of 2829 galaxies. Most of these have been observed by the Sloan Digital Sky Survey (SDSS, York et al. 2000), made public via the *seventh data release* (DR7, Abazajian et al. 2009) and the *eighth data release* (DR8, Aihara et al. 2011). The goal of this study was to provide with optical data for as many as possible galaxies in the original and extended S⁴G, for which we have observed some galaxies and re-reduced those that were already public in the SDSS data releases.

To select the sample, we started out by selecting all those galaxies in the original S^4G sample (as defined by Sheth et al. 2010) that had imaging in DR7. This search yielded 1252 galaxies. Later, we added another 183 galaxies for which imaging was released in SDSS DR8 but which were not in DR7, and 222 galaxies from the new extended S^4G for all but five of which we used DR8 data. The total number of galaxies for which we re-processed and release SDSS imaging is thus 1657.

We also identified those galaxies in the northern hemisphere (defined here as having declination $> -10^{\circ}$) which were not included in the SDSS imaging survey. This yielded 185 galaxies, of which 10 have diameters D_{25} larger than 8 arcmin. A total of 111 of these galaxies with diameters smaller than 8 arcmin was observed by us in only the *g*-band, using the Liverpool Telecope (LT) on La Palma. We thus

²The sample of the S⁴G extension proposal for *Spitzer* has 695 galaxies, but 218 of these overlap with the original S⁴G sample (described in Sheth et al. 2010).

Galaxy	PGC	Source	Bands	FOV (arcmin)	Calibration
UGC 12893	38	SDSS/DR8	u, g, r, i, z	5.0	_
NGC 7814	218	SDSS/DR7	u, g, r, i, z	13.1	_
UGC 00017	255	SDSS/DR7	u, g, r, i, z	7.3	_
NGC 7817	279	SDSS/DR8	u, g, r, i, z	9.9	_
NGC 0014	647	SDSS/DR7	u, g, r, i, z	5.0	_
UGC 00099	757	SDSS/DR8	u, g, r, i, z	7.5	_
UGC 00122	889	LT/RATCam	g'	4.6	1
UGC 00132	924	SDSS/DR8	u, g, r, i, z	5.0	_
UGC 00156	1107	SDSS/DR8	u, g, r, i, z	5.0	_
NGC 0063	1160	SDSS/DR8	u, g, r, i, z	6.0	_

Table E.3 Sample of the table accompanying the data release on the CDS

Only the first ten lines of the file are shown here. Columns 1 and 2 are the galaxy common name and number from the Catalogue of Principal Galaxies (PGC); column 3 is the origin of the image, identifying the data release in the case of the SDSS, and the instrument in the case of the new LT images; columns 4 and 5 are the bands made available and the size of the images (all images are square); and column 6 identifies the calibration method used in the case of the LT images (see Sect. E.2.2)

present in K14 images in the full set of five SDSS bands (ugriz) for 1657 galaxies, and images in the g'-band for an additional 111 galaxies. This amounts to optical imaging for 1768 galaxies in total, or two-thirds of the S⁴G sample. In Table E.3 we find the first ten lines of the long table of CDS containing information about the released 1768 galaxy images. My contribution to this paper is concentrated on the LT observations and data reduction.

E.2.2 Liverpool Telescope Imaging

The LT (Steele et al. 2004) is a 2.0 m robotic telescope situated in the Roque de Los Muchachos Observatory on the island of La Palma. We have used two different cameras for our project, namely RATCam and IO:O, to observe a total of 111 S⁴G galaxies which had not been observed in the SDSS, are smaller than 8 arcmin, and at a declination $> -10^{\circ}$.

RATCam has now been retired from the LT. The FOV was 4.6×4.6 arcmin, with a pixel scale of 0.1395 arcsec/pixel. We observed 5 galaxies with RATCam in August 2011, using a Sloan g'-band filter. Each galaxy was observed for 3×100 s. In Fig. E.7 (left) we see the g'-band image of IC 1711, observed with RATcam.

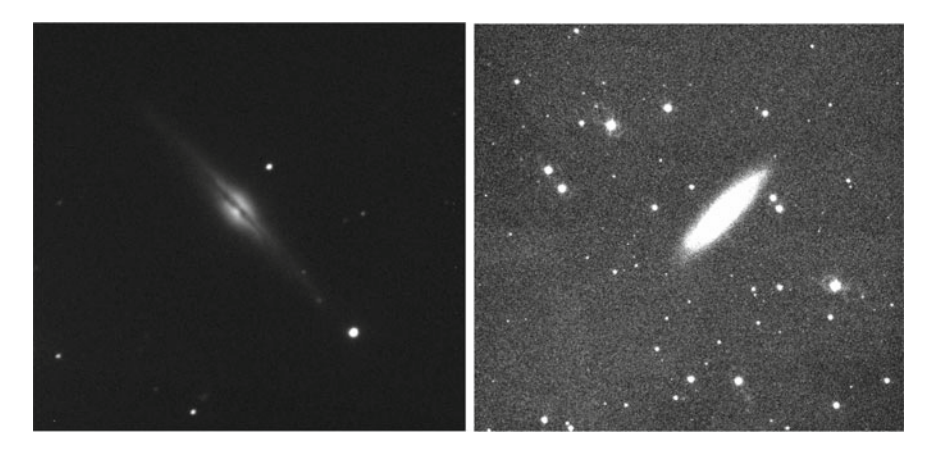


Fig. E.7 *Left g'*-band image of IC 1711 observed with RATcam on the LT. *Right g'*-band image of NGC 7817 observed with IO:O on the LT

RATCam was replaced by the IO:O camera.³ It provides a wider FOV and greater sensitivity than RATCam. The FOV is 10×10 arcmin and the pixel scale is approximately 0.15 arcsec/pixel. However, we used the 2×2 binning because the 1×1 binning was not operative at the time of the observations, with a resulting pixel scale of 0.3008 arcsec/pixel. We observed 106 galaxies with IO:O using a Sloan g'-band filter, also with 3×100 s exposure time, in February 2012 and from July 2012 to January 2013. In Fig. E.7 (right) we see the g'-band image of NGC 7817, observed with IO:O.

LT images are delivered after having passed a basic data reduction pipeline, which includes bias subtraction and flat-fielding correction. The overscan regions are trimmed off, leaving a 2048 × 2048 pixel image. We subtracted the background before, and again after the combination of the three separate exposures by determining the background from regions well outside the galaxy, ignoring emission from, e.g., foreground stars or cosmetic defects by combining with a median algorithm. If one of the three individual exposures had significantly different seeing from the others, it was rejected before the combination. Also, if some of the frames presented strange features (e.g., a satellite track, humidity problems), the corresponding images were rejected. For flux calibration, a set of Landolt standard stars was observed in all the bands every two hours, specifically PG0231+051, RUBIN 149, PG1047+003, PG1525-071A, MARK-A and PG2331-055A. To transform from the $UBVR_cI_c$ filter set used in the literature to ugriz, we used the equations presented in Smith et al. (2002). We computed the corresponding zero-points to perform the photometry, and added them to the headers of the images (stored in keyword COMMENT2). For the nights when no standard stars were observed, we performed the flux calibration by computing the g' magnitude using BVRI photometry values obtained from the NED, as described below.

³http://telescope.livjm.ac.uk/Info/TelInst/Inst/IOO/.

The headers contain a keyword COMMENT3 with information about the calibration method used. This information is expanded in Table E.3, as follows: 1.—standard stars, 2.—cross-calibrated using a total g' magnitude as derived from photometry in NED, from different bands, namely 2.1-g' computed from B and V, 2.2-g'computed from B and R, 2.3—from B and I, 2.4—from B, R and I, and 2.5—from B and J. In all cases we performed linear correlations using predictions based on the MIUSCAT stellar populations models. This set of predictions is an extension of the Vazdekis et al. (2003, 2010) models, based on the Indo-U.S., CaT and MILES empirical stellar libraries. A full description of the models is given in Vazdekis et al. (2012) and applications are provided in Ricciardelli et al. (2012). The equations used are g' = R + 0.7232(B - R) + 0.0224, g' = I + 0.7902(B - I) + 0.0517and g' = J + 0.8413(B - J) + 0.0927, with a correlation coefficient R^2 of over 99.5%. The LT images of four galaxies have a value X in keywords COMMENT2 and COMMENT3. These images, of UGC 09992, UGC 10194, PGC 027825 and PGC 029086, could not be calibrated because we did not have standard star observations, nor photometric information to calculate a total g' magnitude. In spite of this, we do release the images.

The final images have a seeing between 1 and 3 arcsec, with a median seeing value of 1.4 arcsec. The final list of galaxies for which we present LT g'-band images is shown in Table E.4, which also lists other basic parameters of the images such as the instrument and calibration method used.

E.2.3 Image Availability

All science images are released publicly with the publication of K14. They can be used freely by any researcher interested, provided the origin of the images is identified as this paper, SDSS or LT, and the data archive they were downloaded from. Images are available through the NED and the CDS⁴ in FITS format. The headers of the images give information on the origin of the image, filter and other instrumental parameters, and calibration information. A README file accompanies the data release on the CDS, listing the galaxies, the images with their sources, the size of the images, and the calibration method used in the case of LT data. The first ten lines of this README file are shown here as Table E.3.

⁴Via anonymous ftp to cdsarc.u-strasbg.fr (130.79.128.5) or via http://cdsarc.u-strasbg.fr/viz-bin/qcat?J/A+A/xxx/yyy.

Table E.4 Description of the sample of galaxies observed with the LT telescope

Name NGC 7051	i, of						_	
NGC 7051	U1C (First observation)	Instrument	Semester	g' (mag)	Airmass	ZP	Calibration	Seeing
	August 01, 2011—03:55:25	RatCam	11B	0.00	1.26	23.63	1	1.87
NGC 7714	August 03, 2011—04:32:33	RatCam	11B	0.00	1.13	23.49	1	1.29
NGC 7715	August 07, 2011—04:15:31	RatCam	11B	0.00	1.13	23.59	1	1.83
IC 1265	August 07, 2011—22:02:15	RatCam	11B	0.00	1.03	23.60	1	1.09
UGC 00122	August 08, 2011—04:23:31	RatCam	11B	0.00	1.02	23.29	1	1.63
UGC 04623	February 21, 2012—00:00:45	0:01	12A	13.01	1.48	22.71	2.3	1.16
NGC 2715	February 21, 2012—00:17:54	0:01	12A	11.44	1.53	22.22	2.1	1.09
NGC 2655	February 21, 2012—00:35:06	0:01	12A	10.48	1.54	22.32	2.1	1.20
NGC 2978	February 21, 2012—00:59:28	0:01	12A	13.66	1.28	22.69	2.5	1.43
NGC 3403	February 21, 2012—01:51:42	0:01	12A	12.72	1.41	22.28	2.3	1.19
NGC 3952	February 21, 2012—02:45:13	0:01	12A	13.24	1.19	22.57	2.1	1.36
IC 2969	February 21, 2012—03:02:51	0:01	12A	13.79	1.19	22.80	2.4	1.39
PGC 041725	February 21, 2012—03:20:08	0:01	12A	15.12	1.20	23.09	2.4	1.39
NGC 2591	February 21, 2012—21:40:05	0:01	12A	12.70	1.59	22.12	2.3	1.25
IC 0529	February 21, 2012—23:43:28	0:01	12A	12.38	1.42	22.45	2.1	1.01
PGC 046382	February 22, 2012—04:52:20	0:01	12A	13.70	1.27	22.33	2.1	2.49
NGC 5468	February 22, 2012—05:09:41	0:01	12A	12.68	1.21	22.99	2.1	2.55
NGC 5534	February 22, 2012—05:26:53	0:01	12A	12.61	1.24	22.29	2.1	2.16
PGC 053568	February 22, 2012—05:44:37	0:01	12A	15.27	1.23	23.08	2.4	2.72
PGC 015869	February 22, 2012—20:39:47	0:01	12A	14.66	1.29	22.24	2.4	1.35
NGC 1637	February 22, 2012—20:56:59	0:01	12A	11.09	1.25	22.19	2.1	1.24
UGC 04024	February 22, 2012—21:15:47	0:01	12A	14.54	1.25	22.49	2.3	1.37
NGC 2460	February 22, 2012—21:33:00	10:0	12A	12.22	1.21	22.32	2.1	1.33

F
õ
=
Ξ
Ħ
<u>છ</u>
_
4
Ξ
e
abl
<u>_</u>

Table E.4 (confinded)	mueu)							
Name	UTC (First observation)	Instrument	Semester	g' (mag)	Airmass	ZP	Calibration	Seeing
UGC 04169	February 22, 2012—21:50:10	10:0	12A	13.25	1.22	22.00	2.1	1.34
UGC 04305	February 22, 2012—22:07:25	10:0	12A	10.81	1.37	21.85	2.1	1.27
UGC 04121	February 22, 2012—22:24:41	10:0	12A	14.88	1.15	22.04	2.1	1.31
NGC 2748	February 22, 2012—23:20:46	10:0	12A	11.98	1.49	22.21	2.1	1.66
UGC 04483	February 22, 2012—23:39:10	10:0	12A	14.99	1.32	22.17	2.1	1.43
UGC 05139	February 22, 2012—23:57:02	10:0	12A	13.00	1.36	21.97	2.1	1.48
PGC 035271	February 24, 2012—02:38:03	10:0	12A	15.45	1.21	22.54	2.4	1.36
NGC 4129	February 24, 2012—03:16:07	10:0	12A	12.74	1.27	21.42	2.1	1.47
PGC 044906	February 24, 2012—03:37:38	10:0	13A	15.23	1.20	21.62	2.4	1.37
PGC 043679	February 24, 2012—03:58:50	10:0	12A	14.03	1.28	21.73	2.4	1.30
PGC 044506	February 24, 2012—04:17:01	10:0	12A	14.79	1.23	22.79	2.4	1.44
NGC 5472	February 24, 2012—05:00:19	10:0	12A	14.39	1.21	22.46	2.5	1.27
PGC 052460	February 24, 2012—05:28:32	10:0	12A	13.84	1.26	22.53	2.5	1.35
NGC 5729	February 24, 2012—05:48:40	10:0	12A	12.94	1.27	22.56	2.4	1.26
PGC 029653	February 25, 2012—00:58:55	10:01	12A	11.59	1.20	22.16	2.1	1.36
NGC 6140	July 07, 2012—22:40:30	10:0	12A	11.48	1.25	23.77	2.1	1.07
UGC 10806	July 07, 2012—23:26:24	10:0	12A	13.55	1.07	24.51	2.2	1.03
UGC 10608	July 08, 2012—22:43:53	10:0	12A	14.89	1.10	23.93	2.1	1.23
UGC 09992	July 10, 2012—21:39:29	10:01	12A	0.00	1.28	×	X	1.19
UGC 10194	July 10, 2012—21:56:16	10:0	12A	0.00	1.22	X	X	1.13
UGC 10736	July 10, 2012—22:23:08	10:0	12A	14.56	1.32	24.31	2.2	1.36

continued

Table E.4 (continued)

Name	UTC (First observation)	Instrument	Semester	g' (mag)	Airmass	ZP	Calibration	Seeing
NGC 6503	July 10, 2012—22:46:17	0:01	12A	10.48	1.35	23.96	2.1	1.29
NGC 0157	July 12, 2012—04:44:44	0:01	12A	10.68	1.37	24.06	2.1	1.59
PGC 054817	July 16, 2012—22:22:11	10:0	12A	14.42	1.36	24.19	2.5	1.74
PGC 054944	July 16, 2012—22:51:17	10:0	12A	13.26	1.39	23.63	2.3	1.39
NGC 4750	July 18, 2012—23:18:44	0:01	12A	11.57	1.94	23.87	2.5	1.27
PGC 005329	July 20, 2012—04:25:24	10:0	12A	15.09	1.42	24.11	2.4	1.61
NGC 0918	September 09, 2012—03:52:55	10:0	12B	0.00	1.02	24.12	1	1.26
UGC 01999	September 11, 2012—03:52:57	10:0	12B	0.00	1.02	24.22	1	1.25
NGC 1036	September 11, 2012—04:13:43	0:01	12B	0.00	1.01	24.22	1	1.30
PGC 012439	September 11, 2012—05:19:01	10:0	12B	0.00	1.19	24.22	1	1.10
NGC 1073	September 12, 2012—03:47:30	10:0	12B	0.00	1.14	24.19	1	1.37
NGC 1253	September 13, 2012—04:25:38	10:0	12B	0.00	1.18	24.09	1	1.57
PGC 012068	September 13, 2012—05:04:40	0:01	12B	0.00	1.20	24.09	1	1.39
NGC 1337	September 14, 2012—04:03:48	10:0	12B	0.00	1.29	24.11	1	1.48
PGC 014600	September 14, 2012—04:32:30	10:0	12B	0.00	1.29	24.11	1	1.61
NGC 1507	September 14, 2012—04:49:40	10:0	12B	0.00	1.19	24.11	1	1.49
PGC 015625	September 14, 2012—05:08:53	0:01	12B	0.00	1.32	24.11	1	1.40
UGC 03070	September 22, 2012—03:15:23	10:0	12B	0.00	1.17	24.20	1	1.74
NGC 0672	September 23, 2012—01:49:32	0:01	12B	0.00	1.02	24.21	1	1.47
NGC 1222	September 23, 2012—02:17:02	10:01	12B	0.00	1.32	23.95		1.85

Table E. (Commuca)	maca)							
Name	UTC (First observation)	Instrument	Semester	g' (mag)	Airmass	ZP	Calibration	Seeing
NGC 2787	September 23, 2012—05:24:15	0:01	12B	0.00	1.83	24.03	1	1.46
PGC 012130	October 07, 2012—02:08:11	10:0	12B	0.00	1.26	24.15	1	1.90
NGC 2985	October 09, 2012—04:25:28	0:01	12B	0.00	1.96	24.20	1	1.48
NGC 3027	October 09, 2012—04:45:13	0:01	12B	0.00	1.89	24.20	1	1.34
NGC 3147	October 09, 2012—05:02:01	0:01	12B	0.00	1.92	24.20	1	1.41
UGC 05688	October 09, 2012—05:38:17	0:01	12B	0.00	1.81	24.20	1	1.24
UGC 05612	October 13, 2012—04:48:58	0:01	12B	0.00	1.93	24.23	1	1.33
UGC 06378	November 13, 2012—03:58:05	0:01	12B	14.46	1.87	23.53	2.3	1.66
UGC 05979	November 13, 2012—04:44:13	10:0	12B	15.15	1.58	25.00	2.5	1.48
NGC 3654	November 13, 2012—05:01:34	0:01	12B	13.45	1.63	24.17	2.3	1.15
PGC 027747	November 22, 2012—04:52:38	0:01	12B	14.18	1.38	24.34	2.2	2.11
PGC 027616	November 22, 2012—05:21:42	10:0	12B	13.84	1.34	24.58	2.2	1.68
PGC 027825	November 22, 2012—05:38:38	0:01	12B	0.00	1.26	×	×	1.73
PGC 027810	November 22, 2012—05:56:32	10:0	12B	13.73	1.31	24.35	2.2	2.16
UGC 05765	November 23, 2012—03:52:24	0:01	12B	14.64	1.58	24.31	2.5	1.41
NGC 2974	November 23, 2012—05:08:37	0:01	12B	11.33	1.28	23.90	2.1	2.01
PGC 027833	November 23, 2012—05:25:38	0:01	12B	13.33	1.28	24.30	2.2	2.04
IC 0600	December 08, 2012—04:22:28	0:01	12B	13.16	1.33	23.32	2.2	1.60
PGC 031979	December 08, 2012—05:27:12	0:01	12B	13.64	1.35	24.13	2.2	1.13

continued)

Table E.4 (continued)

Name	UTC (First observation)	Instrument	Semester	g' (mag)	Airmass	ZP	Calibration	Seeing
IC 0630	December 13, 2012—06:13:47	10:0	12B	0.00	1.24	23.80		1.94
NGC 3730	December 14, 2012—05:39:37	10:0	12B	8.56	1.38	24.22	2.5	1.55
NGC 3691	December 16, 2012—04:26:10	10:0	12B	0.00	1.22	24.15	1	1.54
NGC 4319	December 17, 2012—04:22:48	10:0	12B	0.00	1.63	24.29	1	1.30
PGC 036274	December 17, 2012—05:17:54	10:0	12B	0.00	1.37	24.29		1.17
IC 2963	December 18, 2012—04:46:15	10:0	12B	0.00	1.47	23.90	1	3.09
NGC 4736	December 21, 2012—03:24:10	10:0	12B	8.56	1.75	22.07	2.1	1.48
PGC 036551	December 21, 2012—04:40:47	10:0	12B	14.24	1.40	24.32	2.2	1.62
UGC 08737	December 22, 2012—03:43:38	10:0	12B	14.15	1.89	24.68	2.3	1.74
PGC 037238	December 22, 2012—04:02:43	10:0	12B	13.88	1.64	24.39	2.2	1.72
NGC 4428	December 22, 2012—05:29:30	10:0	12B	12.98	1.45	24.21	2.5	1.76
NGC 4487	December 22, 2012—05:46:25	10:0	12B	11.74	1.40	24.42	2.2	1.56
PGC 041965	December 25, 2012—06:27:37	10:0	12B	0.00	1.29	23.59	1	1.33
NGC 5194	January 05, 2013—04:06:23	10:0	12B	13.34	1.38	23.83	2.2	1.44
NGC 4593	January 05, 2013—05:28:26	0:01	12B	13.39	1.28	24.35	2.2	1.68
PGC 044278	January 06, 2013—05:16:58	10:0	12B	11.09	1.34	22.05	2.1	1.52
IC 3908	January 06, 2013—05:34:50	10:0	12B	11.50	1.33	24.47	2.1	1.64
NGC 4958	January 06, 2013—05:55:43	10:0	12B	13.60	1.31	24.48	2.2	1.44
								(F 1)

Continued

ntinued)
<u>ુ</u>
le E.4
Tabl

(nonument)	(page)							
Name	UTC (First observation)	Instrument	Semester	g' (mag)	Airmass	ZP	Calibration	Seeing
NGC 4818	January 06, 2013—06:12:43	0:01	12B	13.62	1.28	23.76	2.1	1.20
NGC 4546	January 10, 2013—05:42:17	0:01	12B	0.00	1.20	24.18	1	1.22
NGC 4775	January 10, 2013—06:09:06	0:01	12B	0.00	1.24	24.18	1	1.30
PGC 044358	January 11, 2013—05:28:23	0:01	12B	13.60	1.34	24.48	2.2	1.62
NGC 4948A	January 11, 2013—06:16:45	0:01	12B	13.62	1.26	23.76	2.1	1.88
NGC 4731	January 11, 2013—06:33:42	0:01	12B	11.61	1.22	23.88	2.1	1.38
NGC 4504	January 13, 2013—04:56:28	0:01	12B	0.00	1.30	24.16	1	1.70
NGC 4981	January 13, 2013—05:30:26	0:01	12B	0.00	1.29	24.16	1	1.47
NGC 4995	January 13, 2013—06:07:39	0:01	12B	0.00	1.26	24.16	1	1.93
NGC 4942	January 13, 2013—06:25:40	I0:0	12B	0.00	1.24	24.16	1	1.36

Column I Galaxy name. Column II Time of the first observation of the three exposures of 100 s/galaxy. Column III Instrument. Column IV Semester of mages of UGC 09992, UGC 10194 and PGC 027825 have a value X in Columns VII and VIII. These images could not be calibrated because we did not have text). Column VI Mean airmass of the three exposures. Column VII Zero-point value for flux-calibration. Column VIII) Calibration method: 1.—standard observation. Column V g' theoretical magnitude calculated using the stellar libraries and photometric values of B, V, R, I and J magnitudes from NED (see 2.2—computed from B and R, 2.3—from B and I, 2.4—from B, R and I, and 2.5—from B and J. Column IX Seeing of the combined image. Note The LT stars, 2.—cross-calibrated using a total g' magnitude as derived from photometry in NED, from different bands, namely 2.1—g' computed from B and V, standard star observations, nor photometric information to calculate a total g' magnitude

E.3 Kinematic Detection and Constraints on the Origin of an Occulting Companion Galaxy Near NGC 7241 and UGC 11964

Ryan Leaman, Santiago Erroz-Ferrer. et al., MNRAS, 450, 2473

E.3.1 Introduction

The observation of interacting galaxies is a rare phenomena. In K14 we find that 5% of the sample analysed show significant morphological evidence of an ongoing interaction. The inspection of our kinematic data for NGC 7241 revealed a starforming companion, which had been previously identified by Giovanelli and Haynes (1984) from examination of a peculiar HI envelope around the galaxy. NGC 7241 is an edge-on galaxy that belongs to the HIPASS J2215+19 group with the other Scd galaxy UGC 11964 (~5 arcmin of separation). The goal of L15 is to characterize the kinematic properties and stellar population of the low mass merger remnant, studying the impact of such phenomena on the host galaxy and possible origin scenarios for this companion within the group. My contributions to this paper are: (i) the kinematical detection of the companion in the H α FP data, (ii) kinematical study of the velocity moment maps of NGC 7241 and the companion individually, (iii) observations and data reduction of the longslit data, (iv) analysis of the GALEX UV images, (v) measurements of the SFRs. L15 also includes surface brightness and dust models, stellar population analysis, spectral energy distribution (SED) fitting and discussions of the formation scenarios of the companion and dynamical state of the group.

E.3.2 Observations and Data Analysis

In L15 we have used several kinds of data. In this section I will focus on those that I have observed and/or reduced. Apart from those described here, in L15 we explain the observations and reduction of SDSS ugriz images from DR8 (Aihara et al. 2011), 2MASS J, H and K_s images from NED, Spitzer 3.6 and 4.5 μ m images from the S⁴G collaboration and VLA HI data from the NRAO archive (PI: Giovanelli).

Hα Fabry-Perot data

The observations of NGC 7241 is part of our group's large programme to analyse the kinematics of disc galaxies. Concretely, NGC 7241 was observed for 2.1 h on June 6th, 2011 with the GH α FaS instrument at the 4.2-m WHT in La Palma. All the information about the observing programme, observations and further data reduction can be found in Chap. 3.

Broad- and narrow-band images

 ${\rm H}\alpha$ narrow-band images were obtained together with the FP data using the ACAM instrument at the WHT in June 2011. However, due to seeing restrictions, we reobserved the galaxy taking advantage of the Service Time of the WHT on June 20th, 2013. Two images were obtained with ACAM: 3×30 s images using a Johnson R filter, with central wavelength 6228Å and FWHM 1322Å; and 3×100 s ${\rm H}\alpha$ images, using a narrow filter having a central wavelength 6589 Å and FWHM 15Å. These data have been reduced as explained in Sect. 3.4.2. Continuum subtraction was performed using the ACAM R-band image following the procedures outlined in Knapen et al. (2004), and the image was flux calibrated with spectrophotometric standard stars. The R-band image was scaled by a factor of 0.0189 and subtracted from the ${\rm H}\alpha$ image during this process.

GALEX UV data of NGC 7241 and UGC 11964 were obtained from the MAST archive. Concretely, we obtained GALEX FUV and NUV images that belong to the AIS survey. The scientific objectives and characteristics of *GALEX*, as well as the surveys are described in Martin et al. (2005) and Morrissey et al. (2005). The *GALEX* FOV is 1.2° and is circular. The effective wavelengths of the two channels (FUV and NUV) are 1516 and 2267 Å, and the image resolution (FWHM) is 4.3″ and 5.3″, respectively, for the FUV and NUV channels. These images have been background-subtracted using the bgsky images provided by the MAST archive.

Longslit data

We obtained longslit spectra using the ISIS spectrograph on the WHT for five hours on August 24th, 2013; using Director's Discretionary Time. The spectrograph was used with the 5300 Å dichroic and the R600B/R gratings. Using the 1×2 binning on the dispersion direction, the final dispersion was $\delta\lambda\approx0.86$ Å. The resulting observed wavelength range was from $\lambda3987-5398$ Å on the blue arm, and from $\lambda6014-7235$ Å on the red arm. Four pointings were selected using the $1.0''\times4.0''$ slit: one along the major axis of NGC 7241, one across the isolated parts of the companion which lie to the west of the major axis of NGC 7241, one along the major axis of UGC 11964, and a final one along the stellar stream in the HI tail protruding from the SE of NGC 7241 (see Fig. E.8).

Bias frames and sky and lamp flats were taken to provide the necessary calibration data, along with CuAr arc lamp exposures which were taken at every pointing. Along with the four science targets, we observed three flux standard stars at three times throughout our five hour observing period. The seeing conditions were excellent, ranging from 0.4–0.8 arcsec. The spectra were reduced using standard long slit reduction procedures in IRAF. First, bias and flat corrections were performed, after which we corrected for illumination before combining the different exposures. Finally, the spectra were wavelength calibrated, sky-background subtracted and flux calibrated.

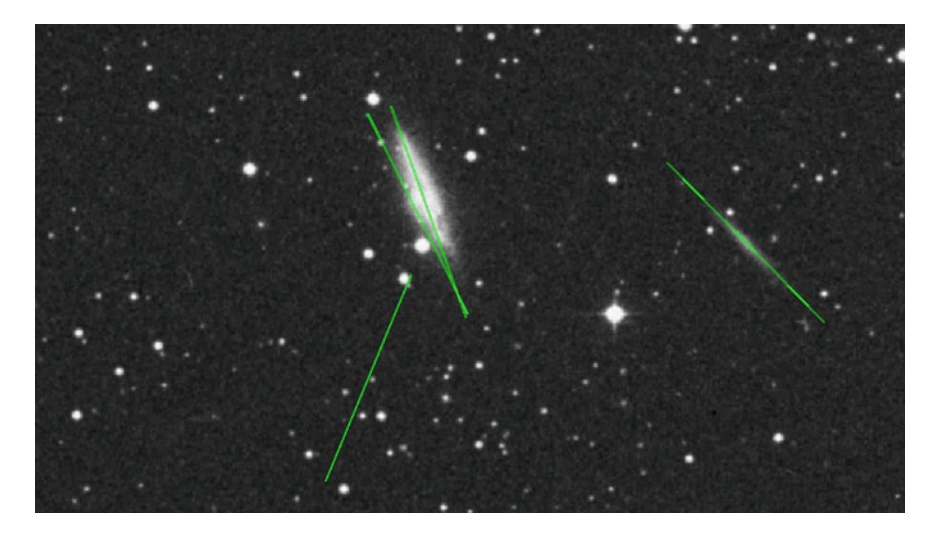


Fig. E.8 DSS image of the group, from NED. Overlaid in green, the four positions of the slit for the ISIS longslit observations: one along the major axis of NGC 7241, one across the isolated parts of the companion which lie to the west of the major axis of NGC 7241, one along the major axis of UGC 11964, and a final one along the stellar stream in the HI tail protruding from the NE of NGC 7241. In the image, North is *up*, East is *left*

E.3.3 Kinematic Detection of the Occulting Compation

GH α FaS data of NGC 7241 were presented in Chap. 3. The inspection of the velocity map of NGC 7241 (see Fig. E.9) revealed a portion of the emission that had significantly different kinematical behaviour than the rest of the edge-on disc. There is a pink-coloured region with velocities systematically higher than those of the edge-on galaxy. The inspection of the spectra (see Fig. E.9) revealed that there were double peaks that did not come from the NII contamination or from other interference order (see the reduction processes of GH α FaS data on Sect. 3.4.1). Therefore, this emission at offset velocity represents a feature which is not physically associated with NGC 7241—a possible star-forming object, which we refer to as the "companion" object throughout this work for clarity.

We have computed the PV diagram along the major axis of NGC 7241 to identify this velocity difference (Fig. E.10). We find that there are some regions where there is both emission from NGC 7241 and the companion (which are the positions where there are two velocities), and we confirm that there is a separation of \sim 40–60 km/s in their emission.

The next step is to divide the data cubes in two, to study each component individually. In Fig. E.11 we have presented the resulting moment maps of the galaxy and the companion, together (left column) and with each feature separately (NGC 7241 middle column, companion right column). The velocity maps reveal the kinematic difference between the galaxy and the companion: unlike NGC 7241 which

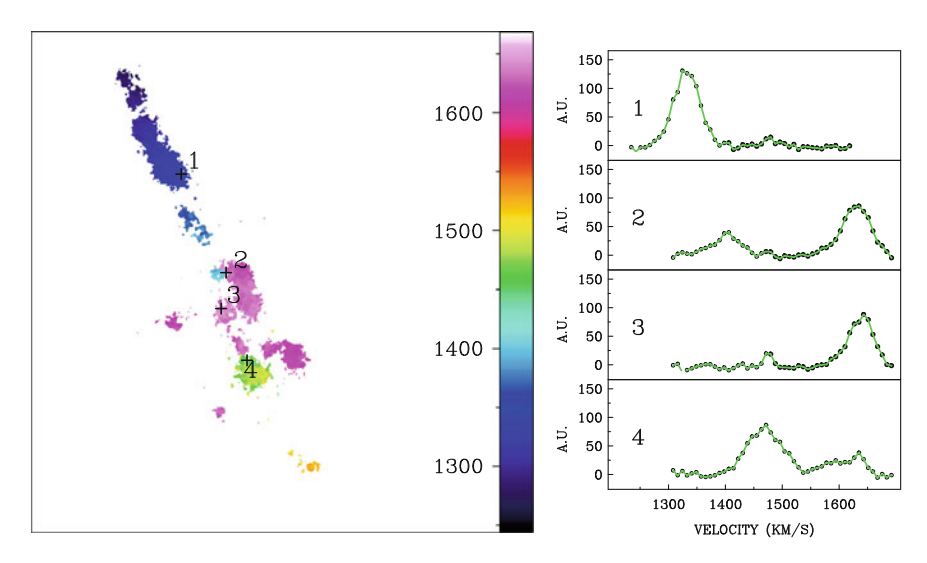


Fig. E.9 Velocity map of NGC 7241 from the H α FP observations. We see emission from two sources: NGC 7241 and the possible companion, with an obvious velocity difference. Four regions have been selected to study the spectra, marked with crosses on the velocity map. In regions 2–4, we see double peaks, corresponding to the emission of both NGC 7241 and the companion

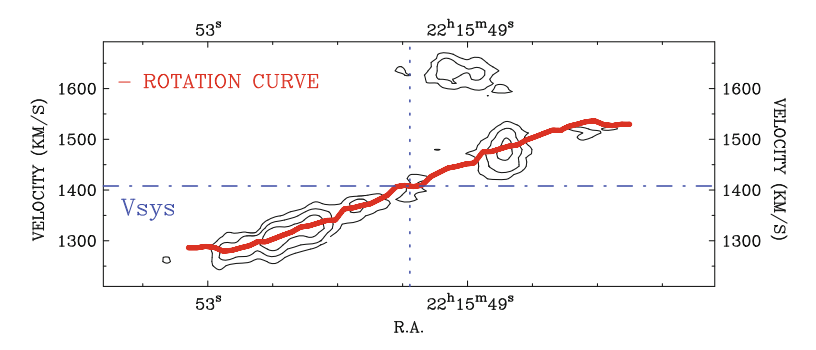


Fig. E.10 PV diagram of NGC 7241 and companion. Overlaid in red, the rotation curve of NGC 7241. The *horizontal dash-dot-dash blue line* corresponds to the systemic velocity of NGC 7241, whereas the *vertical dotted blue line* corresponds to the position of the dynamical centre of NGC 7241. Note the clear separation between the emission of NGC 7241 (below \sim 1550 km/s) and that of the companion (over \sim 1600 km/s)

shows rotation, the companion does not present regular kinematical pattern. In the second moment maps, we see that the velocity dispersion of the companion is not significantly different from that of the HII regions in the body of NGC 7241. Note, however, that the highest velocity dispersions are found near the centre of the galaxy, where it is close to the overlap with the companion.

In L15, we also confirm the findings of Giovanelli and Haynes (1984), by also identifying a secondary velocity peak in the HI moment map centred on NGC 7241.

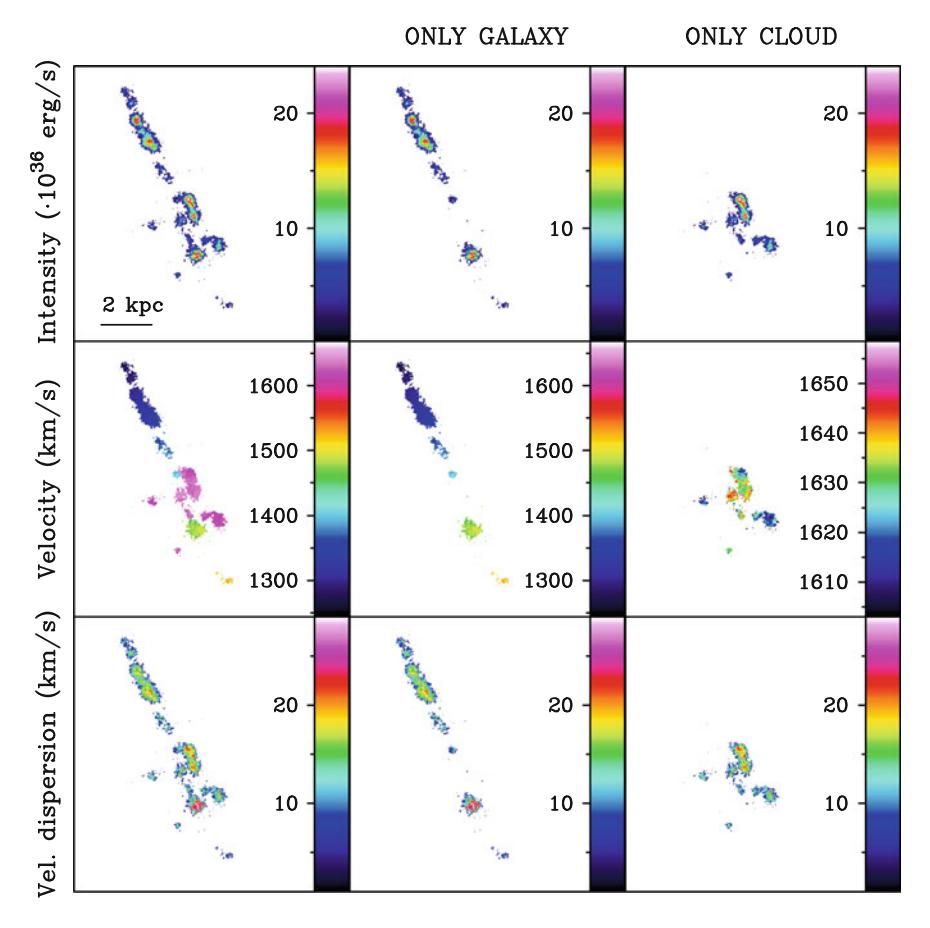


Fig. E.11 Moment maps of NGC 7241 and of the possible companion: intensity map (*top* figures), velocity map (*middle* figures) and velocity dispersion map (*bottom* figures). The first column shows the moment maps for the galaxy and companion together—as observed. The middle panel shows the moment maps just for emission from NGC 7241, and the right hand panels the moment maps for the companion alone. In all panels, the black cross marks the dynamical centre of NGC 7241

While the HI data have much poorer angular resolution, the general velocity signatures are in good agreement, with the companion appearing at nearly the same velocity offset.

E.3.4 Star Formation Rates

We know that the companion is forming stars due to its appearance in $H\alpha$. We have measured the recent SFRs (as measured from the GALEX FUV and NUV and ACAM



Fig. E.12 Colour-composite (3.6 μ m, ugriz) image of NGC 7241 and its occulting companion, presented in L15 (credit to Nik Szymanek). North is up, East left. The image size is approximately 3.7 \times 6.2 arcmin. The occulting companion is distinguished in blue, overlaid with respect to the massive spiral NGC 7241 (color online)

Hα images) of NGC 7241 and the companion, using Eqs. 2.9–2.11. The luminosities have been corrected for Galactic absorption and internal absorption. The Galactic absorption was taken from NED, with a value of A(R) = 0.116 mag (adopting the Schlafly and Finkbeiner 2011 recalibration of the Schlegel et al. 1998 infrared-based dust map and the Galactic extinction curve of by Cardelli et al. 1989 with a total-to-selective extinction of RV = 3.1). Specifically for the FUV and NUV, A(FUV) = 7.9E(B - V), A(NUV) = 8.0E(B - V) and $A(H\alpha) = 2.5E(B - V)$ (Lee et al. 2009), where E(B - V) = A(B) - A(V). The internal extinction was taken from the SED fitting found in L15.

To measure the SFRs and SFR densities (Σ SFRs), we designed a mask that divided the targets in four regions: the region of NGC 7241 that does not overlap with the companion (background hereafter), the region of NGC 7241 that overlaps with the companion (overlap hereafter), the part of the companion that is not overlapping with NGC 7241 (foreground) and UGC 11964. The resulting Σ SFRs can be found in Table E.5.

For the non-overlapping part of NGC 7241 (background), we see that ΣSFR (H α) $\approx \Sigma SFR(FUV) \approx \Sigma SFR(NUV)$, indicating that the galaxy has been forming stars continuously. However, for the foreground part of the companion, the fact that $\Sigma SFR(H\alpha)$ is higher than $\Sigma SFR(FUV)$, $\Sigma SFR(NUV)$ indicates that there has been a recent enhancement in the formation of stars. The overlap region is forming stars at a higher rate than the foreground and background regions, indicating again the triggering of star formation due to the interaction. The fact that UGC 11964 presents such high values of ΣSFR is due to the internal extinction derived from the SED

Region	$\Sigma SFR(H\alpha)$ $M_{\odot} \text{ yr}^{-1} \text{ kpc}^{-2}$	$\Sigma SFR(FUV)$ $M_{\odot} \text{ yr}^{-1} \text{ kpc}^{-2}$	$\Sigma SFR(NUV)$ $M_{\odot} \text{ yr}^{-1} \text{ kpc}^{-2}$
NGC 7241 (Background)	0.010 ± 0.004	0.010 ± 0.004	0.017 ± 0.007
Companion (foreground)	0.019 ± 0.008	0.013 ± 0.005	0.017 ± 0.007
Companion (overlap)	0.060 ± 0.026	0.028 ± 0.011	0.040 ± 0.016
UGC 11964	_	0.076 ± 0.030	0.114 ± 0.046

Table E.5 Σ SFRs (H α , FUV and NUV) measured for the four regions subject to study: background, foreground, overlap and UGC 11964

fitting, which is very difficult to constrain in such thin target, and also for the lack of photometric data (especially *Spitzer* data). If we adopt the same internal extinction as for NGC 7241, we obtain $\Sigma SFR(FUV) = 0.010 \pm 0.004$ and $\Sigma SFR(NUV) = 0.015 \pm 0.006 \, M_{\odot} \, \text{yr}^{-1} \, \text{kpc}^{-2}$, very similar to those of NGC 7241.

E.3.5 Concluding Remarks

We have performed a multi-wavelength photometric and kinematic study of an undetected optical companion of NGC 7241. This study has enabled us to constrain the evolution of the group formed by NGC 7241, the companion and UGC 11964. The companion is detected as an offset velocity component of NGC 7241, which lies beneath the line of sight and overlaps partially with NGC 7241. The stellar populations, SF, and dust properties, as derived from our H α data, spectroscopy and SED fitting suggest that this star forming object has formed only within the last couple of Gyr (see L15 for more details).

References

K.N. Abazajian, J.K. Adelman-McCarthy, M.A. Agüeros et al., ApJS 182, 543 (2009)

H. Aihara, C. Allende Prieto, D. An et al., ApJS 193, 29 (2011)

G. Bruzual, S. Charlot, MNRAS **344**, 1000 (2003)

J.A. Cardelli, G.C. Clayton, J.S. Mathis, ApJ 345, 245 (1989)

D.M. Elmegreen, B.G. Elmegreen, S. Erroz-Ferrer et al., ApJ 780, 32 (2014)

M. Fujimoto, ApJ 152, 391 (1968)

R. Giovanelli, M.P. Haynes, in *Bulletin of the American Astronomical Society*, vol. 16 (Bulletin of the American Astronomical Society, 1984), p. 961

R.C. Kennicutt Jr, ARA&A 36, 189 (1998)

R.C. Kennicutt Jr., J.C. Lee, S.J. José G. Funes, S. Sakai, S. Akiyama, ApJS 178, 247 (2008)

J.H. Knapen, S. Erroz-Ferrer, J. Roa et al., A&A **569**, A91 (2014)

J.H. Knapen, S. Stedman, D.M. Bramich, S.L. Folkes, T.R. Bradley, A&A 426, 1135 (2004)

R. Leaman, S. Erroz-Ferrer, M. Cisternas, J.H. Knapen, MNRAS 450, 2473 (2015)

J.C. Lee, A. Gil de Paz, C. Tremonti et al., ApJ 706, 599 (2009)

D.C. Martin, J. Fanson, D. Schiminovich et al., ApJ 619, L1 (2005)

E. Mentuch, R.G. Abraham, S. Zibetti, ApJ 725, 1971 (2010)

P. Morrissey, D. Schiminovich, T.A. Barlow et al., ApJ 619, L7 (2005)

J. Moustakas, R.C. Kennicutt Jr, ApJS 164, 81 (2006)

E. Ricciardelli, A. Vazdekis, A.J. Cenarro, J. Falcón-Barroso, MNRAS 424, 172 (2012)

M.S. Roberts, AJ 74, 859 (1969)

E.F. Schlafly, D.P. Finkbeiner, ApJ 737, 103 (2011)

D.J. Schlegel, D.P. Finkbeiner, M. Davis, ApJ 500, 525 (1998)

K. Sheth, M. Regan, J.L. Hinz et al., PASP 122, 1397 (2010)

M.F. Skrutskie, R.M. Cutri, R. Stiening et al., AJ 131, 1163 (2006)

I.A. Steele, R.J. Smith, P.C. Rees et al., in *Society of Photo-Optical Instrumentation Engineers* (SPIE) Conference Series, vol. 5489, ed. by J.M. Oschmann Jr. Ground-Based Telescopes (2004), pp. 679–692

A. Vazdekis, A.J. Cenarro, J. Gorgas, N. Cardiel, R.F. Peletier, MNRAS 340, 1317 (2003)

A. Vazdekis, E. Ricciardelli, A.J. Cenarro et al., MNRAS 424, 157 (2012)

A. Vazdekis, P. Sánchez-Blázquez, J. Falcón-Barroso et al., MNRAS 404, 1639 (2010)

D.G. York, J. Adelman, J.E. Anderson Jr et al., AJ 120, 1579 (2000)

Index

A	M
ACAM, 48, 51, 67	Morphological classification, 3, 25, 36, 44,
ALFOSC, 26	45, 71
Arm class, 71, 88, 94	
Asymmetric drift correction, 107	
	N
В	Non-circular motions, 55, 81, 91
Bar strength, 88, 92, 116	
Bulges, 116	
	R
	Rotation curve slopes, 109
D	Rotation curves, 52, 72, 101
Dark matter, 126	
Dust correction, 33, 38	
	S
G	S ⁴ G survey, 15, 70, 88
GALEX, 28	SAURON, 69
GHαFaS, 44, 46, 48, 68	Star formation tracers, 12, 33, 38